UNIVERSITY OF SOUTHAMPTON
School of Civil Engineering and the Environment

INFLUENCE OF SOME PARTICLE CHARACTERISTICS ON THE SMALL STRAIN RESPONSE OF GRANULAR MATERIALS

by

Man T. Bui

A Thesis Submitted in Partial Fulfilment for the
Degree of Doctor of Philosophy

April 24, 2009

To my Grandmother, my parents

my wife, Thanh Huong
and my sons, An–Vinh & An–Phu

UNIVERSITY OF SOUTHAMPTON
SCHOOL OF CIVIL ENGINEERING AND THE ENVIRONMENT

ABSTRACT

Doctor of Philosophy
by Man T. Bui

The key parameters representing the small strain response of geomaterials are the very small strain shear modulus, G_{max}, shear modulus degradation G/G_{max}, and damping ratio. These are also important parameters in the design of foundations where only small deformation takes place. A review of the literature suggests that shear modulus and damping ratio at small strain are significantly influenced by void ratio and mean effective stress. They are also influenced by other parameters such as confinement time, anisotropy, number of loading cycles, and OCR, etc. However, there was little evidence in the literature showing the influence of particle characteristics on the small strain response of geomaterials.

In this research the effects of some particle characteristics such as particle size and particle shape on the small strain response of soils are investigated. Granular materials with different particle shapes, namely glass Ballotini with various diameters, Leighton Buzzard sand fraction B and E, glass glitter, glass nugget, as well as mixtures of Leighton Buzzard sand fraction B and 0.1 mm mica, are tested using a fixed-free resonant column apparatus (RCA).

The test results suggest that particle shape significantly influences the small strain response of geomaterials. Both particle form and particle roundness have correlations with the values of G_{max} normalised by a void ratio function, $F(e)$. Normalised G_{max} increases with increasing sphericity and roundness of the particle. At the same void ratio, the stress exponent, n, elastic threshold strain, γ_e, and shear modulus degradation, G/G_{max}, for granular materials decrease with an increase in sphericity and roundness. Material damping ratio also increases with increasing sphericity and roundness.

Particle size was also found to significantly influence the small strain response of glass Ballotini. At the same void ratio and effective stress, G_{max} increases with an increase in particle diameter. Elastic threshold strain, γ_e, and G/G_{max} also increase with an increase in particle diameter. In addition, stress exponent, n, and material damping ratio decrease with increasing particle diameter. It can be concluded that fine soils are more susceptible to an increment in shear strain and effective stress than coarse soils.

The addition of a small proportion of 0.1 mm mica to Leighton Buzzard sand fraction B (LBSB) considerably reduces G_{max}, even though the void ratios of the mixtures are lower than those of the sand alone. The stiffness reduction of the mixtures of LBSB and 0.1 mm mica can be attributed to the effects of both platy particle shape and fine particle size of mica.

The effects of particle characteristics on the small strain response of geomaterials can be explained using the proposed porous discontinuous-solid model. A dry soil element is assumed to consist of two phases, namely the pore and the discontinuous solid, where the stiffness of discontinuities is represented by a shear wave velocity through the contact network, $V_{contact}$, which is a function of particle characteristics. Particle size and particle shape create both macro effects (e.g. effect of void ratio) and micro effects (at the contact level) on the small strain response of granular materials. The model postulates that an increase in void ratio will increase travel length, and hence decrease V_s. The model suggests that the macro effect of void ratio on G_{max} can be normalised using the theoretical (universal) void ratio function, $F(e) = (1 + e)^{-3}$, which can be applied for both clays and sands with various void ratio range. And by doing so, the micro effects of particle shape and particle size can be observed and taken into account using a particle characteristic coefficient, C_p, which increases with increasing particle diameter, sphericity, and roundness.

In addition, during testing relatively stiff specimens using the RCA, equipment compliance was observed, leading to an significant underestimation of the natural frequencies of the specimens. In order to identify the source of compliance and evaluate the influence of equipment compliance on the measured data using the RCA, several finite element (ABAQUS) models were developed. The numerical analysis results suggest that the stiffness of the drive mechanism, the mass and/or fixity of the test base, and calibration bar design significantly affect the test results. To correct for the effects of system compliance, a new model termed *two spring model* is developed. The model key parameters i.e. stiffness of the equipment, $K_{equipment}$, and mass polar moment of inertia of the drive mechanism, I_0, can be calibrated through testing of a series of aluminium calibration bars.

Declaration of Authorship

I, Man Tan Bui, declare that the thesis entitled "Influence of Some Particle Characteristics on The Small Strain Response of Granular Materials" and the work presented in it are my own and has been generated by me as the result of my own original research. I confirm that:

1. This work was done wholly or mainly while in candidature for a research degree at this University;
2. Where any part of this thesis has previously been submitted for a degree or any other qualification at this University or any other institution, this has been clearly stated;
3. Where I have consulted the published work of others, this is always clearly attributed;
4. Where I have quoted from the work of others, the source is always given. With the exception of such quotations, this thesis is entirely my own work;
5. I have acknowledged all main sources of help;
6. Where the thesis is based on work done by myself jointly with others, I have made clear exactly what was done by others and what I have contributed myself;
7. Parts of this work have been published as:
    - Clayton C. R. I., Priest J. A., Bui M. T., Zervos A., and Kim S.G., (2009) "The Stokoe resonant column apparatus: effects of stiffness, mass and specimen fixity" Géotechnique, 58,(article number 700096):1-9 (accepted for publication).
    - Bui M. T., Priest J. A., (2007). "Discussion of 'particle shape effects on packing density, stiffness, and strength: natural and crushed sands' by Gye-Chun Cho, Jake Dodds, and J. Carlos Santamarina", Journal of Geotechnical and Geoenvironmental Engineering, ASCE, 133(11):1473-1474.
    - Bui M. T., Clayton C. R. I., Priest J. A., (2007). "Effects of particle shape on G_{max} of geomaterial", Proceeding of the 4th International Conference on Earthquake Geotechnical Engineering, Thessaloniki, Kyriazis D. Pitilakis (ed), Paper No. 1536.
    - Bui M. T., (2007). "Supplementation torsional forced vibration model for fixed-free resonant column test", Proceeding of the 4th International Conference on Earthquake Geotechnical Engineering, Thessaloniki, Kyriazis D. Pitilakis (ed), Paper No. 1452.

Signed: ....

Date: April 24, 2009

Acknowledgements

First of all, the Author would like to thank the Ministry of Education and Training of Vietnam and the School of Civil Engineering and Environment, University of Southampton, who kindly supported this research. Without the support, the study is unlikely to be done.

The Authors sincerely thank the expertise, the useful advice and discussion, and the constant support and guidance of his supervisor, Prof C.R.I. Clayton. During the research period, Professor Clayton guided the author in the right direction to achieve the research goals.

The Authors sincerely thank the regular help, comments, discussions of his co-supervisor, Dr. Jeffrey A. Priest, who was very enthusiastic in discussion with the author about the study. The discussions helped the author understand more about the research. Dr. Priest, with his experience, assisted the author to solve many laboratory technical problems. He also helped the author to improve his writing in English.

Deep in his heart, the author would like to thank his grandmother, who always encouraged his study, who always supported his spirit, who was always his study inspiration and motivation, and who always wished the author to succeed in his career. Very sadly, she was not patient enough to see her grandson success.

Above all, the Author would like to express his deep gratitude to his parents, who brought him up in love, who constantly encourage his study, who always wish all the best to the Author.

The Author very grateful his wife, Thanh-Huong, who sacrificed her time to take care of the family whilst the Author was busy with this study, and thank his beloved sons, An-Vinh and An-Phu, who had inadequate care of their father during the study, who often smiles, and who are the author endless source of working inspiration.

Finally, the Author would like to thank other individuals, who helped the author complete the research:

- The lab-supervisor Mr. Harvey Skinner, and the lab-technician Mr. Earl Peter. Without their helps, the laboratory test could not be completed.
- Mrs. Jacqui A. Holmes, the research secretary/postgraduate program coordinator, for her kindly supports during the research

- Dr. H.C. Le, University of Cardiff, for his helps in taking high quality microscope images of the granular particles used in this research.
- His colleagues, such as Dr. Sonia Heaven, Dr. Chandu Chandra Reddy, Mr. Athma R. Bhandari, Mr. Gerrit Smit, Miss Emily Kingston, Mr. Emmanuel Fleris, Mr. Majed Alsaydalani, who shared their time in office and in laboratory with the author.

Contents

List of Tables

List of Figures

List of symbols

α	Shear wave velocity at 1.0 kPa
α_0	Material coefficient, $\alpha_0 = C_p \times F(e)$
α_r	Ratio of resonant frequency to natural frequency
β	Pressure exponent reflecting the sensitivity of pressure on V_s
δ	Logarithmic decrement or attenuation constant
ΔG	Change in shear modulus (with time)
ΔW_d	Energy lost per cycle
δ_x	Harmonic tangential compliance
δ_0	Tangential compliance vibratory amplitude
γ	Shear strain
μ_c	Material viscosity
μ	Constant coefficient of friction
ν	Material Poisson's ratio
σ_0'	Mean effective stress
θ	Angle of twist
ρ	Mass density
ρ_s	Specific density
τ	Shear stress
ψ	Phase angle
ψ	True sphericity
ψ_d	Phase angle of damped oscillation
ψ_p	Maximum projection sphericity
ψ_O	Operational sphericity
ψ_w	Working sphericity
ω	Angular velocity
ω_d	Resonant circular velocity of damped oscillation
ω_r	Resonant circular velocity
ω_0	Natural circular velocity
σ_0'	Applied effective stress
σ_r	Reference pressure ($\sigma_r = 1.0kPa$)
A	Acceleration amplitude
a	Contact radius

AI	Angularity index
A_{max}	Maximum acceleration amplitude
B	Empirical parameter used in Eq. 2.12 (Iwasaki & Tatsuoka, 1977)
C_p	Particle characteristic coefficient
CSF	Corey's shape factor
C_u	Coefficient of uniformity
d	Diameter
D	Damping ratio
D_5	Grain size with 5% finer
D_{50}	Mean grain size with 50% finer
D_{min}	Minimum damping ratio
D_r	Relative density
E	Young's modulus
E_{grain}	Young's modulus of a particle
E_{max}	Maximum Young's modulus of a soils
e	Void ratio
e_{max}	Maximum void ratio
e_{min}	Minimum void ratio
f_r	Resonant frequency
f_0	Natural frequency
f_1, f_2	Half power frequencies
$F(e)$	Void ratio function
$F(e)_V$	Theoretical void ratio function for V_s
$F(e)_G$	Theoretical void ratio function for G_{max}
G	Shear modulus
G_{max} or G_0	Maximum shear modulus
G/G_{max}	Stiffness degradation
G_{grain}	Shear modulus and a particle
G_s	Specific gravity
I_0	Mass polar moment of inertia of the drive mechanism
I_a	Moment of inertia of top disc
$I_c = 2D^2I_0$	Virtual damping moment of inertia of the system
I_G	Time normalised shear modulus
I_m	Mass polar moment of inertia of additional disc
I_p	Area polar moment of inertia of circular cross section of specimen
k	Shear stiffness
$k_{equipment}$	Shear stiffness of RCA
k_T	Ratio of tangential force at contact to frictional force, $k_T = \dfrac{T}{\mu \times P}$
$k_{specimen}$	Shear stiffness of specimen
k_0	Ratio of horizontal to vertical effective stress
L	Sample height
n	Stress exponent

N	Number of loading cycles
$\bar{N}_c$	Coordination number
$\bar{N}_v$	Number of contact per unit solid volume
OCR	Overconsolidation ratio
P	Normal contact load
R	Radius
RMS	Root mean squared
$V_{RMS.peak}$	Peak RMS amplitude
$V_{RMS.noise}$	RMS noise amplitude
R_n	Roundness index
r	Radial distance from specimen axis
$SEES$	Scalene ellipsoid equivalent sphericity
t	Time
$t_{dis.solid}$	Travel time through discontinuous solid phase
t_{grain}	Travel time through a particle
$t_{contact}$	Travel time through the contact network
T	Tangential force or harmonic torsional force, $T = T_0 \sin(\omega t + \varphi)$
T_R	Resisting torque
$V_{contact}$	Shear wave velocity through contact network
V_s	Shear wave velocity
W_d	Work done

Chapter 1

Introduction

1.1 Background and study objectives

Small strain[1] behaviour of geomaterials is one of the important topics in soil mechanics. Generally, stress-strain relationship of geomaterials is non-linear. However, there is a narrow range of shear strain (e.g. less than 0.001%), where the relationship is linear. The ratio of the shear stress to the shear strain at the linear range is termed maximum shear modulus, G_{max}. When the shear strain increases beyond the linear range, damping ratio increases and the shear modulus, G, decreases. Therefore, the ratio G/G_{max} is the key parameter used for benchmarking the non-linear stress-strain behaviour of soil under both monotonic and cyclic loading. Based on the isotropic elastic theory, G_{max} can be calculated from shear wave velocity, V_s, propagating in a soil medium with mass density, ρ, from the following relationship:

$$G_{max} = \rho \cdot {V_s}^2 \tag{1.1}$$

In geotechnical design, deformations of some geotechnical structures, such as deep excavation beside existing building, tunnelling, integral bridge abutments, bridge piers, pile foundations, road, machine foundations (Fig. 1.1), under repetitive and rapidly applied loads (e.g. dynamic compaction, earthquakes, pile driving, machine vibrations, vehicles, winds, waves, etc.) must be small. The prediction of the stress-strain response of these geotechnical structures requires knowledge of the small strain shear modulus of soils. Therefore, understanding of the parameters influencing the small strain response of the geomaterials is crucial.

It is recognised that void ratio and mean effective stress greatly affect the small strain behaviour of soils. Other parameters affecting the small strain behaviour of soils are inherent anisotropy, confinement time, number of loading cycles, cementation/bonding etc. Overconsolidation ratio significantly affects the small strain properties of clay but not sand.

However, whether or not particle characteristics influence the small strain behaviour of

---

[1] e.g. less than 0.01%.

geomaterials is still inconclusive. Hardin & Drnevich (1972*b*); Iwasaki & Tatsuoka (1977); Menq & Stokoe (2003) gave different conclusions on influences of particle size on G_{max}. Recently, Cho *et al.* (2006) drew a conclusion that V_s increase with particle regularity, which was defined as the average of sphericity and roundness; however their observation could be attributed to the variation in particle size and void ratio.

How and why particle characteristics influence the small strain behaviour of geomaterials is not well understood, e.g. the reasons why stress-strain behaviour of geomaterials is linear only in a very small region are not clearly known. Contrary to experimental observations of many researchers, Wood (2007), according to his numerical study, has suggested that the elastic region may not exist.

More than 40 years ago, Hardin & Richart (1963) suggested that particle shape affects G_{max} only by changing the void ratio range ($e_{max} - e_{min}$). Hardin & Drnevich (1972*b*) classified particle characteristics (including particle size, particle shape, particle gradation and mineral composition) as relatively unimportant parameters when measuring small strain shear modulus. They assumed that particle characteristics caused changes in void ratio and effective strength envelope. The question is that if the effect of void ratio is normalised (removed), does particle characteristics influence G_{max} of geomaterials? For example, are G_{max}, shear modulus degradation, and damping ratio of round Ottawa sand and those of angular crushed quartz *at the same void ratio* different? The results of the previous studies are ambiguous with regarding this question.

This research, therefore, is aimed at exploring the influence of some particle characteristics on the small strain behaviour of granular materials. The goals of the study are to answers the main following questions:

- If the effect of void ratio is removed, does particle size and particle shape influence the small strain response of geomaterials? For example, at the same void ratio is G_{max} of specimens of 1.0 mm and 2.0 mm glass Ballotini is the same? The Author's preliminary research results obtained from the first studying year showed that particle shape influences G_{max} of geomaterials. Therefore, further study was planned and carried on to answer the two following questions:

- How do the particle size and particle shape influence the small strain response of geomaterials? For example, is there any correlation between G_{max} and particle sphericity or particle angularity?

- Why do particle characteristics influence the small strain response of geomaterials?

1.2 Limitation, scope, and views points of the study

In this research, the Stokoe resonant column apparatus (RCA) was used to measure the small strain properties of granular materials with different particle size and shape, i.e. Glass Ballotini with size ranging from 0.1 mm to 3.0 mm, Leighton Buzzard sand fraction B (LBSB), Leighton Buzzard sand fraction E (LBSE), 1.0 mm crushed glass nugget, 1.0

mm platy glass glitter, and mixtures of LBSB and fine (0.1 mm) platy mica[2].

Particle characteristics may include particle size, shape, mineral, inter-particle coefficient of friction, and elastic constants etc. In this research, only effects of particle size and particle shape were investigated. Effects of other parameters on the small strain response were out of the scope of this study.

In general, particle shape includes three independent parameters namely, particle form (e.g. sphericity), particle roundness, and particle roughness. This research did not investigate the effects of particle roughness due to technical difficulties, e.g. lack of a particle roughness descriptor that is suitable for using with the available measurement technology.

Effects of particle size were investigated via testing specimens of single (mono) size spherical particle (i.e. glass Ballotini) with different particle diameters. The reason is that the packing density of single size spherical particles is generally independent of particle diameter. Miura *et al.* (1997); Maeda & Miura (1999); Cubrinovski & Ishihara (2002) suggest that void ratio range is influenced not only by particle shape, but also particle size, gradation, and D_{50}.

Comparison of G_{max} of two specimens with different particle size and particle shape, but with the same void ratio will allows the effects of particle size and particle shape on the small strain behaviour of geomaterials to be assessed. However, Miura *et al.* (1997); Maeda & Miura (1999); Cubrinovski & Ishihara (2002) suggest that two geomaterials having different particle shape will have different void ratio range (e.g. minimum density of Leighton Buzzard sand fraction B is higher than maximum density of glass nugget or glass glitter). Therefore, in this research, the effect of void ratio was normalised by using the theoretical (universal) void ratio function developed in Chapter 6.

In order to give some explanations into the effects of particle characteristics on the small strain response of the geomaterials, this study examined the small strain response of soil from the viewpoint of micro mechanics.

Furthermore, during testing relatively stiff specimens using the Stokoe RCA, certain assumption related to derivation of the analytical solutions is violated, leading to a significant error in measurement of shear modulus at small strain. It was largely accepted that the Stokoe RCA was single-degree-of-freedom (SDOF) torsional vibratory system. However, due to effects of equipment compliance (e.g. compliance of the driving system, of the base mass, and base fixity etc.) this was not the case. Results of calibration tests conducted using aluminium bars (presented in section 3.4.1) show that the measured resonant frequencies of aluminium calibration bars are considerable lower than their calculated natural frequency. For instance, the measured resonant frequency of aluminium bar No 4 is about 21 Hz less than the calculated natural frequency. Therefore, several ABAQUS finite element models of the RCA were developed and analysed to investigate the influence of equipment compliance. The material of each model component is linear

---

[2] Chapter five will present in detail the properties of the materials.

elastic and the connections between each component are rigid.

Finally, to correct the effects of the equipment compliance, a new mathematical model named the two spring model, was proposed. The model consists of a spring with finite torsional stiffness (representing the equipment compliance), $k_{equipment}$, serially connected to a spring representing the specimen stiffness. The equipment stiffness, $k_{equipment}$, and the mass polar moment of inertia of the driving system, I_0, can be obtained using a new calibration process presented in Section 4.6.

1.3 Organisation of the thesis

The thesis consists of seven chapters, of which the content can be briefly described as follows.

Chapter 1 presents a brief background into the small strain response of geomaterials, effects of particle characteristics on the small strain response, and why the topic is of interest. The chapter highlights shortcomings in our knowledge regarding the effect of particle shape and size on the small strain response of geomaterials, as well as the objectives, the viewpoints, the scope and limitation of the study

Chapter 2 provides a literature review on the small strain behaviour of geomaterials. The chapter presents effects of several parameters, especially particle characteristics, on the small strain behaviour of the geomaterials. The effects are presented from the viewpoint of micro-mechanics. This chapter discusses results of previous researchers, and reveals gaps in our current knowledge. In addition, this chapter reviews several techniques used to characterise the particle form and the particle roundness of a particle.

Chapter 3 describes the RC testing, which is employed in this research to measure G_{max} and other small strain properties of geomaterials. This chapter reviews theoretical considerations for data reduction, presents calibration results (e.g. the mass polar moment of inertia of the drive mechanism, the inherent apparatus damping) of aluminium rods, and address the apparatus compliance issue.

Chapter 4 investigates the effects of system compliance mentioned in Chapter 3 using numerical simulation. This chapter analyses the effects of each apparatus component e.g. apparatus stiffness, base mass, equipment fixity, and calibration bar design on RC test results. This chapter proposes a new method for correcting the effects of system compliance.

Chapter 5 describes the properties of the test materials used in this research, particle characterisation of the test materials, the test procedure, the methodology for specimen preparation, the apparatus set-up, and the computer program developed for running automatically a RC test. In addition, this chapter presents typical results of the RC tests on the materials used.

Chapter 6 presents and discusses the effects of void ratio, effective stress, shear strain, and especially the effects of particle size and particle shape on the small strain behaviour of the test materials. In addition, this chapter proposes a porous discontinuous-solid model to obtain a universal void ratio function, and uses the model to explain why particle size and particle shape influence the small strain behaviour of the geomaterials.

Chapter 7 draws conclusions, gives recommendations, and suggests further areas of study.

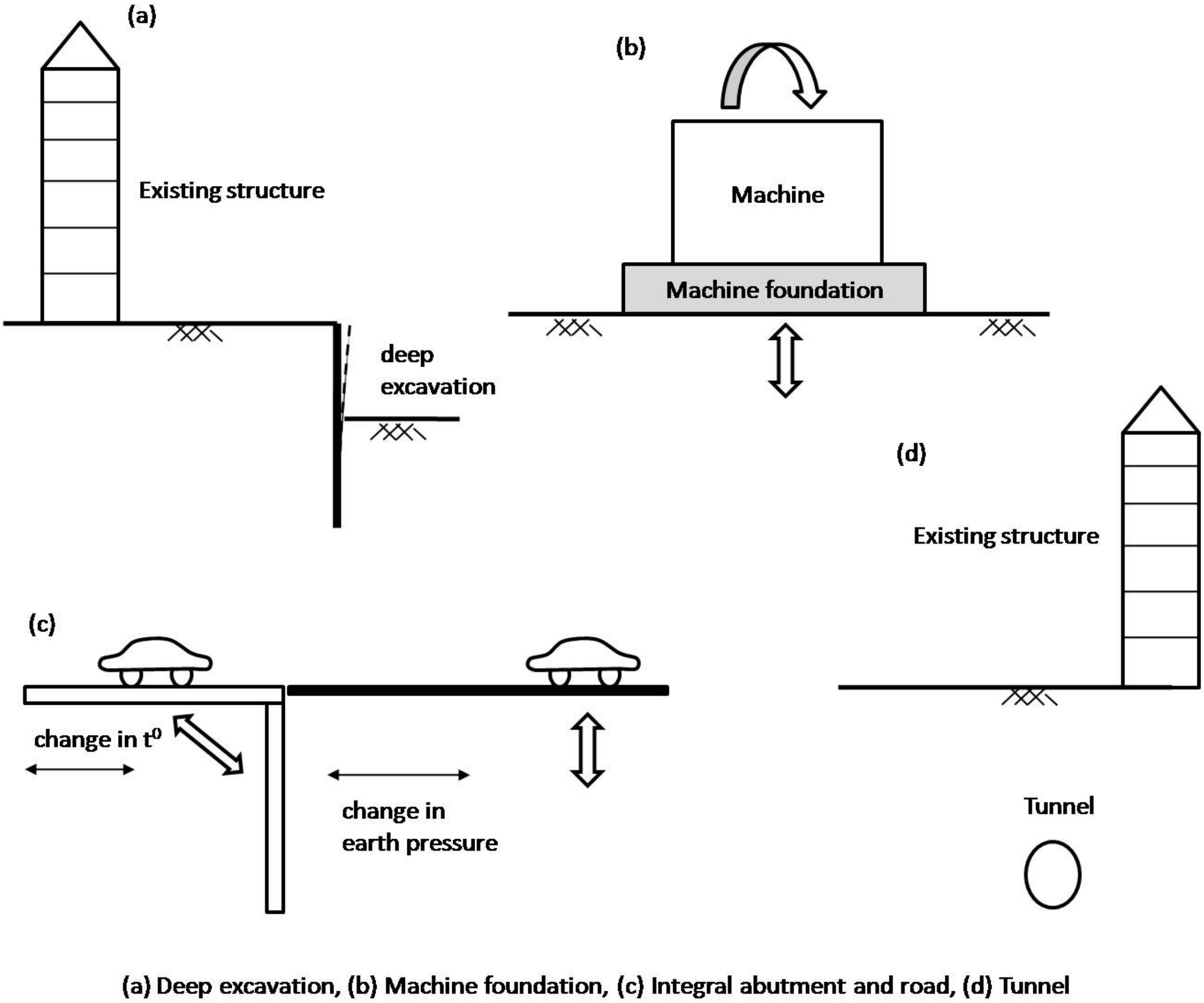

FIGURE 1.1: Typical geotechnical structures subjected to small strain under working loads. (a) Deep excavation near existing building; (b) Machine foundation; (c) Bridge abutment and road surfaces; (d) Tunnel under existing building

Chapter 2

Literature review

The essentials of particle characteristics (i.e. particle size, particle shape, and mineral composition), the small strain response of geomaterials, and the key representative parameters of the small strain response are introduced in this chapter. The effects of some important parameters, especially the particle size and particle shape, on the small strain behaviour of geomaterials are focused. The effects are presented from the viewpoint of micro-mechanics (at particle contact level), which has a strong connection to particle characteristics. The gaps in our current understanding of the effects of the particle size and particle shape on the small strain response of geomaterials are highlighted. In addition, the techniques used to characterise particle shape are also reviewed.

2.1 Essentials of particle characteristics

A particle is the fundamental element of geomaterials, and therefore the physical-mechanical properties of the geomaterials are governed by particle characteristics, such as mineral composition, size, and shape.

2.1.1 Mineral composition

Mineral composition of a particle is the primary parameter governing many properties of the particle. For example, mineral composition controls the specific gravity (Terzaghi *et al.*, 1996), and the particle elastic constants i.e. Young's modulus, shear modulus, and Poisson ratio (Mitchell & Soga, 2005) of a particle. In turn, the elastic constants influence contact mechanical properties, such as (Hertz) contact area, contact pressure, and hence contact compliance etc. Mineral composition is also a key parameter influencing particle surface properties such as water adsorption/absorption, and electro-chemical bonding especially for fine particles such as clay (Mitchell & Soga, 2005). Many researchers (Horn & Deere, 1962; Skinner, 1969; Koerner, 1970; Procter & Barton, 1974; Frossard, 1979) have suggested that the particle mineral composition significantly influences the inter-particle coefficient of friction.

2.1.2 Particle shape

Shape is the expression of the external morphology of a particle. Barrett (1980) suggested that particle shape includes three independent properties namely particle form (the overall shape or the uniformity of the three orthogonal dimensions, e.g. sphericity), particle roundness (expressing the curvature of corners and edges of a particle), and surface texture or particle roughness (Fig. 2.1). In nature, particle form varies over a wide range, from bulky to platy and/or elongate. It is well established that particle shape is a very important parameter controlling packing density. Koerner (1970); Holubec & D′Appolonia (1973); Miura *et al.* (1997); Cho *et al.* (2006) and Reddy (2008) have shown that the void ratio range, $e_{max} - e_{min}$, is a function of particle form and particle roundness/angularity. Bowden & Tabor (1950), and Moore (1975) have suggested that particle roughness strongly influences inter-particle friction. It is recognised that particle shape controls the fabric of soils (especially for clayey soils), e.g. particle orientations and contact patterns between particles (face-to-face or edge-to-face) (Mitchell & Soga, 2005).

2.1.3 Particle size

Skinner (1969) shows that the inter-particle coefficient of friction between two spheres increases with increasing sphere diameter. Lee (1992) suggested that the tensile strength of two kinds of limestone decreases linearly with particle size (Fig. 2.2). This is due to the imperfection of natural sand particles. Larger particles are likely to contain more and larger internal flaws, and hence be more crushable and have lower strength. Mitchell & Soga (2005) suggested that there is a strong connection between grain size and particle shape. Particle size gradation also influences the void ratio range. Miura *et al.* (1997); Lade *et al.* (1998) and Cubrinovski & Ishihara (2002) have suggested that the void ratio range of a mixture of two different sizes is significantly affected by the smaller particle-size fraction.

2.2 Small strain behaviour of geomaterials and influencing parameters

2.2.1 Small strain behaviour of geomaterials

The stress-strain relationship of a geomaterial is nonlinear. A typical stress-strain response of a geomaterial under both monotonic and cyclic load is presented in Fig. 2.3. The relationships are described as hysteretic due to energy loss (or damping) during each stress excursion. In the figure, the ratio of a shear stress, τ, to a corresponding shear strain, γ, is termed shear modulus, G. The area within a hysteretic curve is the energy lost during each stress excursion per unit volume; and the ratio of the energy lost to the total energy produced during each cycle is termed damping ratio, D. Therefore, shear modulus and damping ratio are essential parameters representing the small strain behaviour of geomaterials.

Experimental studies have shown that G of a geomaterial is strain dependent (Hardin &

Drnevich, 1972*b*; Kokusho *et al.*, 1982; Shibuya & Tanaka, 1996; Lo Presti *et al.*, 1997; Stokoe *et al.*, 1999). Fig. 2.4 presents a general strain dependent behaviour of a geomaterial. It can be seen that there is a plateau of shear modulus at a small shear strain region (zone I), which is termed linear elastic region since the damping ratio in zone I is very small and can be considered equal to zero[1]. The shear modulus obtained within the linear elastic region is termed maximum shear modulus, G_{max}. The maximum shear modulus is also termed very small strain shear modulus or initial shear modulus, G_0. Outside the linear-elastic region, G and D are not constant. As shear strain increases, G decreases and D increases. It is noted that in zone II and zone III[2], the strains are fully recoverable (or hysteretic-elastic), hence behaviour of soils in these zones is called visco-nonlinear elastic (Mitchell & Soga, 2005). The reason why geomaterials behave linear-elastically only in a very small region (zone I) is not fully understood. Mitchell & Soga (2005) hypothesised that the stiffness degradation at small strain is due to plastic strains development inside the yield envelope. However plastic strains are irrecoverable, and this hypothesis, therefore, conflicts to the previous fact that stress-strain excursions in zone II and zone III are fully recoverable. Perhaps the elastic region does not exist (Wood, 2007).

The ratio of G (at a certain shear strain level) to G_{max} is termed shear modulus degradation or stiffness degradation; and a curve expressing the ratio G/G_{max} against shear strain is termed shear modulus degradation curve. It is recognised that the curve is influenced by many parameters such as mean effective stress, relative density, soil fabric, number of loading cycles, etc. Seed & Idriss (1970) showed that stiffness degradation curves for a number of sands fall in a relatively narrow range (within the dashed lines in Fig. 2.5). However, for soils such as cohesive soils or sands subjected to an increase in mean effective stress, σ'_0, the curves shift to the right; and for loose materials and round materials under a low effective stress, the curves shift to the left. Hardin & Drnevich (1972*b*) showed that no single curve can describe the relationship between G/G_{max} and shear strain, even for cohesionless soils, and that the shear modulus at 0.1% might vary from 15% to 80% of G_{max}. The reduction in shear modulus as shear strain increases is one of the reasons why the shear moduli obtained from static tests, conducted in the past, were generally smaller than those measured by seismic or vibration techniques (Hardin & Drnevich, 1972*b*; Burland, 1989; Clayton & Heymann, 2001).

2.2.2 Maximum shear modulus, G_{max}

G_{max} and G/G_{max} are very important parameters in design of geotechnical structures, such as deep excavations beside existing buildings, tunnelling, integral bridge abutments, bridge piers, pile foundations, roads, machine foundations (Fig. 1.1), of which the deformation is small. Burland (1989) reported that the yield strain (as result of breakdown of cementation bonds) measured in the field, of various types of geotechnical structures, was small (less than 0.1%). Campanella (1994) suggested that G_{max}, shear modulus degrada-

---

[1] If the material is linear elastic, the damping ratio is theoretically zero, and the measured damping (e.g. using a RCA) is considered to be only due to the apparatus damping.

[2] The strain range in this research is limited in zone *I* and zone *II*.

tion, and damping ratio are the important parameters for evaluating soil response under dynamic load such as shocks, blasting, dynamic compaction, earthquakes, pile driving, machine vibrations, vehicles, winds, waves, etc. Under these loads, effects of inertia forces are accumulated and become significant, even if the shear strain is small, since the inertia forces increase proportionally to the square of vibration frequency. Consequently the fatigue phenomena may occur if the number of repetitions is large (Ishihara, 1996). Santamarina & Cascante (1996) and Mitchell & Soga (2005) suggested that G_{max} (or shear wave velocity, V_s) can be employed to assess the state and natural soil structure or quality of soil samples without altering the soil fabric. Insitu V_s can also be used to indirectly estimate other soil engineering properties, such as residual undrained shear strength, via empirical relationships (Campanella, 1994).

2.2.3 Parameters influencing G_{max}

G_{max} is influenced by both soil packing characteristics (e.g. void ratio, structural anisotropy, OCR, soil fabric, cementation, etc.) and testing environment (e.g. mean effective stress, confining time, stress anisotropy, number of loading cycles, and etc). To account for the influence of these parameters, a number of empirical equations, have been proposed for estimating G_{max}, and they can be generalised as (Hardin & Blandford, 1989; Jamiolkowski *et al.*, 1995; Stokoe *et al.*, 1999)

$$G_{max(ij)} = S_{ij}\, F(e)\, OCR^k\, {\sigma_r}^{1-n_i-n_j} {\sigma'_i}^{n_i} {\sigma'_j}^{n_j} \ (MPa) \tag{2.1}$$

where

- The i and j subscripts denote the direction of wave propagation and wave polarisation (particle motion), respectively;
- S_{ij} is dimensionless coefficient for a given soil. It is also termed material constant (Mitchell & Soga, 2005). It is hypothesised that S_{ij} reflects the soil anisotropy (Hardin & Blandford, 1989), soil fabric (Jamiolkowski *et al.*, 1995; Shibuya *et al.*, 1997), confinement time (Marcuson & Wahls, 1972), and perhaps particle characteristics (as investigated in the thesis) etc;
- $F(e)$ is a void ratio function;
- OCR is the overconsolidation ratio;
- $\sigma'_{i/j}$ (in kPa) is the effective stress applied in the i/j direction, respectively;
- k is an empirical exponent dependent on both plasticity index and void ratio of soil. For sand, $k \approx 1$;
- $n_{i/j}$ is the empirical stress exponents dependent on void ratio, particle size, particle shape, and degradation, $n_i \approx n_j$;
- σ_r is a reference pressure (1.0 kPa).

For the specific case where the G_{max} of a particular non-cohesive geomaterial is measured using the RCA, Eq. 2.1 can be rewritten more simply as:

$$G_{max} = G_{vh} = S_{vh} \times F(e) \times {\sigma_r}^{1-n} \times {\sigma'_0}^{n} \ (kPa) \tag{2.2}$$

where

- The v and h denote the vertical (wave propagation) and horizontal (wave polarisation) direction, respectively;
- G_{vh} is the maximum shear modulus in the plan perpendicular to the direction of wave propagation;
- σ'_0 is the mean effective stress.

2.2.3.1 Mean effective stress

Based on Hertz theory of elastic bodies in contact, Duffy & Mindlin (1957) and Duffy (1959) theoretically showed that the shear modulus of close packed arrays of elastic spheres (i.e. face-centre-cubic and hexagonal-close-packed) is proportional to the cubic root of effective stress, ${\sigma'_0}^{1/3}$. This can be explained by the influence of Hertz contact radius and Hertz contact pressure, which are also proportional to ${\sigma'_0}^{1/3}$. However, their experimental results with steel spheres show that the stress exponent is larger than 1/3 (Fig. 2.6). The theoretical stress exponent of other regular packing of spheres (Petrakis & Dobry, 1987; Wang & Nur, 1992) and a random packing of spheres (Walton, 1987; Chang *et al.*, 1991; Liao *et al.*, 2000) has been shown to be 1/3. However, Cascante & Santamarina (1996) observed that the stress exponent for high precision steel spheres is slightly lower than the theoretical value of 1/3. This is possibly due to the compliance of the "SBEL-D1128" Stokoe RCA used in their research. Priest (2004); Kumar & Clayton (2007); Clayton *et al.* (2009) have reported that the compliance of the SBEL Stokoe RCA apparatus causes significant reduction in measured resonant frequency of relatively stiff specimens. As a result, apparatus compliance leads to a reduction in the stress component.

Experimental work undertaken by many researchers with variety of soils has suggested that G_{max} increases in an exponential manner with σ'_0 (see Eq. 2.2). Table 2.1 shows that stress exponents, n, in practice varies from 0.40 to 0.62; and a value of 0.5 was proposed by many researchers[3]. The greater stress exponents in practice may be due to differences in particle characteristics, and hence inter-particle contact properties between theoretical packing of smooth spheres and a real geomaterial, such as:

- A real soil is more susceptible to effective stress than a packing of spheres. When subjected to an increase in effective stress, the orientations soil particles may rearrange, hence the soil density may change, plastic deformations and even crushing may also happen.

---

[3] This is the reason why this value of stress exponent was used in this chapter to normalise the influence of σ'_0 on G_{max}.

- A theoretical packing of smooth spheres may have higher co-ordination number, $\bar{N}_c$, than a real soil does. $\bar{N}_c$ for a real soil is dependent on particle characteristics (e.g. particle form, angularity, particle roughness, etc.).
- In practice, particle size is not uniform and particle form may not be spherical. Therefore, the contact area between soil particles and the number of contact per unit solid volume, $\bar{N}_v$, for a real soil may be considerably different from those of a theoretical packing of spheres. In addition, soil structures/fabric in practice, with existence of bonding and cementation, are much more complex than a theoretical packing of smooth spheres.

2.2.3.2 Void ratio

Void ratio, which is directly related to packing characteristics of geomaterials, has a strong impact on G_{max}. Wood (1941) established a porosity-velocity[4] relationship. Later, Biot (1956) developed poro-elastic model for saturated geomaterials. Using Hertz and Mindlin contact theories, other researchers, such as Walton (1987); Chang *et al.* (1991); Liao *et al.* (2000), have established theoretical relationships between void ratio and G_{max} of a random packing of spheres. However, these relationships do not well represent the effect of void ratio on G_{max} of soils in practice.

Based on experiment, it is recognised that G_{max} decreases with an increase in void ratio. The influence of void ratio can be taken into account by using an empirical void ratio function, $F(e)$. Various forms of $F(e)$ have been proposed for various types of soil. They can be classified into two groups; hyperbolic functions, and exponential functions (Table 2.1). It is noted that each void ratio function can be applied for a certain soil within a limited void ratio range. There is no universal void ratio function that can be applied for all soils over a wide range of void ratios.

The effect of void ratio on G_{max} may be partly due to changes in inter-particle contact properties. It has been shown that co-ordination number, $\bar{N}_c$, strongly depends on void ratio (Fig. 2.7). McGeary (1961) and Oda (1977) have shown that $\bar{N}_c$ for regular packing of single-size spheres decreases with an increase in void ratio (Table 2.2). Smith *et al.* (1929); Field (1963) and Chang *et al.* (1991) have suggested that $\bar{N}_c$ for a random packing of spheres also decreases with an increase in void ratio. Santamarina & Cascante (1996) suggested a relationship between the average contact force and the void ratio of a random packing of spheres. The relationship indicates that an increase in void ratio will increase the average contact force. The influence at particle level of void ratio presented above may be some of the reasons why soil stiffness decreases with increasing void ratio, and why loose materials are more susceptible to shear strain and effective stress than dense materials.

---

[4] Compressional wave velocity, V_p.

2.2.3.3 Anisotropy

G_{max} of cohesive soils is influenced by anisotropy of both their inherent structure and stress state. Work done by many researchers (Roesler, 1979; Hardin & Blandford, 1989; Jamiolkowski *et al.*, 1995; Stokoe *et al.*, 1995; Hight *et al.*, 1997; Pennington *et al.*, 1999; Kuwano & Jardine, 2002) has shown that G_{max} in the direction perpendicular and parallel to the bedding plane are different.

The effects of fabric anisotropy on G_{max} have strong connections with particle shape. The effects are observed to be significant for platy/elongate particles (such as mica or clay), but insignificant for rotund particles. The form anisotropy of platy particles causes the anisotropy of soil structure, where the contact area in direction perpendicular to particle orientation (face-to-face contact) is much larger than that of the direction along the particle orientation (edge-to-edge or edge-to-face contacts, Mitchell & Soga, 2005). This causes a significant difference in the magnitude of contact forces for the two directions. As a result, the anisotropy in contact area and contact force causes anisotropic effects on G_{max}.

2.2.3.4 Overconsolidation ratio

Overconsolidation ratio, OCR significantly affects G_{max} of clayey soils. Humphries & Wahls (1968) hypothesise that the effect of OCR on G_{max} of Bentonite and Kaolinite is due to the change of void ratio. Hardin & Black (1969) and Hardin & Drnevich (1972*b*) show that G_{max} of clayey soils increases with OCR. Kokusho *et al.* (1982) point out that the effect of OCR on G_{max} of soft clay cannot be explained by the change in void ratio alone. Shibuya *et al.* (1992, 1997); Jamiolkowski *et al.* (1995) conclude that the influence of OCR on G_{max} of sands is negligible.

The influence of OCR on G_{max} possibly relates to particle characteristics. Clay particles are very fine, platy, and even elongate. G_{max} of clay particles are strongly influenced by physical, chemical surface forces (e.g. electro static force at surfaces especially with the existence of adsorbed water), which are much greater than the particle gravity force (Terzaghi *et al.*, 1996). Preconsolidation pressure, P'_c, can change particle orientations and therefore can bring clay particle closer together (reducing void ratio and water content). The particles tend to rotate more into horizontal position, reducing the number of edge-to-face contacts, and increasing the number of face-to-face contacts. As results, P'_c changes the soil fabric, increases the contact area, and increases the surface forces (Terzaghi *et al.*, 1996). Once the soil is rearranged to a highly structured fabric, the fabric will exist even when the effective stress is reduced. In contrast, the fabric of an (unbonded) rotund particle soil does not change (or changes less) due to a change of effective stress.

2.2.3.5 Confinement time

Hardin & Black (1968) and Marcuson & Wahls (1972) showed that G of commercial plastic kaoline and bentonite increases with an increase in secondary consolidation time, and the increase could not be due to void ratio change. Anderson & Stokoe (1978) identified two time phases, namely the initial phase, due to primary consolidation, and the second phase relating to linear increase in G with logarithm of time. They observed that coarse soils only reveal the long-term effect, while fine particle soils reveal the effect of both phases, and expressed the time effect via the following equations:

$$I_G = \frac{\Delta G}{\log\left(t_2/t_1\right)} \tag{2.3}$$

$$N_G = \frac{I_G}{G_{1000}} \tag{2.4}$$

where t_1, t_2 are time after primary consolidation, ΔG is change in shear modulus from t_1 to t_2, G_{1000} is shear modulus after 1000 minutes of constant confinement time, and N_G is time normalised shear modulus. Fig. 2.8a shows that the measured N_G of NC clays is from 0.05 to 0.20, higher than that of OC clays (from 0.03 to 0.10), and that of sands is the lowest ($< 0.01 - 0.03$).

Anderson & Stokoe (1978) explained that the time effect is due to soil structure rearrangement occurred after completion of the primary consolidation. Kokusho *et al.* (1982) suggested further that the increase in G during the primary consolidation phase is simply due to a decrease in void ratio, and the increase of G during the secondary consolidation phase is possibly due to an increase in plasticity index, which relates to chemical activities of clay particles.

The time dependent structure rearrangement is thought to have a strong link to particle characteristics. A packing of rotund sand is relatively stable, and hence less affected by confinement time. In contrast, the structure of fine and platy particle soils is less stable than. Fine and platy particles easily rearrange themselves to approach a more stable structure (e.g. lower void ratio, larger contact area, and stronger bonding, etc.). This hypothesis is supported by the observation of Anderson & Stokoe (1978) and Kokusho *et al.* (1982) that finer particles are more affected by confinement time (Fig. 2.8b). Because of the time effect Anderson & Stokoe (1978) recommended that G_{max} of soils should be compared at similar confinement time.

2.2.3.6 Number of loading cycles

In the elastic region, geomaterials behave linear elastically; hence G_{max} is only slightly affected by number of loading cycles, N. When the shear strain exceeds the elastic threshold strain, it has been shown that G decreases as N increases (Hardin & Drnevich, 1972*b*; Bolton & Wilson, 1989; Lo Presti *et al.*, 1993; Stokoe *et al.*, 1995, 1999). G_{max} of cohesive soils are more influenced by N than cohesionless soils (Hardin & Drnevich, 1972*b*).

A high number of loading cycles (and hence a high strain rate induced in a specimen tested using a RCA) perhaps cause a fatigue effect, which may break the bonding between contacts, decrease the inter-particle friction. Cascante & Santamarina (1996) hypothesised that the effect of N may be related to the contact deterioration, which cause a reduction in contact stiffness during cyclic loading.

2.2.4 Damping ratio, D

Damping ratio, D, is the other key parameter routinely used to represents the small strain behaviour of geomaterials. Damping or lost energy during vibration leads to a hysteretic-elastic stress-strain relationship of geomaterials as shown in Fig. 2.9b. Based on Hertz contact theory, Mindlin & Deresiewicz (1953) and Johnson (1987) defined the lost energy, ΔW_d, per cycle for two elastic spheres (with the same elastic constants) in contact subjected to a small tangential oscillating force, $T = T_0 \sin(\omega t + \varphi)$ (Fig. 2.9a), as follows:

$$\Delta W_d = \frac{1}{36a\,\mu\,P} \times \frac{2-\nu}{G_{grain}} {T_0}^3 \tag{2.5}$$

where P is the normal contact force, μ is the inter-particle frictional coefficient, a is the Hertz contact radius, G_{grain} and ν are the shear modulus and Poisson's ratio of the particle, respectively. D defined as the ratio of the lost energy to the total work-done, W_d, can therefore be estimated by:

$$D = \frac{\Delta W_d}{W_d} = \frac{\Delta W_d}{2\pi\,T_0\,\delta_0} = \frac{1}{36a\,\mu\,P} \times \frac{2-\nu}{G_{grain}} \times \frac{{T_0}^2}{2\pi\,\delta_0} \tag{2.6}$$

The tangential vibratory compliance amplitude, δ_0 (Fig. 2.9a), can be estimated by (Mindlin & Deresiewicz, 1953; Johnson, 1987):

$$\delta_0 = \frac{3\mu\,P}{8a}(\frac{2-\nu}{G_{grain}})\left[1-(1-k_T)^{2/3}\right] \tag{2.7}$$

where $k_T = \dfrac{T_0}{\mu\,P}$ is the ratio of the tangential force amplitude and the frictional force. Substituting Eq. 2.7 into Eq. 2.6 leads to:

$$D = \frac{{k_T}^2}{27\pi} \times \frac{1}{\left[1-(1-k_T)^{2/3}\right]} \tag{2.8}$$

Eq. 2.8 is valid for a small tangential force ($k_T < 1$). Eq. 2.8 shows that D at small strain is proportional to the square of the tangential force (${k_T}^2$). In other words, D at small strain is proportional to the square of tangential compliance (or shear strain). It is necessary to establish the explicit relationship between damping ratio and shear strain. The shear strain can be defined as the ratio of the vibration amplitude to the diameter of the sphere (Fig. 2.9a), therefore:

$$\gamma = \frac{\delta_0}{d} = \frac{3\mu\,P}{8a\,d}(\frac{2-\nu}{G_{grain}})\left[1-(1-k_T)^{2/3}\right] \tag{2.9}$$

Rearrangement of Eq. 2.9 yields the relationship between shear strain and tangential force:

$$k_T = 1 - \left[1 - \frac{8a\,d}{3\mu\,P} \times \frac{G_{grain}}{2-\nu} \times \gamma\right]^{3/2} \tag{2.10}$$

Equations 2.5 to 2.10 explicitly indicate that (i) the small strain damping ratio[5] of two spheres in contact is a function of shear strain, and (ii) at a certain shear strain, the damping ratio is dependent on the sphere characteristics (elastic constants, inter-particle frictional angle, diameter), the normal contact force, and the Hertz contact radius. These equations are employed to predict D of the two spheres in contact (subjected to an small oscillating tangential force) at different shear strain, different contact force (or contact pressure), different inter-particle frictional angle, and difference sphere diameter. The results presented in Fig. 2.10 to Fig. 2.13 clearly show that:

- D at small strain decreases with an increase in contact force (Fig. 2.10). The increase in contact force will increase the Hertz contact area, the contact pressure, and hence the friction strength. The increase in friction strength will restrict the compliance (and restrict the *stick-slip* motion) and therefore less energy loses.
- D at small strain decreases with an increase in inter-particle friction angle (Fig. 2.11).
- At the same contact force, D increases with an increase in diameter of the spheres (Fig. 2.12), since the Hertz contact pressure is inversely proportional to $d^{2/3}$. When the diameter increases, the contact pressure decreases, and hence the more energy is lost. Fig. 2.13 shows that at the same contact pressure, D is independent of diameter of the sphere.
- D increases with an increase in shear strain, suggesting that the plateau of damping is theoretically non-existent. Fig. 2.10 to 2.13 indicate that the material damping is very small at small shear strains (e.g. D increases from 0.002% to 0.02% when γ increases from 10^{-5}% to 10^{-4}%). The instrumentation accuracy, which is significantly reduced at small strains due to background noise effects, is unable to detect the small variation (from 0.002% to 0.02%) in damping. This suggests that, in the linear elastic region, D measured in practice is only due to the apparatus damping, which is caused by back EMF (Stokoe *et al.*, 1995; Meng & Rix, 2003; Cascante *et al.*, 2003; Wang *et al.*, 2003), and fixity of apparatus equipment (Avramidis & Saxena, 1990; Cascante *et al.*, 2003).

It has been observed that the pattern of increase in damping ratio with shear strain strongly links to the pattern of decrease in shear modulus. A few attempts have been make to establish relationship between D and G/G_{max} (e.g. Hardin & Drnevich, 1972*a*; Tatsuoka *et al.*, 1978) (Fig. 2.14a). For example, the theoretical hyperbolic model (e.g.

---

[5] It will be noted that the damping ratio estimated using Eq. 2.7 is sometime termed hysteretic damping ratio (e.g. Tatsuoka *et al.*, 1978; Isenhower *et al.*, 1987). It is twice the loss coefficient (Ishihara, 1996). It is proved that hysteretic damping ratio and viscous damping, estimated from logarithmic decrement, $D = \dfrac{2\,\pi\,\delta}{4\,\pi^2 + \delta^2}$, is theoretically identical (Kramer, 2003).

Ishihara, 1996) shows that:

$$D = \frac{4}{\pi\left(1 - G/G_{max}\right)}\left[1 + \frac{G/G_{max}}{1 - G/G_{max}}\ \ln\left(G/G_{max}\right)\right] - \frac{2}{\pi} \tag{2.11}$$

Relationship 2.11 is plotted in Fig. 2.14b. It can be seen that relationship 2.11 lies within the experiential data (Fig. 2.14a) in small strain range, suggesting that D is influenced by parameters that influence G/G_{max}. Hardin & Drnevich (1972*a*) suggested that D at a given strain level is significantly influenced by mean effective stress, void ratio, and number of loading cycles. The effect of number of loading cycles on D is more significant at medium to large strain (Tatsuoka *et al.*, 1978). Lo Presti *et al.* (1997) conclude that D is considerably influenced by shear rate (or frequency). Seed *et al.* (1986) observed that D of gravels and sands at medium to large strain ($\geq 10^{-2}\%$) are similar, leading to the conclusion that D is not affected by particle size. Effects of other parameters such as particle shape, soil structure, OCR, (Hardin & Drnevich, 1972*a*), degree of saturation, specimen preparation (Tatsuoka *et al.*, 1978), stress history (Tatsuoka *et al.*, 1979) on D are insignificant.

In the literature, there were different conclusions about the effect of void ratio on D. Contrary to Hardin & Drnevich (1972*a*), Tatsuoka *et al.* (1978) and Seed *et al.* (1986) suggested that the influence of void ratio on D is insignificant. This discrepancy may be attributed to the difference in damping mechanisms at different strain levels. Tatsuoka *et al.* (1978) and Seed *et al.* (1986) measured D at medium to larger strain levels ($> 10^{-2}\%$, Fig. 2.15), where the damping is caused by particle sliding and structure destruction, etc. In contrast, Hardin & Drnevich (1972*a*) measured D at small strain level, where damping is due to the *stick-slip* motion of particles in contact[6]. Thus, D at small strain is influenced by micro behaviour at contact, which links to void ratio (see section 2.2.3.2).

2.3 Effects of particle characteristics on small strain behaviour of particulate materials

2.3.1 Effect of particle shape on G_{max}

Hardin (1961) observed that shear wave velocity, V_s, of Ottawa sand and crushed quartz sand linearly varied with void ratio, and that V_s in dense crushed quartz was similar to that in loose Ottawa sand (Fig. 2.16). The particle size of both materials was the same i.e. fraction No20 - No30. The results led to the conclusion that V_s at $D_r = 100\%$ might be different for two sands, however at the same void ratio V_s was similar. Hardin (1961) suggested that particle shape affected V_s through void ratio; the void ratio of the crushed quartz sand (extremely angular grain) was greater than that of Ottawa sand (rotund grain), causing V_s to be lower in the angular material. Hardin & Richart (1963) and Hardin & Drnevich (1972*b*) confirmed that the influence of particle characteristics

---

[6] At small strain, the tangential force at contact between two particles is much smaller than frictional force (Mindlin & Deresiewicz, 1953).

on G_{max} was only to change the void ratio range, and classified particle characteristics as relatively unimportant parameters for soil modulus.

Iwasaki & Tatsuoka (1977) supported the premise that particle shape did not affect G_{max}, provided that the effect of void ratio was taken into account. They performed RC tests on a few sands with different coefficients of uniformity, C_u and medium particle size, D_{50}. They suggested that shear moduli of sand at small and medium strain levels could be expressed by the following empirical equation without considering the particle size and particle shape

$$G = A(\gamma).B.\frac{(2.17-e)^2}{1+e}p^{m(\gamma)} \tag{2.12}$$

where $A(\gamma)$, $m(\gamma)$ were functions of shear strain γ; and B is a parameter, which was determined irrespectively of effective stress, shear strain, and void ratio.

G_{max} of various geomaterials including bentonite (Humphries & Wahls, 1968), soft clays (Kokusho *et al.*, 1982), kaolinite clays (Humphries & Wahls, 1968; Hardin & Black, 1968), silt (Hardin & Drnevich, 1972*b*), and sands (Hardin & Richart, 1963; Hardin & Drnevich, 1972*b*; Lo Presti *et al.*, 1993; Robertson *et al.*, 1995; Lo Presti *et al.*, 1997) have been collected from the literature and plotted in Fig. 2.17. To remove the effect of σ'_0, they were normalised by ${\sigma'_0}^{0.5}$, and plotted versus void ratio in Fig. 2.18. The figure shows that G_{max} decreases with an increase in void ratio. However, where the void ratios of different soils overlap (e.g. at $e = 0.8$), the small strain shear moduli are quite variable, and hence could not be predicted via void ratio alone.

Santamarina & Cascante (1998) prepared two specimens using metal spheres with different degrees of surface roughness, namely the mild rust and the rusted. They showed that V_s reduces with increasing surface roughness and the damping of the rusted specimen was stress independent. However, their evidence was limited, with only two specimens. V_s of the smooth metal spheres was not presented in the publication. Their test results indicated that V_s of the mild rust and the rusted specimen at 100 kPa are approximately 270 m/s and 140 m/s respectively. The corresponding G_{max} of the mild rust specimen ($e = 0.61$) is 354MPa, nearly four time higher than that of the rusted specimen ($e = 0.62$). A previous publication (Cascante & Santamarina, 1996, Fig. 1a p.833) showed that V_s of the smooth steel spheres (D = $3.18 \pm 0.00254mm$) at a lower void ratio (e = 0.60) is similar to that of the mild rust spheres ($V_s = 270\,m/s$). This suggests that the method they used to rust the spheres might produce a weak material at the surfaces of the rusted spheres. The weak material at the surfaces causes a low contact stiffness or high contact compliance, and hence a lower V_s.

Data on the G_{max} of Toyoura and Quiou sands measured by Lo Presti *et al.* (1997) using a RCA under an effective stress of 100 kPa are collected and plotted versus void ratio in Fig. 2.19. The graph shows that at the same void ratio G_{max} of round Toyoura quartz sand is higher than that of sub-angular carbonate Quiou sand. Considering G_{max} as a function of effective stress, Lo Presti *et al.* (1997) observed a large stress exponent, n, (see Eq. 2.1) for Quiou sand ($n = 0.62$) compare to that for Toyoura sand ($n = 0.45$). Lo Presti *et al.* (1997) hypothesised that the difference in stress exponent between Toyoura sand

and Quiou sand may be due to the difference in particle roundness, particle mineralogy and coefficient of uniformity, C_u.

Recent research has shown that the effect of particle shape on soil stiffness has been more widely recognised. Clayton *et al.* (2004) observed a considerable reduction in the undrained Young's modulus (at medium strain and large strains) for a coarse rotund particulate material mixed with a small quantity of fine mica, even though the void ratio of the mixture was lower than that of the coarse material alone. Chang & Heymann (2005) measured V_s of gold tailings that consisted of rotund particles and fine platy particles, using bender elements. The relatively low small strain stiffness of gold tailing (Fig. 2.18) could be attributed to the platy shape of the gold tailing particles[7].

Cho *et al.* (2006) suggested relationships between particle characteristics (i.e. roundness, sphericity, and regularity[8]) and V_s for some natural and crushed sands by using the relationship (proposed by Hardin & Richart, 1963):

$$V_s = \alpha\,(\frac{\sigma'_0}{1\ kPa})^{\beta} \tag{2.13}$$

where α was defined as V_s at 1.0 kPa and β ($\beta = n/2$) was the stress exponent reflecting the sensitivity of V_s to σ'_0 in the polarisation plane (Cho *et al.*, 2006). Their data suggested that there were correlations between α, β and particle shape, leading to the conclusion that small strain stiffness decreased with increasing irregularity.

However, re-evaluation of the data of Cho *et al.* (2006) shows that the correlations between V_s, at two arbitrary values of σ'_0 (such as 100 kPa and 400 kPa) and particle shape are limited (Fig. 2.20). The small coefficients of determination ($R^2 = 0.3295$ at 100 kPa and $R^2 = 0.1054$ at 400 kPa) as shown in Fig. 2.20c indicate a poor correlation between particle regularity and V_s. It is also difficult to conclude that there is a correlation between roundness and V_s. It can be seen in Fig. 2.20a that V_s increases with roundness smaller than 0.2, however fluctuates with larger degrees of roundness. Similarly, values of V_s do not tend to increase with sphericity. In fact, Fig. 2.20b even shows that V_s, at 400 kPa, decreases with sphericity.

It is noted that Cho *et al.* (2006) did not take into account the variation in particle size. The D_{50} of the materials used by Cho *et al.* (2006) varied from 0.15 to 0.6. In addition, the observation (α and β are functions of particle shape) of Cho *et al.* (2006) may not be attributable to particle shape but instead to variations in void ratio. This argument could not be substantiated as the void ratios of the soils in their test were unknown[9]. Hardin & Richart (1963) suggested that α is a linear function of void ratio; $\alpha = 50.95(2.973 - e)$. It is also shown that the stress exponent, β, is also a function of void ratio (Clayton *et al.*, 2005).

---

[7] Chang & Heymann (2005) also showed that values of normalised V_s of the gold tailing were higher than those of clays. However, their calculation of normalised V_s of clays may be wrong. The normalised V_s of clays with void ratio less than 0.8 should be much higher. In addition, V_s of the gold tailing could be underestimated.

[8] Defined by Cho *et al.* (2006) as the average of sphericity and roundness.

[9] Void ratios of the sands are not available in the publication.

More recently, Lee *et al.* (2007) mixed Ottawa sand with different mica percentages and various mica-to-sand size ratios (L_{mica}/D_{sand}). Based on the test results obtained from a conventional oedometer cell equipped with bender elements, they suggested that as the mica content increases (in mixtures with $L_{mica}/D_{sand} \geq 1$), V_s decreases, and becomes more susceptible to effective stress (Fig. 2.21). However, the effect of void ratio was not taken into account. In addition, the size of the mica was relatively high compared to that of the sand ($L_{mica}/D_{sand} = 0.33$, 1, 3). Due to bridge packing of the mica, the void ratios of the mixture significantly increased (Fig. 2.22). In this case, the effect of particle shape on V_s could be attributed to the changing void ratio as suggested by Hardin (1961); Hardin & Richart (1963); Hardin & Drnevich (1972*b*). The susceptibility of effective stress in this case could also be attributed to the change in void ratio, since mica is extremely deformable material; The more mica is added, the higher the void ratio of the mixtures, and hence the more volume changes as the effective stress increases. Therefore, in qualifying the effect of particle shape on G_{max}, the effect of void ratio must be taken into account.

2.3.2 Effect of particle size on G_{max}

Hardin & Drnevich (1972*b*) suggested that the particle size affects G_{max} of sands only through influencing the void ratio. They explained that fine soils are more porous than the coarse soils. Iwasaki & Tatsuoka (1977) supported the premise that the effect of particle size on G_{max} was only to change void ratio. They measured G_{max} of clean sands with different particle size and gradation, and used Eq. 2.12 to express the G_{max} of the sands. Based on the fact that the B parameter was independent of D_{50} (Fig. 2.23), they suggested that G_{max} was independent of particle size (because void ratio had been already accounted for via using the void ratio function in Eq. 2.12).

Ishihara (1996) collected G_{max} values for various sands and gravels with different particle size and plotted them against void ratio (Fig. 2.24). The difference in G_{max} was suggested to be due to different types of gravel. The results presented also suggest that G_{max} is possibly influenced by particle size (e.g. G_{max} of crushed rocked > G_{max} of gravel > G_{max} of sandy gravel). Menq & Stokoe (2003) tested gravely soils with different coefficients of uniformity, C_u, and mean particle sizes, D_{50} using a large scale RCA. They showed that G_{max} increases with an increase in D_{50} and C_u. However, the effect of void ratio on G_{max} was not taken into account in their observation.

2.4 Particle shape characterisation

2.4.1 Characterisation of particle roundness

Wadell (1932) defines Roundness (cf. angularity) as the ratio of the average radius of corners and edge to the radius of the maximum inscribed circle (Fig. 2.1). Even though Wadell (1932) suggested that roundness is a 3D term, it is often considered as a 2D parameter due to the fact that sand grains under a microscope are naturally arranged in such a manner that their maximum projected areas are visible and photographed to obtain 2D images for analysis. Based on this concept, Powers (1953); Krumbein & Sloss (1963) developed visual charts for estimating roundness.

Lees (1964) argued that Wadell's roundness might not be applicable to crushed rock particles and proposed angularity number defined as:

$$Angularity\,number = \sum \frac{(180 - \alpha)x}{R} \tag{2.14}$$

where r was the radius of the largest inscribed circle, x is a distance between the centre of the largest inscribed circle and a corner tip, and α is the angle of the corner (Fig. 2.25). Angularity number may be a better estimation of roundness than the visual charts (Powers, 1953; Krumbein & Sloss, 1963) which are subjected to personal judgment and limited to the number of categories (in the visual charts). However, in practice it is difficult to determine the centre of the largest inscribed circle.

Vallejo (1995) employed the concept of fractal theory (Mandelbrot, 1977) to analyse a particle outline and suggested that a particle outline can be represented by a fractal dimension. The fractal analysis method has the advantage of objectivity in that computer software can be used to estimate the fractal parameters. However, the fractal analysis is less sensitive to the particle morphology (Sukumaran & Ashmawy, 2001) as it mainly measures the texture rather than the roundness of a particle. Therefore, Bowman *et al.* (2001) suggested that it should be used in combination with other methods to comprehensively define the particle roundness.

An alternative method of 2D particle shape characterisation is Fourier analysis proposed by Ehrlich & Weinberg (1970). The concept of Fourier analysis is that each point in the particle outline can be represented by a vector $\overrightarrow{R}$ with the radius R and the angle θ. The combination of all the vectors will provide the perimetric profile resembling a wave form that can be represented in term of Fourier series (Fig. 2.26). One problem of this method is that a radius may intersect the outline twice. Thus highly irregular perimeters containing 're-entrant' angles (where the particle profile 'doubles back' upon itself, such as concave shell-like particles) cannot be analysed (Clark, 1981). However, this problem can be overcome by Fourier descriptor method suggested by Bowman *et al.* (2001).

With the recent development of digital image analysis techniques, many researchers (Wilson *et al.*, 1997; Yudhbir & Abendizadeh, 1991; Sukumaran & Ashmawy, 2001; Alshibli & Alsaleh, 2004) have developed different methods for evaluating angularity. One of the simplest indicators is roundness index, R_n, defined as the square of the ratio between the perimeter of a circle with the same area of the particle and the particle perimeter (Wilson *et al.*, 1997)

$$R_n = \left(\frac{\pi \times \sqrt{\dfrac{4A}{\pi}}}{p} \right)^2 = \frac{4\pi A}{p^2} \tag{2.15}$$

where A and p are the area and perimeter of the 2D particle image, respectively. R_n

is equal to 1.0 for a circle, and less than 1.0 for increasingly angular particles. The roundness index is largely used for quantifying angularity of rock aggregates. However, improvements in computing and image analysis software has allowed roundness index being used for sands.

Some of the advantages of roundness index are its simplicity and effectiveness. It is apparently that when the angularity of a particle increases, the 2D particle area decreases and the particle perimeter increases, resulting in a decrease in roundness index calculated using Eq, 2.15. Reddy (2007) suggested that roundness index can well differentiate angularity of various irregular geometry shapes (Fig. 2.27).

2.4.2 Characterisation of particle form

The concept of *true sphericity*, a 3D descriptor of particle shape, was first suggested by Wadell (1932). True sphericity, denoted as ψ, is defined as the ratio of the surface area of a particle to the surface area of a sphere of the same volume. When dealing with particles in suspension, true sphericity is very important since the settling velocity of a particle is related to it (Wadell, 1932). Due to the difficulty in measuring surface area, the ratio of the volume of a particle to the volume of the circumscribing sphere is preferred. The cubic root of this ratio is termed *operational sphericity* (Wadell, 1933). In other words, Wadell's operational sphericity is the ratio of the equivalent diameter, d,[10] to the largest diameter, L, of a particle.

Krumbein (1941) assumed a particle to be a triaxial ellipsoid having three diameters, namely the largest, L, the intermediate, I, and the shortest, S, and proposed (Krumbein's) operational sphericity, ψ_o, calculated as:

$$\psi_o = \sqrt[3]{\frac{(\pi/6)L \times I \times S}{(\pi/6)L^3}} = \sqrt[3]{\frac{I \times S}{L^2}} \tag{2.16}$$

Corey (1949) reasoned a particle generally fall with its largest projected area normal to the direction of motion, and therefore flatness is the shape factor having the most significance to the falling velocity of a particle. He combined the two flatness ratios S/L and S/I to form shape factor:

$$CSF = \sqrt{\frac{S}{L} \times \frac{S}{I}} = \frac{S}{\sqrt{L \times I}} \tag{2.17}$$

This shape factor is used by hydraulic engineers to express the effect of shape on settling velocity and it is termed *Corey's shape factor*, CSF, (Blatt *et al.*, 1980). CSF has been shown to have good correlation with the settling velocities of particles (Corey, 1949; Dietrich, 1982). CSF is also the square root of the ratio between the cross section of the maximum inscribed sphere and the maximum projected area of a particle. Therefore, CSF can be considered as a sphericity index.

Aschenbrenner (1956) suggested that a particle could be better approximated to a tetrakaideka-

---

[10] The diameter of the sphere having the same volume.

hedron, a solid with 14 plane faces, than an ellipsoid. The reasons given were that the shape can be handled mathematically, and sedimentary sand grains do not have smooth surfaces like an ellipsoid. Applying the original concept of true sphericity given by Wadell (1932), Aschenbrenner (1956) proposed *working sphericity*, ψ_w, defined as:

$$\psi_w = 12.8 \frac{\sqrt[3]{p^2 q}}{1 + p(1+q) + 6\sqrt{1 + p^2(1+q^2)}} \tag{2.18}$$

where p is the ratio of the smallest to the intermediate diameter, and q is the ratio of the intermediate to the largest diameter.

Sneed & Folk (1958) claimed that Wadell's sphericity does not correctly express the dynamic behaviour of particles in a fluid. An ellipsoid has a tendency to orient itself with the maximum projected area normal to the flow. Hence, the drag force on an ellipsoid is proportional to the maximum projected area. Therefore, they proposed *maximum projection sphericity*, ψ_p, defined as the cubic root of the ratio between the projected area of the inscribing sphere and the maximum projected area of a particle:

$$\psi_p = \sqrt[3]{\frac{S^2}{L \times I}}. \tag{2.19}$$

Maximum projected sphericity shows a better linear correlation with observed settling velocities than does Wadell's operational sphericity (Sneed & Folk, 1958; Krumbein & Sloss, 1963). However, this definition is similar to that of Corey's shape factor (Eq. 2.17). In addition, Sneed & Folk (1958) set up a triangular diagram for representation of particle shape.

Other form descriptors have also been suggested such as elongation (the ratio of the intermediate to the largest length), flatness (the ratio of the smallest to the largest length) (Zingg, 1935)[11], shape factor $F = \dfrac{L \times S}{I^2}$ (Aschenbrenner, 1956), and normalised shape factor (Sukumaran & Ashmawy, 2001) etc.

Recently Reddy (2008) argued that the above methods might not be applicable to small and platy particles such as mica or glass glitter due to the difficulty in measuring the smallest dimension. To overcome the problem, he assumed a particle to be a scalene ellipsoid with equivalent volume. From this the smallest dimension of the particle can be indirectly estimated if the average volume of the particle can be measured[12]. The new form descriptor, named *Scalene Ellipsoid Equivalent Sphericity* (SEES), is defined as the ratio of the smallest length to the largest length. The meaning of this ratio is similar to that of the flatness ratio. SEES is good for differentiating platy particles.

Fig. 2.28 illustrates the sphericity of two simple geometric solids (i.e. a cylinder and an ellipsoid) obtained using the above concepts. It can be seen that the various form descriptors gives somewhat similar values of sphericity for bulky particles. However, the

---

[11] Cited in Krumbein (1941); Aschenbrenner (1956).

[12] Instead of measuring the volume of one sand particle, the volume of a number of a certain particles with similar grain size is measured. Then the average volume is estimated from the number particles.

values of sphericity for elongated and platy particles given by different descriptors are considerably different. Operational sphericity and true sphericity are less sensitive to the flatness and therefore do not well differentiate platy particles. $SEES$ is suitable for symmetric particles, but not for asymmetric particles (Fig. 2.28b), since it ignores the intermediate length. Maximum projection sphericity can be used to differentiate platy particles; however it overestimates the sphericity of elongated particles. CSF may overcome the disadvantages of the others. For elongated particles (see the left hand side of Fig. 2.28a), CSF somewhat agrees with working sphericity and operational sphericity. More over, CSF is sensitive to particle flatness, and hence can be used to differentiate particles with small difference in flatness.

2.5 Summary

- The small strain response of geomaterials can be described by stress-strain hysteretic loops, of which maximum shear modulus, G_{max}, shear modulus degradation as a function of shear strain, G/G_{max}, and damping ratio, D, are the main representative parameters. They are also the key parameters in design of soil structures with small deformations under rapid and repetitive loads.

- Void ratio and mean effective stress significantly affect the small strain response of soils. The effect of void ratio can be taken into account using a void ratio function. Many empirical void ratio functions have been proposed. However, they can only be applied for certain soils over a narrow void ratio range. Other parameters affecting the small strain behaviour of soils are inherent anisotropy, confinement time, number of cyclic loadings, particle characteristics, OCR, and cementation/bonding etc.

- Particle characteristics (e.g. particle shape, particle size and mineral composition), are fundamental to the behaviour of soils. They control many soil parameters such as void ratio range ($e_{max} - e_{min}$), soil fabric, particle strength, inter-particle friction, contact force, contact area, and co-ordination number etc.

- Hardin (1961); Hardin & Richart (1963); Hardin & Drnevich (1972*b*); Iwasaki & Tatsuoka (1977) suggested that particle size and particle shape was an unimportant parameter for G_{max}. They suggested that particle shape and particle size influences G_{max} through changing void ratio range, and when a void function $F(e)$ was taken into account, particle size and particle shape could be ignored. Recently, Cho *et al.* (2006), despite the variation in void ratio and particle size, suggested that particle shape was an important parameter influencing G_{max}. These differences in whether particle characteristics influence G_{max} may be due to the fact that each researcher focused on a single parameter without considering other parameters.

Therefore, a full assessment of the roles of particle characteristics on the small strain behaviour is essential.

TABLE 2.1: Various void ratio functions and stress exponents (modified from Mitchell & Soga, 2005)

References	soils	void ratio	$F(e)$	n
Hardin & Richart (1963)	Ottawa sand	0.37-0.78	$\frac{(2.174-e)}{(1+e)^2}$	0.5
	Crushed quartz	0.63-1.26	$\frac{(2.973-e)}{(1+e)^2}$	0.5
Hardin & Black (1966)	Ottawa sand	NA	$\frac{(2.174-e)}{(1+e)^2}$	0.5
	Crushed quartz	NA	$\frac{(2.973-e)}{(1+e)^2}$	0.5
Hardin & Black (1968)	NC Kaolinite	0.76-0.9	$\frac{(2.973-e)}{(1+e)^2}$	0.5
Hardin & Black (1969)	Various soils	0.59-1.98	$\frac{(2.973-e)}{(1+e)^2}$	0.5
Hardin & Drnevich (1972*b*)	Various soils	0.57-0.98	$\frac{(2.973-e)}{(1+e)^2}$	0.5
Marcuson & Wahls (1972)	Kaolinite	1.1-1.31	$\frac{(2.973-e)}{(1+e)^2}$	0.5
	Bentonite	1.61-2.48	$\frac{(4.4-e)}{(1+e)^2}$	0.5
Kokusho *et al.* (1982)	NC clay in Japan	1.73-3.86	$\frac{(7.32-e)}{(1+e)^2}$	0.6
Athanasopoulos & Richart (1983)	Powdered kaolinite clay	0.9-1.2	$(0.3+0.7e^2)^{-1.361}$	0.49
Lo Presti *et al.* (1993)	Ticino sand	0.61-0.80	$\frac{(2.27-e)}{(1+e)^2}$	0.43
Jamiolkowski *et al.* (1995)	Panigaglia Clay	1.4-1.8	$e^{-1.3}$	0.5
	Pisa Clay	0.8-1.8	$e^{-1.43}$	0.44
	Garigliano	0.9-1.2	$e^{-1.11}$	0.58
	Fucino	1.6-3.0	$e^{-1.52}$	0.40
	Montalvo di Castro	0.6-0.8	$e^{-1.33}$	0.40
	Avezzano	1.0-1.8	$e^{-1.27}$	0.46
Shibuya & Tanaka (1996)	Insitu slight OC clay	1.3-4.5	$e^{-1.5}$	0.5
Shibuya *et al.* (1997)	Natural sediment	1.0-6.0	$(1+e)^{-2.4}$	0.5
Lo Presti *et al.* (1997)	Toyoura	0.81-0.98	$e^{-1.3}$	0.45
	Quiou sand	0.84-1.18	$e^{-1.3}$	0.62
Wichtmann & Triantafyllidis (2004)	fine, medium sands	0.57-0.76	$\frac{(1.46-e)}{(1+e)^2}$	0.42

Table 2.2: Co-ordination number for various regular packing of spheres

Systematic arrangement	Nc	solid volume	void ratio
simple cubic	6	$\frac{\pi}{6}$	0.910
body-centred-cubic (orthorhombic)	8	$\frac{\pi}{3\sqrt{3}}$	0.654
Tetragonal	10	$\frac{2\pi}{9}$	0.432
face-centred-cubic	12	$\frac{\pi}{3\sqrt{2}}$	0.350
close packed hexagonal (Rhombohedral)	12	$\frac{\pi}{3\sqrt{2}}$	0.350

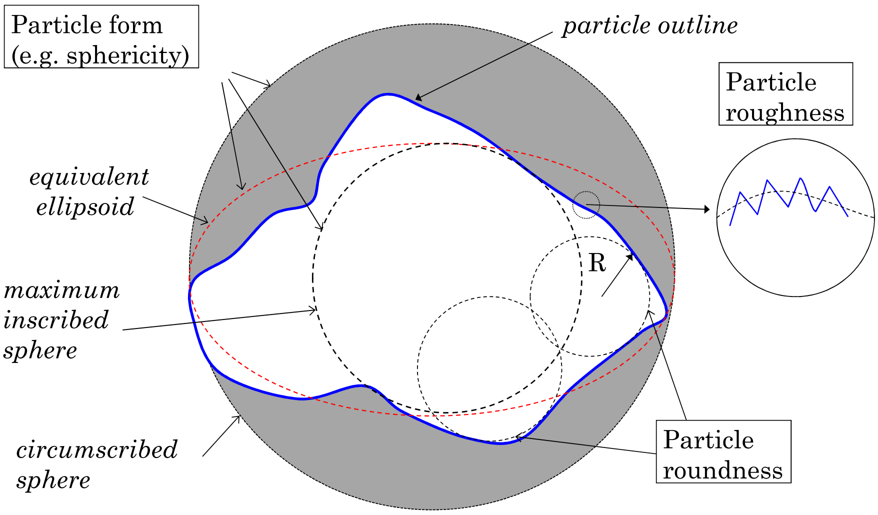

FIGURE 2.1: Particle shape terminology (modified after Barrett, 1980)

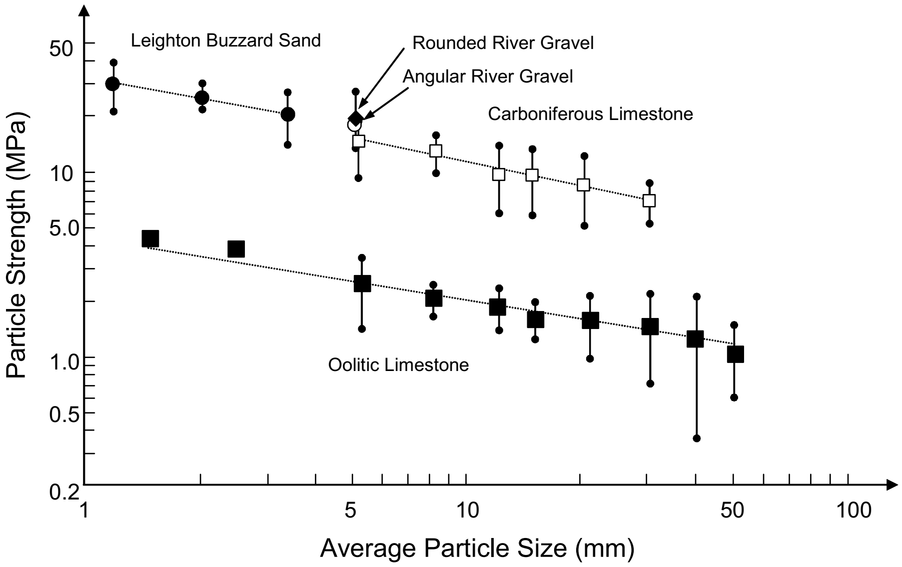

FIGURE 2.2: Relationship between tensile strength and particle size (Lee, 1992)

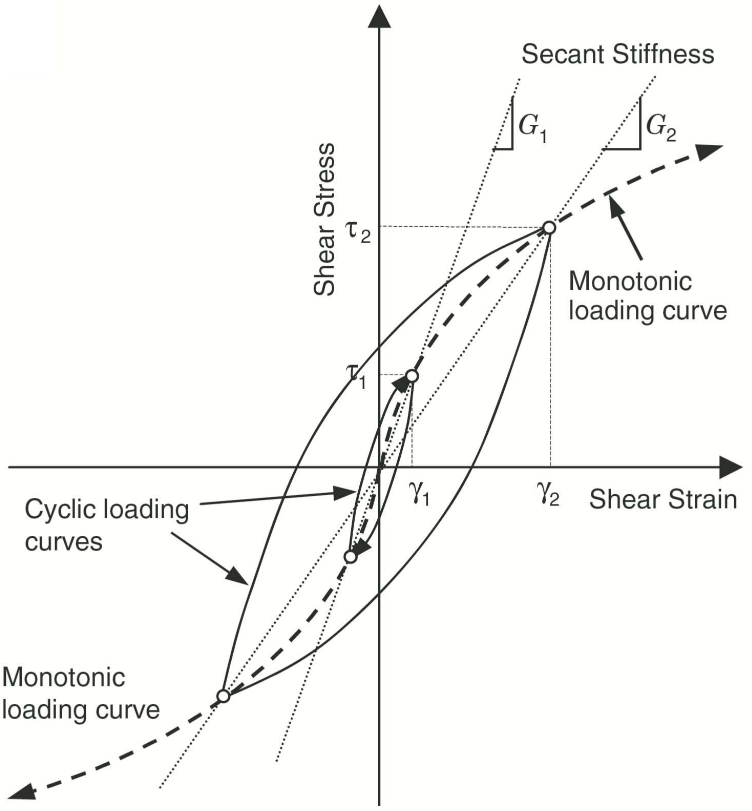

FIGURE 2.3: Monotonic and cyclic stress-strain relationships (redrawn after Mitchell & Soga, 2005)

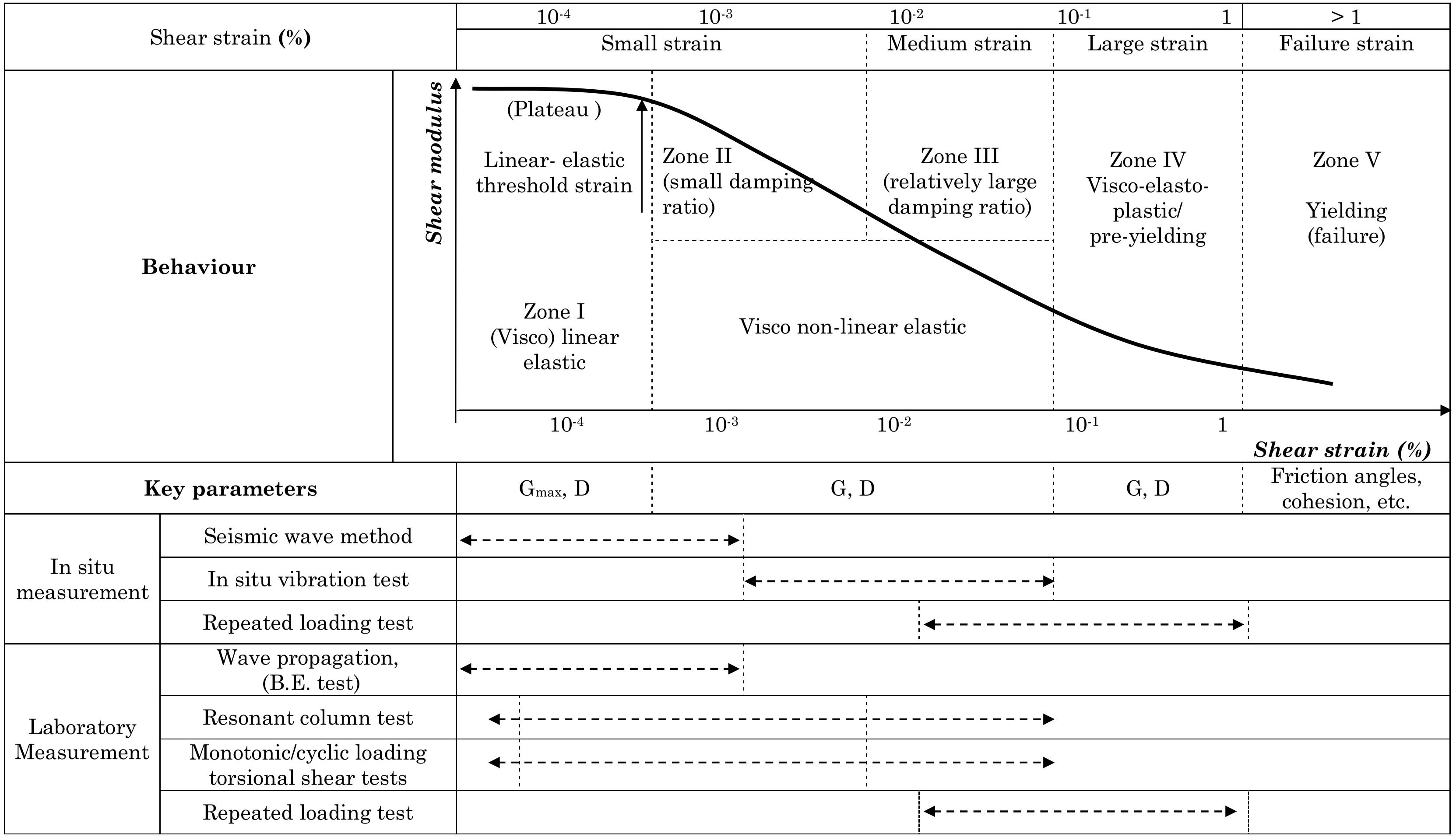

FIGURE 2.4: Strain dependent behaviour of geomaterials (modified from Ishihara, 1996)

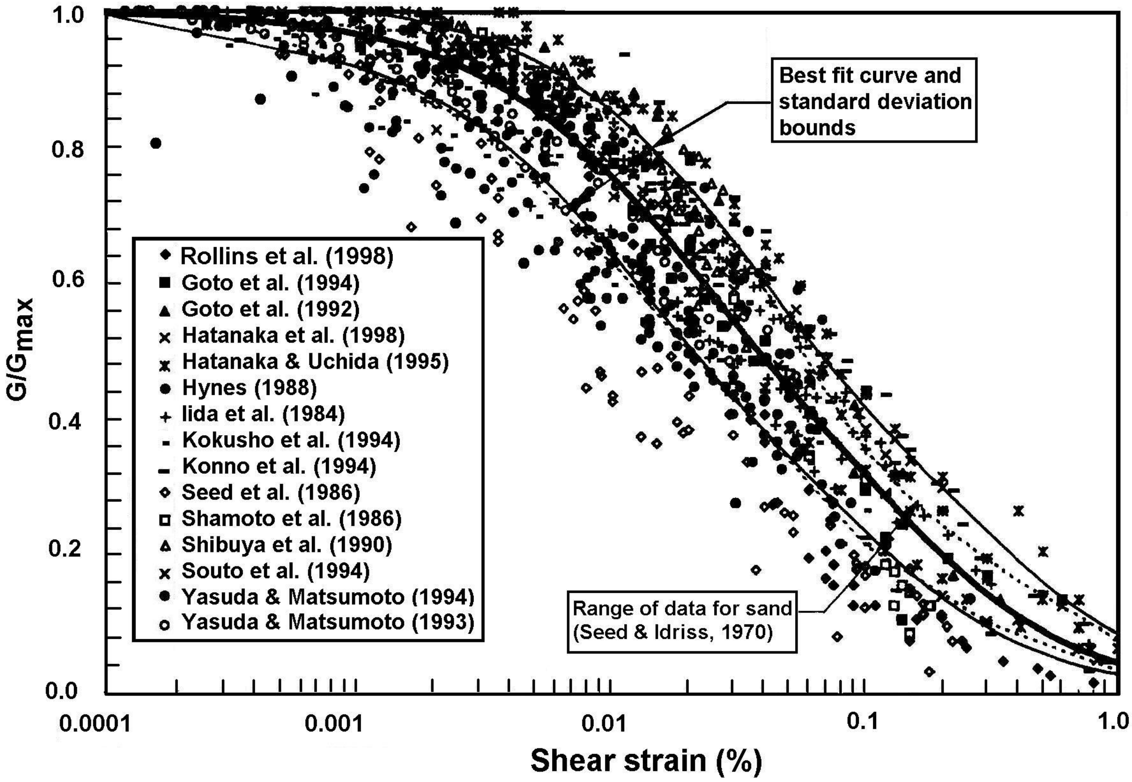

FIGURE 2.5: Shear modulus degradation curves of many soils as a function of shear strain (Rollins *et al.*, 1998)

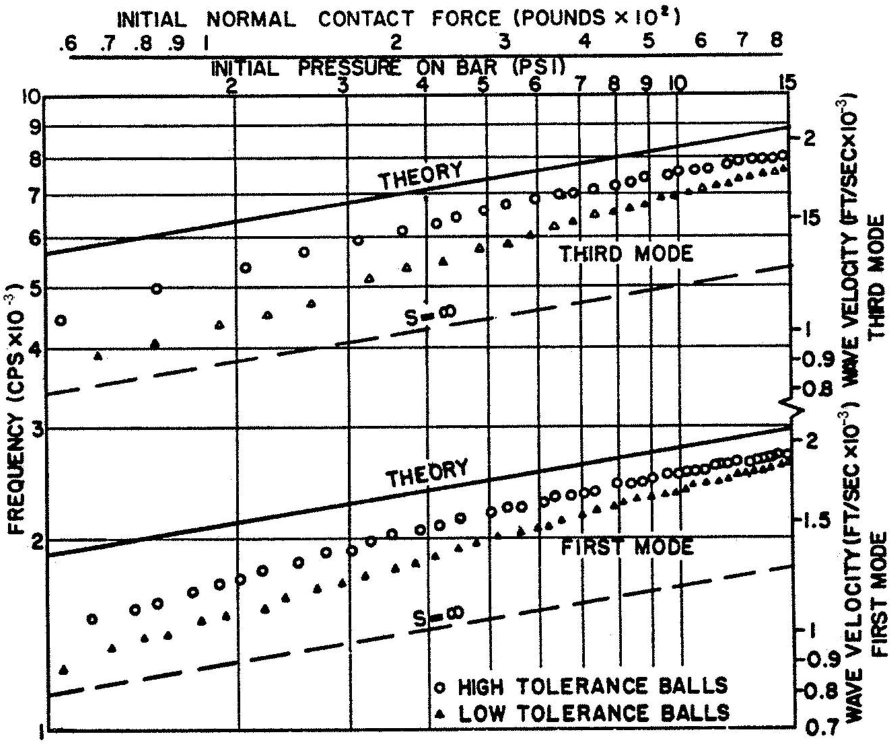

Resonant Frequency of Bar as a Function of Pressure for [1, 0, 0] Orientation

Figure 2.6: Theoretical and experimental wave velocity of close packed steel spheres (Duffy & Mindlin, 1957)

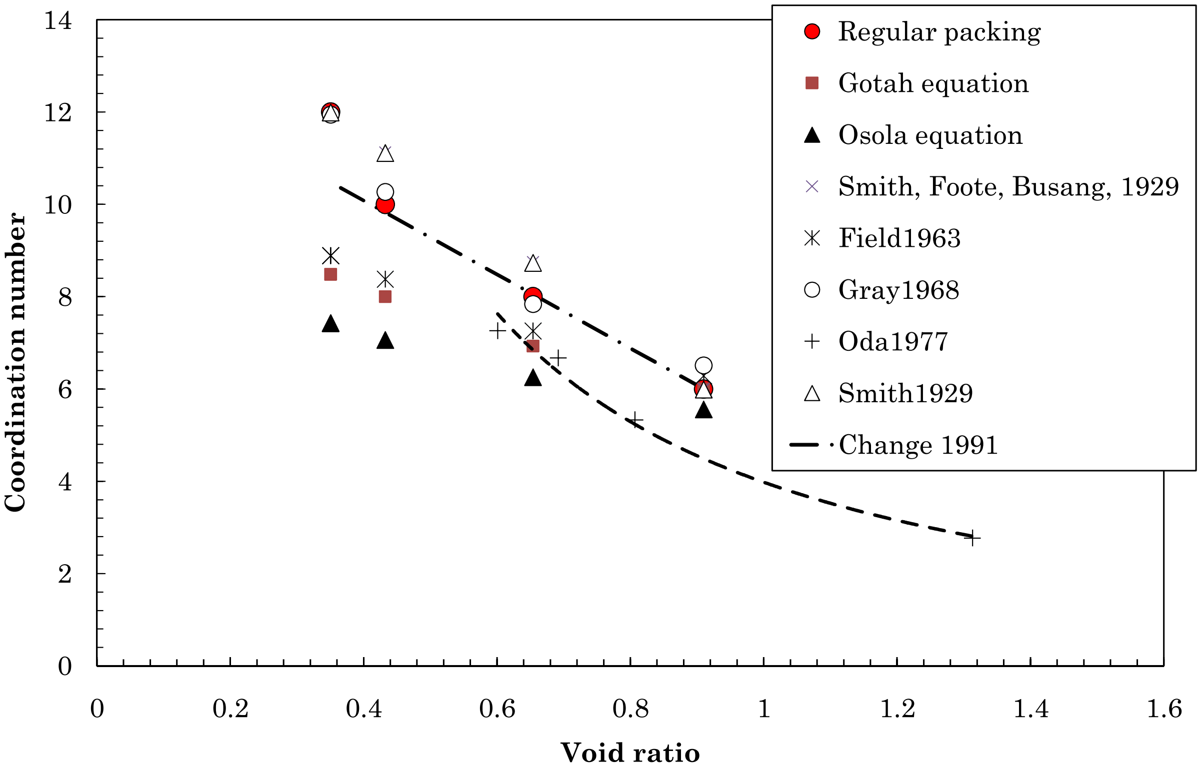

FIGURE 2.7: Co-ordination number of packing of single-size spheres as a function of void ratio

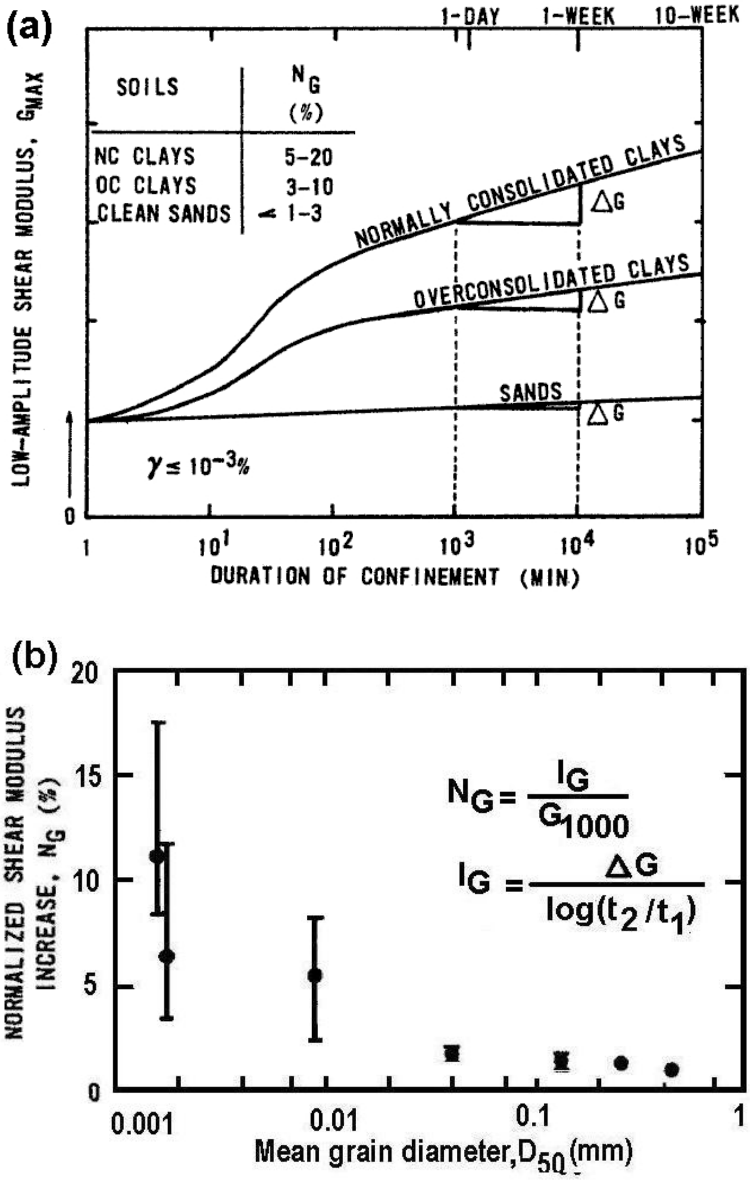

FIGURE 2.8: Effect of confinement time on shear modulus. (a) Effect of confinement time on G_{max} of various soils; (b) Effect of particle size on I_G (Anderson & Stokoe, 1978)

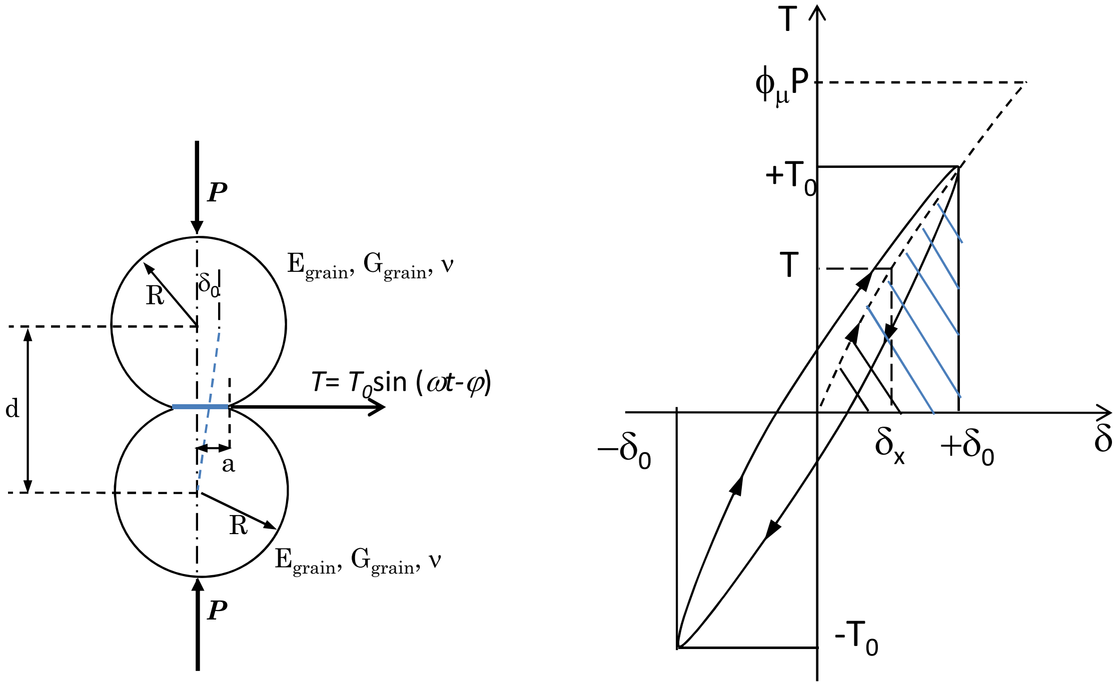

(a) Vibration of two spheres in contact

(b) Hysteretic force-displacement loop

FIGURE 2.9: Vibration of two elastic spheres in contact (Johnson, 1987)

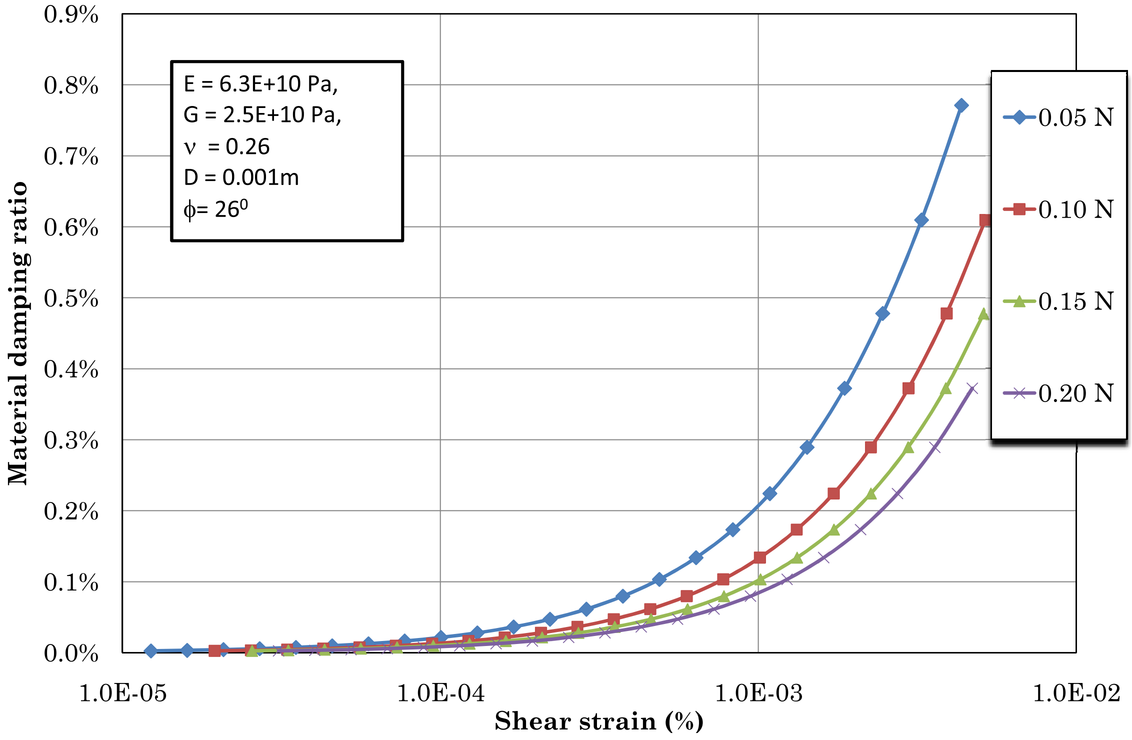

FIGURE 2.10: Effect of contact force on damping ratio of two spheres in contact

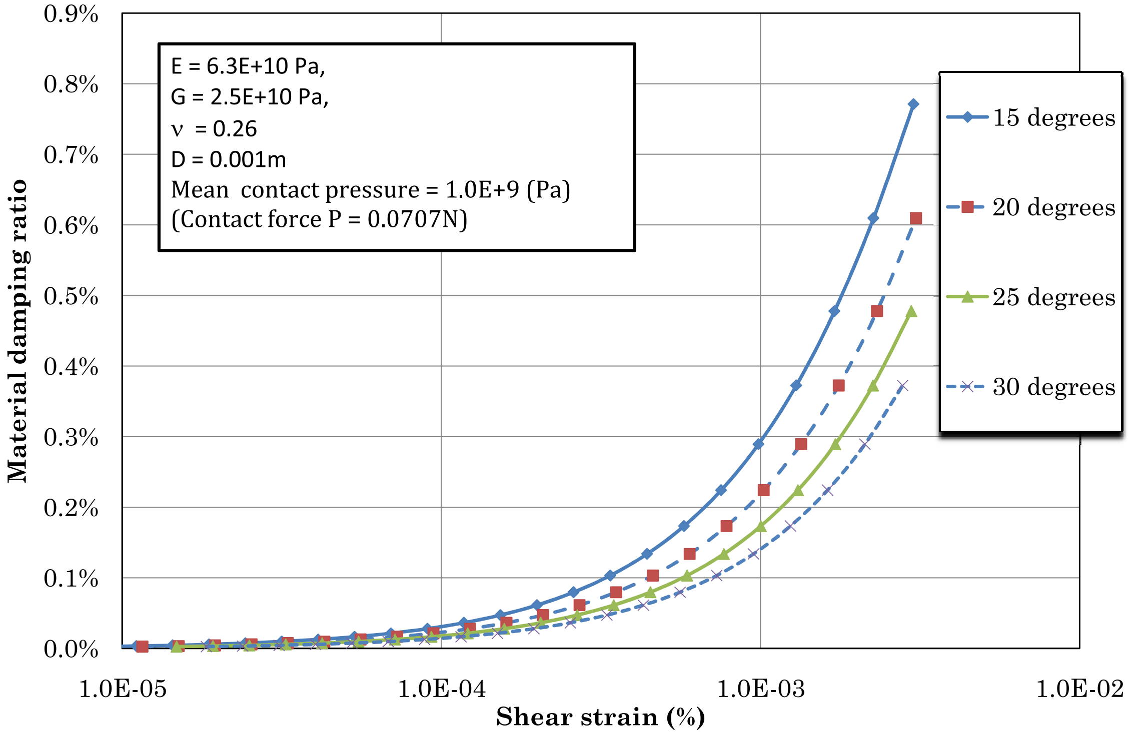

FIGURE 2.11: Effect of inter-particle friction angle on damping ratio of two spheres in contact

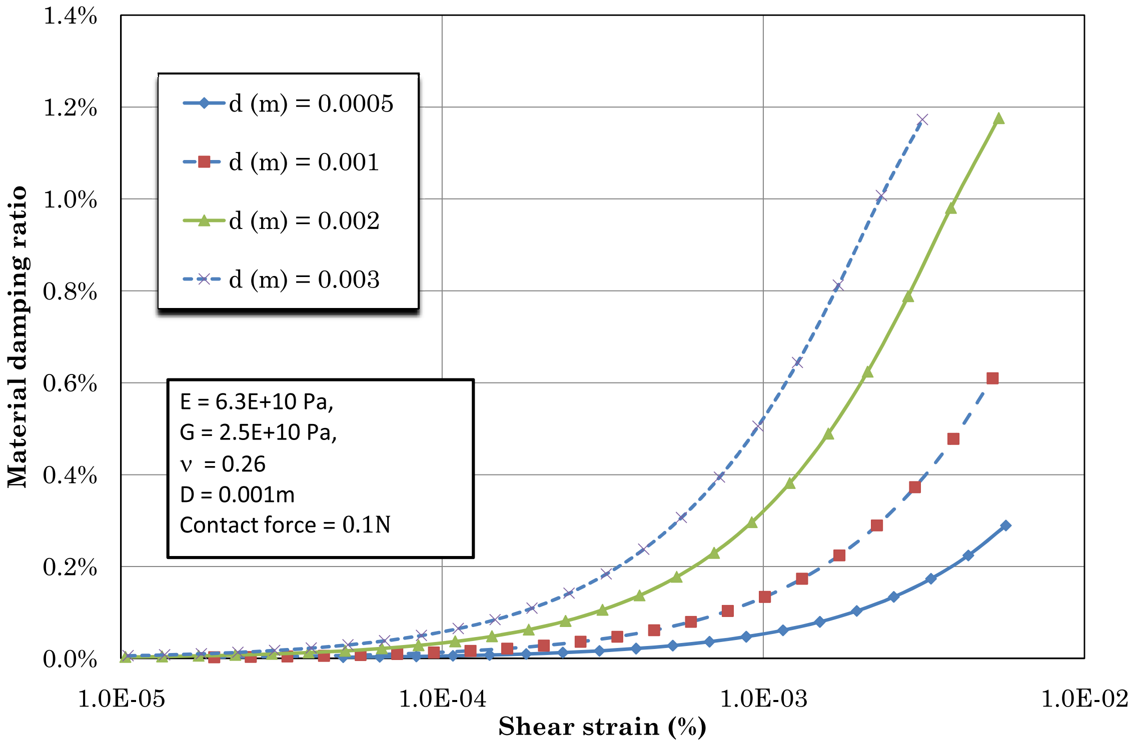

FIGURE 2.12: Effect of diameter on damping ratio of two spheres in contact under the same contact force

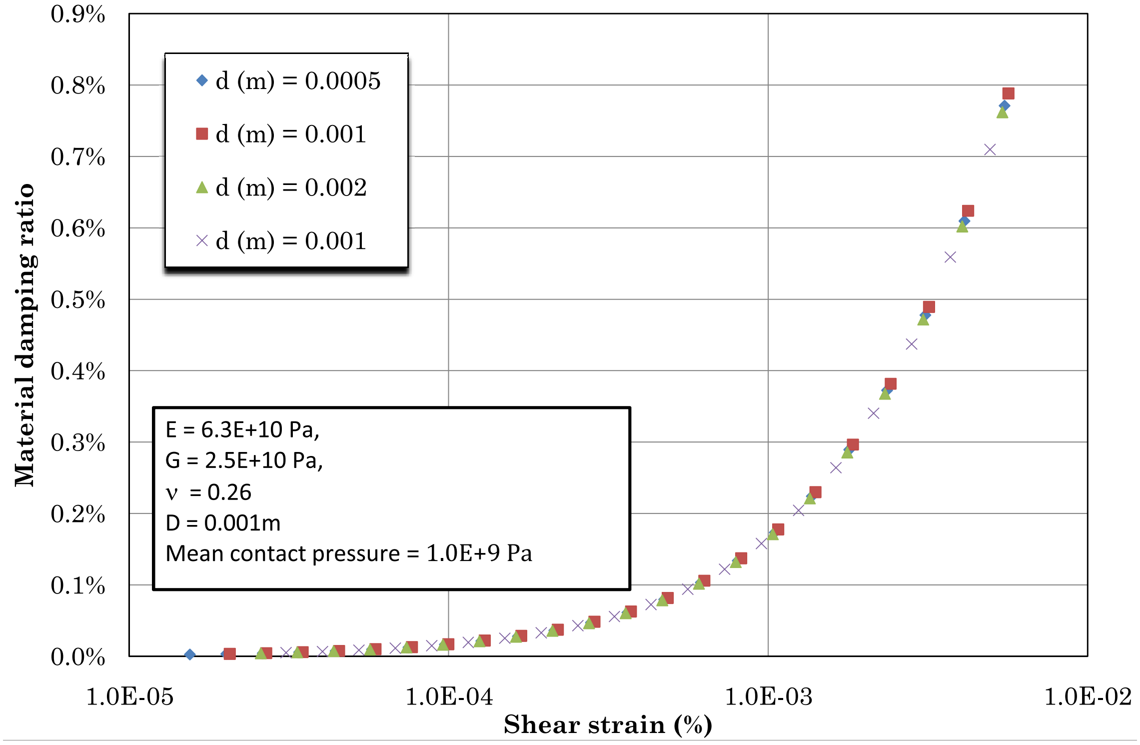

FIGURE 2.13: Effect of diameter on damping ratio of two spheres in contact under the same mean contact pressure

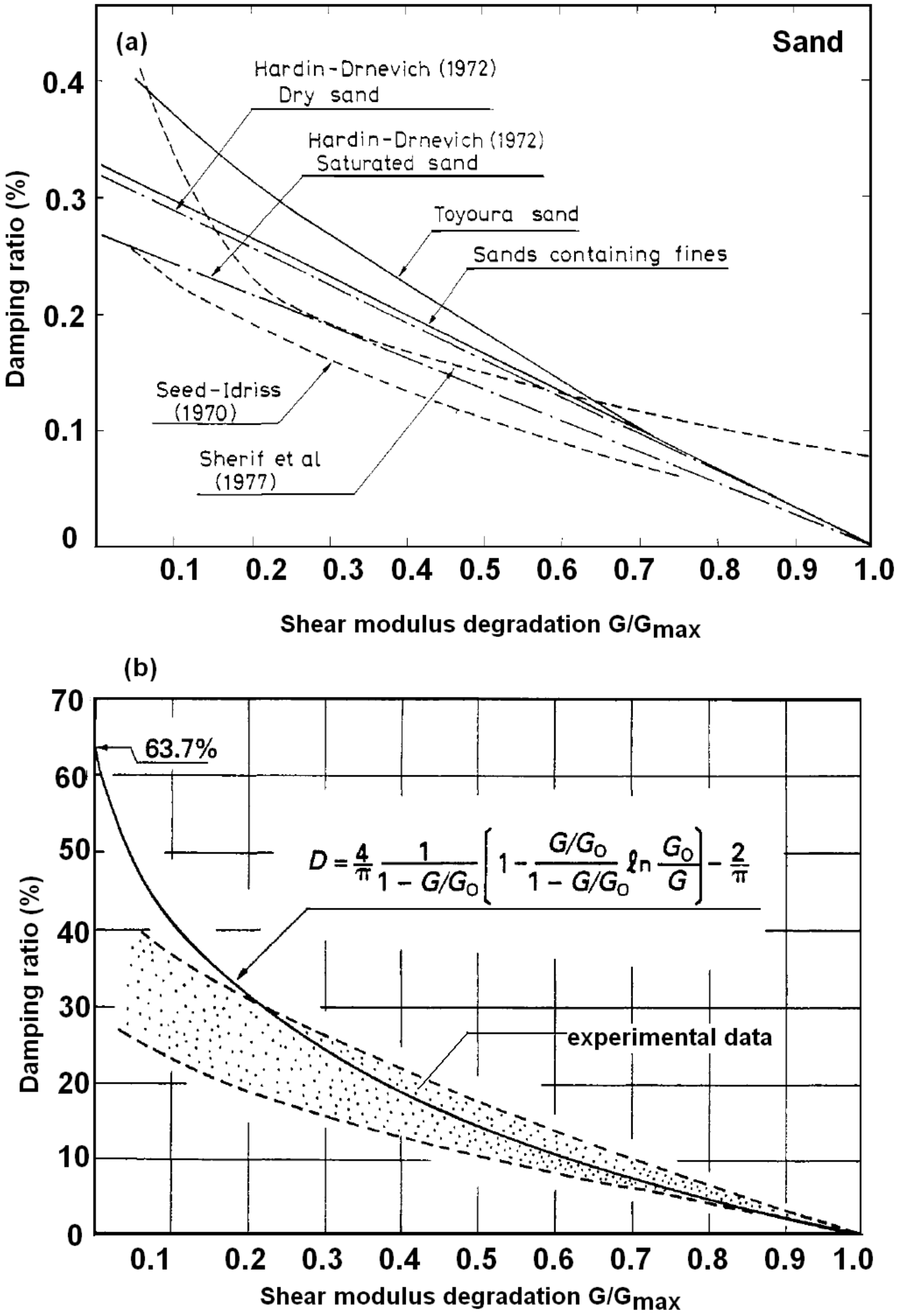

FIGURE 2.14: Relationship between damping ratio and stiffness degradation. (a) Experimental data; (b) Hyperbolic model (Ishihara, 1996)

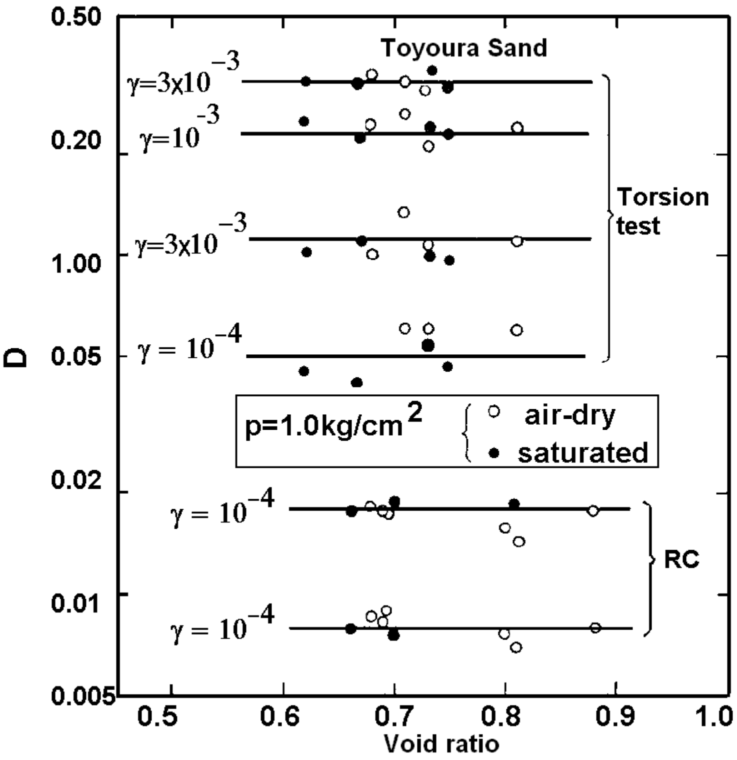

FIGURE 2.15: Damping ratio at medium to large strain versus void ratio of Toyoura sand at 1.0kg/cm2 (Tatsuoka *et al.*, 1978)

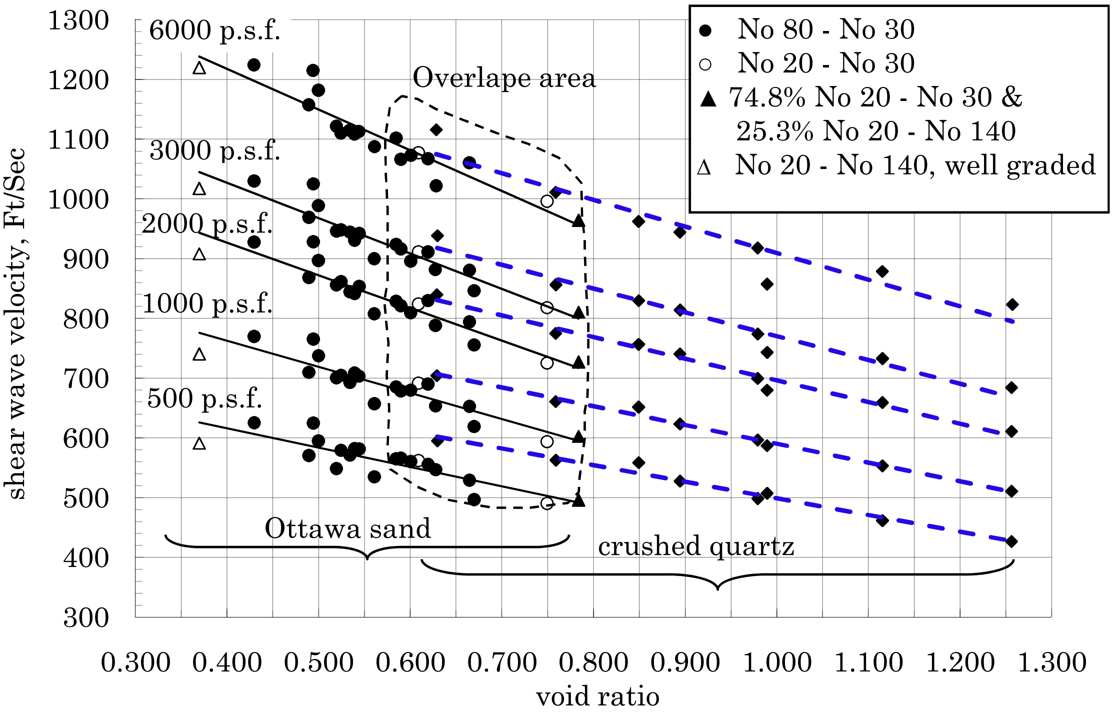

FIGURE 2.16: Comparison of V_s and G_{max} between Ottawa sand & crushed quartz (plot based on data of Hardin & Richart, 1963)

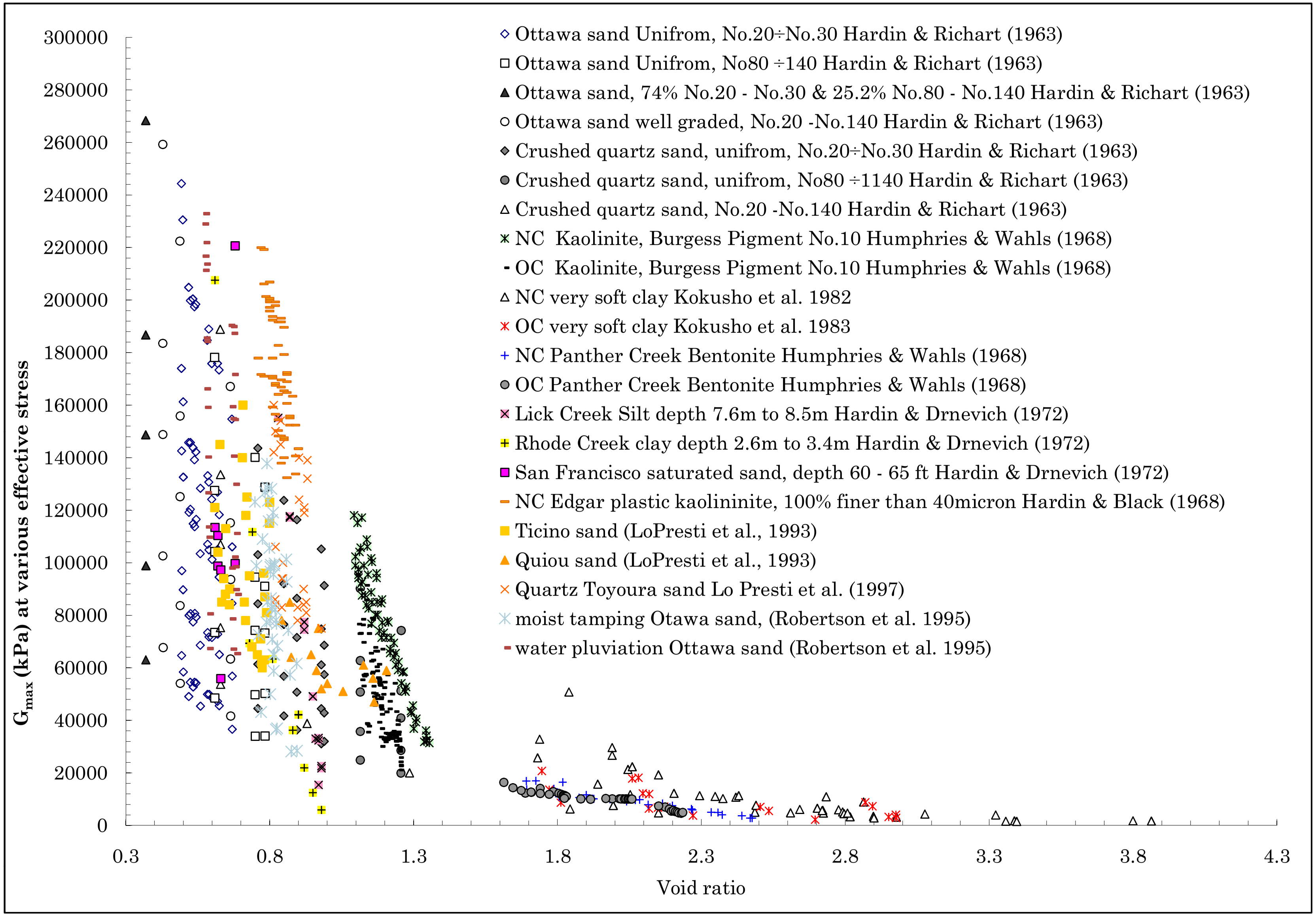

FIGURE 2.17: G_{max} versus void ratio of several geomaterials

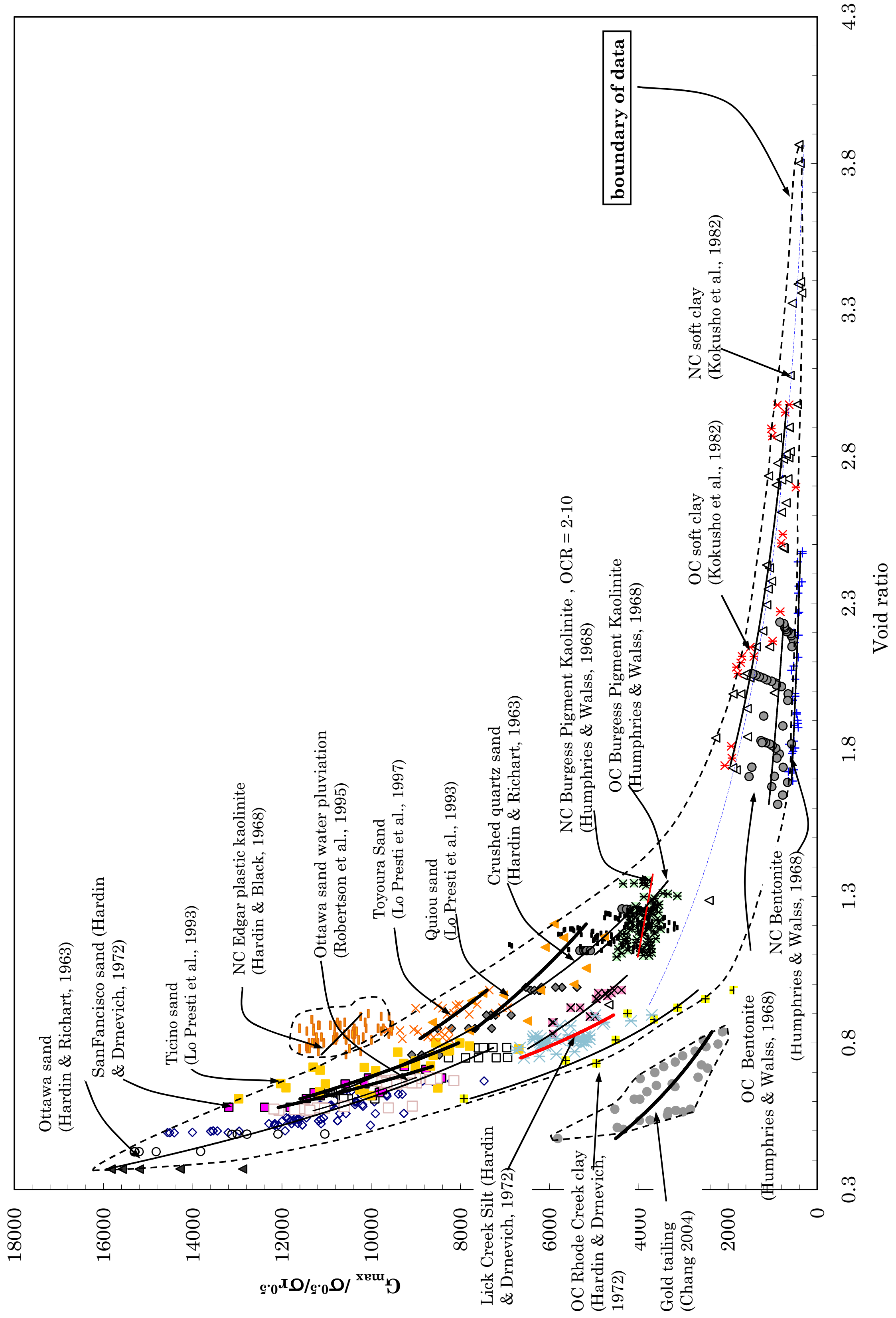

FIGURE 2.18: G_{max} normalised by $\sigma'_0{}^{0.5}$ versus void ratio of many geomaterials

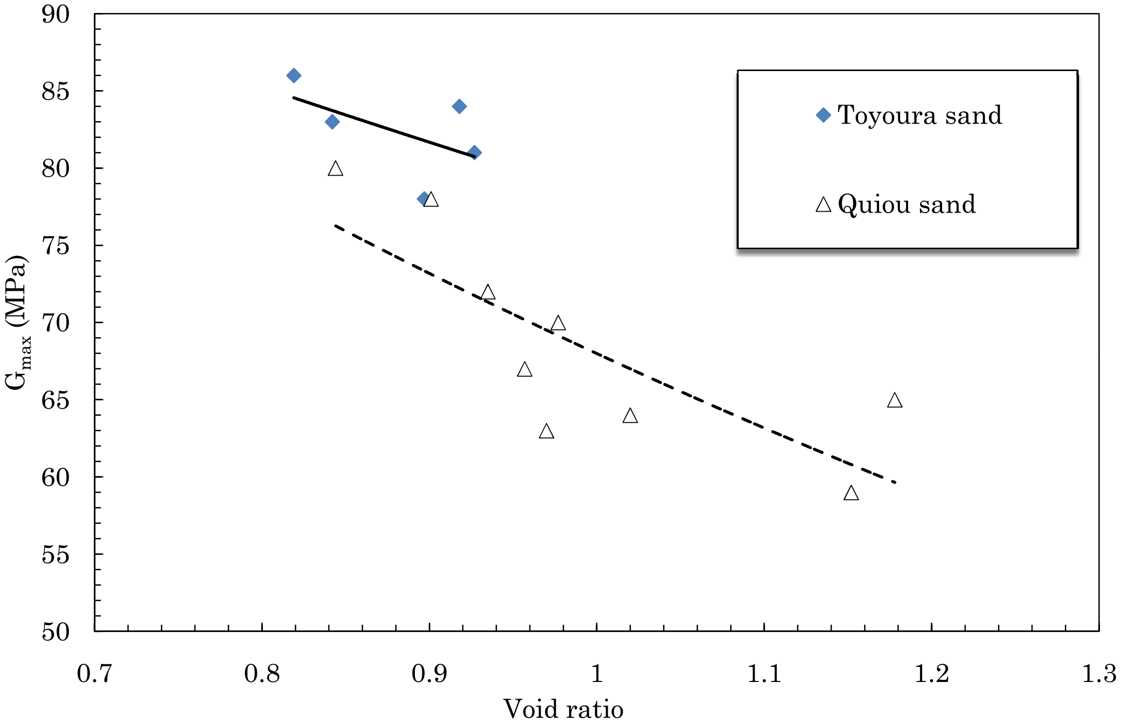

FIGURE 2.19: Small strain shear modulus of sands tested by RCA at 100 kPa (data from Lo Presti *et al.*, 1997)

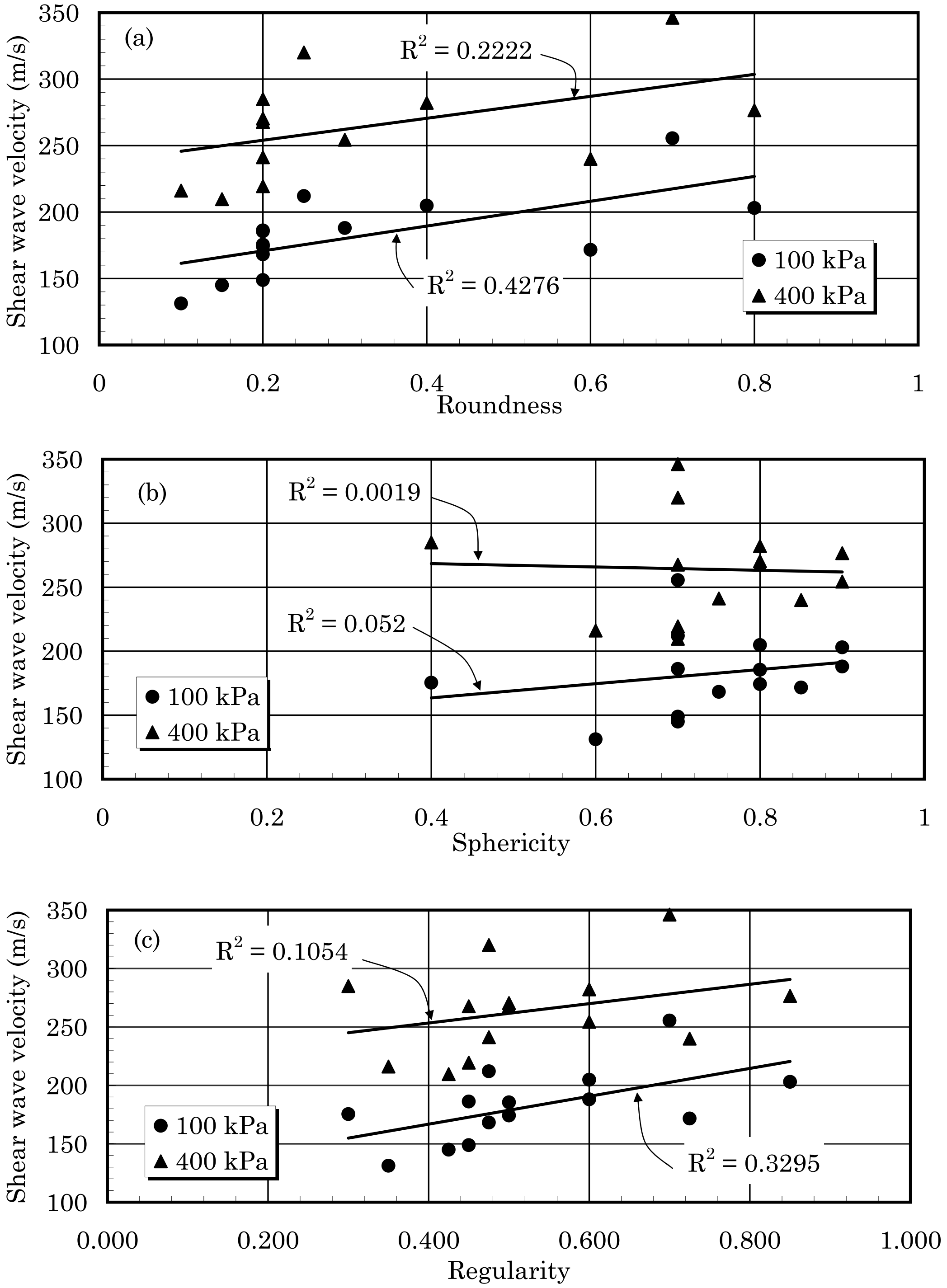

FIGURE 2.20: Effect of particle shape on V_s at $\sigma_0 = 100\ kPa$. Values of V_s were computed based on data of Cho *et al.* (2006)

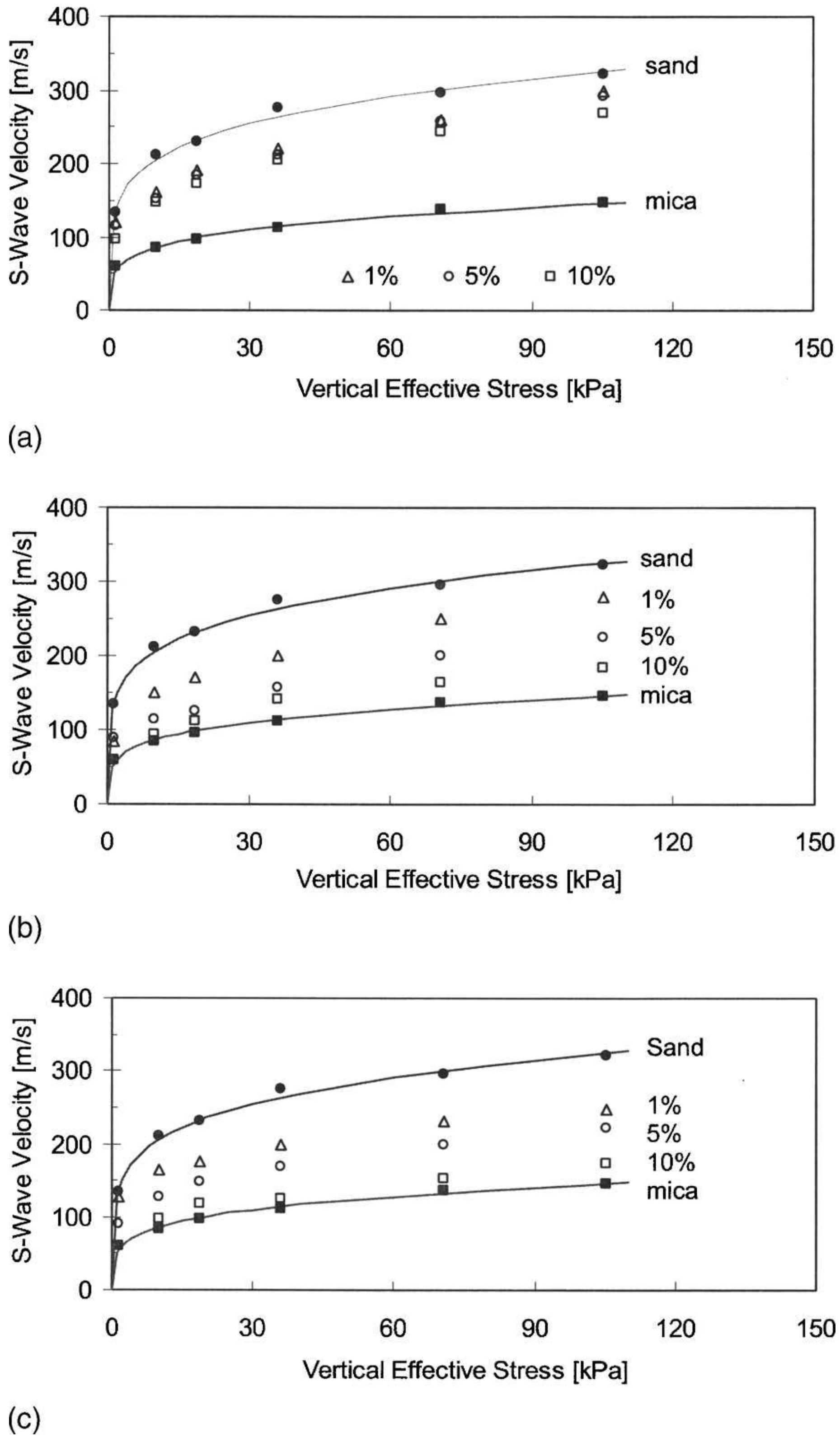

FIGURE 2.21: Shear wave velocity versus vertical effective stress for mixtures of Ottawa 5070 sand with mica. (a) $L_{mica}/D_{sand} = 0.33$; (b) $L_{mica}/D_{sand} = 1$; (c) $L_{mica}/D_{sand} = 3$ (Lee *et al.*, 2007)

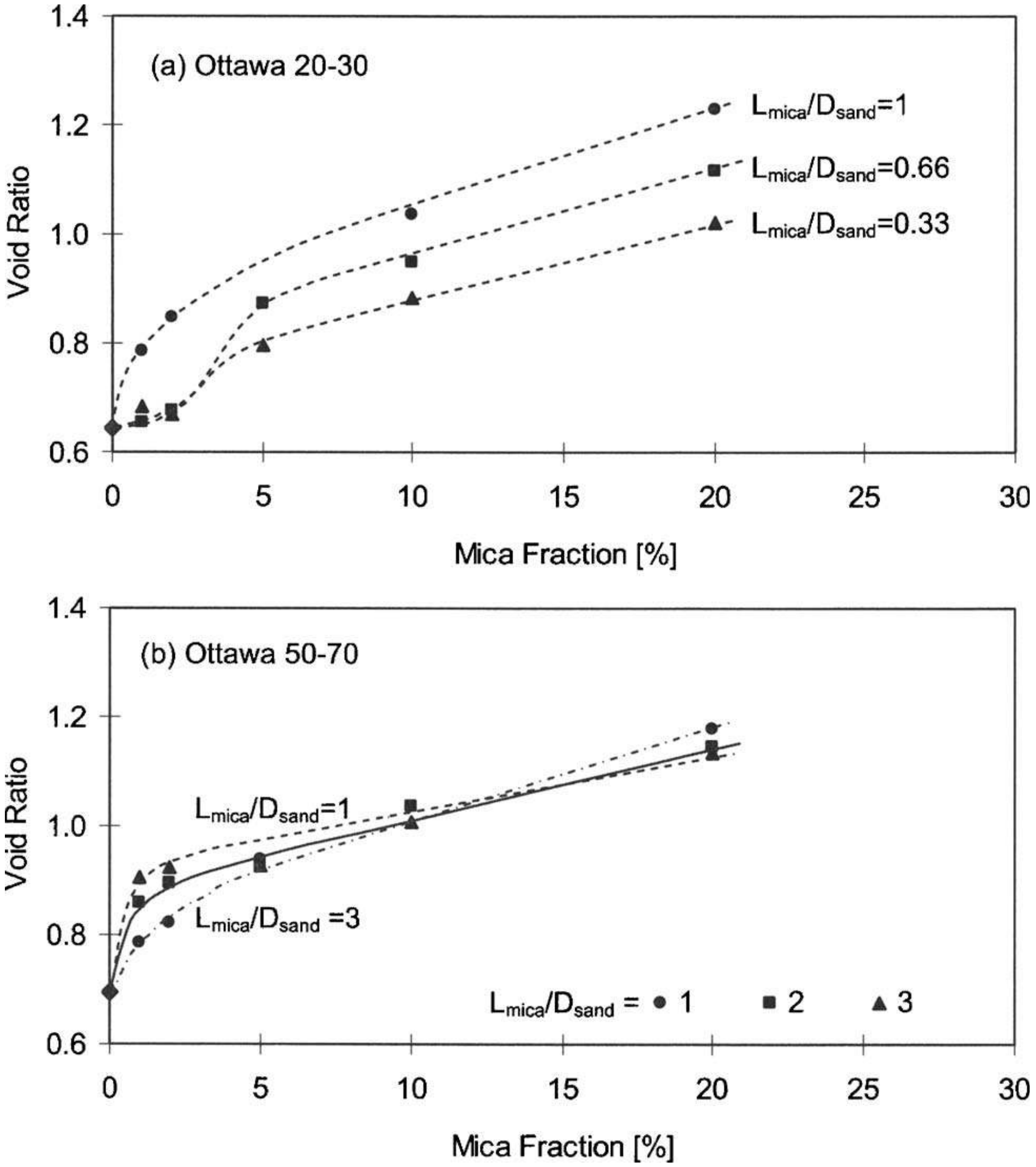

Figure 2.22: Void ratio versus mica content (Lee *et al.*, 2007)

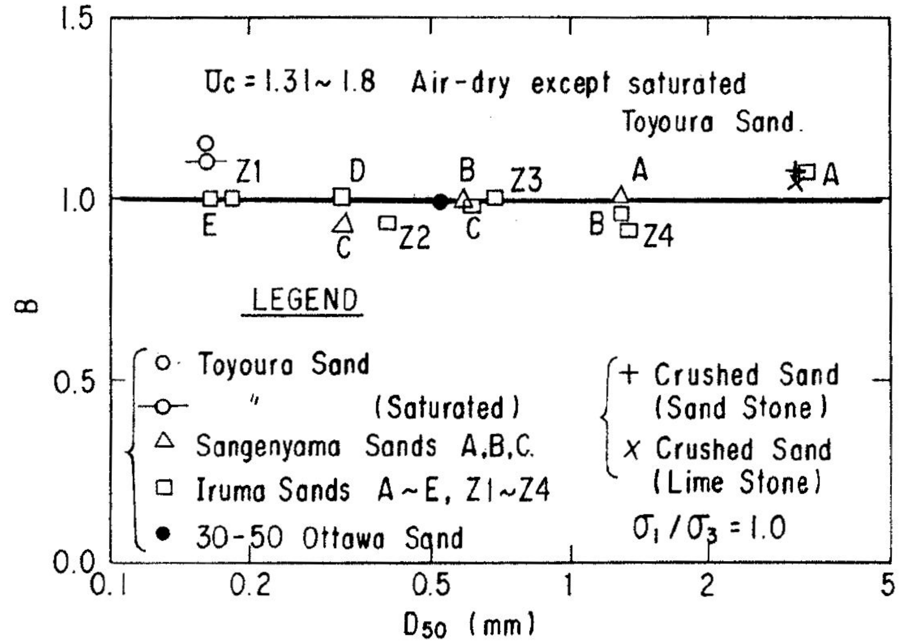

FIGURE 2.23: Relationship between B-value (Eq. 2.12) and D_{50} for clean sands (Iwasaki & Tatsuoka, 1977)

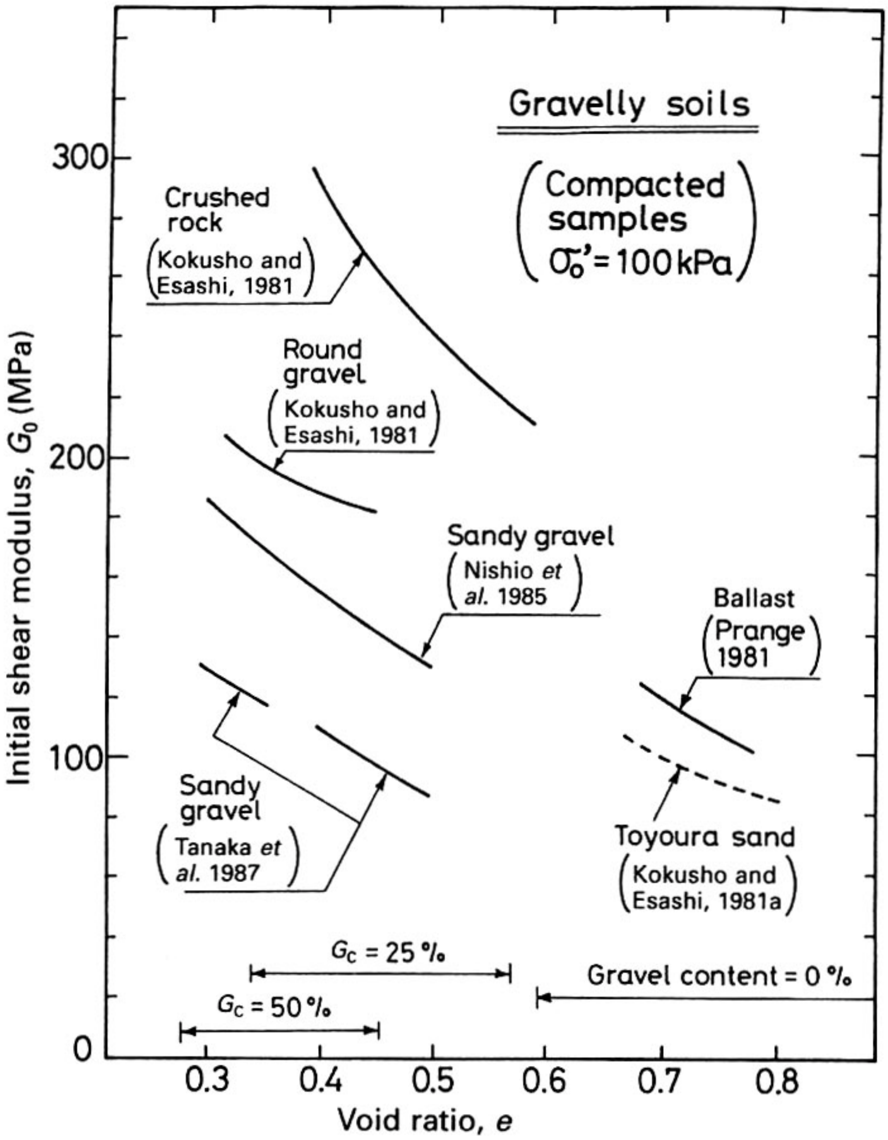

FIGURE 2.24: G_{max} versus void ratio of gravelly soils (Ishihara, 1996)

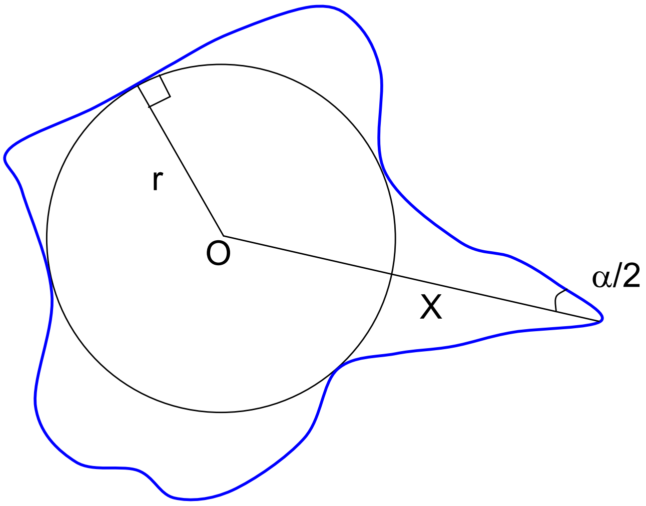

FIGURE 2.25: Measurement of angularity (Lees, 1964)

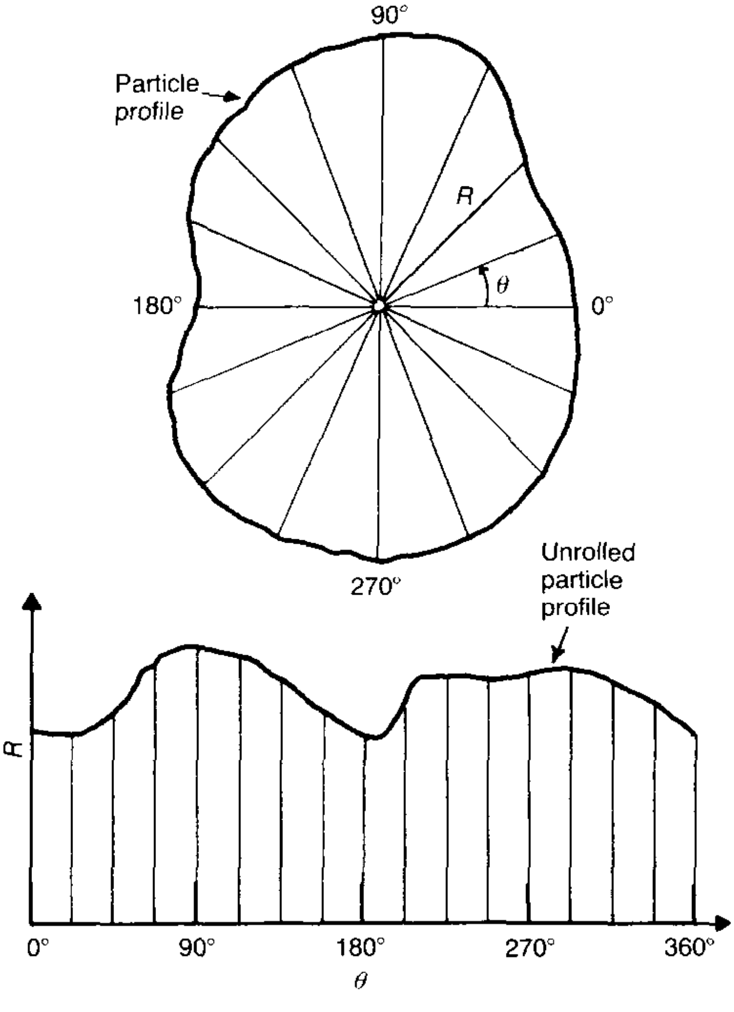

Figure 2.26: Particle profile in closed form and unrolled form for Fourier Analysis (Vallejo, 1995)

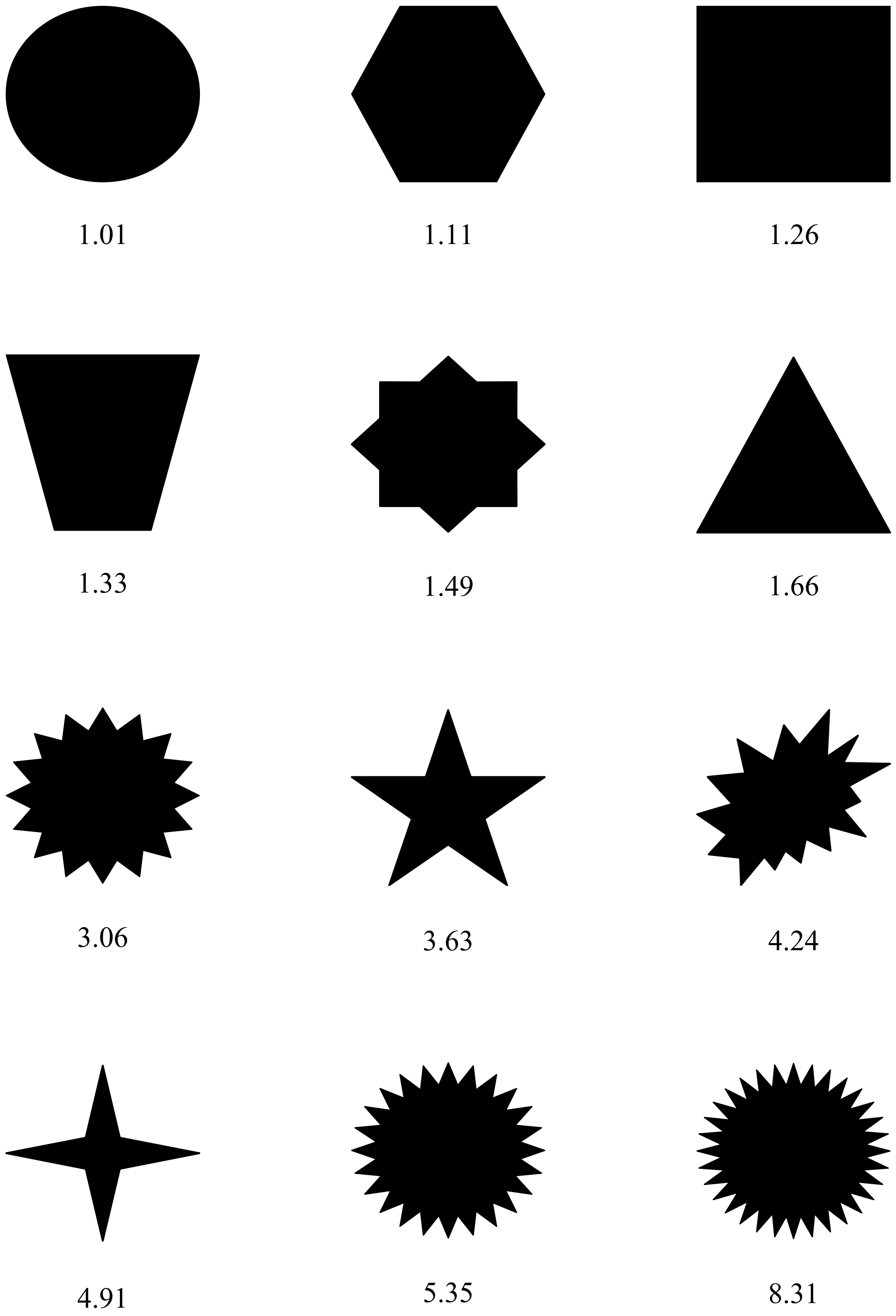

FIGURE 2.27: *Angularity index* (reverse of *roundness index*) for various irregular geometrical shapes of same size (Reddy, 2007)

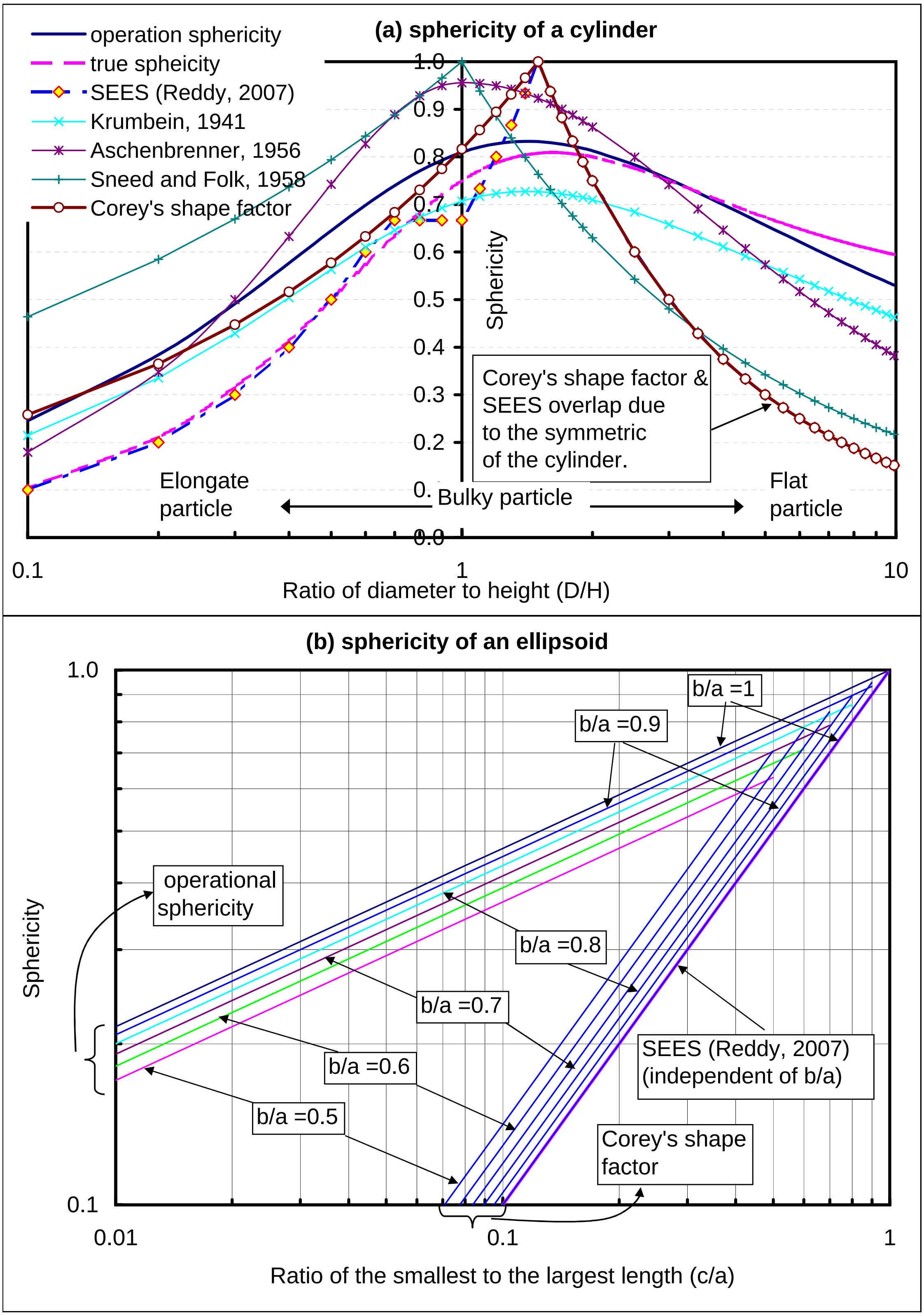

FIGURE 2.28: Examples of sphericity of simple solids

Chapter 3

Laboratory testing method: resonant column apparatus

3.1 Introduction

Resonant column (RC) testing is one of the popular laboratory techniques used to measure the small strain response of a soil specimen. Bender element (BE) testing is also a common technique used to determine G_{max}. However, interpretation of a travel time in a BE test is problematic (Wood, 2007). In addition, bender elements can neither change nor measure a shear strain. Monotonic and cyclic loading torsional shear testing, in which applied torques are calculated using a torque-voltage calibration curve, and shear strains are determined using a pair of proximity transducers (Lo Presti *et al.*, 1993, 1997), can also be employed for the same purpose. Cyclic triaxial testing is extensively used to measure Young's modulus of soils, however, the relationship between Young's modulus and shear modulus for soils is not well known; The ratio of Young's modulus to shear modulus is often assumed to be 3.0 (Shibuya *et al.*, 1992).

RC testing was initially developed in the 1930s by Ishimoto & Iida (1936, 1937). The technique was further developed in the 1960s, and has become a standard technique used to study the small strain response of geomaterials ranging from soft soil to weak rock (e.g. Hardin & Richart, 1963; Hardin & Black, 1966, 1968; Hardin & Drnevich, 1972*b*; Iwasaki & Tatsuoka, 1977; Roesler, 1979; Kokusho *et al.*, 1982; Stokoe *et al.*, 1995; Lo Presti *et al.*, 1997; Cascante *et al.*, 2003; Clayton *et al.*, 2005; Hardin & Kalinski, 2005).

RC testing has some advantages over the other techniques. A RCA is capable of controlling shear strains induced in a soil specimen, and accurately measuring the resonant frequency, f_r, of a specimen even at very small vibratory amplitude, allowing estimation of G_{max} (or V_s) accurately without measuring applied torque. In addition, a RCA can widely vary the shear strain from very small to medium range (e.g. from 10^{-5}% to 10^{-2}%), allowing not only G_{max} but also G/G_{max} at a shear strain to be defined. A shear strain range produced by RC testing is similar to that produced by in-situ seismic testing, therefore a shear modulus and damping ratio measured using RC testing is comparable to that measured using geophysics surveying (see Fig. 2.4, Ishihara 1996). Furthermore, RC testing is a non-destructive technique, which allows a soil specimen to be tested repeatedly at different effective stress levels.

RC testing also has some minor disadvantages. A specimen, tested using a RCA, is subjected to a large number of loading cycles at a very high strain rate, which is proportional to both shear strain and frequency (Lo Presti *et al.*, 1997). In practice, a number of loading cycles and a strain rate during an earthquake (for example) is much lower. Perhaps, this is one of the reasons why RC testing is not commonly used in Japan[1]. However, it has been shown that in the elastic region, soil properties are insignificantly influenced by either number of loading cycles or strain rates.

Regarding boundary conditions in a RCA, there are three types of equipment configurations (Fig. 3.1) i.e. fixed-free, fixed-spring top, and free-free (Drnevich, 1985; Ashmawy & Drnevich, 1994). The top mass in Fig. 3.1 represents the mass polar moment of inertia of the drive mechanism and the rigidly attached instrumentation. Due to the simplicity of equipment and data reduction technique, the fixed-free (Fig. 3.1a) is one of the most popular types of RCA for determining dynamic properties of soils (Drnevich, 1985).

3.2 Working principle of the RCA

Fig. 3.2 presents a schematic diagram of the Stokoe RCA used in this research. A specimen is fixed to the test base at one end, attached to the drive mechanism (Fig. 3.3) at the other end, and subjected to an isotropic effective stress. A digital sinusoidal waveform generated by a computer program is converted to an analogue signal by an A/D controller box connected to a computer via a *DT open layers DT3016* PCI card. The signal is then amplified by an *HP 6826A BIPOLAR* power amplifier before going to the coils. The magnetic field produced by the current in the coils generates a harmonic electro-magnetic force, which oscillates the specimen. The motion of the specimen free end is measured using a *DJB A20* high sensitivity piezo-electric accelerometer (charge sensitivity = $37.7pC_{peak}/G_{peak}$) mounted on one arm of the drive plate. The accelerometer generates charges proportional to acceleration of the specimen free end. The charges are then converted to voltages and amplified by a *4102M-220 Columbia Research Laboratories* charge amplifier. The charge amplifier is set in a manner that 5.0 peak-to-peak Volts is equivalent to $K \times g$ (m/s^2) input acceleration, in which $K = 1/10/100$ is an amplifying factor, and $g = 9.81m/s^2$ is the gravitational acceleration at the earth surface. The analogue voltages are converted to a digital signal, stored and then analysed by the computer program.

By varying the vibratory frequency, a frequency response curve at a given shear strain can be determined (Fig. 3.8). Via data analysis, the resonant frequency of the system can be determined. Based on analytical solutions which are derived based on the soil behaviour model used (e.g. linear elastic or visco-elastic etc.) and apparatus configuration (i.e.

---

[1] Private conversation with Professor T. Kokusho in June 2007 during the 4th Geotechnical Earthquake Engineering in Thessaloniki, Greece.

stiffness and boundary conditions), both the shear modulus and the damping ratio (at a given shear strain) of the specimen can be calculated.

3.3 Theoretical considerations for the Stokoe RCA

Three are three classic mechanical problems, namely wave propagation in a cylindrical elastic rod (Timoshenko *et al.*, 1974; Richart *et al.*, 1970), single degree of freedom (SDOF) torsional vibration (Timoshenko *et al.*, 1974), and wave propagation in a cylindrical visco-elastic rod (Hardin, 1965), which are applicable to the Stokoe RCA. Since the problems are well documented, this section reviews only the main aspects such as governing equations, final solutions, etc., and highlights the assumptions applied during the mathematical derivation. However the simplifying assumptions in some degree are violated in practice, causing errors in measurement of shear modulus.

3.3.1 Shear wave propagation in a fixed-free cylindrical elastic rod

Governing equation

In the small strain region, the damping ratio is small and can be ignored. The shear wave propagating in a soil specimen is assumed similar to that in a cylindrical elastic rod as illustrated in Fig. 3.4a. Denote θ as the rotation about the rod axis of a cross section located at a distance x from one end. The equilibrium condition between torsion force and the polar moment of inertia of the cross segment (Fig. 3.4b) yields:

$$\frac{\partial T}{\partial x}dx - I\frac{\partial^2\theta}{\partial x^2} = 0 \tag{3.1}$$

where I_p and $I = \rho\, I_P\, dx$ are the polar moment of inertia and the mass moment of inertia of the segment, respectively, and ρ is the density of the rod. From elementary theory of torsion, the applied torque, T, at the cross section can be written as:

$$T = GI_P\frac{\partial\theta}{\partial x} \tag{3.2}$$

where $\partial\theta/\partial x$ is the angle of twist per unit length. $\partial\theta/\partial x$ may not necessarily be a constant since θ in general is not a linear function of distance x. The substitution of T from Eq. 3.2 into 3.1 gives:

$$\frac{\partial^2\theta}{\partial x^2} = {V_s}^2\frac{\partial^2\theta}{\partial t^2} \tag{3.3}$$

$$V_s = \sqrt{\frac{G}{\rho}} \tag{3.4}$$

Eq. 3.3 is the one-dimensional wave equation, in which the shear wave velocity, V_s, is defined by equation 3.4.

Solution

Eq. 3.3 is a partial differential equation, which can be solved by a variable separation method. A single solution of the equation has a general form:

$$\theta(x,t) = U(x) \times V(t) \tag{3.5}$$

where $U(x)$ and $V(t)$ are two independent functions shown to be:

$$U(x) = A_i \cos\omega\frac{x}{V_s} + B_i \sin\omega\frac{x}{V_s} \tag{3.6}$$

$$V(t) = C_i \cos\omega\, t + D_i \sin\omega\, t \tag{3.7}$$

where A_i, B_i, C_i, D_i are constants dependent on the boundary conditions of the RCA, and ω is circular frequency. If the material is linear elastic, the wave will propagate freely (without losing energy due to viscosity) in the rod at its natural frequency ($\omega = \omega_n$). The substitution of both Eq. 3.6 and Eq. 3.7 into Eq. 3.5 leads to a general solution of Eq. 3.3:

$$\theta(x,t) = \sum_{i=1}^{n}\left[\left(A_i \cos\omega_n\frac{x}{V_s} + B_i \sin\omega_n\frac{x}{V_s}\right)(C_i \cos\omega_n\, t + D_i \sin\omega_n\, t)\right] \tag{3.8}$$

Boundary conditions To apply solution 3.8 to the specific boundary conditions of the RCA, the following assumptions are made (e.g. Richart *et al.*, 1970):

1. The specimen is totally fixed at the bottom. In other word, the test base should be rigid and its mass polar moment of inertia is much greater than that of the specimen.

2. The driving mechanism (included the cross-arms, four magnets, the instrumentation, and the counter balance) and the specimen top cap are non-deformable, and can be lumped together as a rigid mass (Fig. 3.1a). The torsional motion of the rigid mass can be represented by its mass polar moment of inertia, I_0.

It should be noted that, due to the system compliance (Priest, 2004; Kumar & Clayton, 2007; Clayton *et al.*, 2009), the above assumptions may not be valid. If the specimen is fixed at one end, the angle of twist at the fixed end is zero, leading to $A_i = 0$, and therefore:

$$\theta(x,t) = \sum_{i=1}^{n}\left[B_i \sin\omega_n\frac{x}{V_s} \times (C_i \cos\omega_n\, t + D_i \sin\omega_n\, t)\right] \tag{3.9}$$

It has been shown (Richart *et al.*, 1970) that by applying the equilibrium condition (Eq. 3.1) at the free end, the relationship between natural frequency and V_s is obtained:

$$\frac{I}{I_0} = \beta \tan\beta \tag{3.10}$$

where

$$\beta = \omega_n\frac{L}{V_s} \tag{3.11}$$

3.3.2 SDOF torsional vibration model

As a shear strain increases beyond the linear elastic region, the shear modulus decreases, and the damping ratio increases and can become significant. The model for wave propagation in an elastic rod may not applicable, especially in the medium to large strain regions. In addition, the model of wave propagation in an elastic rod does not provide a tool for estimating damping ratio. Therefore, a visco-elastic material model, such as Kelvin-Voigt model, should be used. The solutions for wave propagation in a visco-elastic cylindrical rod with the specific boundary conditions of the Stokoe RCA are given by Hardin (1965). However, the solutions are quite complex and the application of Hardin's solutions requires a computer programme (ASTM, 1995), which is time consuming when dealing with a large data set. The model of SDOF torsional vibration (Fig. 3.5a), from which the shear modulus and damping ratio can be reasonably estimated, overcomes the disadvantages of other models.

Governing equation

To establish the SDOF torsional vibration governing equation for the RCA, the following assumptions are given:

1. The test material follows the Kelvin-Voigt model.
2. The system is SDOF, i.e. the drive mechanism is non-deformable, assumed to be a lumped rigid mass, and the specimen is totally fixed at the bottom.
3. The angle of twist per unit length is constant. This assumption conflicts with Eq. 3.9, which indicates that θ is a *sin* function of distance x along the specimen. However, this assumption can be satisfied if the specimen is short and the moment of inertia of the specimen is significantly smaller than that of the drive mechanism.

Since the apparatus is modelled as SDOF system, only the torsional vibration of the cross section at the free end is considered. The applied harmonic torque, $F_0 sin\omega t$, induces in the cross section at the free end a shear stress proportional to the shear modulus and material viscosity, μ_c, as follow

$$\tau = G\gamma + \mu_c \frac{\partial \gamma}{\partial t} \tag{3.12}$$

where γ is the shear strain at a radial distance r from the axis (Fig. 3.5b). The assumption that the angle of twist is constant allows the shear strain to be calculated from:

$$\gamma = \frac{r\,\theta}{L} \tag{3.13}$$

Substituting Eq. 3.13 to Eq. 3.12 gives:

$$\tau = G\,\frac{r}{L}\,\theta + \mu_c\,\frac{r}{L}\,\frac{\partial \theta}{\partial t} \tag{3.14}$$

The total torque about the axis at the free end is the summation of the element moments:

$$T = \int \tau\,(dA)\,r = G\frac{\theta}{L}\int r^2 dA + \frac{\mu_c}{L}\frac{\partial\theta}{\partial t}\int r^2 dA = \frac{GI_p}{L}\theta + \frac{\mu_c I_P}{L}\frac{\partial\theta}{\partial t} \tag{3.15}$$

where dA is the area of an element at a radial distant r from the axis (Fig. 3.5b). Eq. 3.15 can be simplified as:

$$T = k\theta + c\frac{\partial\theta}{\partial t} \tag{3.16}$$

where

$$k = \frac{GI_p}{L} \tag{3.17}$$

and

$$c = \frac{\mu_c I_P}{L} \tag{3.18}$$

are the stiffness and the damping coefficient of the specimen, respectively. Eq. 3.16 indicates that the motion of the free end (caused by the total torque, T) is partially absorbed by a damping force , which is proportional to damping coefficient of the specimen, c, and angular velocity of the lumped mass, $\partial\theta/\partial t$. The equilibrium condition of the cross section at the free end yields:

$$F_0\sin\omega t - T \quad = \quad I_0\frac{\partial^2\theta}{\partial t^2} \tag{3.19}$$

Substituting Eq. 3.16 to Eq. 3.19 leads to:

$$I_0\frac{\partial^2\theta}{\partial t^2} + c\frac{\partial\theta}{\partial t} + k\theta \quad = \quad F_0\sin\omega t \tag{3.20}$$

Eq. 3.20 is the well-known governing equation for SDOF torsional forced vibration.

Solution

It can be shown (by e.g. Timoshenko *et al.*, 1974) that if the damping of the specimen is less than the critical damping, $c_{cr} = \sqrt{4kI_0}$, the solution of Eq. 3.20 has a general form:

$$\theta = A\sin(\omega t + \pi - \psi) \tag{3.21}$$

where A and ψ are the vibratory angular amplitude and the phase angle, respectively.

$$A = \frac{F_0}{\sqrt{(k - I_0\omega^2)^2 + (c\omega)^2}} \tag{3.22}$$

$$\cos\psi = \frac{-k + I_0\omega^2}{\sqrt{(k - I_0\omega^2)^2 + (c\omega)^2}} \tag{3.23}$$

It will be recalled that the motion of the free end in a RCA is usually recorded by an accelerometer. From Eq. 3.21 the acceleration of the free end can be derived:

$$\ddot{\theta} = \frac{\partial\theta^2}{\partial t^2} = -A\,\omega^2\sin(\omega t + \psi) = A_{cc}\sin(\omega t + \psi - \pi) \tag{3.24}$$

where

$$A_{cc} = A\omega^2 = \frac{F_0\omega^2}{\sqrt{(k - I_0\omega^2)^2 + (c\omega)^2}} \tag{3.25}$$

is accelerative vibratory amplitude. Equations 3.22 to 3.25 are the fundamental solutions, from which further data-reduction can be derived.

Relationship between natural frequency and resonant frequency

Resonance is the condition at which a system oscillates at maximum amplitude at a certain frequency, known as the system resonance frequency, f_r. It can be shown that when damping is small, the resonance frequency is approximately to the natural frequency. Eq. 3.23 (and Fig. 3.6b) indicate that, despite the magnitude of damping ratio, the phase angle ψ will be equal to 90 degrees (or Lissajous figure will be a right ellipse) only if $k - I_0\omega^2 = 0$, leading to the condition that the oscillating frequency coincides with the natural frequency:

$$\omega = \sqrt{\frac{k}{I_0}} = \omega_n \tag{3.26}$$

Denoting:

$$\alpha = \frac{\omega}{\omega_n} \tag{3.27}$$

and

$$D = \frac{c}{\sqrt{4kI_0}} = \frac{c}{2I_0\omega_n} = \frac{\mu_c I_p}{2I_0\omega_n L} \tag{3.28}$$

the vibratory accelerative amplitude and the phase angle can be rewritten as:

$$A_{cc} = \frac{F_0}{I_0} \times \frac{\alpha^2}{\sqrt{(1-\alpha^2)^2 + 4D^2\alpha^2}} \tag{3.29}$$

$$\cos\psi = -\frac{\left(1-\alpha^2\right)}{\sqrt{(1-\alpha^2)^2 + 4D^2\alpha^2}} \tag{3.30}$$

These equations are plotted in Fig. 3.6 showing that the difference between resonant and natural frequency increases with damping ratio. It can be shown that the vibratory accelerative amplitude will attain the maximum value if:

$$\omega = \frac{\omega_0}{\sqrt{1-2D^2}} = \omega_r \tag{3.31}$$

Alternatively:

$$\frac{\omega_r}{\omega_0} = \frac{1}{\sqrt{1-2D^2}} > unity \tag{3.32}$$

Eq. 3.32 indicates that the resonant frequency is higher than the natural frequency and the difference between them depends on the damping ratio, D. Furthermore, Eq. 3.32 can be rearranged as:

$$\omega_r = \sqrt{\frac{k}{I_0(1-2D^2)}} = \sqrt{\frac{k}{I_0 - I_c}} \tag{3.33}$$

In Eq. 3.33, $I_c = 2D^2 I_0$ can be termed *viscous moment of inertia of the system.* Eq. 3.33 is similar to that derived by Li *et al.* (1998) via a more complex approach.

3.3.3 Relationship between V_s and natural/resonant frequency

Substituting Eq. 3.26 to Eq. 3.17 leads to

$$G = \frac{k\,L}{I_P} = \frac{L\omega_0^2 I_0}{I_P} \tag{3.34}$$

Rearranging Eq. 3.34 gives the relationship between V_s and the natural frequency:

$$V_s = \sqrt{\frac{G}{\rho}} = \omega_n L\sqrt{\frac{I_0}{I}} \tag{3.35}$$

Alternatively:

$$\beta = \frac{\omega_n\,L}{V_s} = \sqrt{\frac{I}{I_0}} \tag{3.36}$$

In practice, the natural frequency can be determined from the phase relationship technique (analysing phase angle or adjusting Lissajous figure). If the resonant frequency is measured using the maximum amplitude technique, V_s can be estimated from the following relationship:

$$\beta = \frac{\omega_n\,L}{V_s} = \sqrt{\frac{I}{I_0}}\,\sqrt{(1-2D^2)} \tag{3.37}$$

3.3.4 Measurement of damping ratio, D,

In general, D at a given shear strain includes both the material damping and the system generated damping. D can be measured in a RCA using either the free vibration decay (FVD) or the half-power-point (HPP) method.

Free vibration decay method Without an excitation force ($F_0 = 0$), the vibration amplitude decays with time. It can be shown (by e.g. Timoshenko *et al.*, 1974) that if the lost energy is small compared to the stored energy (or damping coefficient is smaller than critical damping, $c < c_{cr} = 2I_0\omega_n$), the amplitude decrement in one cycle is small, and hence the motion can be considered as (pseudo) sinusoidal:

$$x = Xe^{-\delta(t/T)}\sin\left(\omega_d t - \psi_d\right) \tag{3.38}$$

In Eq. 3.38, X is a constant; $T = 2\pi/\omega_d$ is the pseudo-period; ω_d and ψ_d are the damped frequency and phase angle of damped oscillation, respectively; and the term $Xe^{-\delta(t/T)}$ is the vibratory amplitude varying with time. Parameter δ, known as the logarithmic decrement, or the attenuation constant (or the decay rate), represents the energy loss per cycle of vibration. It is shown (by e.g. Timoshenko *et al.*, 1974) that c and δ has the following relationship:

$$c = \frac{I_0\omega_d}{\pi}\,\delta \tag{3.39}$$

As defined (see Eq. 3.28), damping ratio can be calculated from:

$$D = \frac{c}{c_{cr}} = \frac{c}{2I_0\omega_n} = \frac{\delta}{2\pi}\frac{\omega_d}{\omega_n} \tag{3.40}$$

where

$$\frac{\omega_d}{\omega_n} = \sqrt{1-D^2} \tag{3.41}$$

Substituting Eq. 3.41 to Eq. 3.40 and rearranging Eq. 3.40 yields a relationship between D and δ:

$$D = \frac{\delta}{\sqrt{4\pi^2+\delta^2}} \tag{3.42}$$

In a RC test, a specimen is vibrated at its resonant frequency, then the excitation source is cut off. Based on an analysis of the recorded vibration decay curve, δ can be estimated. Consequently D can be calculated using Eq. 3.42.

Half-power-point method An alternative method of determining D is to measure the half-power frequencies (f_1 and f_2) of two points, where the amplitude is equal to $1/\sqrt{2}$ times the peak amplitude (point A and B in the response curve illustrated in Fig. 3.8). The points are usually referred to as half-power points (HPP), and the bandwidth between these points is termed the half-power bandwidth, a term borrowed from the analysis of electrical systems. If the damping ratio is small ($D \ll 1$), it can be estimated from the following relationship:

$$D \approx \frac{f_2-f_1}{2f_r} \tag{3.43}$$

3.3.5 Strain amplitude measurement

In a RCA, the magnitude of shear strain induced in a specimen can be calculated from the peak accelerative amplitude (at resonance), the resonant frequency, the relative position of the accelerometer, the geometry of the specimen, and the equipment setup. Fig. 3.9 presents a schematic of the shear strain measurement in the Stokoe RCA used in this study.

From elementary theory of torsion, the shear strain in a cross section subjected to pure torsion is proportional to a radial distance r from the specimen axis (Fig. 3.5b). The shear strain is zero at the centre, maximum at the outer of the cross section, and average at a radial distance of 0.79R from the specimen axis (see e.g. Timoshenko & Young, 1962). Assuming that the angle of twist per unit length is constant, Eq. 3.13 can be used to estimate the average shear strain in a specimen:

$$\bar{\gamma}(\%) = 100 \times 0.79\frac{d}{2}\frac{\theta}{L} = 79\frac{d}{2L}\theta \tag{3.44}$$

The angle of twist, θ (in radian), at the cross section at the free end is proportional to the vibratory acceleration amplitude, A_{cc}, inversely proportional to the radial distance, l, between the accelerometer and the specimen axis, and inversely proportional to the square of the resonant frequency:

$$\theta = \frac{y}{l} = \frac{A_{cc}}{(\omega_r)^2\, l} = \frac{A_{cc}}{(2\pi\, f_r)^2\, l} \tag{3.45}$$

where y is the displacement vibration amplitude (see Fig. 3.9a), and $l = 0.05m$. The acceleration amplitude, A_{cc}, is estimated from the peak output voltage and the set-up of the charge amplifier (see section 3.2 and Fig. 3.9):

$$A_{cc} = \frac{2\sqrt{2}\, V_{RMS}}{5} \times g \tag{3.46}$$

where V_{RMS} is the peak root mean squared amplitude in Volts. Substituting Eq. 3.46 to Eq. 3.45 gives the angle of twist in the specimen:

$$\theta = \frac{9.81 \times 2\sqrt{2}}{4 \times 5 \times 0.05\, \pi^2} \frac{V_{RMS}}{{f_r}^2} = \frac{9.81 \times 2\sqrt{2}}{\pi^2} \frac{V_{RMS}}{{f_r}^2} \tag{3.47}$$

Substitution Eq. 3.47 into Eq. 3.44 produces the formula used to calculate the average shear strain in a specimen:

$$\bar{\gamma}(\%) = \frac{79 \times 9.81\sqrt{2}}{\pi^2} \frac{V_{RMS}}{{f_r}^2} \frac{d}{L} = SF \times \frac{V_{RMS}}{{f_r}^2} \frac{d}{L} \tag{3.48}$$

where $SF = 79 \times 9.81\sqrt{2}/\pi^2 = 111.05$ is termed the strain factor.

3.4 Calibration of the Stokoe RCA

3.4.1 Calibration of I_0

Experimental method It is obvious that in either the elastic model (Eq. 3.11) or the SDOF forced vibration model (Eq. 3.35) I_0 is an essential parameter for data reduction. The complex shape of the drive mechanism as shown in Fig. 3.3 causes the difficulty in determination of I_0 from the geometry and the density of the drive mechanism. Therefore, I_0 is usually estimated experimentally from the torsional resonant frequencies of linear elastic calibration bars, normally made from aluminium (Isenhower *et al.*, 1987; ASTM, 1995; Cascante & Santamarina, 1997; Priest, 2004; Clayton *et al.*, 2005; Kumar & Clayton, 2007). Assuming that the Stokoe RCA is SDOF system, Eq. 3.26 can be used to express the relationship between the stiffness of a calibration bar and I_0. When an additional disc is rigidly attached on the top of the cross-arms, Eq. 3.26 becomes:

$$\omega_n = \sqrt{\frac{k}{I_0 + I_a + I_m}} \tag{3.49}$$

where I_a and I_m are the mass polar moment of inertia of the top platen and the additional mass, respectively[2]. Since the loss coefficient, η or Q^{-1}, of aluminium is about 1/350,000,

---

[2] I_m includes the mass polar moment of inertia of bolts and screws used for attaching additional masses to the driving system.

the measured resonant frequency approximates to its natural frequency. By rearranging Eq. 3.49, the following relationship is derived:

$$I_a + I_m = \frac{k}{\omega_r^2} - I_0 \tag{3.50}$$

Eq. 3.50 represents a linear relationship between $(I_m + I_a)$ and $1/\omega_r^2$, in which I_a is constant, k is the slope of the line, and I_0 is the y-intercept. Therefore, Eq. 3.50 can be employed to determine I_0 by measuring the resonant frequencies of a series of aluminium calibration bars (Fig. 3.10). If the additional mass attached to the top of the bar is changed, the measured f_r of the system changes accordingly, resulting in a linear relationship as shown in Fig. 3.12.

Table 3.1 summarised the dimensions, the theoretical stiffness, K_0, of calibration bars, and the calibration results. It was observed in Table 3.1 and in Fig. 3.12 that I_0 increased with calibration bar stiffness, from $0.00271\,kg/m^2$ for bar No 1 to $0.00461\,kg/m^2$ for bar No 4. In Table 3.1 k_1 is the calibration bar stiffness, back-calculated using Eq. 3.50 and the determined I_0 ($0.00271\,kg/m^2$). The table shows that k_1 were lower than (except for calibration bar No 1) the theoretical stiffness, K_0, and the differences between K_1 and K_0 increased with increasing stiffness of calibration bar. In contrast, Fig 3.12 shows that the slopes of the trend-lines, represented by k_2 in Table 3.1, were higher than K_0, and the differences between the two values also increased with increasing f_r. Similar calibration results have been observed by Priest (2004); Clayton *et al.* (2005); Kumar & Clayton (2007). The discrepancy in calibration of I_0 and k suggests that the Stokoe RCA cannot be considered as a SDOF system due to the apparatus compliance. Further investigation of the system compliance will be presented in the next chapter.

In order to increase the accuracy in estimation of shear modulus, Priest (2004) adopted that I_0 was not constant but dependent on measured f_r. Based on the known geometry, G of aluminium and the measured f_r of aluminium bars, Priest (2004) back-calculated I_0 by using Eq. 3.50 and established an empirical relationship between the *adjusted* I_0 and the measured f_r (Fig. 3.13). Application of this technique to the author's initial data (Fig. 3.13), gave:

$$I_0 = 2.43 \times 10^{-8} f_r^2 - 1.11 \times 10^{-6} f_r + 2.80 \times 10^{-3} \tag{3.51}$$

Based on the measured f_r and the adjusted I_0 (Eq. 3.51), the bar stiffness, termed k_3 in Table 3.1, was estimated. As shown in Table 3.1 the differences between k_3 and k_0 were less than 1%. This technique can help to significantly reduce the error in estimation of specimen stiffness. However it does not help to explain the phenomenon (discrepancy in calibration of I_0 and k).

It is noted that the calibration was carried out before the connections between the magnets and the cross-arms were reinforced[3]. As presented in Fig. 3.13, another empirical

---

[3] To reduce the effect of apparatus compliance, the connections between the cross-arms and the magnets were reinforced, see more detail in Chapter 4.

relationship between I_0 and f_r measured after reinforcing the bonding between magnets and cross-arms was also established.

Geometry method The discrepancy in the experimental estimation of I_0 motivated the Author to calculate I_0 from the geometry and the density of the drive mechanism. Attempts have been made to measure the weight and the dimensions of each component (i.e. the cross-arms, four magnets, the accelerometer, and the counter balance) of the drive mechanism. An *Auto*CAD[4] model of the drive mechanism was build (Fig. 3.14). The model was divided into many simple shaped pieces (such as rectangular, triangular, etc.). The dimensions and the distance from the centroid of each piece to the specimen axis were precisely determined (Fig. 3.14). This allowed the mass polar moment of inertia of each piece to be calculated and hence determination of I_0. The calculations are summarised in Table 3.2, showing that I_0 = 2.84E-3 Kg/m^2, of which 90% is contributed by the four magnets.

3.4.2 Calibration of equipment damping

The damping ratio, measured by a RCA at a given shear strain and an effective stress, includes both the intrinsic material damping and the equipment generated damping. Chapter 2 has theoretically shown that in the very small strain region, the material damping is very small and the equipment damping, therefore, becomes relatively significant. In order to accurately evaluate the intrinsic material damping, equipment damping must be measured and subtracted from the total measured damping.

Back EMF is one of the main sources of system damping (Stokoe *et al.*, 1995; Meng & Rix, 2003; Cascante *et al.*, 2003; Wang *et al.*, 2003). The motion of magnets due to a magnetic field produced by a current in the coils also induces an electro-motive force opposing to the magnet motion, thereby causing energy loss. Other important sources causing energy loss are imperfect fixity of bottom pedestal (Drnevich, 1978), coupling between specimen and both end platens (Drnevich, 1978), system compliance (Avramidis & Saxena, 1990), base fixity (Cascante *et al.*, 2003), and back ground noise, etc.

The equipment damping was measured by testing the four aluminium calibration bars (Fig. 3.10) and a very stiff aluminium bar No5 (or *gas hydrate bar* made by Priest 2004, Fig. 3.11). Since the damping of aluminium is very small, the equipment damping is approximately to the measured damping of aluminium bars. The equipment damping ratios measured by both the HPP and the FVD method were plotted versus resonant frequencies of calibration bars in Fig. 3.15. It is noted that the equipment damping ratios were measured after reinforcing the connection between the cross-arms and the magnets. It can be observed in the graph that the equipment damping ratios vary with both f_r and shear strain amplitude, and that the equipment damping ratios estimated by the HPP method is normally higher than those obtained by the FVD method (Fig. 3.15). At small shear strain, the HPP damping ratio decreases with increasing shear strain; in

---

[4] *Auto*CAD is a CAD (Computer Aided Design) software application for 2D and 3D design and drafting, developed by Autodesk, Inc. (111 McInnis Parkway San Rafael, CA 94903, USA).

contrast, FVD damping increases with an increase in shear strain (Fig. 3.16). Beyond a certain shear strain level HPP damping and FVD damping are nearly equal, and almost independent of shear strain.

The discrepancy of the measured equipment damping ratio at low strain may be explained by the effects of background noise. When the ratio of noise amplitude to peak vibratory amplitude is large (e.g. $A_{noise}/A_{peak} > 15\%$), the noise flattens the resonant peak and hence increases the HPP damping ratio. The noise also causes the recorded decay amplitude to be greater than it should be, altering the measured decay rate, and hence decreases the FVD damping ratio. As the peak vibratory amplitude increases, the noise becomes insignificant, and the noise effects can therefore be negligible.

It is suggested that there are two sets of system damping, namely FVD and HPP equipment damping (Fig. 3.21). They should be used corresponding to the material damping measuring method (i.e. FVD or HPP). To reduce the noise effects on measurement of the intrinsic material damping, it is assumed that, when $A_{noise}/A_{peak} > 15\%$, both the HPP and FVD equipment damping are linear functions of peak vibratory amplitude, and when $A_{noise}/A_{peak} < 15\%$, both the FVD and HPP equipment damping ratios are constants (Fig. from 3.16 to 3.20).

TABLE 3.1: Summary of calibration of I_0 and stiffness of the calibration bars

bar	top platen		centre rod		theoretical K_0	measured	Y-intercept	K_1 (slope in	adjusted I_0	k_2	adjusted K_3	error (%) =		
No	d_1	h_1	d_2	h_2	$= GI_p/L$	f_r	I_0	Fig. 3.12)	(Eq. 3.51)	(Eq.3.49)	(Eq.3.49)	$100^*[1 - \frac{K_i}{K_0}]$		
	(m)	(m)	(m)	(m)	(Nm/rad)	(Hz)	$(kg.m^2)$	(Nm/rad)	$(kg.m^2)$	(Nm/rad)	(Nm/rad)	$i = 1$	$i = 2$	$i = 3$
1	0.070	0.015	0.013	0.175	433	61.40	2.71E-03	417	2.82E-03	429	434	3.7	0.9	-0.4
2	0.070	0.015	0.018	0.175	1590	114.00	3.11E-03	1644	2.99E-03	1478	1583	-3.4	7.1	0.5
3	0.070	0.015	0.023	0.175	4239	176.42	3.49E-03	4409	3.36E-03	3540	4246	-4.0	16.5	-0.2
4	0.070	0.015	0.028	0.175	9444	242.15	4.66E-03	11021	3.96E-03	6670	9379	-16.7	29.4	0.7

Table 3.2: Calculation of moment of inertia of the drive mechanism

material	no item	shape	density	dimensions				I_1	$I_2 = md^2$	$I = I_1 + I_2$
			(Kg/m^3)	width (mm)	height (mm)	thickness (mm)	arm (mm)	$(kg.m^2)$	$(kg.m^2)$	$(kg.m^2)$
magnet	4	rectangular	7570	38.00	12.76	25.60	82.13	5.03E-05	2.54E-03	2.59E-03
aluminium	1	rectangular	2700	65.14	65.14	6.50	0	5.27E-05	0	5.27E-05
aluminium	4	rectangular	2700	9.00	9.45	6.50	71.25	8.47E-08	3.03E-05	3.04E-05
aluminium	4	triangle	2700	25.88	22.55	6.50	48.16	1.34E-09	4.75E-05	4.75E-05
aluminium	4	triangle	2700	33.00	9.45	6.50	55.77	7.17E-10	3.40E-05	3.40E-05
steel	2	cylinder	7850	$r = 6.48$	$L = 16.70$		51.46	3.58E-09	9.16E-05	9.16E-05
									Total:	**2.84E-03**

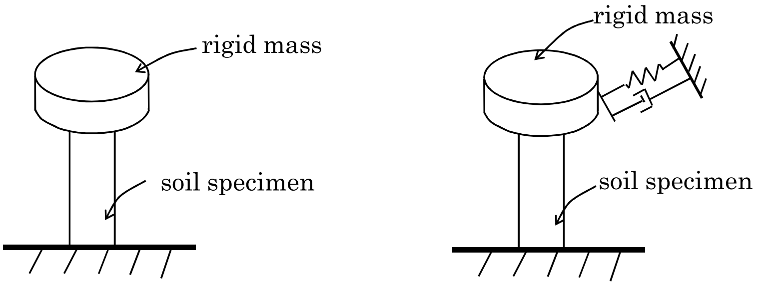

(a) fixed – free configuration

(b) fixed – spring top

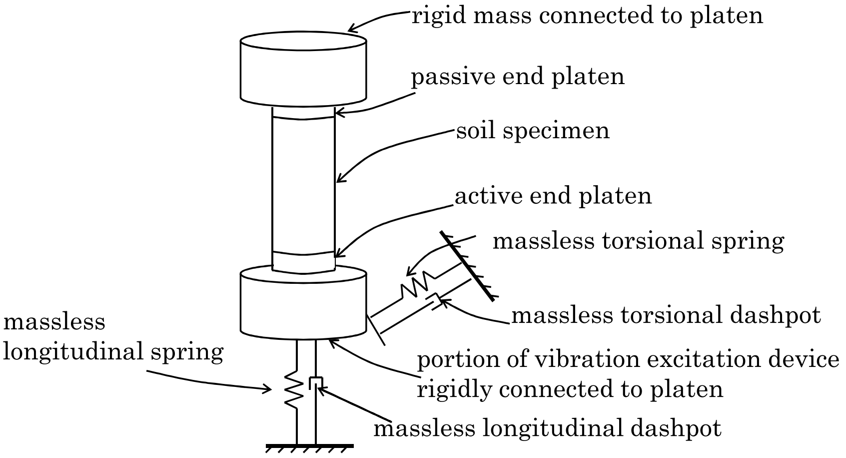

(c) free-free configuration

FIGURE 3.1: Common RC boundary conditions (redrawn after Drnevich 1985; ASTM 1995)

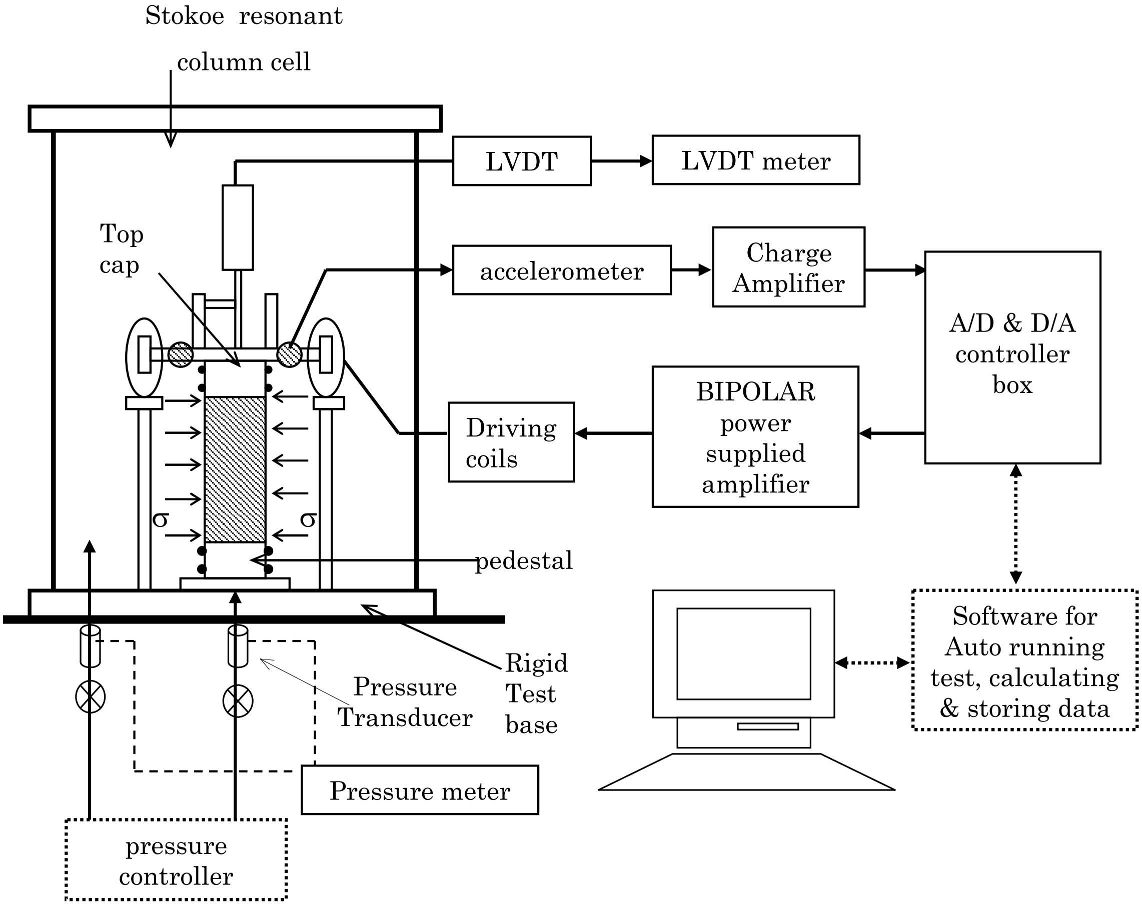

FIGURE 3.2: Schematic diagram of the Stokoe RCA

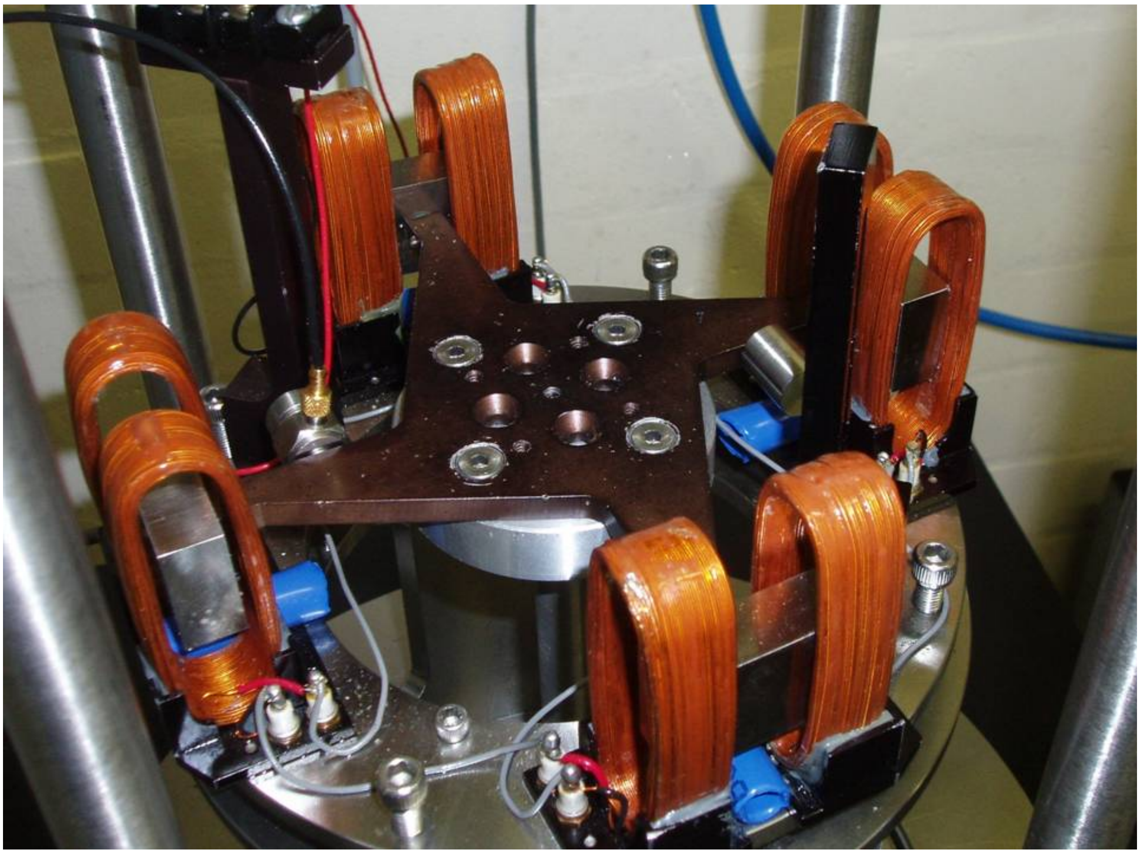

Figure 3.3: Stokoe drive mechanism and attachments

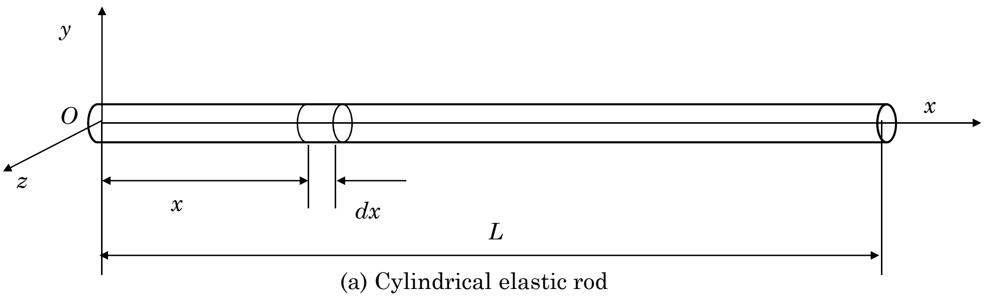

(a) Cylindrical elastic rod

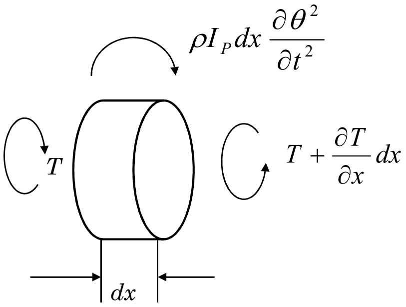

(b) Typical segment

FIGURE 3.4: Torsional vibration of an elastic rod (Timoshenko *et al.*, 1974)

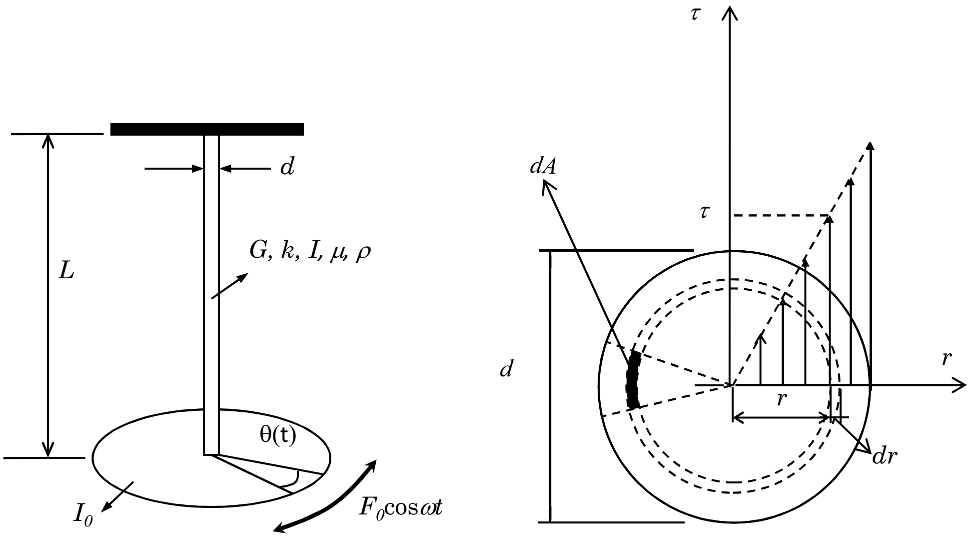

(a) SDOF torsional forced vibration

(b) Shear stress in a cross section

FIGURE 3.5: SDOF torsional vibration

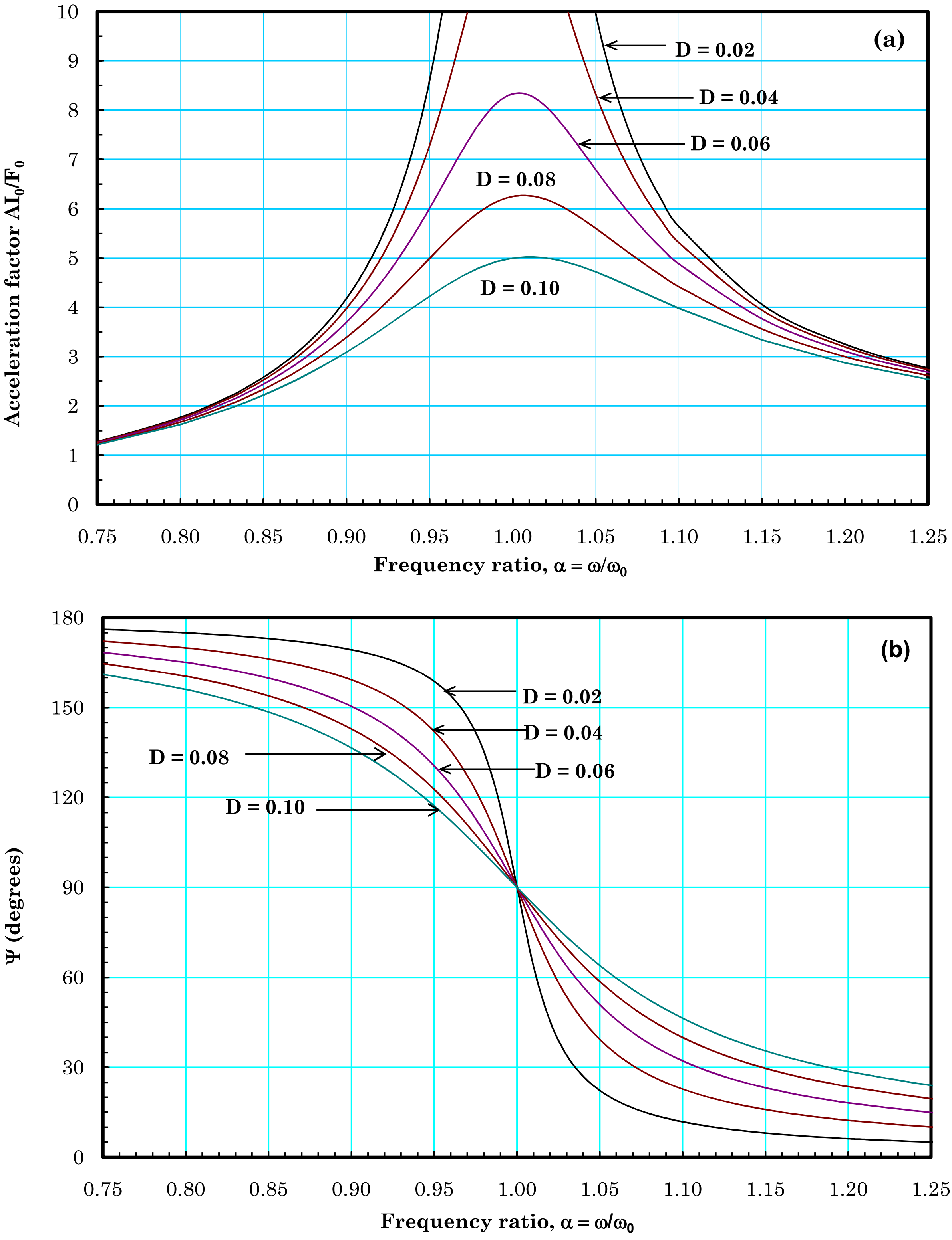

FIGURE 3.6: Response of an accelerometer. (a) Amplitude-frequency response curves; (b) Phase angle-frequency response curves

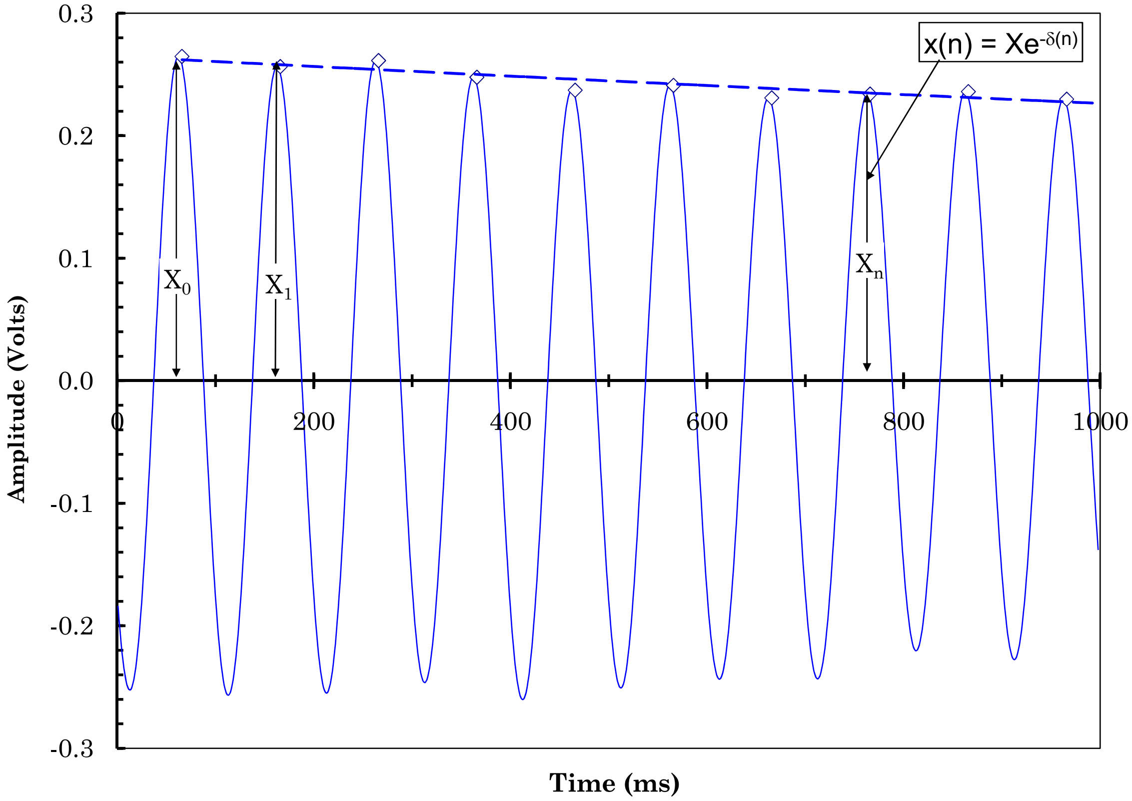

FIGURE 3.7: Free vibration decay curve obtained from a calibration bar

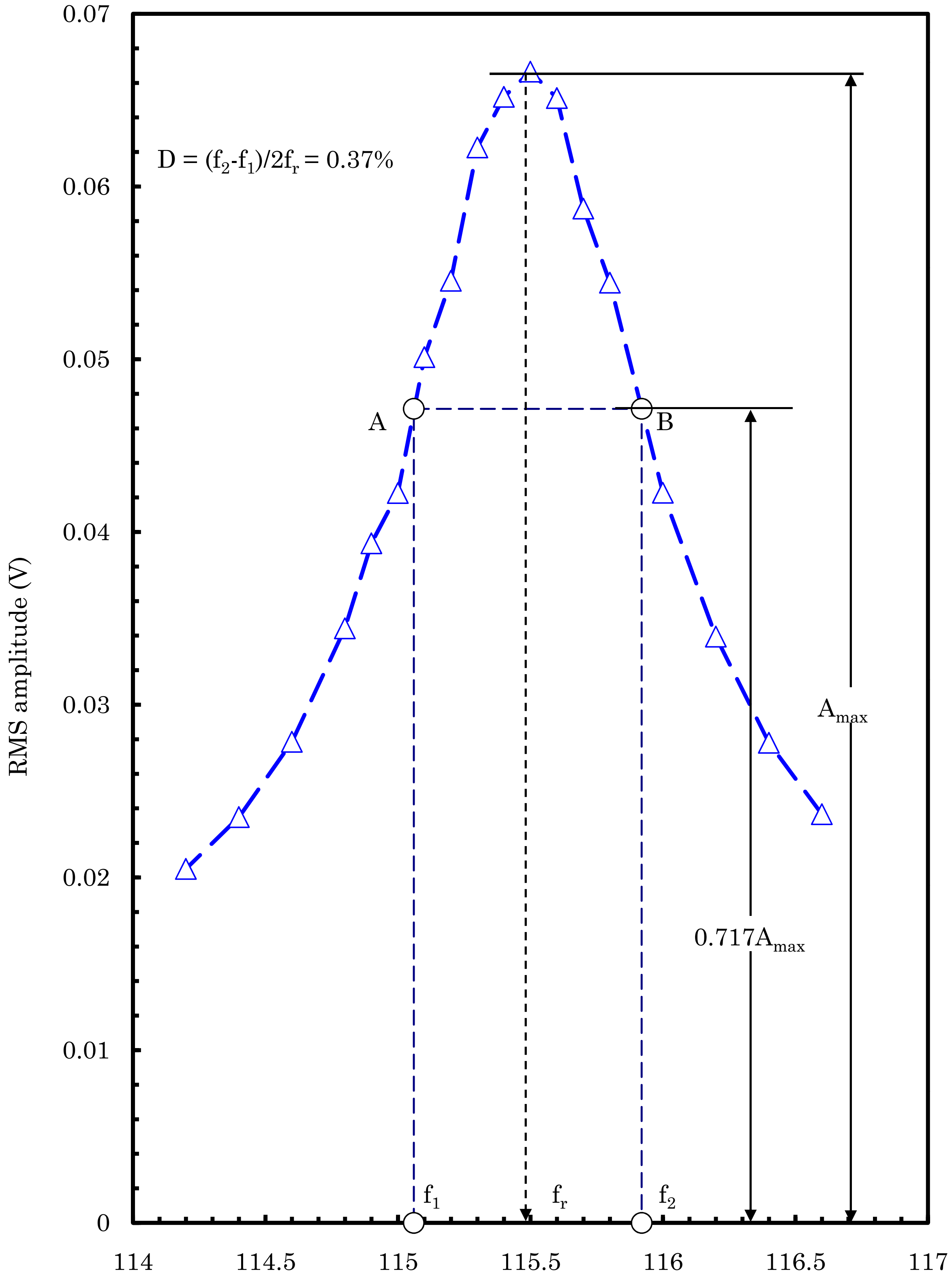

FIGURE 3.8: Half-power bandwidth of calibration bar No 2

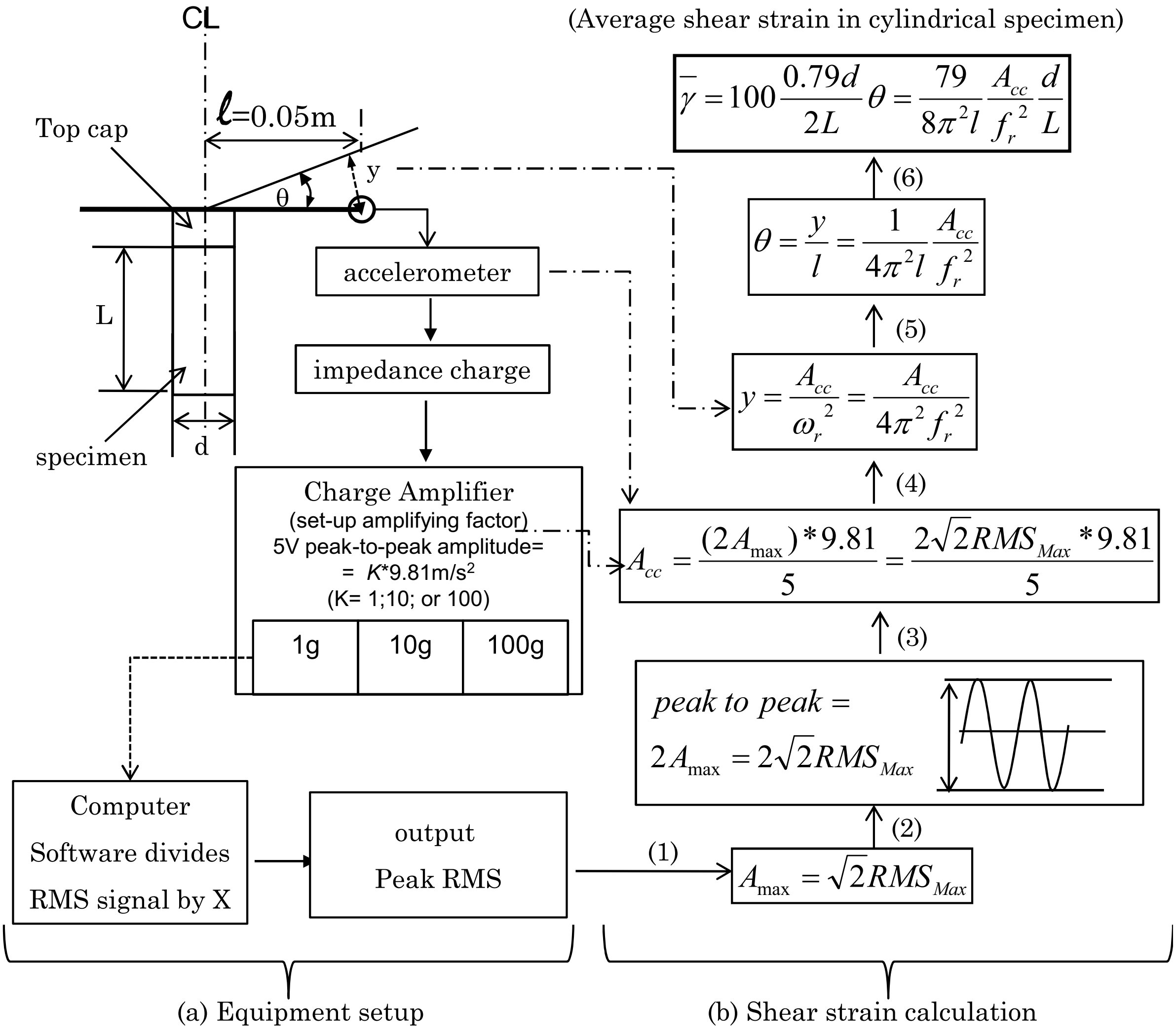

FIGURE 3.9: Schematic of shear strain measurement in the Stokoe RCA

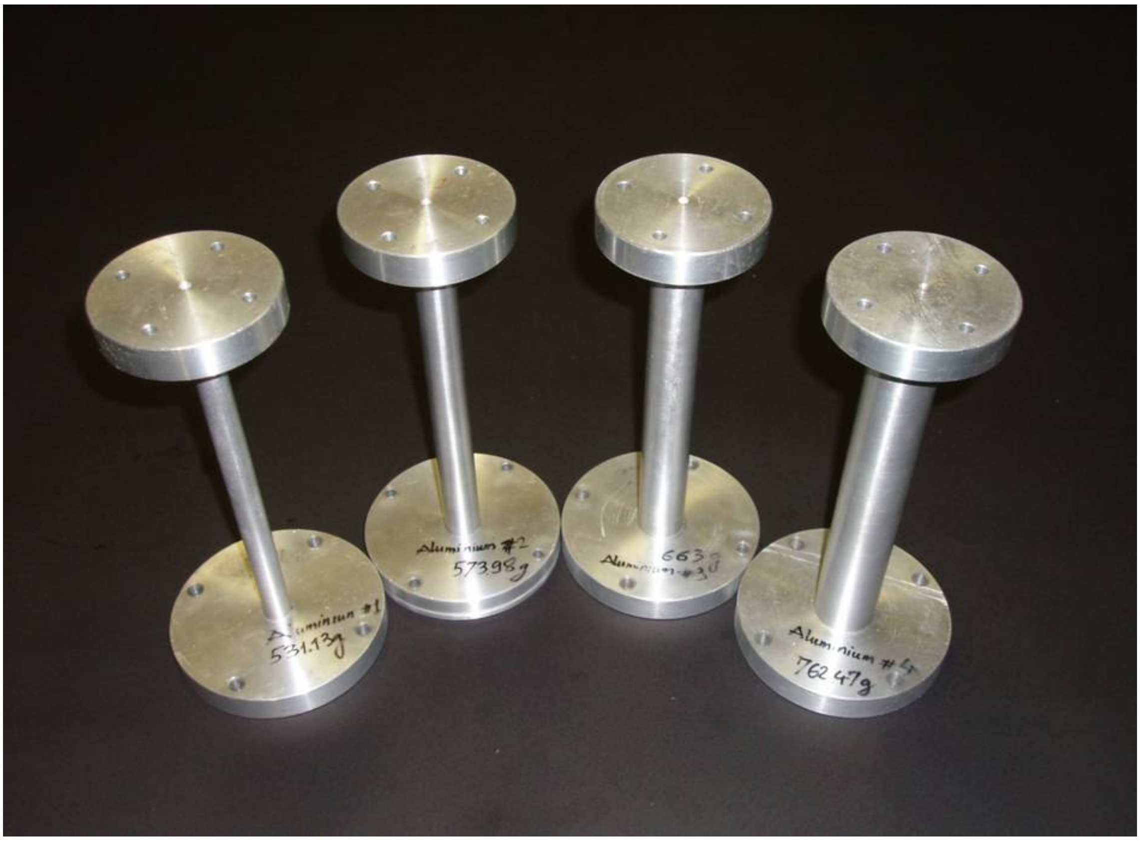

FIGURE 3.10: Aluminium calibration bars No 1 to No 4

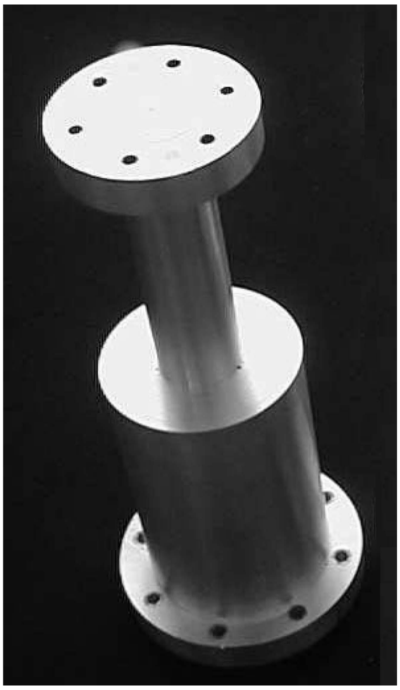

FIGURE 3.11: Aluminium calibration bar No 5 (or *GH bar*, Priest 2004)

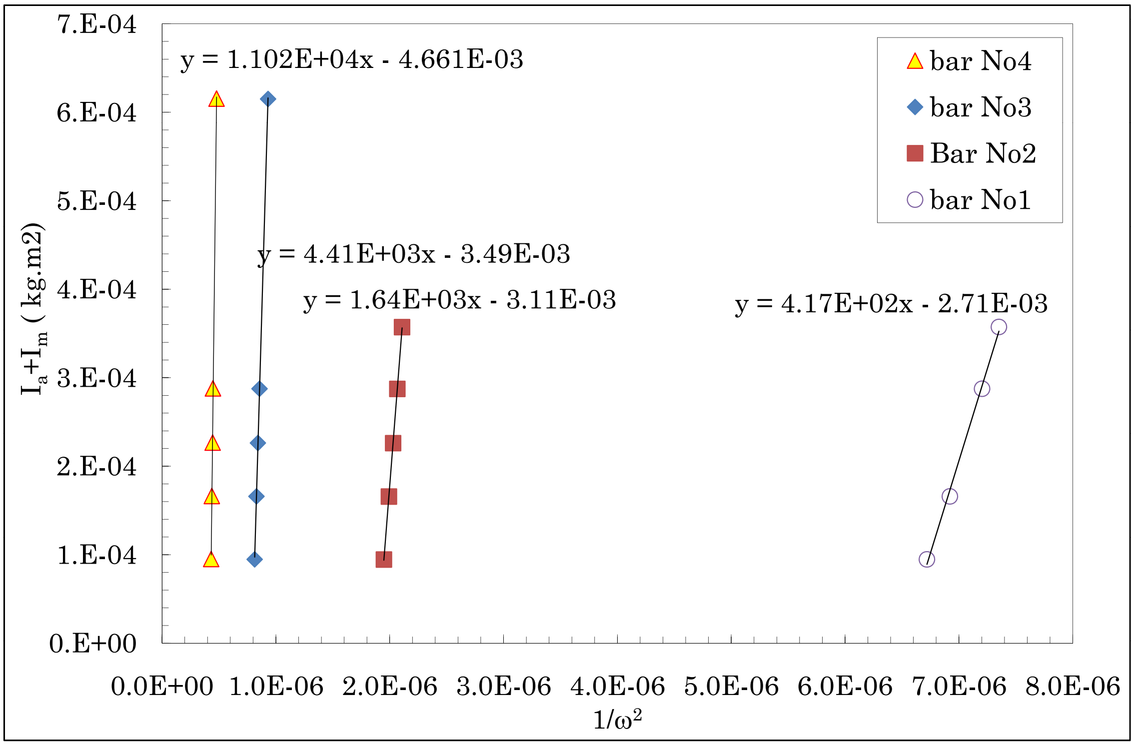

FIGURE 3.12: Calibration of I_0 with assumption that system is SDOF

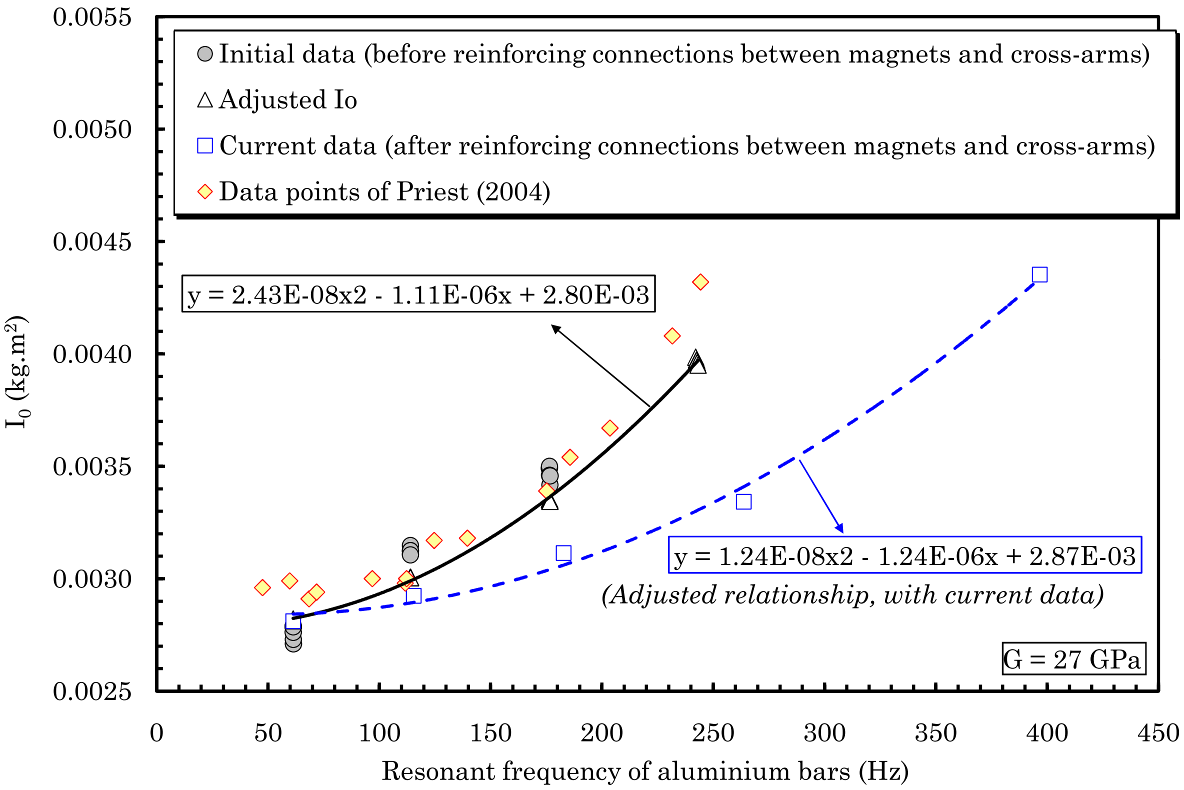

FIGURE 3.13: Values of I_0 with resonant frequency as a result of system compliance

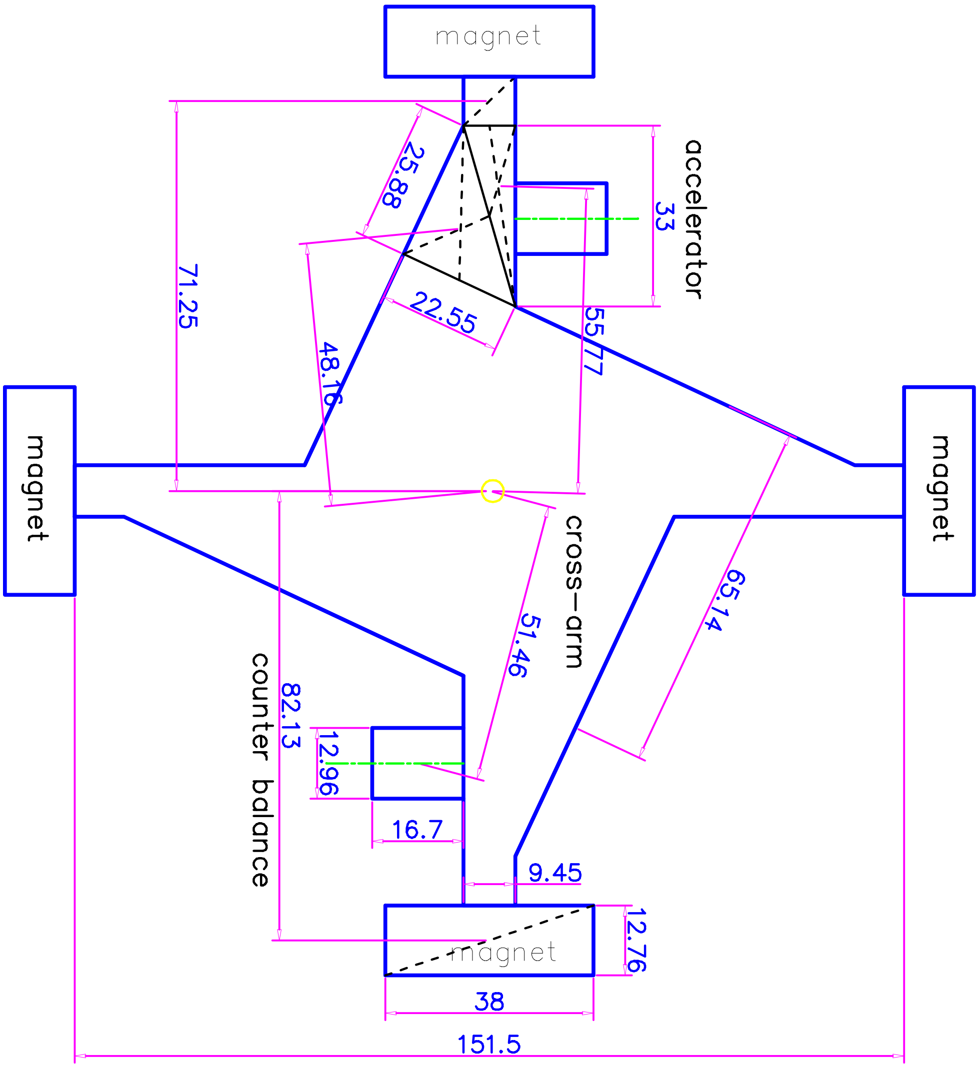

FIGURE 3.14: Top view of the drive mechanism of the Stokoe RCA

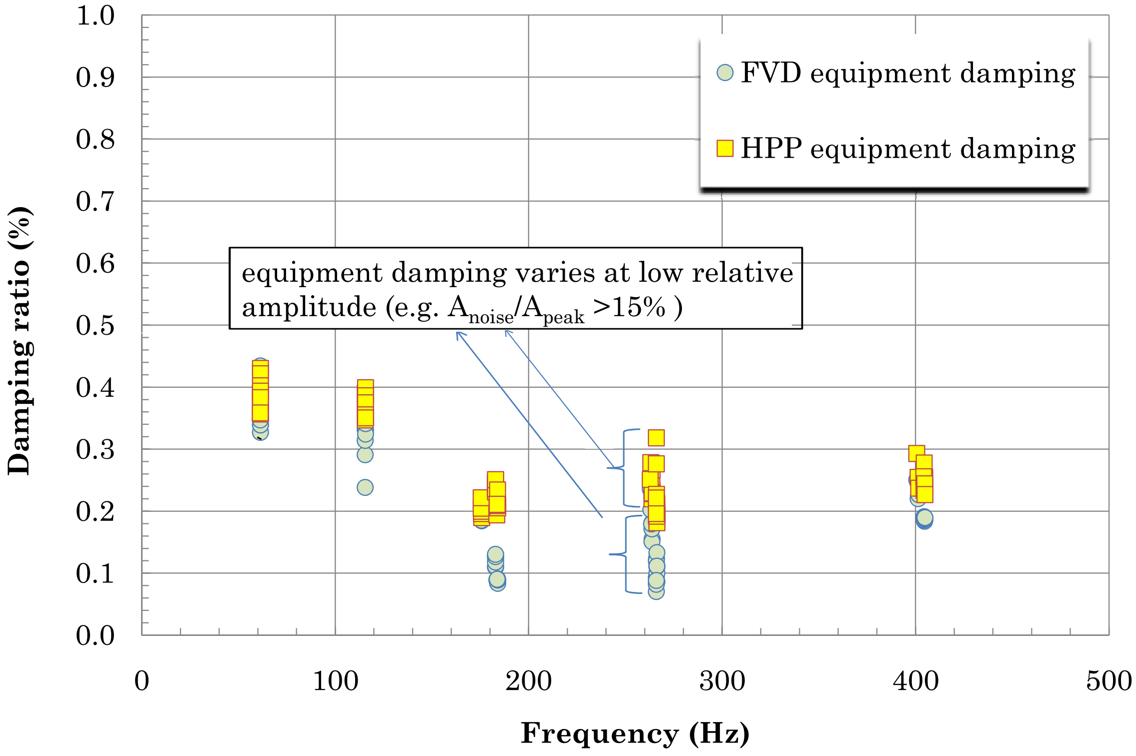

FIGURE 3.15: Equipment damping ratio measured with different aluminium calibration bars at various resonant frequencies

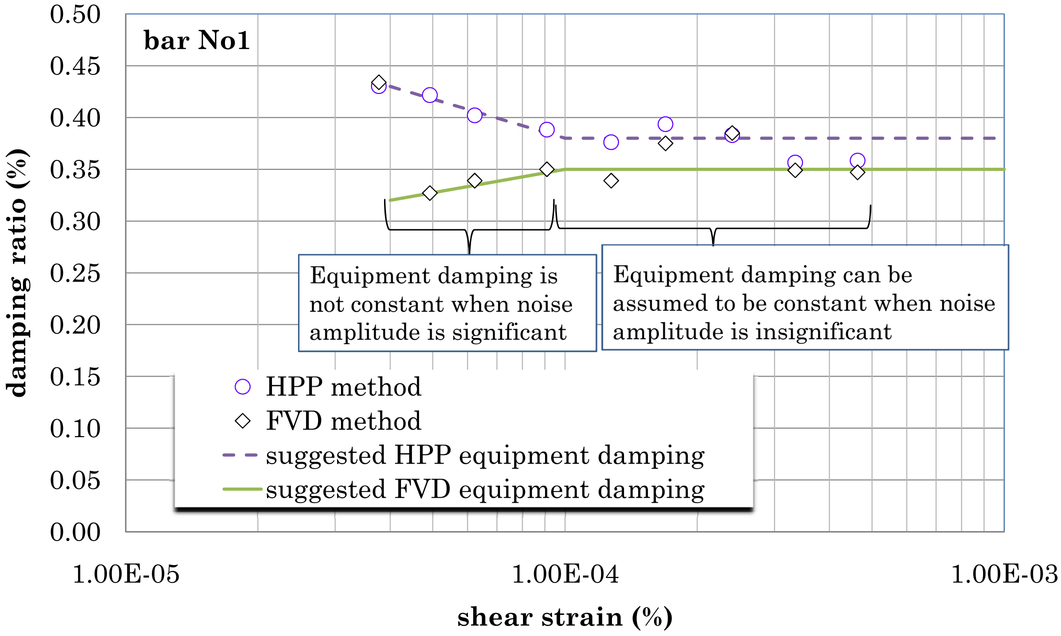

FIGURE 3.16: Equipment damping ratio measured with aluminium calibration bar No 1 at various shear strains

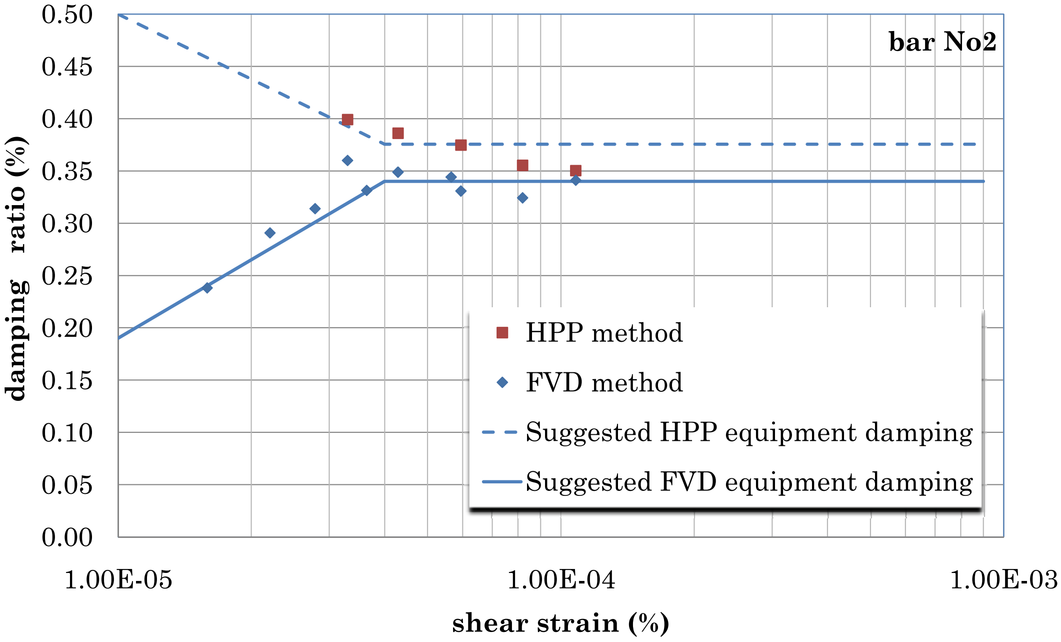

FIGURE 3.17: Equipment damping ratio measured with aluminium calibration bar No 2 at various shear strains

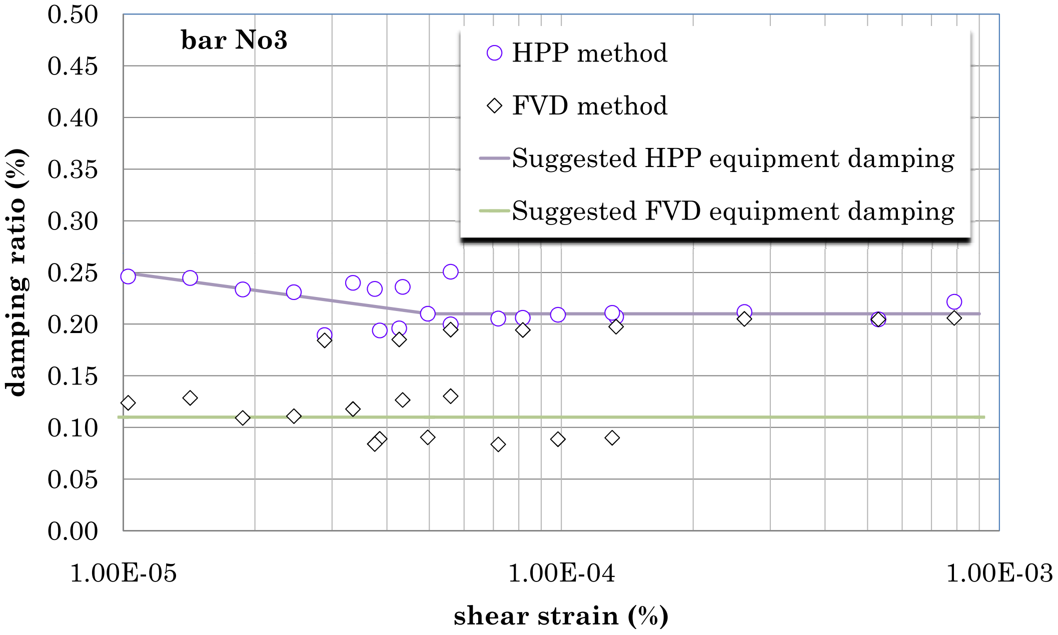

FIGURE 3.18: Equipment damping ratio measured with aluminium calibration bar No 3 at various shear strains

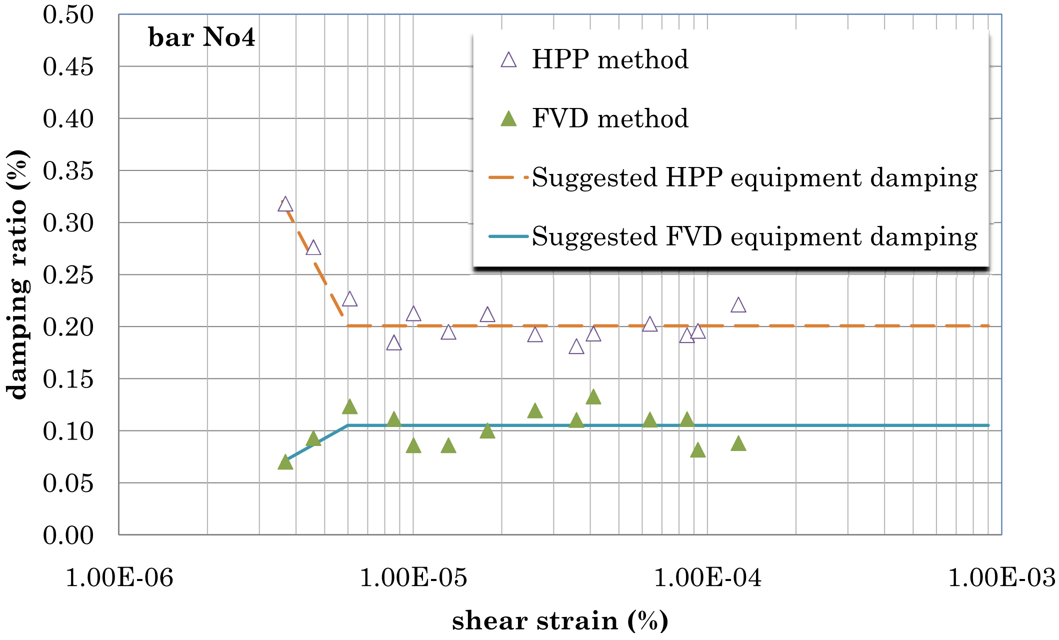

FIGURE 3.19: Equipment damping ratio measured with aluminium calibration bar No 4 at various shear strains

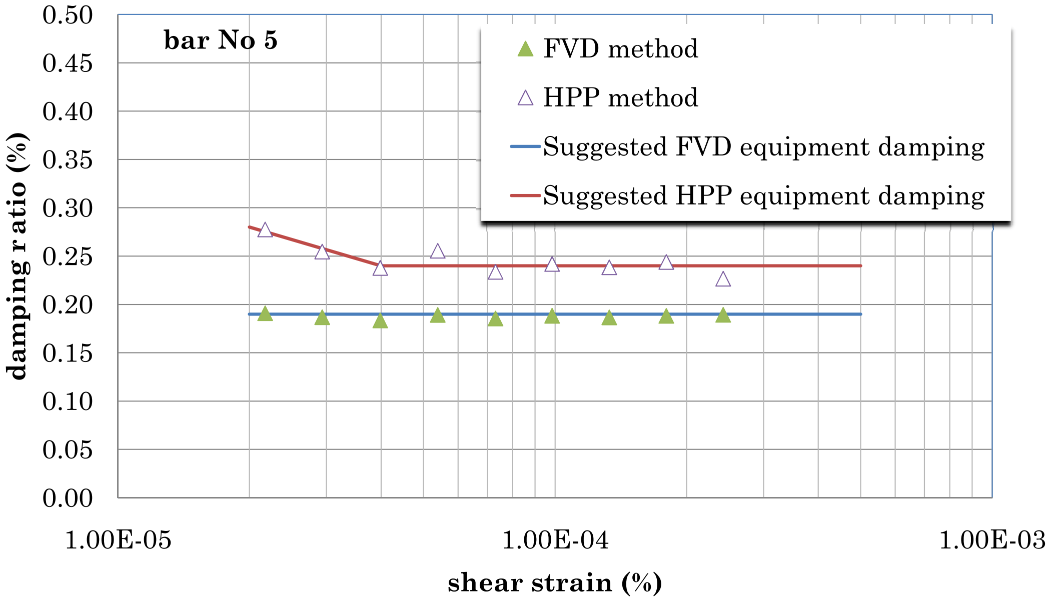

FIGURE 3.20: Equipment damping ratio measured with aluminium calibration bar No5 at various shear strains

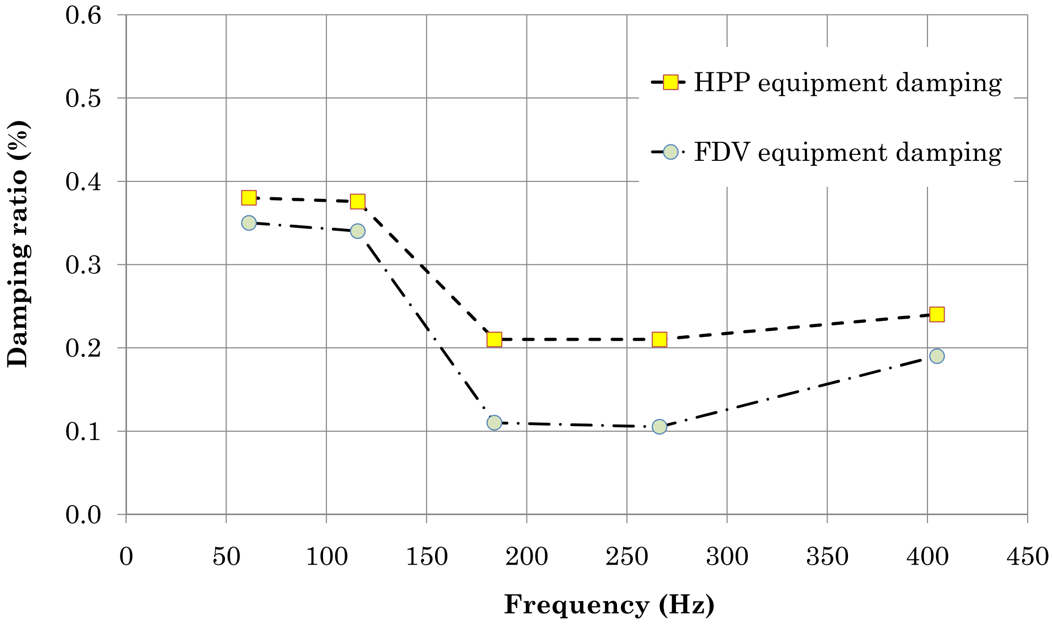

FIGURE 3.21: Equipment damping ratio measured with different aluminium calibration bars with high signal/noise ratio

Chapter 4

Influence of equipment compliance on RC test results

4.1 Introduction

As discussed in the previous chapter, due to the equipment compliance, the Stokoe RCA was not SDOF. Effects of equipment compliance using a RCA have also been reported previously. Avramidis & Saxena (1990) reported that the stiffness of a Drnevich RCA was insufficient to test relatively stiff specimens. They observed two different resonant frequencies (namely the true and the spurious resonant frequency) when testing a specimen of Monterey No.0 sand using their RCA. Therefore, the equipment was stiffened. After the equipment modification, test results of Monterey No.0 sand with various effective stress levels showed no spurious resonant frequency. The values of G_{max} of the sand measured by the modified equipment were up to 28% greater, and the damping ratios were up to five times lower than those measured by the original apparatus. Cascante *et al.* (2003) reported that the displacement of the base (of their apparatus) significantly increased with stiffness of aluminium rod. Thus to reduce the movement of the base, their RC equipment was fixed to a heavy steel frame. They further mentioned that energy emission through the base was a complex problem that required further investigation, especially for large strain measurements where a specimen exhibits nonlinear behaviour. The results of equipment calibration carried out by Priest (2004) and Kumar & Clayton (2007) indicate that system compliance is an issue when testing relatively stiff materials. Therefore, this chapter investigates into the effect of equipment compliance on the RC test results especially of relatively stiff specimens using finite element (FE) method. To correct for the effect of system compliance, a new model named two spring model is developed.

4.2 Possible sources of errors in measurement of shear modulus

Error in measurement of resonant frequency might come from many sources, and those related to equipment compliance can be listed as:

- Compliance of the drive mechanism
  It is assumed that the drive mechanism is a rigid mass. In reality, the cross-arms (or drive plate) might deform since it is made from aluminium, with relatively heavy magnets at the end of the arms of the drive mechanism (see Fig. 3.3). In addition, the screw connections between the magnets and the cross-arms may not be rigid.

- Compliance between specimen and apparatus
  It is assumed that a specimen is rigidly connected to the drive mechanism and to the pedestal. However, a specimen (such as sand) is connected to the top cap and to the pedestal via friction. Therefore, slippage between the top cap and the specimen may be a problem especially when testing relatively stiff materials (Drnevich, 1978). In addition, the top cap is connected to the drive mechanism by four countersunk screws, and there may be uncertainty in the rigidity of these fixing.

- Compliance of the support
  The drive mechanism reacts against the support frame attached to the test base. It is assumed that the frame supporting the drive mechanism, the pedestal, and the test base are rigid, and that the pedestal is totally fixed to the test base, which is fully fixed. In reality, these parts may deform during testing. In addition, the pedestal is connected to the test base by four machine screws. The assumption of the base fixity requires that the base is firmly fixed to the floor. This requirement may not be satisfied since the apparatus was mounted above waist height on a table.

- Compliance of calibration bar
  The calibration bar (Fig. 3.10) normally consists of three parts namely the top platen, the central stem (or rod) and the bottom platen. It is assumed that the stem is vertical and totally fixed at the stem base, and that the load transferred from the drive mechanism to the stem without loss. However, the calibration bars were made from aluminium. Deformation of the top platen may affect the load transfer from the drive mechanism to the central stem. The deformation of the bottom platen may affect the base fixity. In addition, if the central stem is weak, it may be bend by the gravitational load of the drive mechanism. Therefore, mode coupling between torsion and flexure may occur.

The above sources of errors were investigated using several ABAQUS version 6.63 FE models, from which the natural frequencies were extracted. Geometry and density of the drive mechanism are modelled based on the design of the Stokoe RCA supplied by Structural Behaviour Engineering Labs (SBEL) of Phoenix, Arizona, U.S.A. Other source of errors related to the accuracy of the instrumentations and improper system/ specimen assembly are out of the scope of this study.

4.3 Numerical study

4.3.1 Numerical models

Three system configurations, namely calibration bars without the test base, full section (70mm in diameter) specimens, and calibration bars with the test base, were modelled (Fig. 4.1). The connections between a specimen (or a bar) and the apparatus were assumed rigid. To ensure the rigid connection between specimen and apparatus, each part of the model (e.g. the drive plate) is carefully partitioned (Fig. 4.1). They are then rigidly attached (merged) to each other before meshing. The models were built using predominately hexahedral elements, however some triangular prisms (wedges) in transition regions are allowed. The elastic properties of the model materials are presented in Table 4.2.

Initial analyses, in particular for bar No 4 without the test base (Fig. 4.1c), were carried out to find the sufficient refinement of mesh size. Maximum (global) element sizes of 5.0 mm, 4.0 mm, 3.0 mm, and 2.5mm were used, resulting in approximately 7000, 11000, 22000 and 38000 elements within each model respectively. The results (Fig. 4.2) show that an element size of 3.0 mm is sufficient to reduce any significant error in the solution without severely increasing the computational need to solve the model. Hence, the global mesh size of 3.0 mm were used in all subsequent analyses.

4.3.2 Modes of vibration and resonant frequencies

Predicted natural frequencies of the first modes of vibration for four aluminium bars and three full section specimens (Fig. 4.1a & Fig. 4.1b) with Young's moduli of 25MPa, 250MPa, and 2500MPa, are presented in Table 4.3. The analyses were carried out with an assumption that the pedestal of the full section specimens and the lower disc of the calibration bars are totally fixed.

The first mode and second mode of vibration are found to be flexural and torsional respectively. It is observed that the torsional mode is well separated from other modes of vibration, suggesting that mode coupling (e.g. coupling between a flexural and a torsional mode) is unlikely. Hence the misinterpretation of acceleration output cannot be an issue[1]. However, if a magnet is assembled incorrectly, both the first mode (flexure) and the second mode (torsional) can be detected as shown in Fig. 4.3.

4.3.3 Effect of the drive mechanism stiffness

As can be seen from Fig. 3.3 and Fig. 3.14 the drive mechanism for the Stokoe RCA consists of a 6.5mm thick aluminium plate with four equidistant spaced arms (cross-arms). At the end of each arm, a relatively heavy magnet fixed 82mm away from the rotation axis, was attached via a very small screw connection. It is likely that the weakest link of the drive mechanism is the connections between the cross-arms and the magnets. In addition, the contact area between each arm and a magnet is relatively small, 9.45mm

---

[1] Under given torsional vibratory excitation only the torsional mode can be detected in a RC test.

by 6.5mm. In this study, the connections between the magnets and the cross-arms are simply assumed rigid.

Analyses were carried out to extract the torsional natural frequency of calibration bar No 4 with the drive mechanism attached. The Young's modulus of the cross-arms was varied. The bottom platen of the calibration bar was assumed totally fixed. The results in Fig. 4.4 show that the compliance of cross-arms is significant, causing a reduction in the torsional natural frequency of this calibration bar by about 9 Hz, more than 20% of the observed difference between the theoretical (Table 4.1) and the predicted natural frequency.

Drnevich (1978) and ASTM (1995) simply specified that a drive mechanism should have a torsional stiffness at least ten times that of the specimen. As shown in section 4.5, the (torsional) calibrated stiffness of the whole RCA approximates 52KNm/rad, or more than 12 times the torsional stiffness of calibration bar No 3. It is apparently that the torsional stiffness of the drive mechanism alone should be higher than this equivalent (combination) stiffness[2]. Using the RCA, the measured resonant frequency of calibration bar No 3 is 182.9 Hz (Table 4.5) or 8 Hz lower than the theoretical natural frequency (190.9 Hz). The difference between measured and theoretical natural frequency lead to 8% underestimation in torsional stiffness of calibration bar No 3. The investigation above shows that the requirement given by Drnevich (1978) and ASTM (1995) underestimated the influence of the drive mechanism stiffness on the measurement of specimen natural frequency.

4.3.4 Effect of base fixity

In order to investigate the compliance of the apparatus support system, a FE model that incorporated the test base supported by springs (Fig. 4.1c) was developed. The dimensions and mass of the base are approximate to those of the actual equipment. A set of twelve 3-DOF springs termed *Cartesian connectors*, with three compressive/tensile stiffness components, namely K_x, K_y, and K_z, were used to simulate the possible connection between the base and the ground. The springs were assigned at all available intersections created by the base's partition process (Fig. 4.5). Although a single Cartesian connector has no torsional restraint capacity, the combination of all connectors creates a 3-dimensional restraint, which varies with the stiffness of a single component.

In contrast to previous analyses, in which the base of the pedestal or base of the bottom disc was fully fixed, the results of this model showed that not only one but two distinguishable torsional modes appear in the current analyses. One of the modes relates to the vibration of the central stem. In this mode, vibratory amplitude of the stem is much more than that of the test base, and the motion of the stem and that of the test base are out of phase. Since the shear modulus of a specimen is derived from this mode, it

---

[2] As shown in Fig. 4.15 (section 4.7) the calibrated equivalent torsional stiffness of the equipment, also the torsional stiffness of the drive mechanism, approximates 96kNm/rad, is more than 10 times the torsional stiffness of calibration bar No 4.

can be termed actual torsional vibratory mode. The other mode relates to vibration of the whole system above the supporting springs. In this mode the motion of the stem and the test base are in phase. This mode can be termed pseudo torsional vibratory mode, or spurious mode (termed by Avramidis & Saxena 1990), which can appear when testing a relatively stiff specimen. Fig. 4.6 shows an example of pseudo modes appeared when weak rock specimens were tested using the RCA.

Fig. 4.7 shows a plot of the predicted natural frequency of bar No 4 as a function of connector component stiffness[3]. It can be observed that the predicted natural frequencies increase with increasing stiffness of spring components. The graph in Fig.4.7 show that the compliance of the base fixity causes about 2 Hz reduction in natural frequency.

From the plot (Fig. 4.7), the torsional restraint, termed K_{base}, of the actual test base can be back-calculated. K_{base} is the representative torsional stiffness created by the combination of all springs (Cartesian connectors), of which the tensile/compressive stiffness of each components [4] was 12.7 MN/m, or 5% of the tensile/compressive stiffness of calibration bar No 4 (the compressive stiffness of bar No 4 is 254MN/m). K_{base} will be referred in next analyses.

4.3.5 Effect of base mass

In order to investigate the influence of base mass, the density of the base material as well as the stiffness of the springs were varied. Fig. 4.8 shows a plot of both pseudo and actual (torsional) natural frequency, as a function of mass polar moment of inertia of the base, for three different values of spring stiffness, namely K_{base}, $2 \times K_{base}$, and $200 \times K_{base}$. It can be seen that the underlying natural frequency of the test specimen (calibration bar No 4 with the drive mechanism attached), in this case at 265.6 Hz, can be lower or higher than the predicted pseudo natural frequency, depending on the interaction between the base mass and the restraint stiffness. The results presented in Fig. 4.8 suggest that if the spring stiffness is low, the base mass should be sufficiently high; or if the base mass is insufficient, the spring stiffness should be very high to stop the pseudo response.

Since the actual natural frequency can be either lower or higher than the pseudo natural frequency, care should be taken to avoid misinterpretation of accelerometer output. Normally, the peak of the actual mode is much sharper and higher than that of the pseudo mode (Fig. 4.8). However, when the pseudo is close to the actual natural frequency, they can interact with each other. The coupling between the actual and pseudo mode will alter the bandwidth, resulting in errors in measurement of both resonant frequency and damping ratio. Fig. 4.9 illustrates the effects of mode coupling on the measurement of the resonant frequencies at different effective stresses for a stiff clay specimen tested by the Stokoe RCA.

The calculated mass polar moment of inertia of the base alone is $0.156 kg.m^2$; addition of the steel cell wall and cell top cap, which has the similar dimensions and mass of the

---

[3] Each connector has three components, and all 12 spring have the same stiffness.

[4] $K_x = K_y = K_z = 12.7 MN/m$.

test base, makes the mass polar moment inertia to be more than $0.312\,kg.m^2$. Fig. 4.8 shows that at this value[5], the actual and pseudo natural frequency of the model of bar No 4 are predicted to be 261.4 Hz and 306.4 Hz, respectively. It is noted that (i) the measured pseudo (torsional) natural frequency of the RCA is from 300 Hz to 400 Hz (depending on the stiffness of a specimen, Fig. 4.6) and (ii) the experimental torsional resonant frequency for bar 4 was 263.8 Hz (the actual mode, Fig. 4.7). The above good agreement between the predicted and the experimental data reinforces the observation of the interaction between the pseudo and the actual torsional vibratory mode whilst testing relatively stiff specimens. Thus, it is required that the base fixity should be improved, e.g. the apparatus should be firmly fixed to a rigid laboratory bench/floor or the base mass should be increased. These measures will cause the pseudo frequency to disappear or at least go beyond the interested frequency range for relatively stiff specimens (e.g. the pseudo frequency should be higher than 500 Hz). In addition, these measures may also reduce the equipment damping since the energy emitted through the base reduces.

4.3.6 Effect of calibration bar design

To calculate the stiffness of a calibration bar in a static torsion test, the angle of twist of the central stem should be known. The angle of twist is normally derived from the tangent displacement recorded by strain gauges. It was assumed that the ratio of the tangent displacement at the periphery to the radius of the top platen was the angle of twist of the bar. This assumption has been largely used in both static and dynamic tests, e.g. in a Stokoe RC test, the angle of twist is derived from the output of an accelerometer mounted at the cross-arms and a distance between the accelerometer and the rotation axis. However, due to the compliance of the top platen, this assumption leads to errors in measurement of the stiffness of a calibration bar as illustrated by the numerical results below.

The way in which a calibration bar in reality is fixed to the test base and to the cross-arms is taken into account in these analyses, accept for the friction between the top platen and the drive mechanism and between the bottom platen and the test base. In the apparatus considered, the pedestal is removed before the base platen (of the calibration bar) is bolted directly to the base of the apparatus using four 5mm diameter machine screws. Therefore, the base restraint can be accounted mainly by the screw fixity. The top platen is fixed to the drive plate using four 4mm countersunk screws. Thus, the torque from the drive mechanism is mainly transferred to the calibration bar through the four screws.

The effect of calibration bar design was investigated using a static ABAQUS analysis. The models consist of just the calibration bars, of which the base platens are assumed to be fixed either at four points, corresponding to the centre of the machine screws, or completely fixed over the entire upper and lower surfaces. At the top platen, four unit concentrated forces are applied at the positions of the countersunk screws, positioned

---

[5] $0.312\,kg.m^2$ is more than 100 times the mass polar moment of inertia of the drive mechanism, $I_0 = 0.00285kg.m^2$.

25.5mm away from the rotation axis. As results, the calibration bars are subjected to a couple of equivalent torques, equal to $2 \times (1.0N \times 0.051m) = 0.102Nm$ (Fig. 4.10).

The tangential displacement of all nodes in the outer edge of the top platen was extracted. It is observed that, due to the stress concentration, the compliance of the top platen is non-uniform. The tangential displacement of nodes near the applied forces is higher than that of other nodes (Fig. 4.11). Therefore, the displacement of these edge nodes was averaged and the averaged displacement was used to estimate the static torsional stiffness. The estimated value was then compared with the theoretical stiffness of the central stem of the bar alone.

Table 4.4 shows the considerable difference between the derived stiffness and the theoretical stiffness of the central stem alone. The difference increases with increasing diameter of the central stem. The derived torsional stiffness of the thinnest calibration bar (No 1) is 3.5% lower than the actual stiffness of the central stem. For bar No 4, assuming the entire top and bottom surfaces are fixed, there is 5.5% difference between the derived and the actual torsional stiffness.

If the top platen is rigid, the tangential displacement at the outer edge is caused only by the rotation of the central stem. However, because the top platen deforms, the tangential displacement also includes the compliance of the top platen. Whilst the tangential displacement is inversely proportional to the fourth power of the diameter of the stem (D^4), the deformation of the top platen decreases linearly with diameter, D, (only). For bar No 1, the displacement caused by the rotation of the stem is significantly larger than that caused by the platen deformation. However, for bar No 4, the displacement caused by the deformation of the platen becomes significant. This explains why errors in measurement of the static stiffness of calibration bars increases with an increase in diameter of the central rod.

Similar effects caused by the compliance of the bottom platen are also observed (4.10b). For Bar No 4, the effect of both the bottom and the top platen compliance causes 9.6% difference between the derived and actual torsional stiffness[6].

If the friction between top platen and the cross-arms, and between bottom platen and the test base are taken into account, the effect of top/ bottom platen compliance could be less significant, since the friction will reduce the non-uniformity of the stress/ displacement concentration and the top/ bottom platen compliance. The friction force, proportional to the screw/ nut fastening force, is relatively high (much more than the torque at small strain).

4.4 Discussions of the equipment compliance

The results of the above numerical investigations suggest that the compliance of the drive mechanism, calibration bar design, fixity, and insufficient base mass contribute to

---

[6] The solution error caused by meshing, and convergent condition etc., although very small, can contribute to the difference between the expected natural frequency and the numerical derived frequency.

the underestimation of resonant frequency observed whilst calibrating the RCA. The natural frequencies extraction from the ABAQUS models of calibration bars and full section specimens have shown that in all cases torsional vibration was the second mode. It was observed that natural frequencies of other vibration modes do not interfere with the resonance in the torsional mode, provided that the base mass or the base fixity is sufficient.

The natural frequencies given in previous sections are brought together in Table 4.6. The difference between the natural frequency (285.0 Hz), predicted using either Eq. 3.49 or the model without compliance (Fig. 4.12a), and the initial measured resonant frequency (242.2 Hz) of calibration bar No 4 is significant, nearly 43 Hz. The factors contributing to this difference can be quantitatively analysed as follows (Table 4.5)

(1) 23.2 Hz difference between the natural frequency (265.4 Hz) of the model with the test base fixed at its bottom surface (Fig. 4.12e) and the initial measured resonant frequency (242.2 Hz) might be the results of *magnet connections.* Stress concentration in the connection between the magnets and the cross-arms is observed in the FE models, suggesting that the screw connections may be a source of compliance. To try and overcome this potential problem, all the magnets were therefore detached and bonded to the cross-arms using cyanoacrylate impact adhesive. Consequently, the measured resonant frequencies of all calibration bars become closer to the theoretical natural frequency (Table 4.6), e.g. the resonant frequency of bar No 4 increased about 21.6 Hz, from 242.2 Hz to 263.8 Hz. It means more than 50% of the difference is caused by compliance of weak magnet connections.

The 21.2 Hz difference between the theoretical (285.0 Hz) and the new measured natural frequency (263.8 Hz) is contributed by other factors, listed in Table 4.7 as follows.

(2) 1.6 Hz difference between the experimental (263.8 Hz) and natural frequency (265.4 Hz) of the *close to real* model in Fig. 4.12e is due to the compliance of the *base fixity* and perhaps the *compliance of the connections* between each equipment component. The real fixity of the test base is less rigid than that of the model and the real connections are not as rigid as assumed in the model.

(3) 0.8 Hz difference in natural frequency between the two models that are different in test base fixity (Fig. 4.12d and 4.12e), can be accounted for the *compliance of the test base.* Both the effect of test base fixity and the test base compliance caused about 2.4 Hz difference in the theoretical and the initial measured natural frequency

(4) 1.2 Hz difference in natural frequency between the model in Fig. 4.12d and the model in Fig. 4.12c, where the bottom platen is rigid due to its entire fixity, is accounted for the *compliance of the bottom platen.*

(5) 9.2 Hz difference between the natural frequency (267.4 Hz) of the model with the best case of fixity (Fig. 4.12c), and that (276.6 Hz) of the same model but having a rigid cross-arms (the Young's modulus of cross-arms was 100 times higher than that of aluminium, Fig. 4.12b) is only a result of *cross-arms compliance.*

(6) 8.3 Hz difference between the natural frequency (284.9 Hz) of the non-compliance model (Fig. 4.12a) and that (276.6 Hz) of the rigid drive-plate model (Fig. 4.12b), can be contributed to *the compliance of magnets, instrumentations, and top platen.* The effect of top platen is presumably similar to that of the bottom platen (see item No 2 above). Hence, the compliance of the magnet and instrumentations can contribute to about 7.0 Hz difference in measurement of natural frequency. Totally, the compliance of the drive mechanism (magnets, cross-arms, instrumentations) can contribute about 16 Hz (or 75%) of the difference between the theoretical and the new measured natural frequency.

(7) 0.1 Hz difference between the natural frequency (284.9 Hz) of the non-compliance model (Fig. 4.12a) and the theoretical (285.0 Hz) is due to the ABAQUS approximate solving errors.

4.5 Simple model for correcting equipment compliance

4.5.1 Introduction

The numerical investigation conducted in the previous sections suggests that the compliance of the RCA is a significant issue when testing relatively stiff specimens, and should therefore be accounted for during data reduction. This section proposes a simple model used to correct for the effects of the equipment compliance, which, in general, can be represented by a torsional spring with a finite stiffness termed $k_{equipment}$ (Fig. 4.13). The combination of $k_{equipment}$ and $k_{specimen}$ forms a new system termed two spring model, which is assumed to be equivalent to the perfect fixed-free configuration (Fig. 4.13b), and the analytical solutions therefore can be simply derived using the SDOF torsional forced vibration model presented in section 3.3.2. Consequently, a new relationship between V_s and resonant frequency is established, and a new method for calibrating $k_{equipment}$ and I_0 is also proposed.

4.5.2 Two spring model

The model is established with the following assumptions:

- I_0 is constant, dependent on the geometry and density of the drive mechanism only, and it is independent of specimen stiffness
- The imperfect fixity of the test base and apparatus deformation can be represented by a spring with a finite, constant torsional stiffness, $K_{equipment}$
- The equivalent system (Fig. 4.13) is SDOF with the equivalent stiffness, k, calculated as:

$$\frac{1}{k} = \frac{1}{k_{equipment}} + \frac{1}{k_{specimen}} \tag{4.1}$$

Eq. Fig. 4.1 indicates that the measured resonant frequency from RCA does not correspond to the specimen stiffness, $k_{specimen}$, but the equivalent stiffness, k. If the stiffness of a Stokoe RCA can be determined (see section 4.6), the stiffness of a specimen can be calculated using Eq. 4.1.

- Shear strains of a section along the equivalent specimen varies linearly to a distant x from the fixed end (or the angle of twist per unit length is constant, Fig. 4.17b). In other words, the mode shape of wave propagation along a specimen is assumed to be a straight line. This assumed mode shape conflicts to Eq. 3.9, which indicates that the mode shape of the wave propagation in general is a *sin* function. It is emphasised that this assumption, largely (and implicitly) accepted (e.g. ASTM, 1995), is one of the fundamental for establishing the governing equation 3.20 and a main source of error that is discussed later in section 4.8.

If the above conditions are satisfied, the motion of the equivalent system will follow governing equation 3.20. Substituting Eq. 3.17 to Eq. 4.1 leads to:

$$\frac{1}{k_{specimen}} = \frac{1}{\omega_0^2 I_0} - \frac{1}{k_{equipment}} \tag{4.2}$$

Substitution of Eq. 4.2 to Eq. 3.34 gives:

$$G = \frac{k_{specimen} L}{I_P} = \frac{L\omega_0^2 I_0}{I_P} \times \left(1 - \frac{\omega_0^2 I_0}{k_{equipment}}\right)^{-1} \tag{4.3}$$

Accordingly, a new equation for calculating shear wave velocity of the specimen can be written as:

$$V_s = \sqrt{\frac{G}{\rho}} = \omega_0 L \sqrt{\frac{I_0}{I}} \times \left(1 - \frac{\omega_0^2 I_0}{k_{equipment}}\right)^{-0.5} \tag{4.4}$$

4.6 Calibration of $k_{equipment}$ and I_0

The two key unknown parameters of the two spring model, $k_{equipment}$ and I_0, can be determined experimentally using Eq. 4.2, which can be rewritten more explicitly as

$$\frac{1}{k_{stem}} + \frac{1}{k_a} = \frac{1}{\omega_0^2 (I_0 + I_a)} - \frac{1}{k_{equipment}} \tag{4.5}$$

where k_{stem} and k_a are the shear stiffness of the central stem and the top platen of a calibration bar, respectively. Eq. 4.5 represents a standard form of a linear function. To obtain the slope and y-intercept of the linear function, the five calibration bars (Table 4.9) were tested. By plotting $(1/k_{stem} + 1/k_a)$ as a function of $1/\omega_0{}^2$ for each test, $1/(I_0 + I_a)$ is defined as the slope of the line and $1/k_{equipment}$ is the Y-intercept. The results presented in Fig4.14a show that I_0 and $k_{equipment}$ are initially found to be $0.00278 kg.m^2$ and $42089 Nm/rad$, respectively.

Considering the initial calibration results, the value of I_0 obtained by the new experimental calibration method ($I_0 = 0.00278\, kg.m^2$) is slightly lower than the value obtained by the geometry method ($I_0 = 0.00284\,kg.m^2$). The value of I_0 and $k_{equipment}$ obtained from the initial calibration results were used to back-calculate the shear modulus of aluminium using Eq. 4.3. The results were summarised in Table 4.7. It can be seen in the table that the calculated shear modulus differs slightly from the reference value of aluminium shear modulus ($G = 27GPa$). The difference increases with an increase in calibration bar stiffness, with a sudden jump (up 13.4%) for the stiffest bar No 5. The difference may be due to (i) the model assumptions and/or (ii) an odd value in the data set.

The discussion in section 4.8 shows that the error coming from the model assumptions can be negligible. Therefore, the error can be associated with the data set. One criterion, normally used to achieve the best linear trendline representing an experimental observation, is that distances between two successive data points should equal, e.g. either the increment $\triangle x$ or $\triangle y$ is constant. This allows equal weighting to each data point. It can be seen in Fig. 4.14 that the distribution of observed data is poor. The distance between data point of bar 1, the most slender bar, to that of bar 2 is about 3/4 the total length of the trendline. Hence the data of bar No 1 has much higher significance compared to the other data points, and controls the slope of the trendline[7].

The numerical investigation highlighted in Section 4.3 suggested that the Stokoe RCA can reasonably measure the resonant frequency of a soft specimen such as aluminium calibration bar No 1. It will be recalled that the theoretical natural frequency and the measured resonant frequency of bar No 1 are 61.0 Hz, and 61.4 Hz, respectively. The difference between the measured and the theoretical natural frequency was only 0.66%. The reasons of the difference are unclear. The difference may be partially caused by inaccuracy of the instrumentations and by the very small difference between the natural frequency and resonant frequency of calibration bar No 1. In addition, the central stem of calibration No1 is weak, and it may be bend under the gravitational load of the drive mechanism. This may also affect the measured resonant frequency of bar No1.

To try to overcome the problem, the measured value for bar No 1 ($f_r = 61.4Hz$) is substituted by the theoretical value ($f_0 = 61.0Hz$). As a result, the error in calculated shear modulus of bar No 5 significantly reduces from 13.4% to 4.6%, thus suggesting that the error possibly came from the data point of bar No 1. It should be noted that the substitution technique above was solely used to identify the source of error.

As another trial, the regression analysis was repeated without using the data point of bar No 1 (Fig. 4.14b). As a result, I_0 and $k_{equipment}$ were found to be $0.00284kg.m^2$ and $51965Nm/rad$, respectively. From these values, the measured stiffness of each calibration bar was calculated, then compared to the theoretical. The maximum error, occurred with bar No5, was found to be 2.2% only (Table 4.9). The I_0 obtained from this adjusted calibration was very close to that computed from the known geometry and mass of the drive mechanism. It is noted that the stiffness of bar No 5 is equivalent to the stiffness of a full section specimen with shear modulus about 1.64GPa, suggesting that the RCA may

---

[7] Although the determination coefficients of the trendline was 0.9998, it does not mean that the line was the closest to the major of points.

be capable of testing a wide range material from soft soil to weak rock, provided that the system compliance can be corrected for.

4.7 Verification of the two spring model by ABAQUS

The (ABAQUS) predicted natural frequencies of four aluminium bars and three full section specimens, presented in the Table 4.2 in Section 4.3.2, were used to verify the two spring models. The plots in Fig. 4.15 have shown that the relationship between $1/k_{specimen}$ and $1/{\omega_0}^2$ was a perfect straight line, suggesting that the two spring model is theoretically valid.

In general, a linear relationship between $1/k_{specimen}$ and $1/{\omega_0}^2$ can be theoretically extended to apply for frequencies beyond the resonant frequency range of calibration bars. Therefore, the two spring model can be used for correcting for the system compliance when testing a specimen stiffer than bar No 5 through extrapolation. Further ABAQUS analyses were carried out to check whether or not the two spring model can be applied to correct for the system compliance when a very stiff specimen (e.g. the shear stiffness of a specimen is greater than the equipment stiffness[8]) is tested. A calibration bar, having geometry similar to that of calibration bar No 4, rigidly connected to the drive mechanism and the test base (Fig. 4.1c), was modelled. The Young's modulus of the calibration bar was varied from $3.3\,GPa$ to $911\,GPa$. The bottom surface of the test base was assumed fully fixed. The natural frequencies extracted from the ABAQUS models are presented in Table 4.10.

The plots in Fig. 4.16 show a linear relationship between $1/k_{specimen}$ and $1/{\omega_0}^2$, from which $k_{equipment}$ and I_0 of the ABAQUS model was found to be $66728 Nm/rad$ and $0.00288 Kgm^2$ respectively. Back analysis to determine the calibration bar stiffness shows only a small difference (less than 3%, Table 4.12) between the calculated and the input values. This suggests that two spring model is independent of calibration bar stiffness.

The initial resonant frequencies of the four aluminium calibration bars, measured during calibration of I_0 before reinforcing the bonding between the magnets and the cross-arms, were also used to double-check the two spring model. The resonant frequency (Table 4.12) of each calibration bar was re-measured as additional masses were attached on top of the cross-arms. The derived values for I_0 and $K_{equipment}$ for the all cases (summarised in Table 4.11) show that I_0 varies from 0.00280 to 0.00281 kgm^2, which is very consistent and close to the calculated value from geometry method ($0.00284 kgm^2$). The calculated stiffness of each calibration bar (using the two spring model) was in good agreement to the theoretical one.

---

[8] ASTM (1995); Drnevich (1978) specified that the stiffness of equipment should be at least ten time higher than that of the specimen.

4.8 Discussion

Despite the difference in mode shape, the analytical solutions for the SDOF torsional vibration model are comparable to those of the viscoelastic model (Hardin, 1965) and the elastic model (Richart *et al.*, 1970). In the two spring model, the mode shape is simply assumed as a linear function (or the angle of twist per unit length is a constant, Fig. 4.17b). For a very special case, in which the material is pure elastic (or damping ratio is very small) and the equipment is very stiff (no equipment compliance), the equation of motion (Eq. 4.3) of two spring model can be simplified as

$$\frac{\omega_0 L}{V_s} = \sqrt{\frac{I}{I_0}} \tag{4.6}$$

Based on the model of wave propagating in elastic rod, Richart *et al.* (1970) suggest that the first mode shape of the fixed-free elastic rod is a *sin* function, $\theta(x) = C\sin(\pi x/2L)$ (Fig. 4.17a). Corresponding to this mode shape, the following equation of motion was derived (see section 3.3.1)

$$\frac{I}{I_0} = \frac{\omega_0 L}{V_s} \tan\frac{\omega_0 L}{V_s} \tag{4.7}$$

Eq. 4.6 and 4.7 will be identical if

$$\sqrt{\frac{I}{I_0}} = \tan\sqrt{\frac{I}{I_0}} \tag{4.8}$$

Eq. 4.8 requires the ratio I/I_0 tends to zero. Studying shear wave propagation in a viscoelastic circular rod, Hardin (1965) also pointed out that the system approaches SDOF (fixed-free configuration) if the ratio I/I_0 approaches zero. The two spring model can practically meet this condition if the moment of inertia of the driving system is much larger than that of soil specimen.

For illustration, values of G_{max} of a few dry granular specimens calculated by two spring model were compared to that calculated by elastic model (Richart *et al.*, 1970) combined with frequency-dependency concept (Priest, 2004). The specimens in general were cylindrical, 70mm in diameter and 140mm in height. It will be recalled that the calibrated $I_0 = 0.00280 - 0.00284$, hence the ratio I/I_0 of these specimens varied from 0.12 to 0.18, which is relatively larger than zero. Thus, the condition in Eq. 4.8 was not well satisfied. For example, the error of the condition Eq. 4.8 was from 5% to 6% (if $I/I_0 = 0.18$, $\sqrt{I/I_0}$ will be 0.42, slightly different from $\tan\sqrt{I/I_0} = 0.45$), leading to a negligible difference in calculated V_s. The results were plotted in Fig. 4.18, showing that the V_s calculated using the two spring model ranges from 1% to 3% lower than that calculated by the other method. It is noted that damping ratios at a small shear strain of these materials were very low.

Another advantage of two spring model is that Eq. 4.4 is convenient in use, especially when dealing with a large number of calculations, since it can be quickly performed in a worksheet. In contrast, Eq. 4.7 needs to be solved using a trial and error method, and the viscoelastic model (Hardin, 1965) requires a computer program (ASTM, 1995). If the data set is large, these methods are time consuming

Table 4.1: Measured and calculated natural frequency of aluminium calibration bars

Bar No	Diameter (m)	Height (m)	specimen stiffness (Nm/rad)	Natural frequency (Hz)	Measured resonant frequency (Hz)	Difference %
1	0.01300	0.17500	433	61.0	61.4	0.66
2	0.01800	0.17500	1590	116.9	114.0	-4.1
3	0.02300	0.17500	4239	190.9	176.4	-9.11
4	0.02810	0.17500	9444	285.0	242.2	-16.42

Table 4.2: Elastic material properties

Material	ν	Density kg/m3	E (Pa)	$G = E/2(1+\nu)$ (Pa)
Aluminium bar	0.33	2.70E+03	7.18E+10	2.70E+10
accelerometer	0.30	7.85E+03	2.00E+11	7.69E+10
Alnico magnet	0.3	7.57E+03	2.00E+11	7.69E+10
Alloy cross-arms	0.33	2.70E+03	7.18E+10	2.70E+10

Table 4.3: Predicted natural frequencies and modes for modelled calibration bars and full section specimens

Mode	Predicted natural frequencies (Hz)						
	Aluminium bars				Full-section specimens with E =		
	Bar 1	Bar 2	Bar 3	Bar 4	25MPa	250MPa	2500MPa
1	36.1	58.3	109.5	164.2	21.4	67.6	207.2
	F	F	F	F	F	F	F
2	59.5	113.2	182.1	267.4	34.2	107.5	322.5
	T	T	T	T	T	T	T
3	194.3	281.1	327.3	349.1	95.1	255.4	348.6
	F	Df	Df	Df	F3	F3	Df
4	371.5	347.2	348	358.8	122.2	298.8	360.5
	Df	Df	Df	Df	L	Df	Df

F = calibration bar or specimen flexure, T = bar torsion, L = longitudinal compression of specimen, Df = drive mechanism flexure

Table 4.4: Effect of calibration bar design on torsional stiffness

Bar No	Derived stiffness (Nm/rad)		Theoretical stem stiffness (Nm/rad)	Difference (%)	
	Full fixity K_{af}	4 points fixity K_{a4}	K_t	$(1 - K_{af}/K_t)$	$(1 - K_{a4}/K_t)$
1	418	417	433	3.5	3.7
2	1524	1513	1590	4.2	4.9
3	4035	3955	4239	4.8	6.7
4	8927	8539	9444	5.5	9.6

Table 4.5: Summary of resonant frequencies of calibration bars obtained from experimental and numerical methods

Bar No	Natural frequency (Hz)	Numerical measured frequency (*) (Hz)	experimental resonant frequency (Hz)	
			Initial	After (**)
1	61.0	59.5	61.4	61.4
2	116.9	113.2	114.0	115.5
3	190.9	182.1	176.4	182.9
4	285.0	267.4	242.2	263.8
5	484.5	NA	NA	396.70

(*) Full drive mechanism geometry modelled, with base of bar stem fixed
(**) After bonding the magnets to the cross-arms with cyanoacrylate glue.

Table 4.6: Summary of resonant frequencies for calibration bar No 4

Descriptions	Resonant frequency (Hz)
Calculated, based on the stem of bar No4 only, $I_0 = 2.85E-3kgm^2$, and $I_a = 9.5E-5kgm^2$ (Table 4.1)	285.0
Initial measured resonant frequency (Table 4.1)	242.2
Measured, after bonding the magnets to the cross-arms with cyanoacrylate glue (Table 4.6)	263.8
ABAQUS, with drive mechanism, without compliance (rigid drive mechanism, rigid top and bottom platen, bottom platen fixed entirely) (Fig. 4.4, 4.12a)	284.9
ABAQUS, static torsion analyses, bottom platen fixed entirely (Table 4.4, Fig. 4.10a)	281.7
ABAQUS, static torsion analyses, fixed at 4 points at the bottom platen (Table 4.4, Fig. 4.10b)	275.5
ABAQUS, $E_{cross\, arm} = 100 \times (71.8GPa)$, without test base, bottom platen fixed entirely (Fig. 4.4, 4.12b)	276.6
ABAQUS, real E, without test base, bottom platen fixed entirely (Table 4.3, Fig. 4.12c)	267.4
ABAQUS with test base fixed at both of its surfaces of the test base (Fig. 4.4, 4.12d)	266.2
ABAQUS with test base fixed at the lower surface (Fig. 4.4, 4.12e)	265.4

Table 4.7: Influence of system compliance on the natural frequency of bar No4

Influence of the compliance of	Cause different in natural frequency (HZ)	Error in measured frequency (%)
(a)	(b)	$(c) = (b)/21.2$
Magnet connections	21.6	(*)
Base fixity, component connections	1.6	8
Test base	0.8	4
Compliance of the bottom platen	1.2	6
Cross arm	9.2	43
Magnets, instrumentations and top platen	8.3	39
Total	21.1	99.5

(*)Was not calculated. The magnets connections was reinforced and this source of error was overcome

TABLE 4.8: Results of calibration tests using the Stokoe RCA with calibration bars of differing stiffness

Bar No	Stiffness	Priest (2004)		Kumar & Clayton (2007)		The author			
						Initial measurement		New data (*)	
	Nm/rad	$F_r(Hz)$	$I_0(kgm^2)$	$F_r(Hz)$	$I_0(kg.m^2)$	$F_r(Hz)$	$I_0(kgm^2)$	$F_r(Hz)$	$I_0(kg.m^2)$
1	433	59.8	0.00299	61.03	0.00274	61.4	0.00281	61.40	0.00291
2	1590	111.7	0.00298	114.64	0.00283	114	0.00301	115.50	0.00302
3	4239	175.2	0.00339	178.46	0.00309	176.42	0.00336	182.90	0.00321
4	9444	244.3	0.00432	247.27	0.00381	242.15	0.00397	263.80	0.00344
5	27635	NA	NA	332.18	0.00778	NA	NA	396.70	0.00445

(*) measured after reinforcing the bonding between magnets and cross-arms

TABLE 4.9: Calibration of $k_{equipment}$ and I_0 using *two spring model*

Bar No	$k_{specimen}$ (Nm/rad)	f_r (Hz)	$\frac{1}{\omega^2}$ $(kg.m^2)$	$\frac{1}{k_{stem}} + \frac{1}{k_a}$ (Nm/rad)	calculated G			
					Initial calibration (Pa)	Difference (%)	Adjusted calibration (Pa)	Difference (%)
1	433	61.4	6.71898E-06	0.002312	2.702E+10	0.1	2.747E+10	1.7
2	1590	115.5	1.89879E-06	0.000629	2.672E+10	-1.0	2.704E+10	0.1
3	4239	182.9	7.57204E-07	0.000236	2.665E+10	-1.3	2.668E+10	-1.2
4	9444	263.8	3.63991E-07	0.000106	2.791E+10	3.4	2.732E+10	1.2
5	27635	396.7	1.60959E-07	3.6E-05	3.062E+10	13.4	2.759E+10	2.2

TABLE 4.10: Verification of two spring model using ABAQUS model having geometry similar to calibration bar 4 with test base

Bar No	Young' Modulus (GPa)	Theoretical $k_{specimen}$ (Nm/rad)	predicted f_r (Hz)	Back-calculation		
				non-corrected K (Nm/rad)	'Two spring model' K (Nm/rad)	Error (%)
1	1.237*	433	60.5	430	433	0.0
2	4.546	1590	115.0	1553	1590	0.0
3	1.212	4239	184.3	3987	4241	-0.1
4	27.00	9444	265.6	8282	9458	-0.1
5	79.01	27635	408.1	19554	27682	-0.2
6	158.0	55270	507.5	30250	55426	-0.3
7	343.1	120000	601.7	42518	117596	2.0
8	395.0*	138174	615.7	44515	134255	2.8

(*) the bar model with $G = 1.237\,GPa$ has the stiffness equivalent to the stiffness of calibration bar No 1, and the bar model with $G = 395\,GPa$ has the stiffness equivalent to that of soil specimen with $G = 7.0\,GPa$

TABLE 4.11: Summary of calibration results using initial measured resonant frequencies obtained during calibration of the RCA

Case of additional mass	Without	No 1	No 2	No 3
I_0 (kgm^2)	0.00280	0.00280	0.00280	0.00281
$K_{equipment}$ $(N.m/rad)$	22890	23810	24221	25285

TABLE 4.12: Verification of the two spring model using the initial measured resonant frequencies

Calibration bar No		1	2	3	4
Theoretical stiffness (Hz)		433	1590	4239	9444
Without additional mass	Measured F_r (Hz)	61.4	114	176.42	242.15
	Calculated K $(N.m/rad)$	440	1590	4217	9491
	Error	1.6	0.0	-0.5	0.5
With additional mass No 1	Measured F_r (Hz)	60.5	112.74	174.74	240.6
	Calculated k $(N.m/rad)$	437	1590	4215	9497
	Error	1.0	0.0	-0.6	0.6
With additional mass No 2	Measured F_r (Hz)	59.425	111.7	173.4	238.6
	Calculated k $(N.m/rad)$	430	1590	4222	9469
	Error	-0.7	0.0	-0.4	0.3
With additional mass No 3	Measured F_r (Hz)	59.3	110.7	171.96	237.9
	Calculated k $(N.m/rad)$	437	1590	4212	9509
	Error	1.0	0	-0.6	0.7

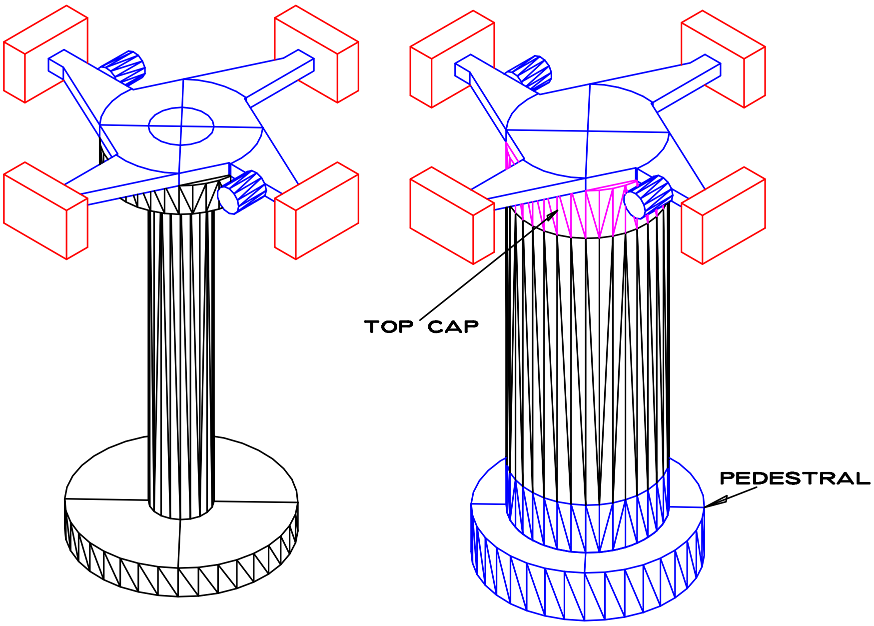

A. CALIBRATION BAR WITHOUT TEST BASE

B. FULL SECTION SPECIMEN

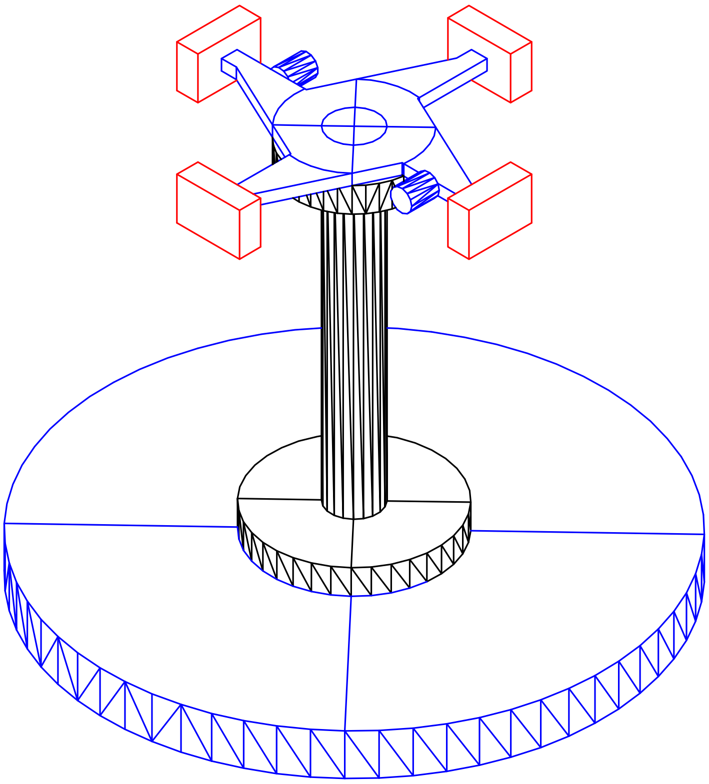

C. CALIBRATION BAR WITH TEST BASE

FIGURE 4.1: Numerical models

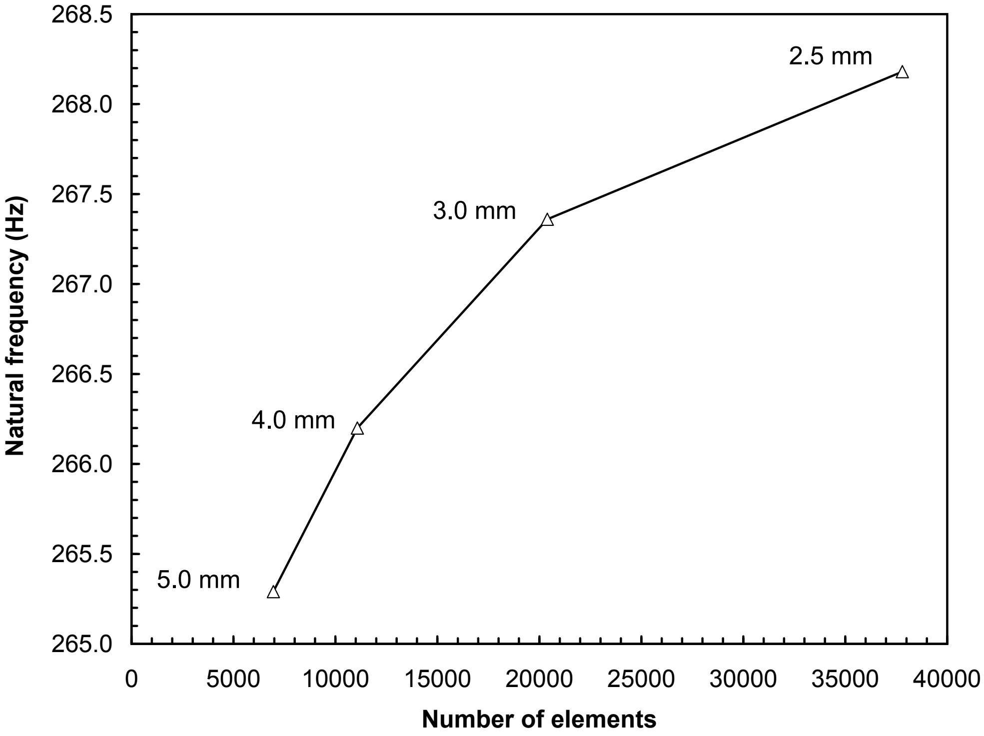

FIGURE 4.2: Effect of meshing on predicted natural frequency - Bar No 4 model

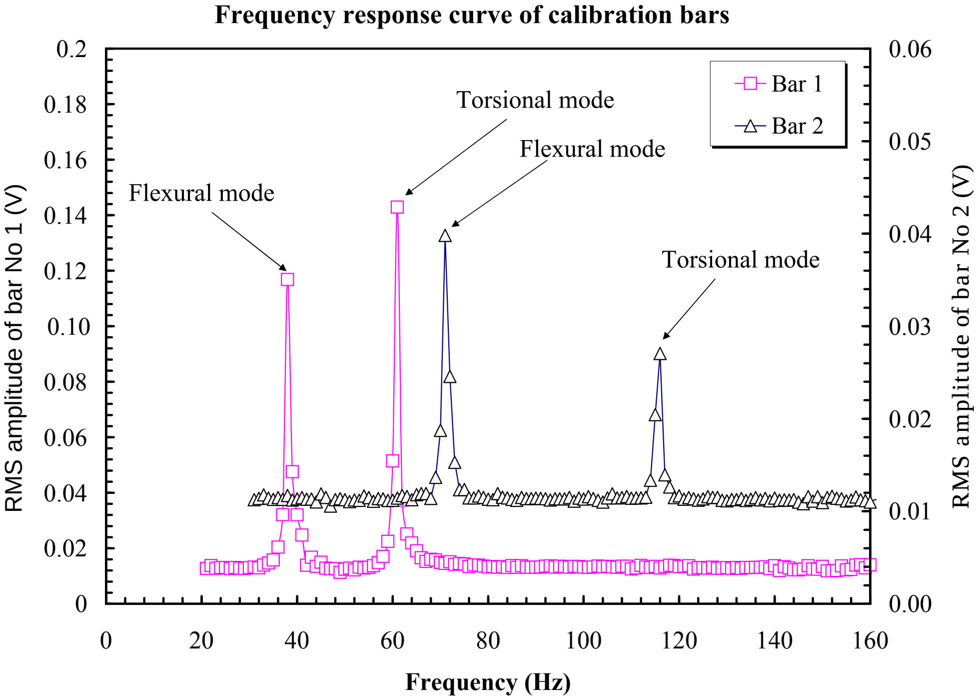

FIGURE 4.3: Detected torsional and flexural vibratory modes of calibration bars

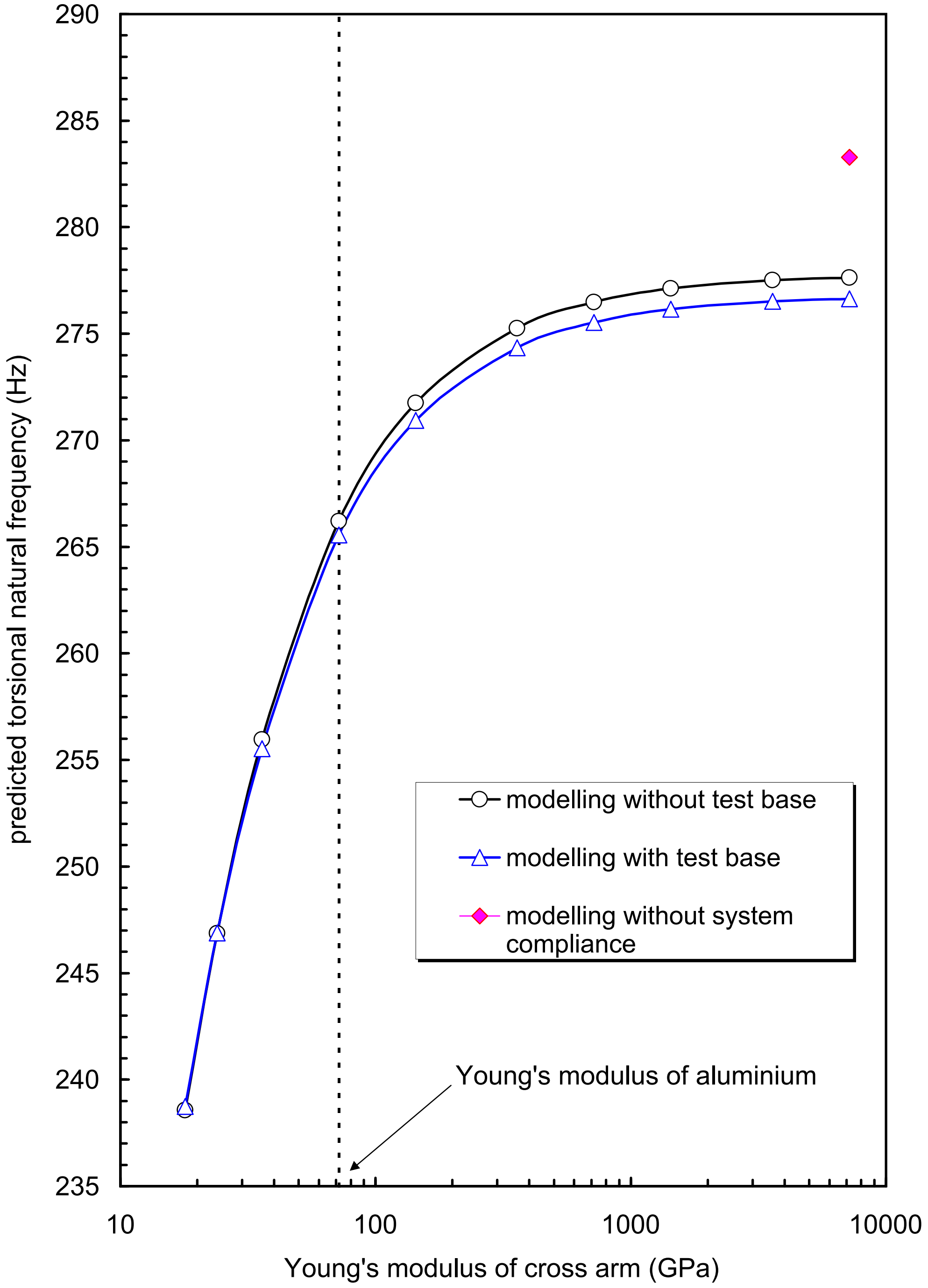

FIGURE 4.4: Effect of cross-arms stiffness on predicted natural frequency, for calibration bar No 4

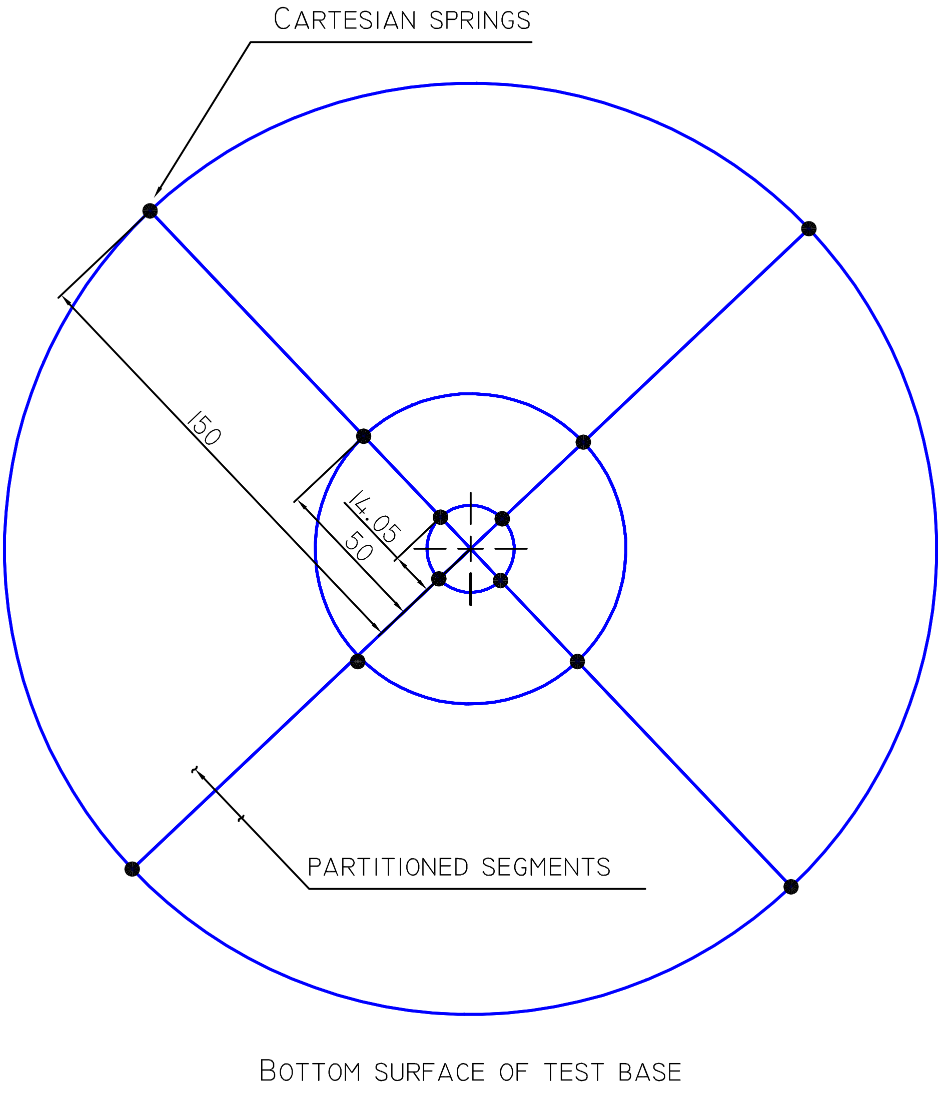

Figure 4.5: Layout of springs supporting partitioned test base

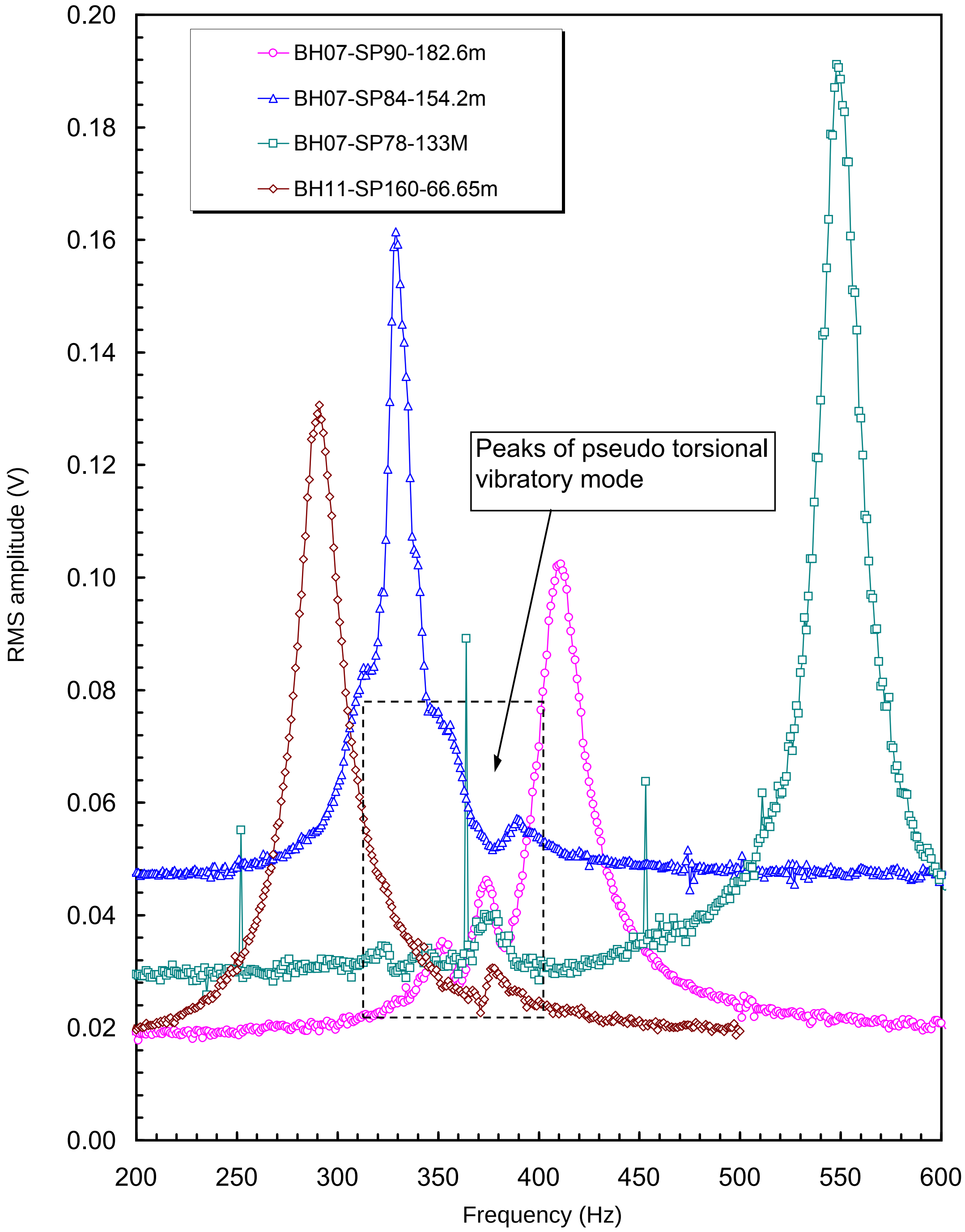

FIGURE 4.6: Frequency response curves of stiff Dubai specimens, showing the pseudo peak of torsional vibratory mode

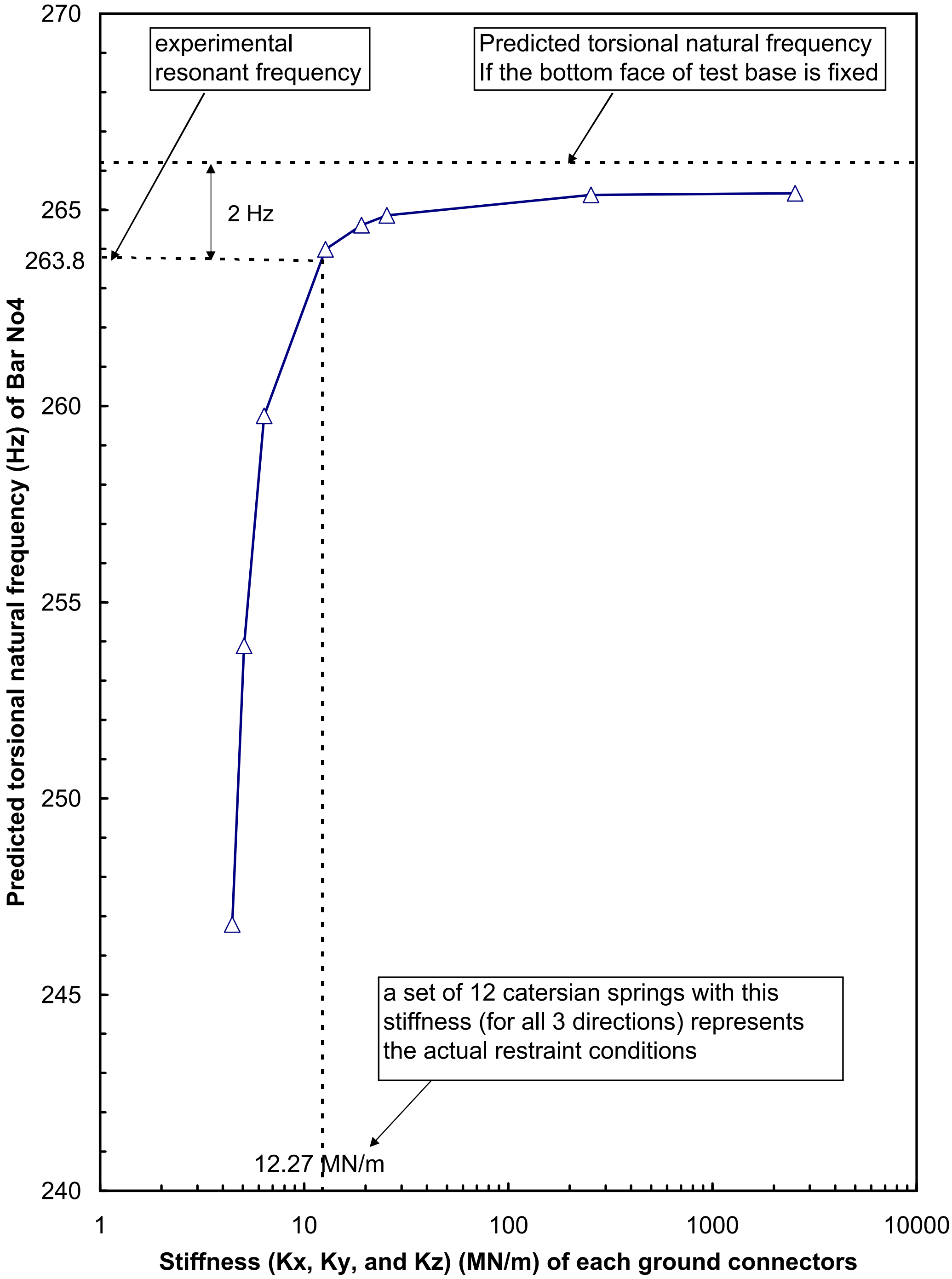

FIGURE 4.7: Effect of spring stiffness on predicted natural frequency for calibration bar No 4

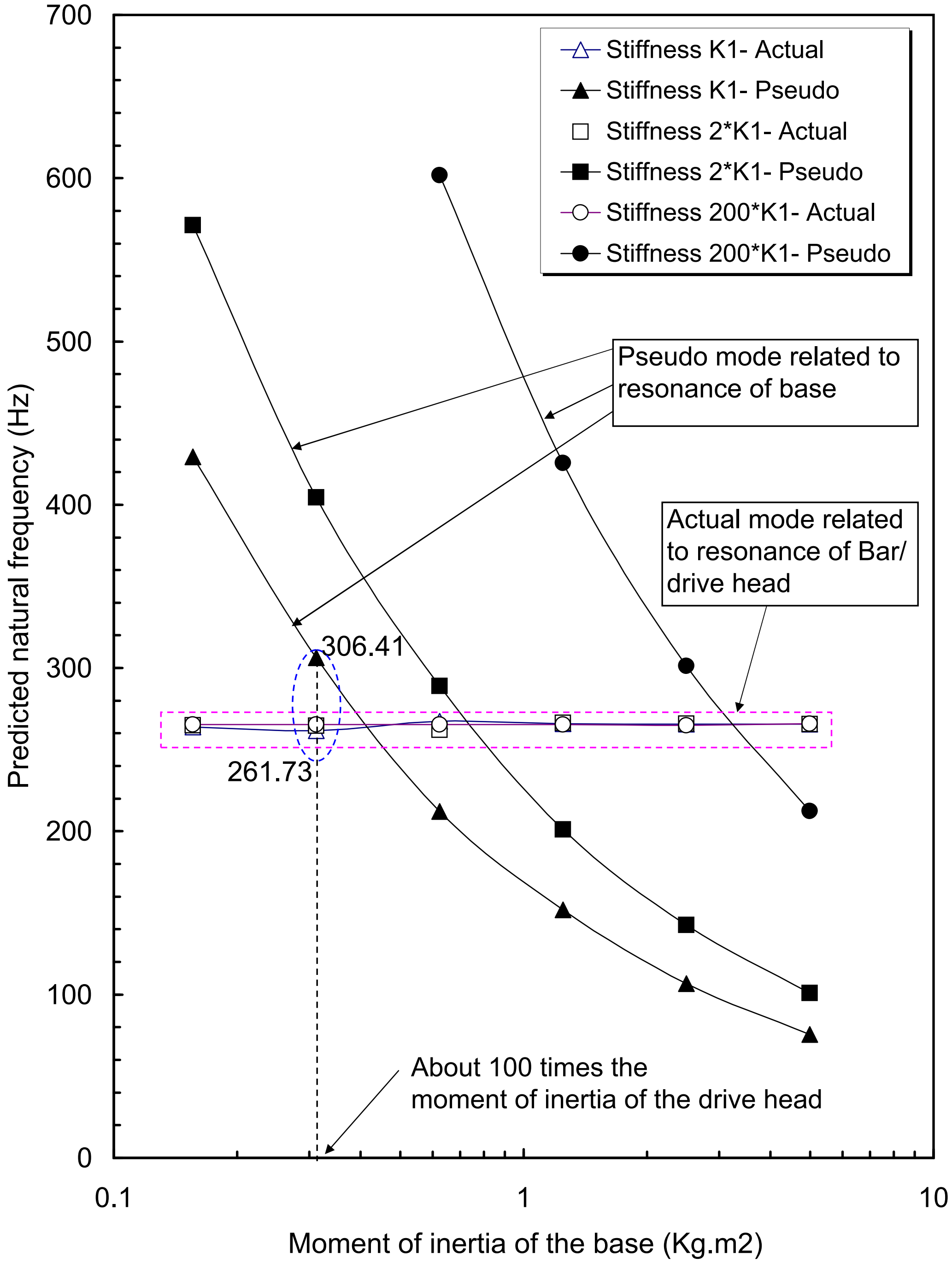

FIGURE 4.8: Effect of base mass on predicted natural frequency for calibration bar No4

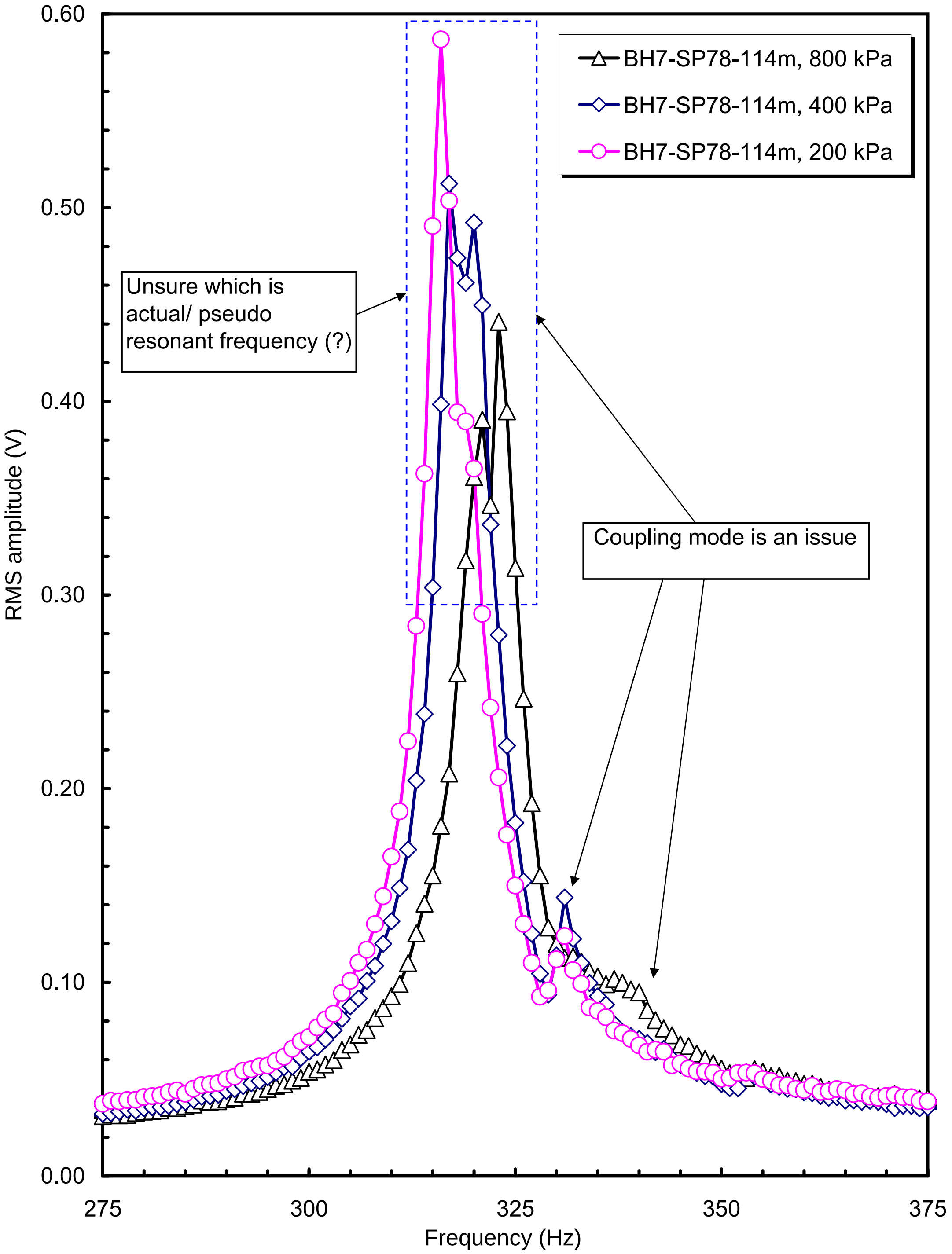

Figure 4.9: Effect of the interaction between the actual and the pseudo mode on the measurement resonant frequency of Dubai stiff clay specimen

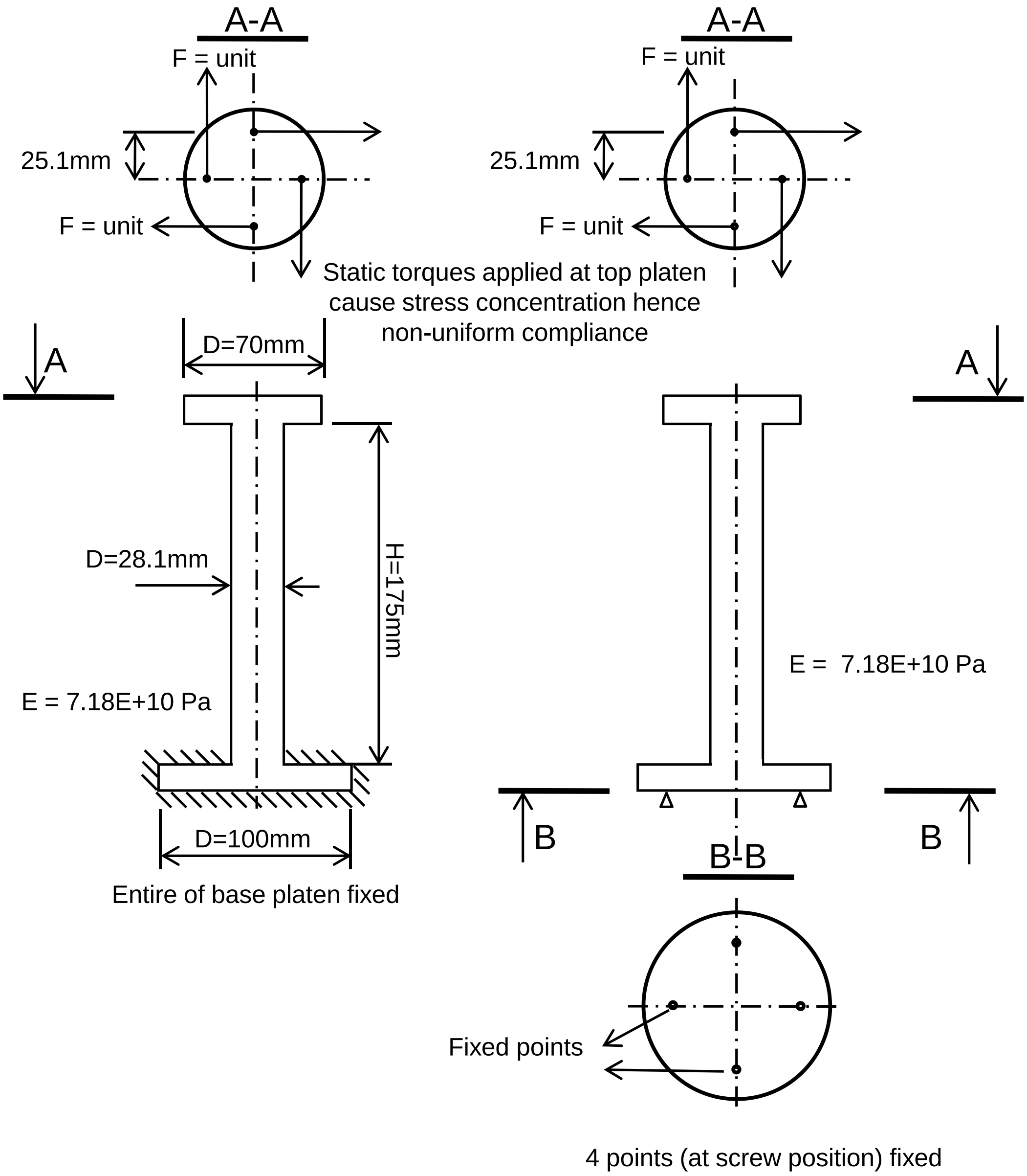

Fr = 281.7 Hz

(a) No fixity compliance

Fr = 275.5 Hz

(b) Base platen compliance

Figure 4.10: Schematics of two No4 models and corresponding natural frequencies estimated from static analysis

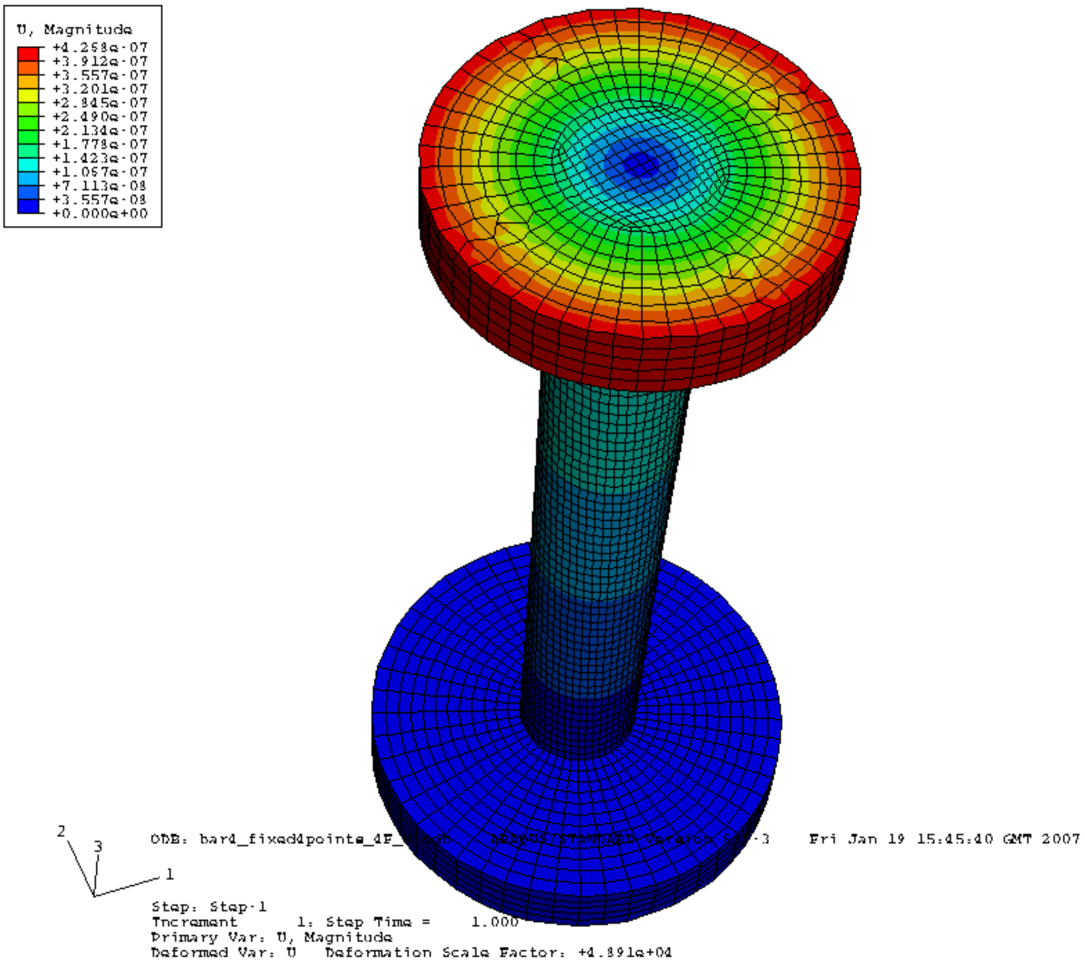

FIGURE 4.11: Static deformation of calibration bar No 4

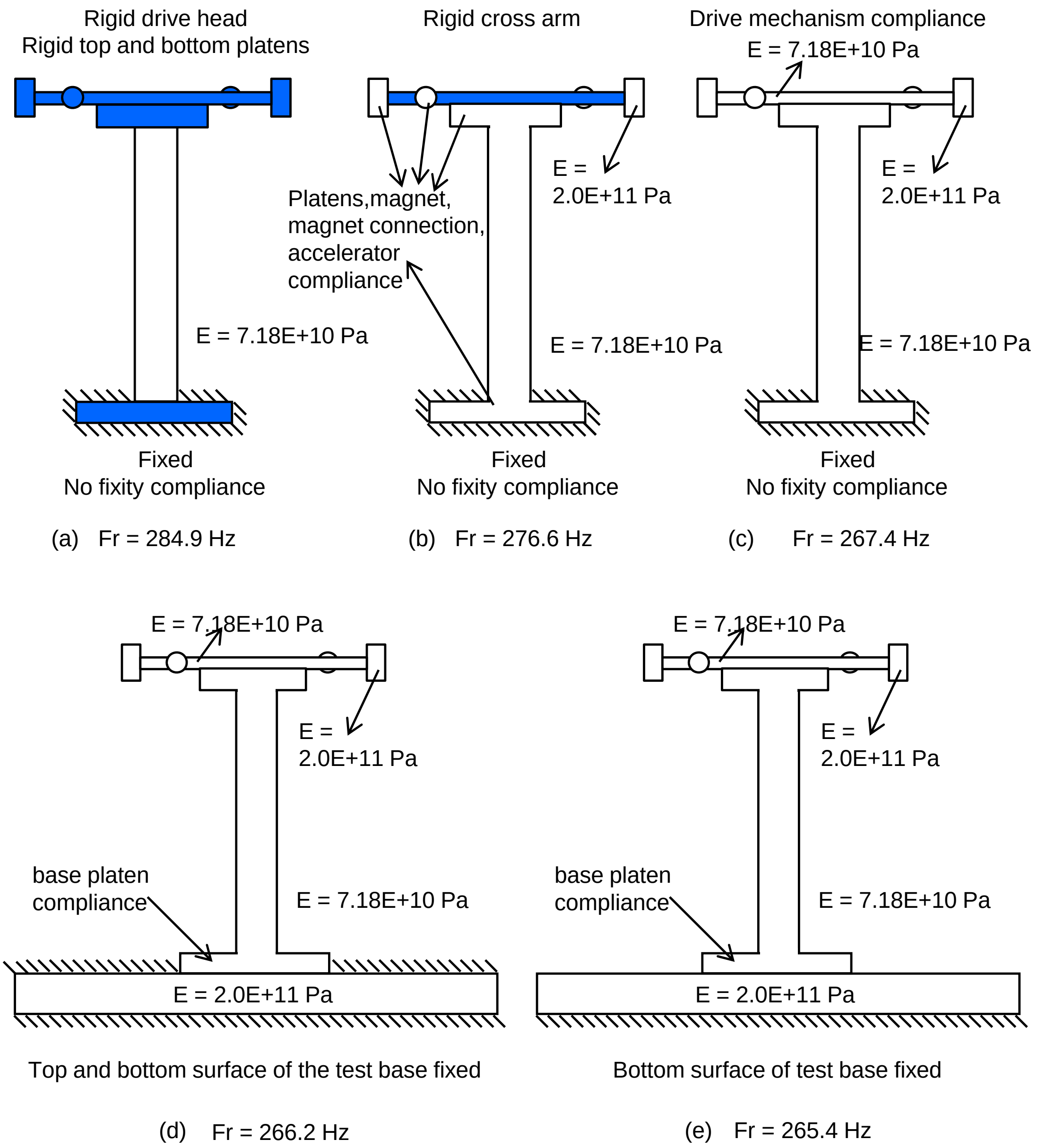

FIGURE 4.12: Schematics of some No4 models and corresponding natural frequencies extracted from dynamic analysis. (a) Without compliance; (b) With compliance of top platen, magnet, magnet connections, and accelerator; (c) Without fixity compliance; (d) Without test base compliance; (e) With test base compliance

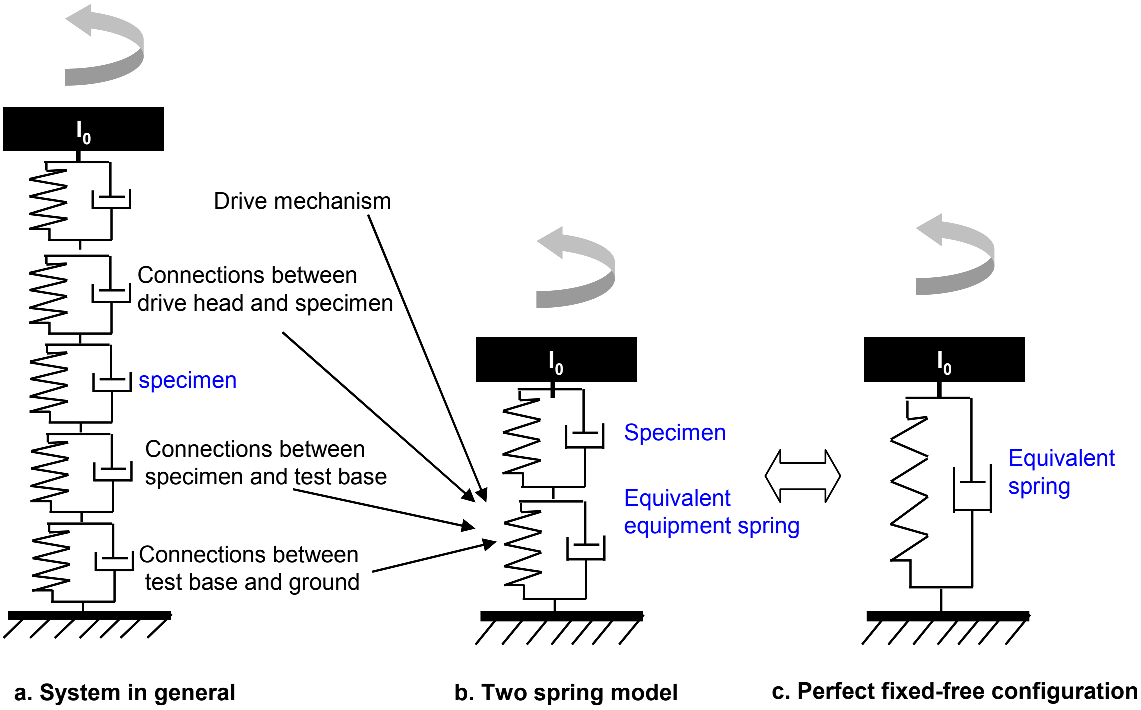

Figure 4.13: Two spring model

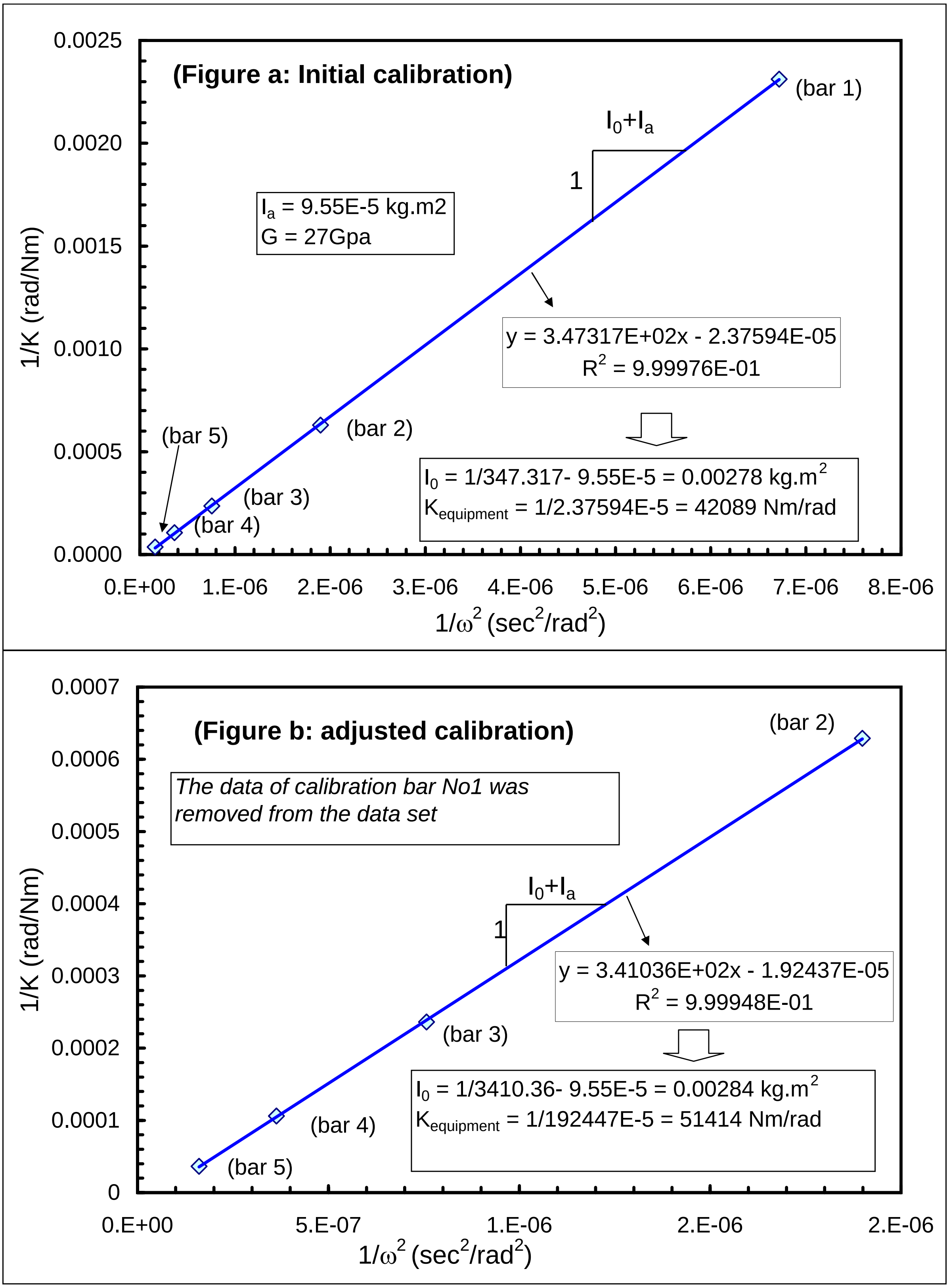

FIGURE 4.14: Preliminary and adjusted calibration parameters of the RCA

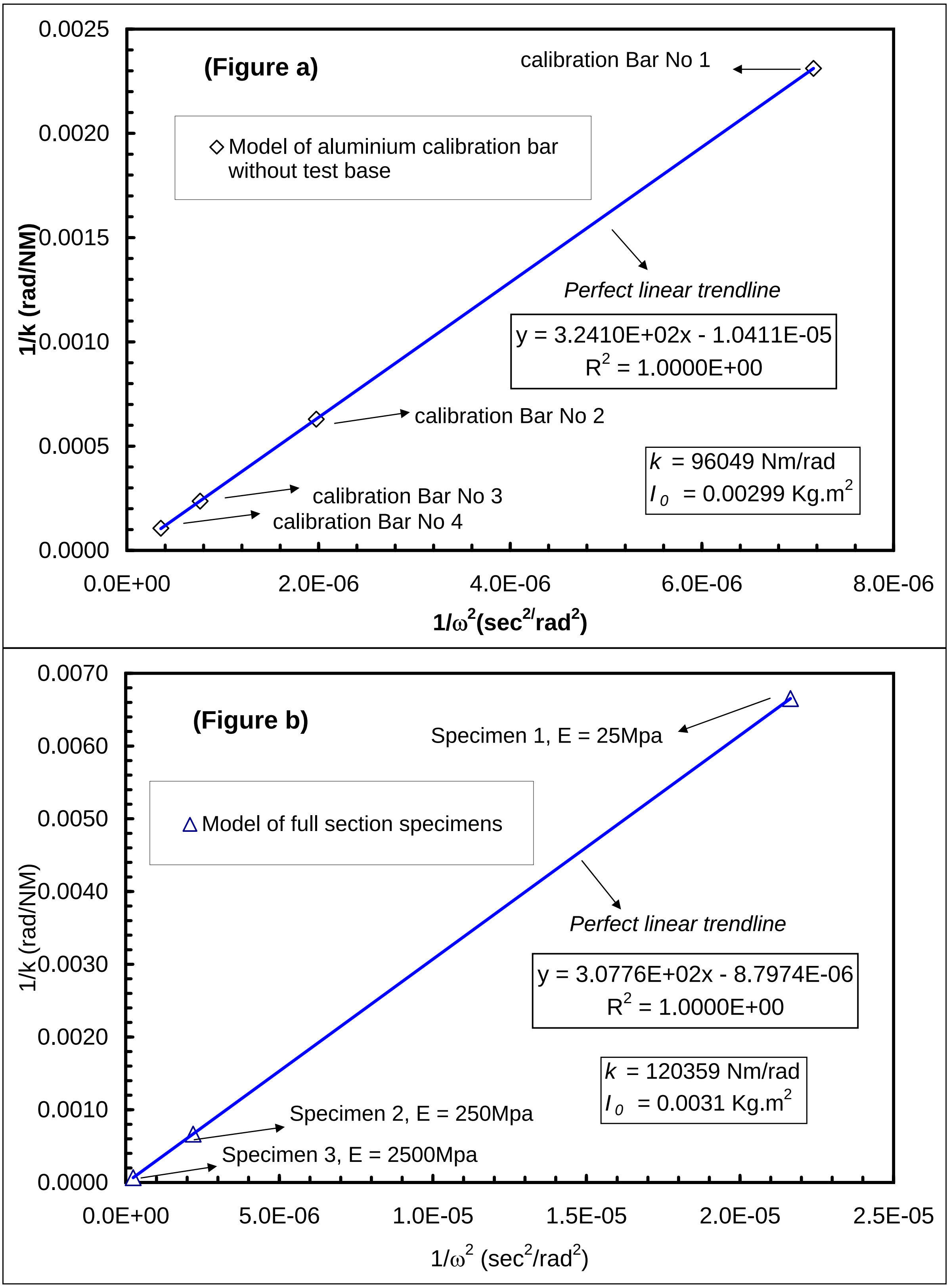

FIGURE 4.15: Linear relationship between $1/k_{specimen}$ and $1/{\omega_0}^2$, data from ABAQUS model of aluminium bars and full section specimens, without test base

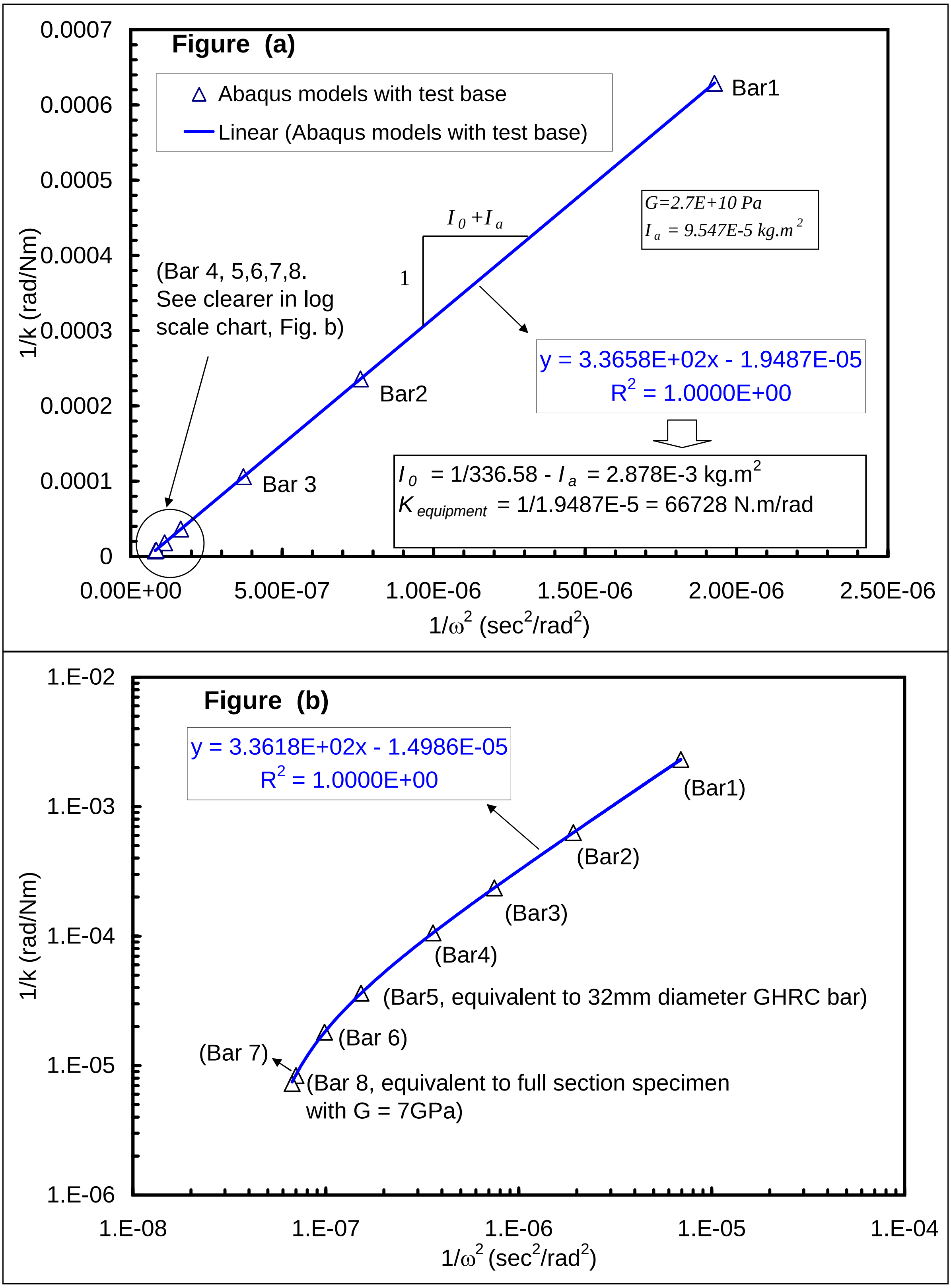

FIGURE 4.16: Verification two spring model using ABAQUS model of aluminium bars with test base

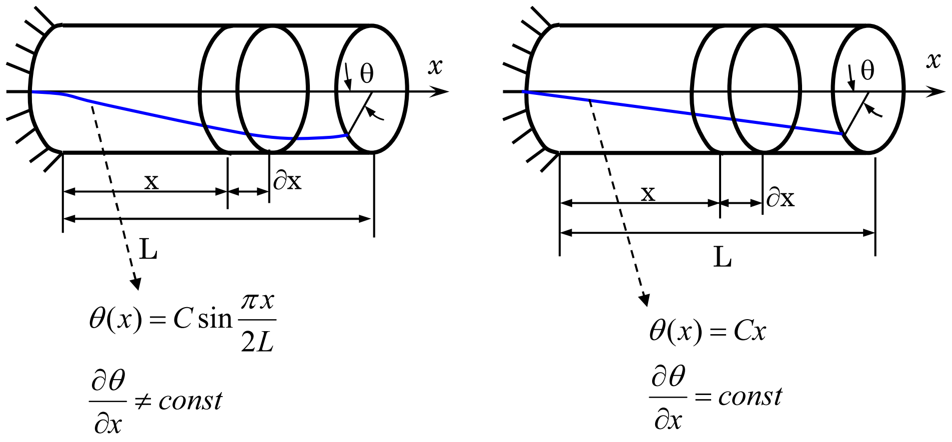

Figure a: shape mode of elastic model is a *sin* function (Richart et al., 1970)

Figure b: Shape mode of SDOF torsional vibration is a linear function

FIGURE 4.17: Difference in mode function of wave propagation in elastic model and torsional forced vibration model

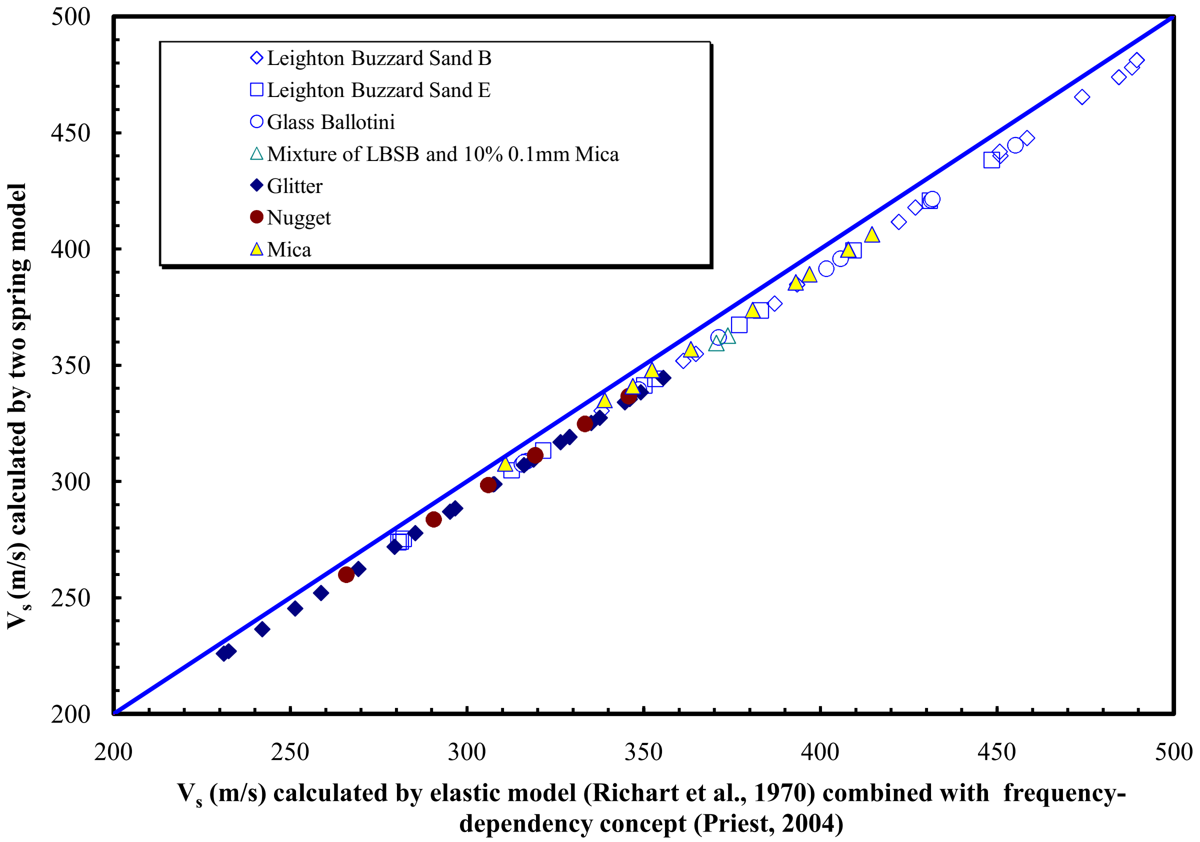

FIGURE 4.18: Comparison V_s calculated by two spring model and other model

Chapter 5

Laboratory testing

This chapter presents a methodology used to determine the small strain response of granular materials with distinct and different particle shape. Techniques used to characterise the granular particles, a methodology for specimen preparation, a RC testing procedure, and a computer program for automatically running a RC test is described. Sample results are presented in this chapter to show general small strain response of geomaterials. More results will be presented and discussed in Chapter 6.

5.1 Material properties

This section presents some general properties, such as the maximum and minimum void ratio, the specific density and particle size of test materials used in this study. The particle shape of the materials is characterised in the next section.

Materials used in this research were granular with differing particle shape, namely Leighton Buzzard sand[1], mica, and glass products[2].

- Leighton Buzzard sand fraction B (LBSB) is a round natural, uncrushed, clean silica sand (Fig. 5.1a and 5.2). The nominal diameter of LBSB is 1.0 mm; the fraction passing the 1.16 mm sieve and retaining by the 0.6 mm sieve was used in this research.

- Leighton Buzzard sand fraction E (LBSE) is an angular, naturally occurring uncrushed, silica sand (Fig.5.1b and 5.3). The nominal diameter of LBSE is 0.1 mm; the fraction passing the 0.15 mm sieve and retained by 63μm sieve was used in this research.

- Glass Ballotini (GB) is composed of smooth soda-silica[3] (Fig. 5.1c). The diameter of different types of GB varied from 0.1 mm to 3.0 mm.

---

[1] Supplied by the David Ball group, Cambridge, UK.

[2] Supplied by *SIGMUND LINDNER GmbH* Oberwarmensteinacher Strasse 38, D-95485 Warmensteinach, Germany, www.sigmund-lindner.com.

[3] According to the product data sheet, the major chemical of the GB is SiO_2 and Na_2O, with the compositions being of 70% and 13.1%, respectively.

- Glass Nugget ("Nugget") is angular, platy, crushed glass with the nominal diameter of 1.0 mm (Fig. 5.1e and 5.4).
- Glass Glitter ("Glitter") is angular, flat, transparent glass with the nominal diameter of 1.0 mm diameter (Fig.5.1f and 5.5).
- Mica is extremely flat natural silica material with the nominal diameter of 0.1 mm (Fig. 5.1d)

Table 5.1 summarises the maximum and minimum dry density and the specific gravity of the test materials. The maximum density of the material was determined using dry pluviation (Cresswell *et al.*, 1999), and the minimum dry density was obtained using the 'tilting test' method of Kolbuszewski (1948). Fig. 5.1 shows scanning electron microscope images highlighting the particle characteristics of the materials.

5.2 Characterisation of particle roundness and particle form

Particle roundness

This research uses roundness index, defined as $4\pi A/p^2$ (Wilson *et al.*, 1997), to characterise roundness of a particle because of its effectiveness presented in chapter 2. Determination of roundness index requires two 2D particle images parameters, namely the area, A, and the perimeter, P, of a particle. The 2D particle images of the test materials are presented in Fig. 5.2 to 5.5. For convenience, in this research, the inverse of roundness index, which is termed angularity index, AI, was used to represent the roundness of a particle since the scale of AI $(1.0 - \infty)$ is larger than that of roundness index $(0 - 1.0)$. Table 5.2 summaries the angularity index, AI, of the test materials used.

Particle form

Due to the advantages of Corey's shape factor (CSF) over other form descriptors (as presented in chapter 2), this method was used to characterise the form of sand particles. Corey's shape factor, defined as $S/\sqrt{L \times I}$, requires three diameters, namely the largest, L, the intermediate, I, and the shortest diameter, S. Since dimensions of the sand particles cannot be directly measured, the three diameters were determined using an image analysis technique combined with the volume method proposed by Reddy (2008). The volume method assumes that sand particles are scalene ellipsoids with the equivalent volumes. When sand particles are dropped onto a microscope slide, they normally rest on their largest surface with the short axes nearly vertical (Wadell, 1932). Reddy (2008) adopted that the largest (L) and intermediate (I) dimensions of a sand particle are the circumscribed circle and the largest inscribed circle, respectively (Fig. 5.6). From digital images of the sand particles, the largest (L) and intermediate (I) dimensions were measured automatically using image analysis software (e.g. Image Pro-plus[4]), and were

---

[4] Developed by Media Cybernetics, Inc., Bethesda, Maryland, USA.

averaged. The shorted dimension, S, was then calculated using the following equation:

$$S = \frac{6 \times \overline{V}}{\pi L \times I} \tag{5.1}$$

where $\overline{V}$ is average volume of a particle. $\overline{V}$ was calculated based on the weight of a specimen, the specific gravity and the number of particles in the specimen. The number of particles in the specimen can be counted manually or automatically using image analysis software (Reddy, 2007). It is noted that calculated values of S should be smaller than both L and I. If the calculated value of S is larger than either L or I, permutation between the roles of the three parameters is made to satisfy the condition: $L \geq S \geq I$.

In this research, the largest (L), the intermediate (I), and the average volume, $\overline{V}$, of a particle given in Table 5.3 were measured in the work of Reddy (2007), who used the same materials. From these data, CSF of the test materials was calculated. For reference, other sphericity descriptors of the materials, such as operational sphericity, ψ_o, (Wadell, 1933) and scalene equivalent ellipsoid sphericity, $SEES$, (Reddy, 2008) were also calculated (Table 5.3).

The volume method, however, is unsuitable for determining particle form of very fine grains such as LBSE or 0.1 mm mica because counting a number of grains for even just a small mass of LBSE or 0.1 mm Mica requires excessive time and effort (for example, 10.0mg of LBSE may have more than 10,000 particle). Based on the SEM images (Fig.5.1), it is suggested that the sphericity descriptors of LBSE are larger than those of Nugget and smaller than those of LBSB. This is the limitation of this research on these particles.

5.3 Software development

A computer program was written using TestPoint[5], to allow complete automation of a RC test, and control the number of loading cycles. The program contains two subprograms namely ‘broad sweep’ and ‘fine sweep’.

The broad sweep undertakes a frequency sweep at 1.0 Hz intervals to quick define the resonant frequency of a specimen with an error $= \pm 1.0 Hz$. The broad sweep generates a sinusoidal waveform with a predefined input voltage and with an initial frequency, and sends the sinusoidal waveform (with 150 cycles) to the A/D control box (Fig. 3.3). The predefined input voltage should be small to ensure that shear strains induced in the specimen is within the elastic limit. The signal is then amplified by the power amplifier before going to the coils to oscillate the specimen (see the working principle of the RCA in Section 3.2). Based on output signals obtained from the accelerometer (via the charger amplifier), the program computes vibration amplitudes of the specimen. The program repeats the above steps with higher excitation frequencies (within a range of excitation frequency, e.g. from 50 Hz to 500 Hz set by the user). This allows the ‘broad sweep’ frequency response curve to be determined, and hence the ‘broad sweep’ resonant frequency (at the peak

---

[5] Trademark of Capital Equipment Cooperation, Billerica, MA, USA.

vibratory amplitude) to be defined. The flow chart for the 'broad sweep' subprogram is presented in Fig. 5.7

Based on the 'broad sweep' resonant frequency, the fine sweep defines the resonant frequencies at various shear strains (various input voltages) with greater precision (error $= \pm 0.1 Hz$). At a given input voltage, the fine sweep undertakes a number of tasks e.g., automatic generation of a digital sinusoidal waveform, determination of a frequency response curve (within the resonant region), defining the peak amplitude and the resonant frequency, estimation of the average shear strain and saving data to a file, etc.

After defining the resonant frequency, the fine sweep measures the specimen damping ratio using both the FVD and the HPP methods. The fine sweep generates a sinusoidal waveform at the resonant frequency to excite the specimen using 200 loading cycles (to ensure that a steady state vibration is archived). The fine sweep then stops exciting the specimen, and starts acquiring a free vibration decay waveform. The fine sweep defines the peak amplitude for each cycle of the free vibration decay response, and computes the logarithmic decay, δ, from which the FVD damping ratio of the specimen is computed. In addition, the fine sweep program, using the frequency response curve, interpolates the half power bandwidth frequencies (f_1 and f_2), from which the HPP damping ratio is computed.

The fine sweep repeats the above tasks with increasing input voltages until either the shear strain exceeds the limiting shear strain (e.g. 0.01%, input by the user) or the digital input voltage exceeds 10.0 Volt, which is the limiting working voltage of the A/D controller box. Since the results (e.g. shear modulus, and damping ratio etc.,) are plotted against shear strain on a logarithmic scale, the amplitude of the sinusoidal waveform is increased in an exponential manner to provide data points with uniform spacing. The flow chart of the fine sweep program is presented in Fig. 5.8.

Attempts have been made to reduce significantly the number of load cycles by reducing the number of points which make up a response curve. At a given input voltage, based on the 'broad sweep' resonant frequency, the fine sweep program predetermines a 'sweep window', a frequency range containing the resonant frequency. The sweep window should be wide enough (wider than the half power bandwidth) for estimating the damping ratio using the HPP method. The fine sweep varies the vibratory frequency with a step interval, Δf, which is not constant but varied depending on the relative position of the vibratory frequency in the sweep window. The program assigns the finest interval of 0.1 Hz, only when the frequency is near the centre of the sweep window. Fig. 5.9 presents an example of a frequency response curve of a specimen defined by 17 points. Obtaining one point in the frequency response curve required 250 load cycles to take place. Therefore, the total number of load cycles induced in the specimen per strain increment was $17 \times 250 = 4250$. If the resonant frequency is 60 Hz, each step will take place in two minutes, and the full test (at a given effective stress) with about 20 strain increments can be accomplished in less than an hour.

5.4 Specimen preparation

This section describes the methodology adopted to prepare uniform cylindrical specimens with a predetermined void ratio.

5.4.1 Preparation of a uniform granular specimen

A specimen were formed using a thin-walled cylindrical split mould. The diameter of the mould could be finely adjusted using a Jubilee clip. Once the diameter was set, the opening in the spit mould was sealed by tape. O-rings were placed on the outside at one end of the mould before a membrane was placed inside the mould, with its end folded over both ends of the mould and the o-rings [6]. Suction was applied to pull the membrane onto the split mould through the air vent in the middle of the mould. The mould was placed on the pedestal coated with a thin layer of silicon grease. The use of silicon grease helps create an air tight seal. The membrane was pulled down over the pedestal and the o-rings were then pulled down to firmly seal the membrane onto the pedestal. Porous stones were not used as they are unnecessary for dry specimens. In addition, the porous stones could affect the coupling between the specimen and the end platens, and alter the stiffness of the composite specimen (two porous stones and sand). Two small pieces of filter paper were placed over two air entering inlets in the base of the pedestal to prevent particles that are smaller than the inlet diameter from entering the pedestal.

Before testing, a desired void ratio of the specimen was predetermined (based on the specimen dimensions and specific density of the test material). To achieve a given void ratio, the weight of the dry material was calculated and only this amount of dry material was used. Specimens were formed using a pluviation method described in detail by Cresswell *et al.* (1999). The method involves raining the sands (into a cylinder) through diffuser meshes. One of the advantages of pluviation over tamping and vibratory compaction is that it can attain uniform density without particle crushing (Lo Presti *et al.*, 1992). Other advantage of the pluviation method is the repeatability. The Author has used the pluviation method (see Cresswell *et al.*, 1999) to determine the maximum density of all the materials and observed that the results are very repeating. Care was taken during pluviation so that no sand was lost. To obtain denser specimens, the free falling height and sand flow (through a funnel tube) were adjusted to increase the pluviation time. Further slight tapping (using a rubber hammer) on the outside of the mould was sometimes necessary until a desired specimen height (corresponding to the predetermined void ratio) was obtained.

5.4.2 Mixing LBSB with 0.1 mm mica

Two specimens of LBSB mixed with 0.1 mm mica with different Mica contents, 10% and 20% by mass, could not be pluviated due to the segregation of heavier sand particles

---

[6] O-rings cannot be lowered from the top to the bottom of the mould to seal the membrane against the pedestal due to the existing of a pipe attached at the air vent in the middle of the mould. This is the reason why the O-rings should be placed on the outside at one end of the mould in advance.

from lighter mica particles. Therefore, the specimens of sand mixed with fine mica were prepared by a specific method. This section describes the specimen preparation method for the specimen of LBSB with 10% mica. The specimen of LBSB with 20% mica was prepared in a similar manner.

To achieve a very dense specimen with homogenous distribution of LBSB and 0.1 mm mica, a thin layer of sand (10 g by mass) was placed in a mould before 1.0 g of mica (or 2.0 g for 20% mica content) was rained over the top of the sand. This mixture was then well compacted using a rubber tamper. In addition, the sample mould was tapped lightly on the outside. This procedure was repeated until a required specimen height was obtained. In total there were more than 180 thin layers of sand and mica placed in the mould. Therefore, mica was well distributed throughout the entire specimens.

5.4.3 Specimen assembly

After a specimen was formed, the pedestal, the mould and the specimen were placed on the test base of the RCA, and firmly fixed to it by four machine screws. To provide a sufficient air seal between the top cap and the membrane, the lateral surface of the top cap was coated with a thin layer of silicon grease before the top cap was placed on top of the specimen. The membrane was then pulled up to cover the top cap. A level was used to check the level of the top cap. Light tamping on the top cap was necessary to level the top cap and to ensure no gap existing between the top cap and the specimen. A suction of 50 kPa was applied to allow the mould to be removed. Then three o-rings were placed to seal the membrane onto the top cap[7].

5.4.4 Specimen dimension measurement

Specimen dimension measurement was undertaken before the drive mechanism was attached on top of the top cap. Dimensions of all specimens were measured at a suction of 50 kPa, with the thickness of the membrane taken into account.

Diameters of a specimen was measured at four different heights along the specimen; and at each height two readings at perpendicular directions were taken. Four specimen heights were measured around a specimen.

During specimen preparation, a membrane was stretched. Hence, the thickness of the (stretched) membrane would be different from its original thickness. To measure the thickness of the membrane, a steel solid cylinder that has the similar diameter (D = 70 mm) and height (L = 140 mm) of a specimen was used. The diameter of the cylinder plus the membrane was measured. Subtraction of the diameter of the cylinder from the diameter of the cylinder and membrane gives twice the thickness of the stretched membrane.

---

[7] The mould could not be removed if O-rings were placed before removing the mould.

5.5 Apparatus set-up

Once the specimen is formed and the top cap secured, the support frame with the drive mechanism attached to it was gently lowered onto the specimen top cap. The support frame was bolted to the test base using four machine screws. The drive mechanism was gently and firmly fixed to the top cap using four countersunk screws. The support ring holding the coils was aligned until the magnets attached to the cross-arms were centred in the middle of the coils, and then the support ring was clamped to the support frame. The LVDT was fitted and adjusted to give sufficient vertical displacement during application of effective stress.

The cylindrical pressure vessel was carefully lowered until it rested on the o-ring placed on the test base. All electrical connections for the LVDT, the accelerometer, and the coils were made. The 'broad sweep' program was run with very low input voltages and the output signals were checked to ensure that the electrical connections were fully working before the top cap of the pressure vessel was bolted down.

5.6 Testing

A testing programme is designed to characterise the small strain response of dry granular specimens. Isotropic loading is applied in small steps until an effective stress of 100 kPa is achieved. To remove the possible variation of shear modulus due to effects of confinement time (Hardin & Black, 1968; Marcuson & Wahls, 1972; Anderson & Stokoe, 1978), the pressure was maintained for a constant duration of two hours before torsional vibration was applied. In general, all specimens was subjected to increasing shear strain from $10^{-5}\%$ to $10^{-2}\%$. At a given shear strain magnitude, a frequency response and free vibration decay response of a specimen were measured, allowing the resonant frequency, the HPP and FVD damping ratio of the specimen to be determined.

The confining pressure was increased[8] and the above steps were repeated. Normally, an effective stress increment of 100 kPa was applied. However, for crushable particle specimens such as Nugget and Glitter, an increment of 100 kPa may suddenly alter the soil structure (e.g. cause significant change in void ratio and particle orientations) due to the possibility of excessive particle crushing. Therefore, stress increments applied to Nugget and Glitter specimens were less than 100 kPa (e.g. 50 kPa). Most of the specimens were tested at different effective stresses varying from 100 kPa to 600 kPa[9].

5.7 Test results

This section presents typical results of the RC tests conducted in this research. In addition, this section presents effects of noise on damping measurements.

---

[8] A loose specimen of LBSE (e=0.748) and a specimen of LBSB mixed with 10% mica were tested (manually us) only at 100 kPa.

[9] Three were three specimens tested at effective stresses up to 400 kPa.

5.7.1 Void ratio calculation

The initial void ratios of all specimens were measured at a suction of 50 KPa. The void ratio of a specimen was calculated using on the weight and the average dimensions of the specimen. Due to the fact that a specimen was held by suction before the mould was removed, the shape of the specimen is the same as the shape of the mould, which is right cylindrical as shown in Fig. 5.10. It was observed that the differences in diameters measured along a specimen were very small. For example the diameters measured at four positions from the bottom to the top along the weakest specimen (the loose glitter with void ratio of 1.034) were 69.75 mm, 69.44 mm, 69.56 mm, and 70.05 mm, respectively. If the specimen is divided into four cylinders with the same height and the above diameters along the specimen are used to calculate the volume of each cylinder, the volume of the entire specimen will be 512254 mm^3, or 0.001% different from the volume (512248 mm^3) calculated using the average diameter (69.7 mm) of the specimen. This suggests that the error in measurement of void ratio due to the variation in specimen diameter along a specimen was very small.

When the isotropic confining pressure was increased, the volume of the specimen changes. The height of the specimen at any effective stress level is determined using the vertical displacement measured by the LVDT. Since the specimen was isotropically confined, the diameter of the specimen was calculated with the assumption that the radial strain is equal to the vertical strain. It observed that the variation of void ratio due to the variation of effective stress was insignificant for LBSB, GB, LBSE. For instance, when subjected to an increment of effective stress from 50kPa to 600kPa, the vertical deformation of loose 3mm GB specimen (e = 0.606) was 0.11 mm, corresponding to a volumetric strain of 0.24%. This vertical deformation led to 0.62% reduction in void ratio of the specimen. Volumetric strains due to increments of effective stress for Nugget and Glitter were higher than that of LBSB, GB, LBSE. For example, when subjected to an increment of effective stress from 50 kPa to 600 KPa, the void ratio of the loose Glitter specimen decreases from 1.034 to 0.958, or 7.4%. It is noted that the effect of void ratio on G_{max} will be removed using the universal void ratio function presented in Chapter 6.

5.7.2 Shear modulus measurement

The stiffness of a specimen was computed using the two spring model presented in Section 4.5. It is noted that due to small measured material damping ratios (less than 3%), the shear modulus of the test materials can be estimated using Eq. 4.3.

Fig. 5.11 presents a typical frequency response curve for a dense LBSE specimen. The data in the figure was recorded by the software presented in the Section 5.3. The clear and sharp peak of the frequency response curve allows the resonant frequency and HPP damping ratio of the specimen to be precisely determined. The shear strain corresponding to the resonant frequency was estimated using Eq. 3.48. Fig. 5.12a presents a typical shear modulus response curve with respect to shear strain at an effective stress of 100 kPa for the specimen. It can be seen in the graph that there is a plateau where the shear modulus can be considered as constant G_{max}. Fig. 5.12b presents a typical shear modulus degradation, G/G_{max}, versus shear strain for the specimen. In this research, elastic threshold strains, γ_e, was taken at a point where $G/G_{max} = 98\%$. Fig. 5.13 presents a typical plot of G_{max} versus effective stress for the specimen.

5.7.3 Damping measurement

Fig. 5.14 presents a typical free vibration decay curve obtained from 35 cycles for the LBSE specimen. The curve was recorded at a rate of 100 samples per decay cycle. The amplitude of each cycle was determined and plotted against cycle number in Fig. 5.15. The logarithmic decrement, δ, was obtained by regression analysis from which the FVD damping ratio of the specimen was then computed using Eq. 3.42.

The damping ratio was also computed using the HPP method. Fig. 5.11 presents half power frequencies f_1, f_2, from which the HPP damping ratio could be determined. Through calibration (see Section 3.4.2), the inherent apparatus damping ratio varying with resonant frequency was interpolated. This value was subtracted from the measured (system) damping ratio to give the material damping ratio of the specimen. Fig. 5.16 presents the typical damping ratios at various shear strains for the specimen obtained by both the HPP and the FVD method.

5.7.4 Problems of measuring damping ratio

As was shown in Section 3.4.2 material damping at low shear strain can be affected by the inherent noise of the system. Fig. 5.17 shows that the root mean squared (RMS) amplitude of the noise, $V_{RMS.noise}$, produced by the RCA varied from $18 - 20mV$. If the peak RMS amplitude, $V_{RMS.peak}$, is less than $\sqrt{2} * V_{RMS.noise} = 28mV$, the half power bandwidth frequencies f_1 and f_2 (where the vibration amplitude is equal to 0.717 times the peak RMS amplitude) could not be determined as they would fall with the value of the noise as shown in Fig. 5.18a. It can also be seen in Fig. 5.18b that the relatively high noise amplitude also significantly affects the FVD signal. Therefore, the damping ratio of the specimen cannot be precisely estimated using either the HPP or the FVD method, if $V_{RMS.peak}$ is less than 28mV. It was shown (see Eq. 3.48, Section 3.3.5) that the shear strain is a function of the resonant frequency and the peak RMS. Eq. 3.48 shows that the damping ratio cannot be measured below a strain level given by:

$$\bar{\gamma}(\%) < 111.05 \times \frac{0.028}{{f_r}^2}\frac{d}{L} = \frac{1.6}{{f_r}^2} \tag{5.2}$$

where the ratio d/L is approximately 0.5. In addition, the calibration of equipment damping reported in Section 3.4.2 suggests that the noise significantly affects the measured damping ratio if $RMS_{peak} < (5\ to\ 6) \times RMS_{Noise} = 100$mV. This condition is equivalent to:

$$\bar{\gamma}(\%) < 111.05 \times \frac{0.1}{{f_r}^2}\frac{d}{L} = \frac{5.6}{{f_r}^2} \tag{5.3}$$

The two expressions are plotted in Fig. 5.19, showing that only in zone 3, where $\bar{\gamma}(\%) > 5.6/{f_r}^2$, is the measured damping ratio reasonably unaffected by the noise. Therefore, to avoid the influence of the noise, only damping ratios estimated in zone 3 are taken as valid measurements.

It was observed that the automatic measurement of damping ratio using the FVD method may be underestimated. After the steady state of vibration (at resonant frequency) is obtained, the power to the coils is immediately cut off. The software then records a free vibration decay waveform, filters the signal, determines the amplitude of each cycle, and then computes the FVD damping ratio. However, Fig. 5.20a shows that the recorded waveform sometimes includes a number of cycles with constant vibratory amplitudes, which are automatically taken into the calculation for damping. Consequently, the damping ratio may be underestimated by the software (Fig. 5.20b). Therefore, all of the damping ratios reported in this thesis was double-checked by examining the raw recorded data. Fig. 5.20b shows that the value of damping ratio, which is automatically calculated using the slope of the best fit curve (dashed line) through all the data points (included the steady vibratory amplitudes), was underestimated. The value of damping ratio, which is manually calculated using the slope of the best fit curve (the solid line, Fig. 5.20b) through the data points excluded the steady amplitudes, is more accurately determined.

TABLE 5.1: Material density and void ratio

No	Materials	G_S	γ_{max} (kg/m^3)	γ_{min} (kg/m^3)	e_{min}	e_{max}
1	GB	2.5	1635	1478	0.53	0.69
2	LBSB	2.65	1793	1450	0.48	0.83
3	LBSE	2.65	1631	1317	0.63	1.01
4	Fine Nugget (*)	2.5	1435	1118	1.24	0.74
5	Coarse Glitter (*)	2.5	1448	1061	1.36	0.73
6	Mica	2.85	NA	NA	NA	NA

(*) Data of Reddy (2007).

TABLE 5.2: *Angularity index*, *AI*, of test materials

Material	Roundness index	Angularity index, *AI*	
		This study	Reddy (2007)
GB	0.96	1.04	1.04
LBSB	0.87	1.15	1.24
LBSE	0.79	1.28	NA
Fine Nugget	0.77	1.32	1.38
Coarse Glitter	0.74	1.36	1.44

Note: $AI = p^2/4\pi A$

TABLE 5.3: Shape parameters of test materials

Material	$L/2$ (μm)	$I/2$ (μm)	$S/2$ (μm)	CSF	$SEES$	ψ_O
GB	486	458	438	0.93	0.90	0.94
LBSB	568	440	286	0.57	0.50	0.72
Fine Nugget	1233	862	269	0.26	0.22	0.53
Coarse Glitter	1215	801	118	0.12	0.10	0.39

Note: The value in the table is the average. L,I, and S are the maximum, intermediate and minimum dimensions, respectively; $L \geq I \geq S$. Values of average volume and projected dimensions of particles (L and I) are provided by Reddy (2007).

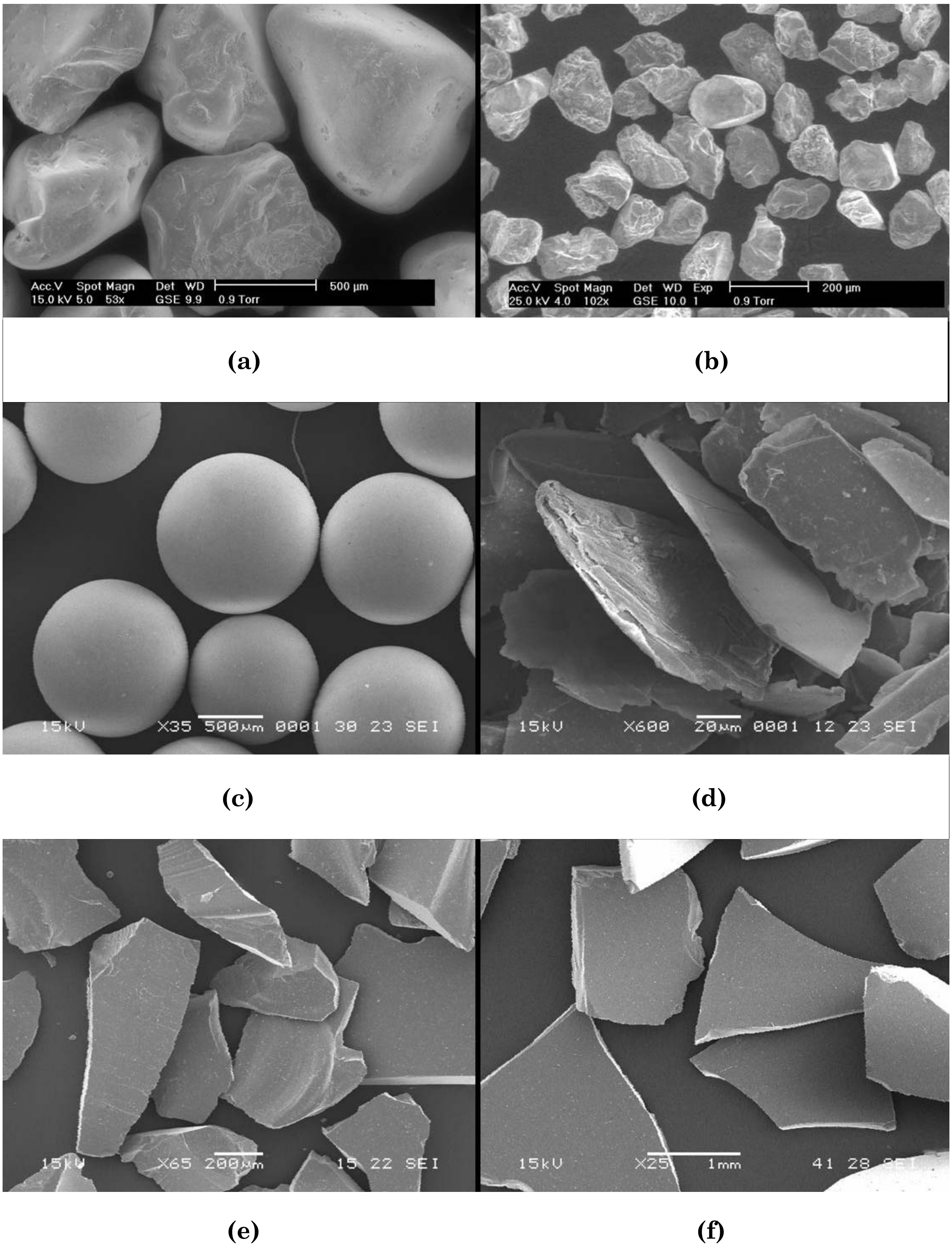

(a) **(b)** **(c)** **(d)** **(e)** **(f)**

Figure 5.1: Scanning electron microscope images of test materials showing differences in particle shape. (a) Leighton Buzzard Sand B (Ming, 2005); (b) Leighton Buzzard Sand E (Clayton *et al.*, 2004); (c) 1.0 mm Glass Ballotini Ming (Ming, 2005); (d) 0.1 mm Mica; (e) Glass Nugget (Reddy, 2008) and (f) Glass Glitter (Reddy, 2008)

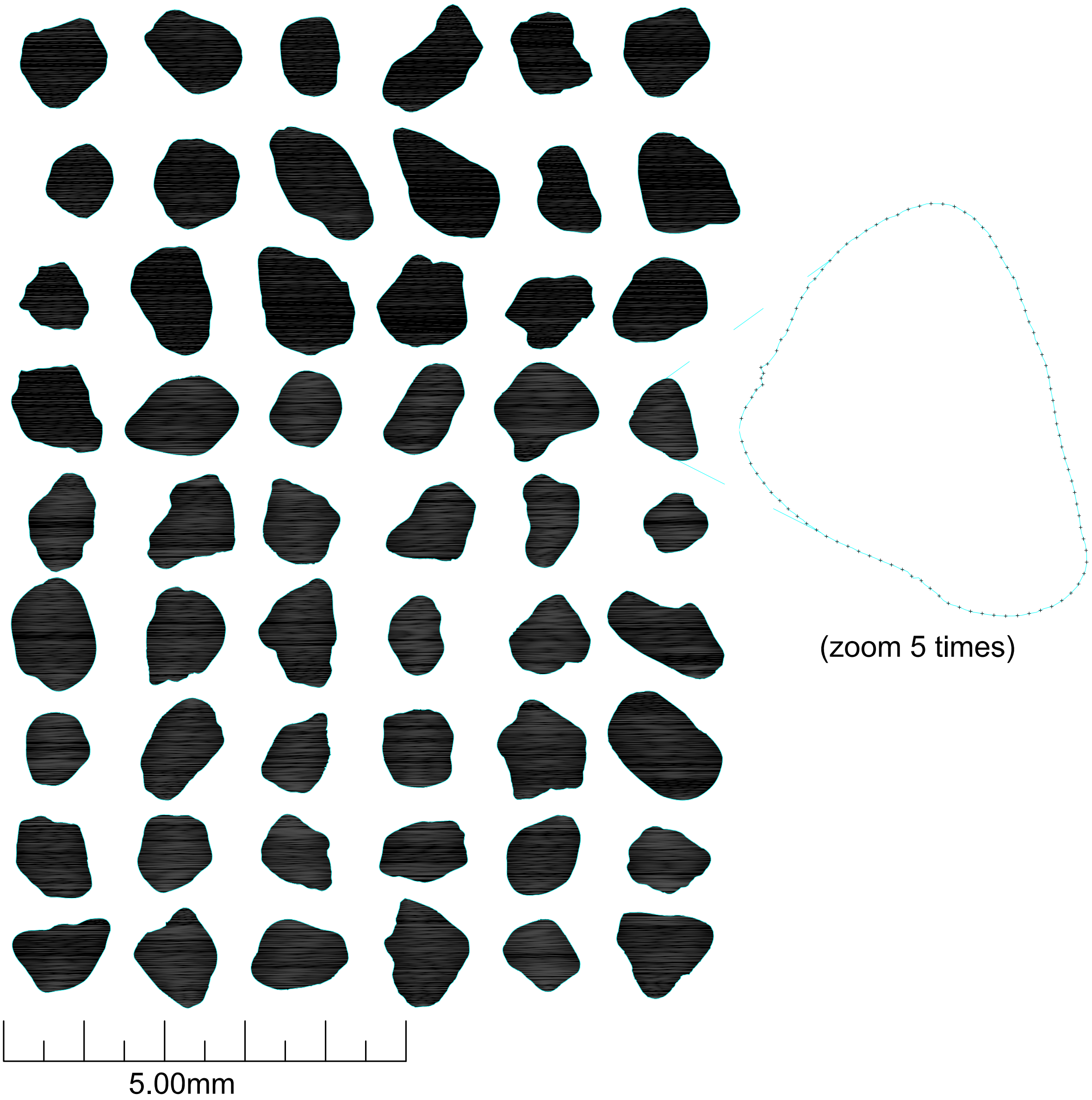

(a) 2D particle outline of Leighton Buzzard Sand B

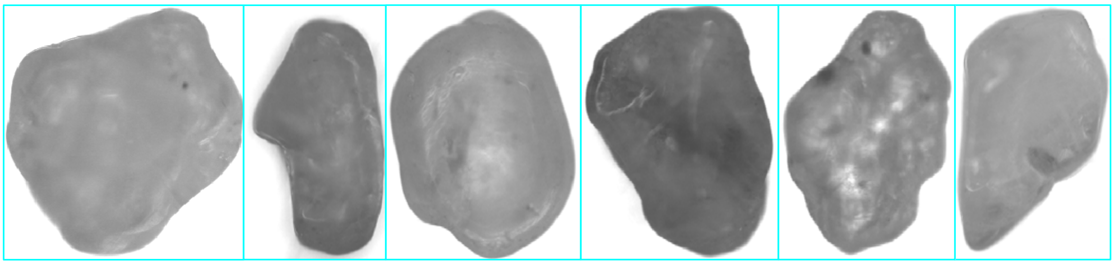

(b) Microscope images (different scale)

FIGURE 5.2: Microscope images of LBSB

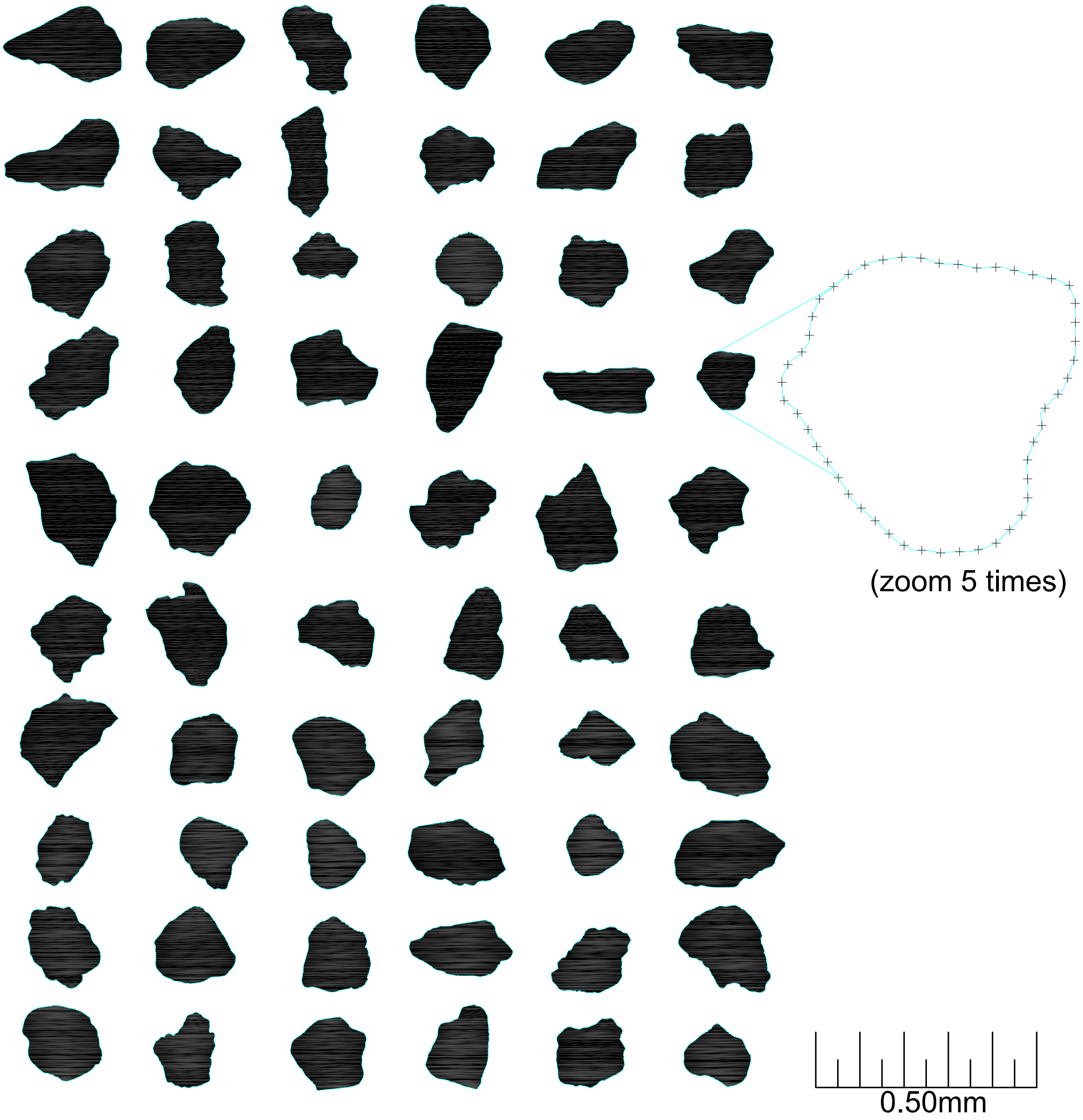

(a) 2D particle outline of Leighton Buzzard Sand E

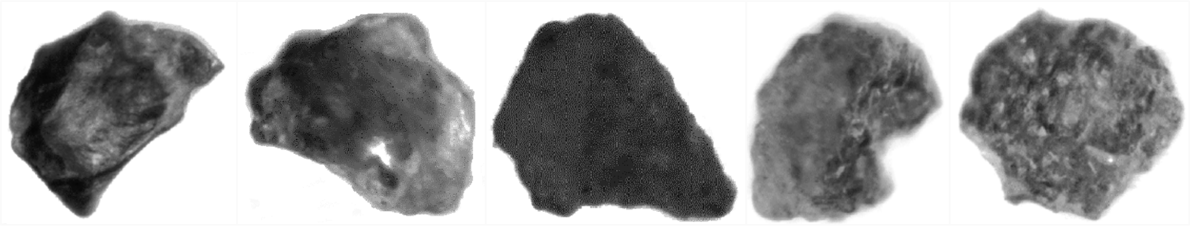

(b) Microscope images (different scale)

FIGURE 5.3: Microscope images of LBSE

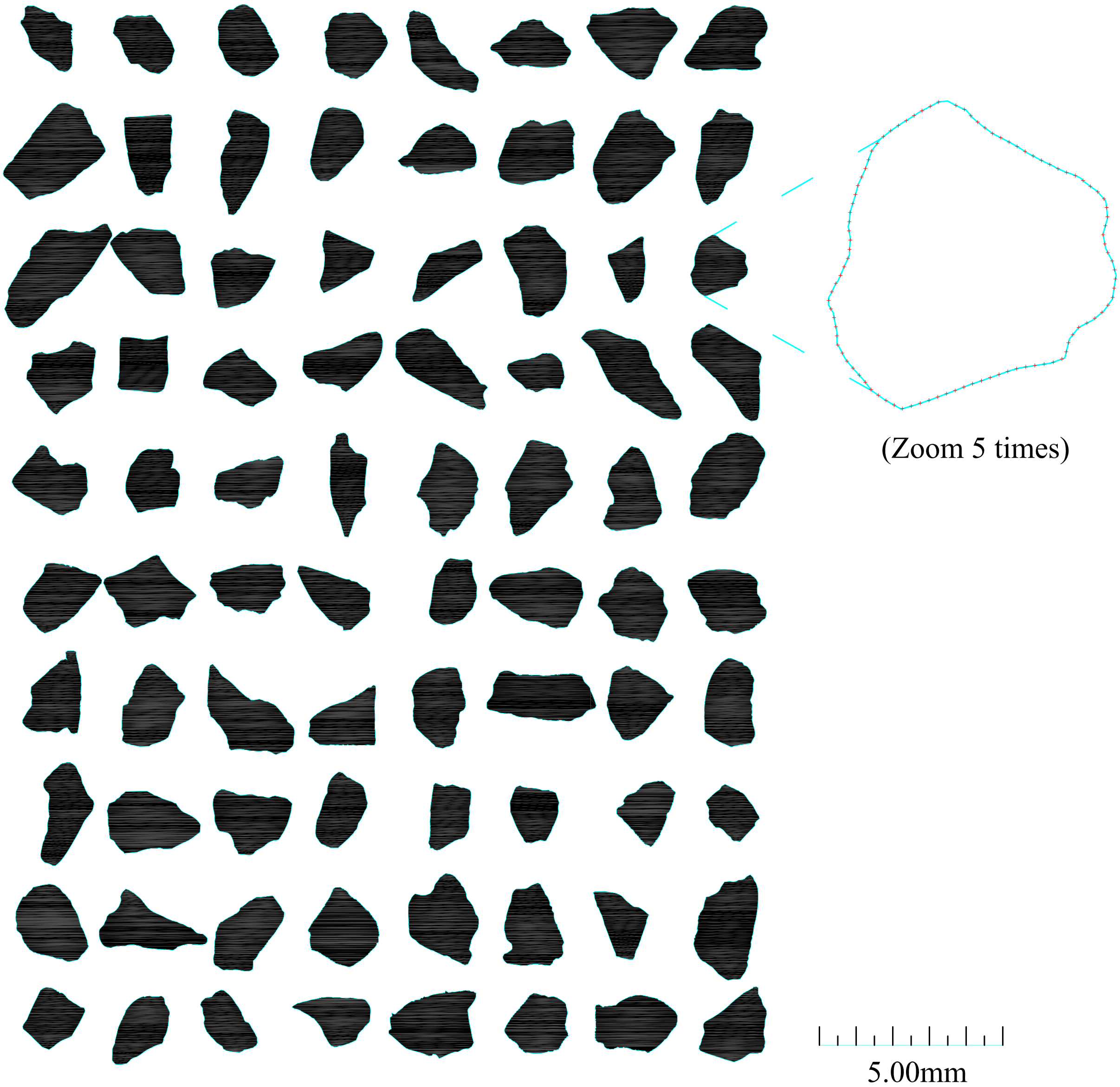

(a) 2D image outline of Nugget

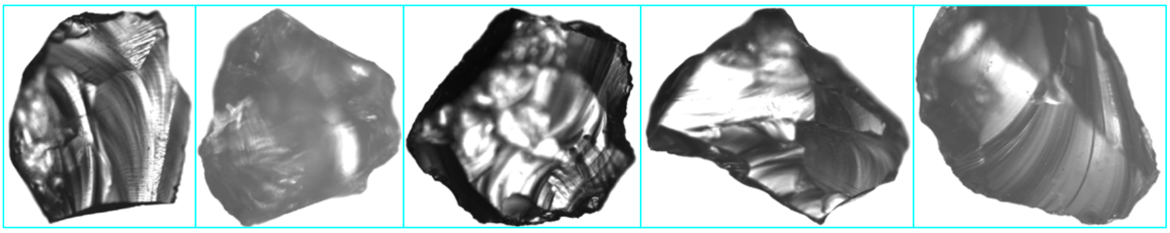

(b) Microscope images (different scale)

FIGURE 5.4: Microscope images of Nugget

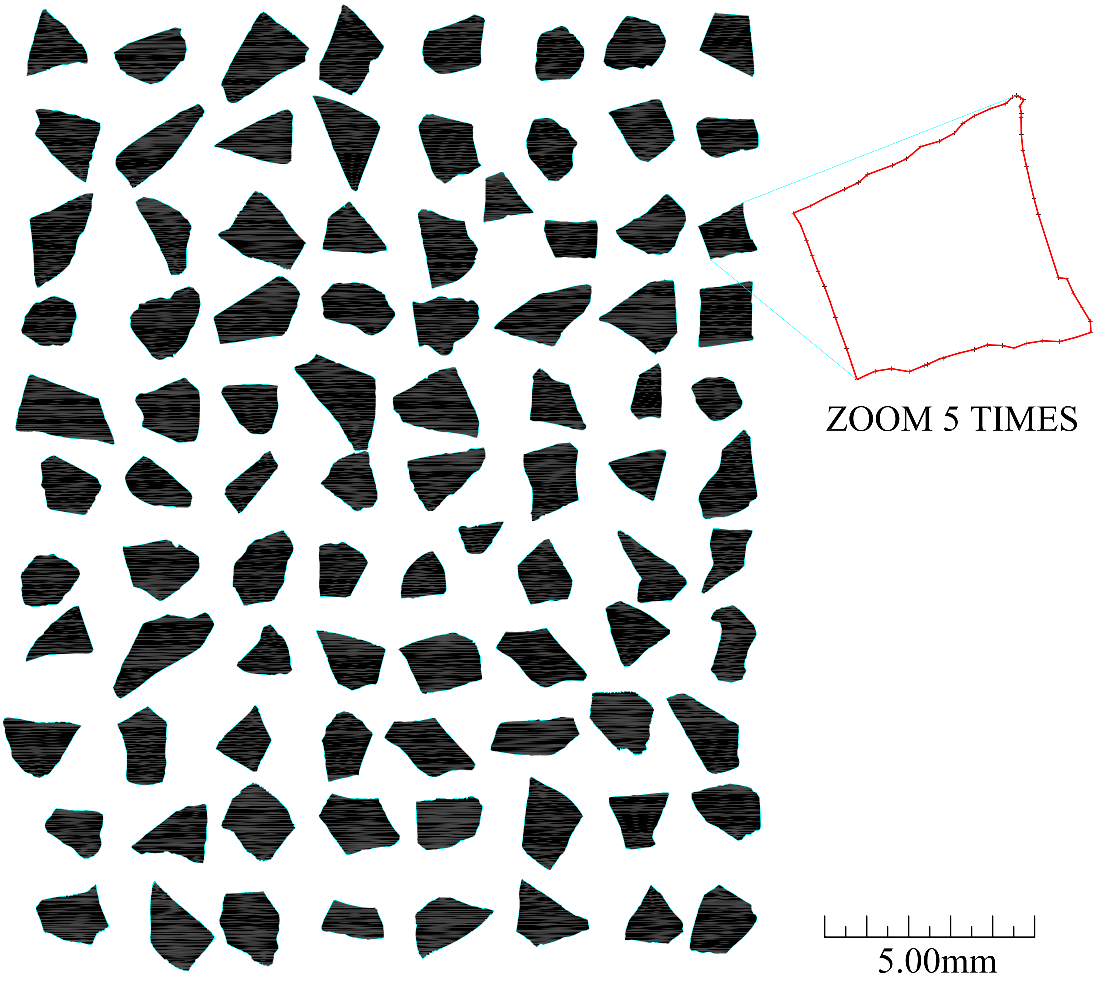

(a) 2D particle outline of glitter

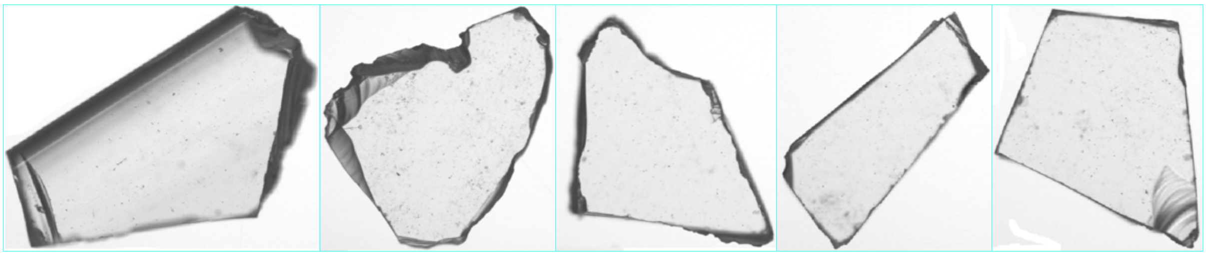

(b) Microscope images (different scale)

FIGURE 5.5: Microscope images of Glitter

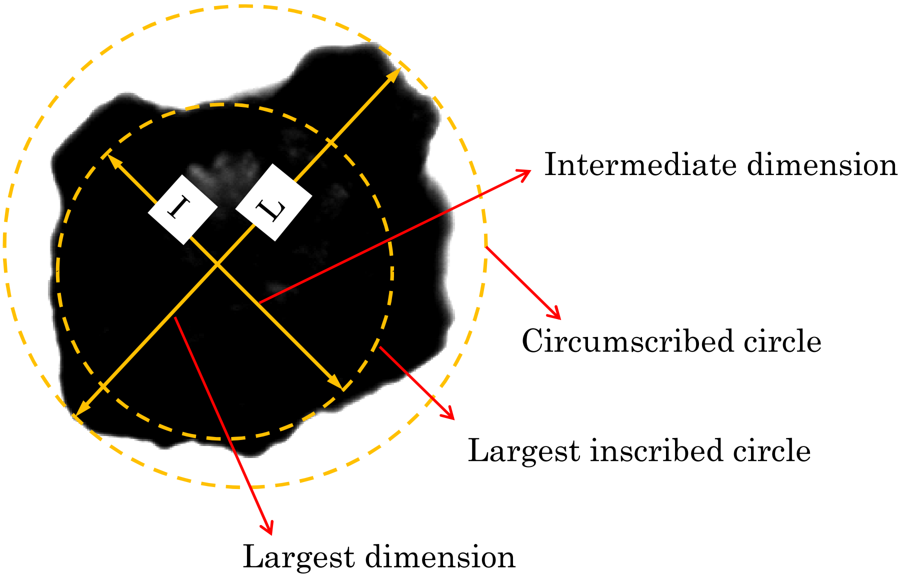

FIGURE 5.6: Determination of largest, L, and intermediate, I, dimensions from 2D particle image in volume method (redrawn after Reddy, 2008)

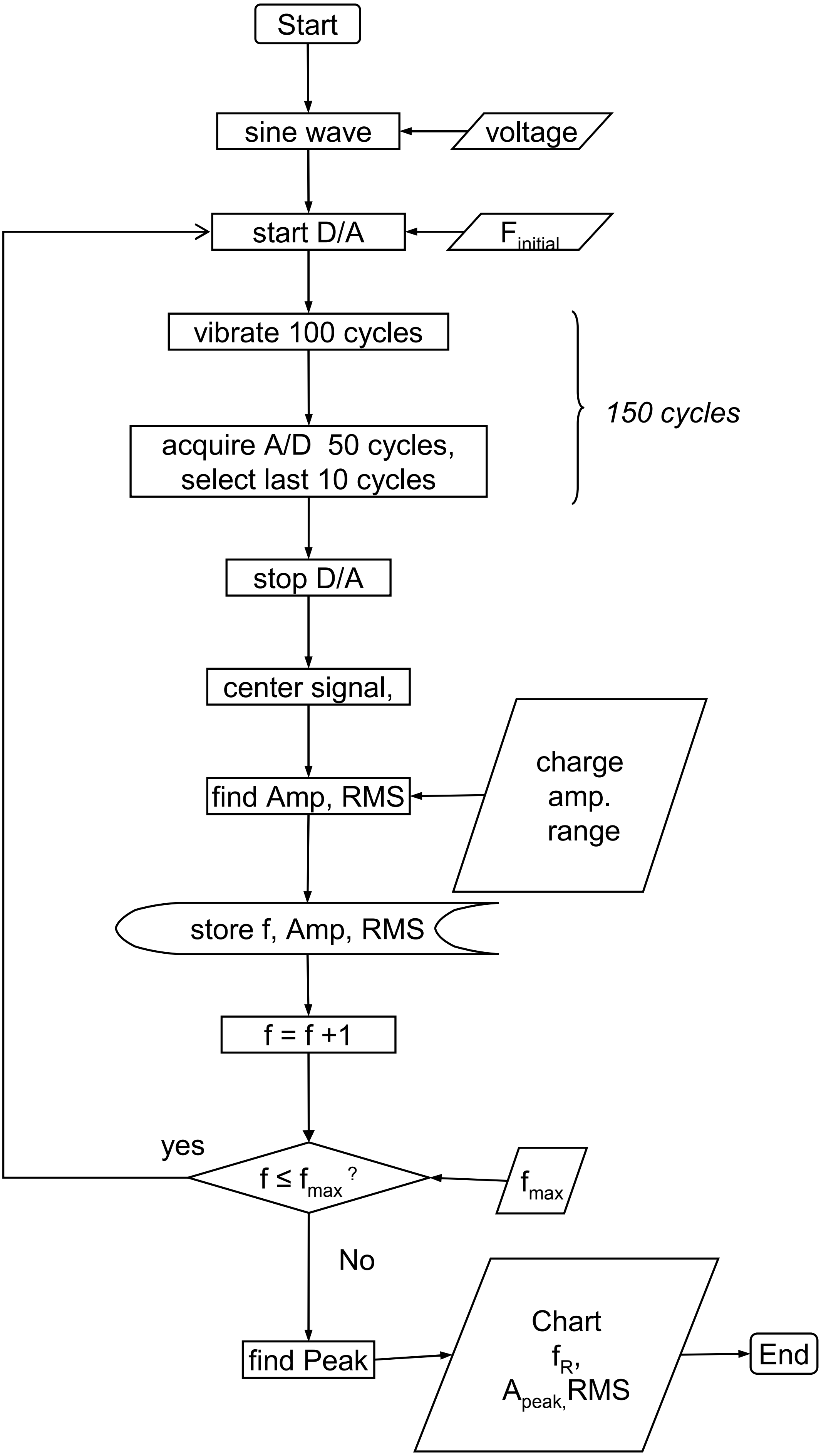

Figure 5.7: Flow chart for broad sweep

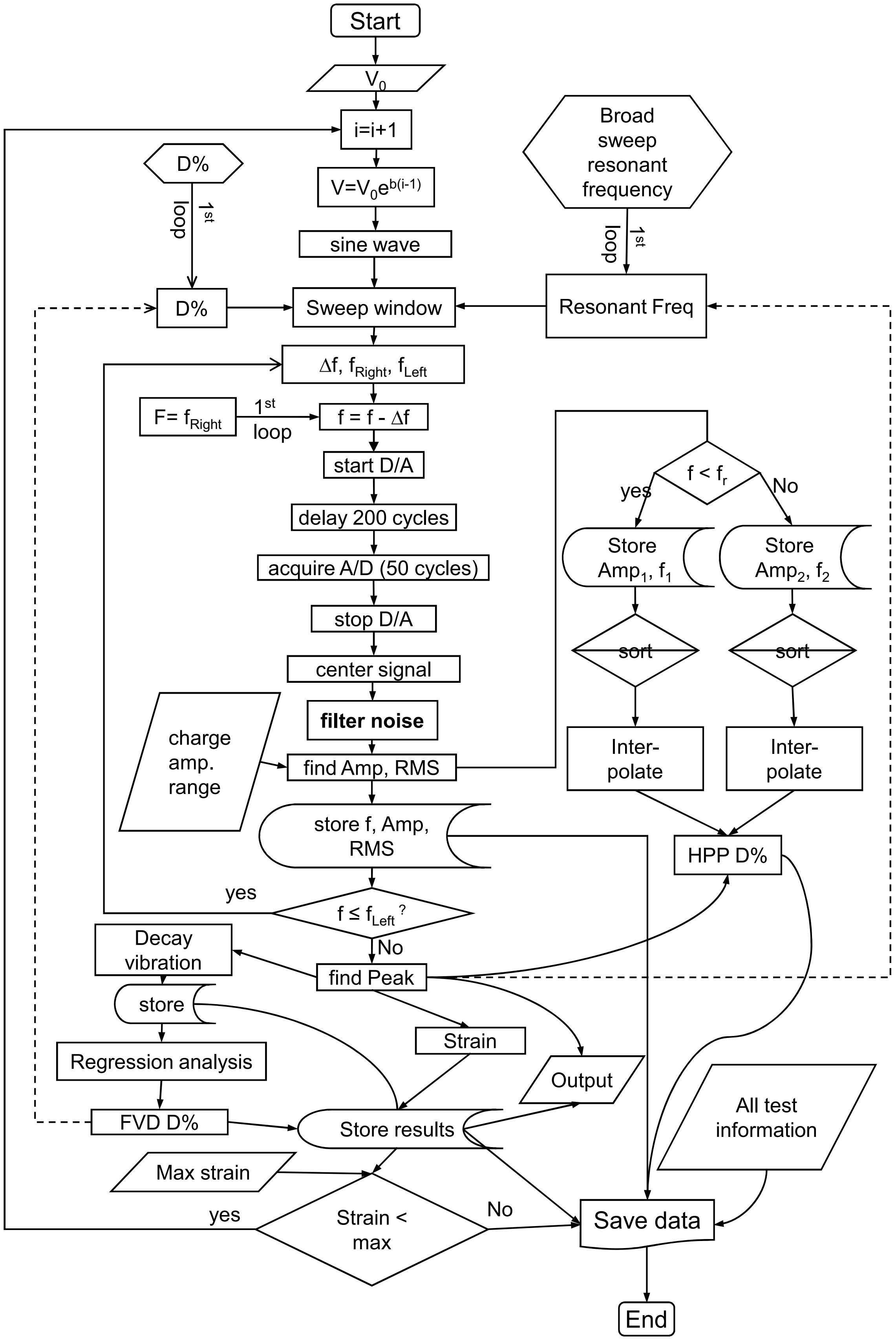

FIGURE 5.8: Flow chart for fine sweep

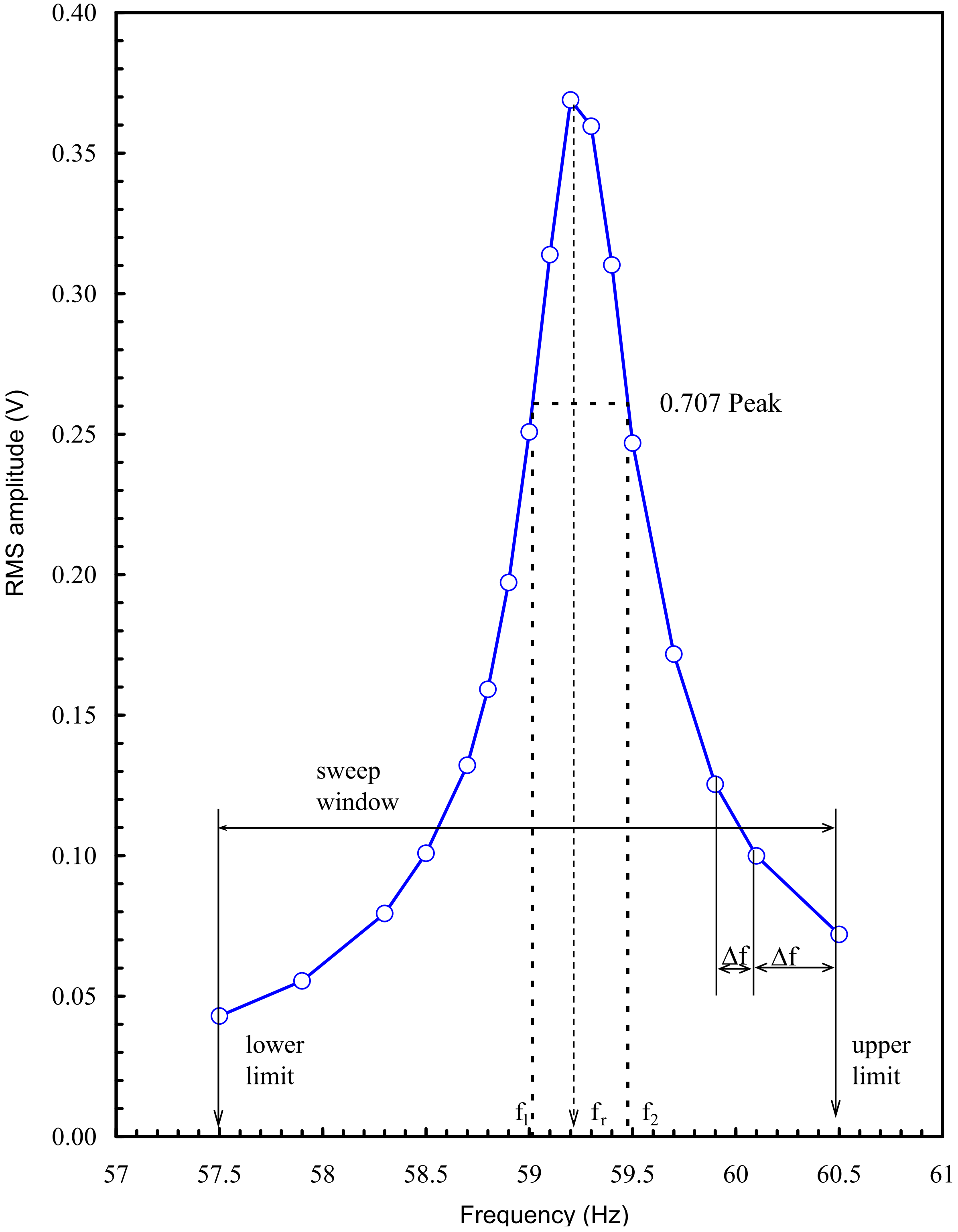

FIGURE 5.9: Response curve of Aluminium bar No 1

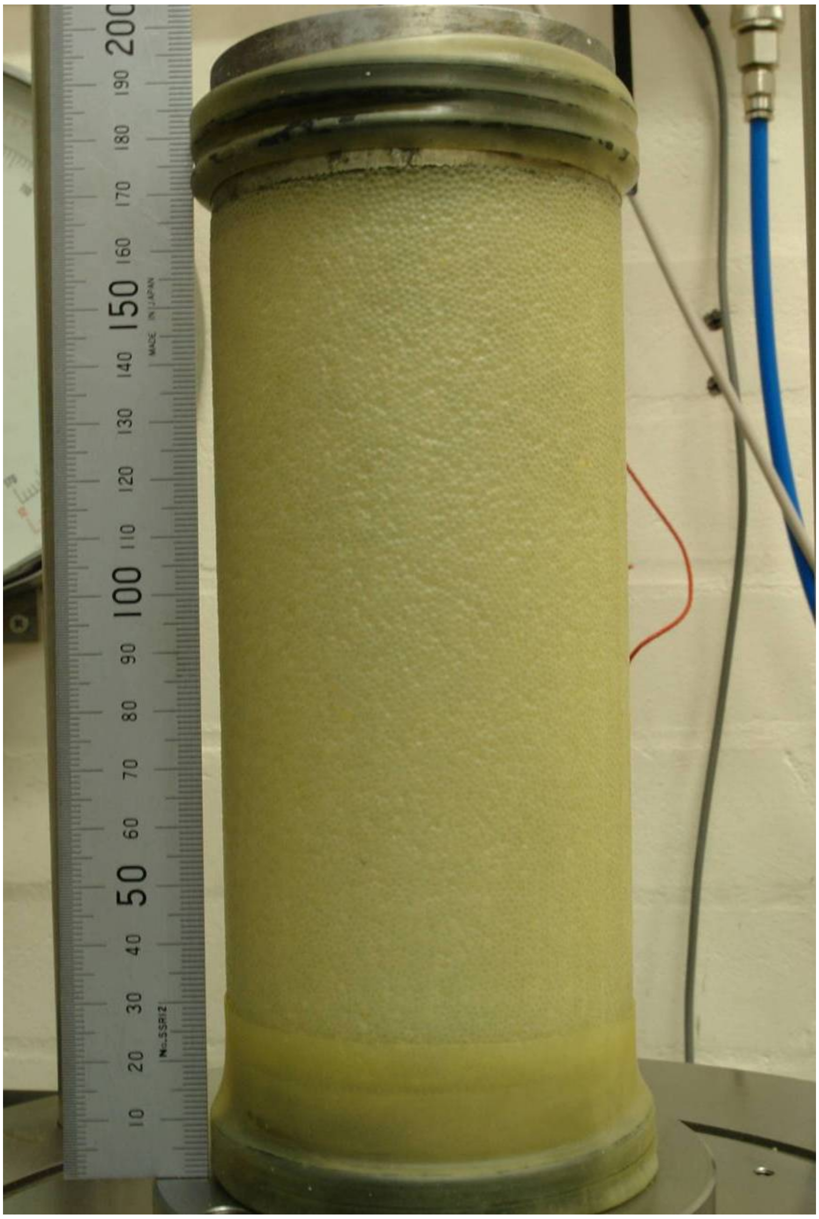

Figure 5.10: Right cylindrical shape of a 1.0mm Glass Ballotini specimen

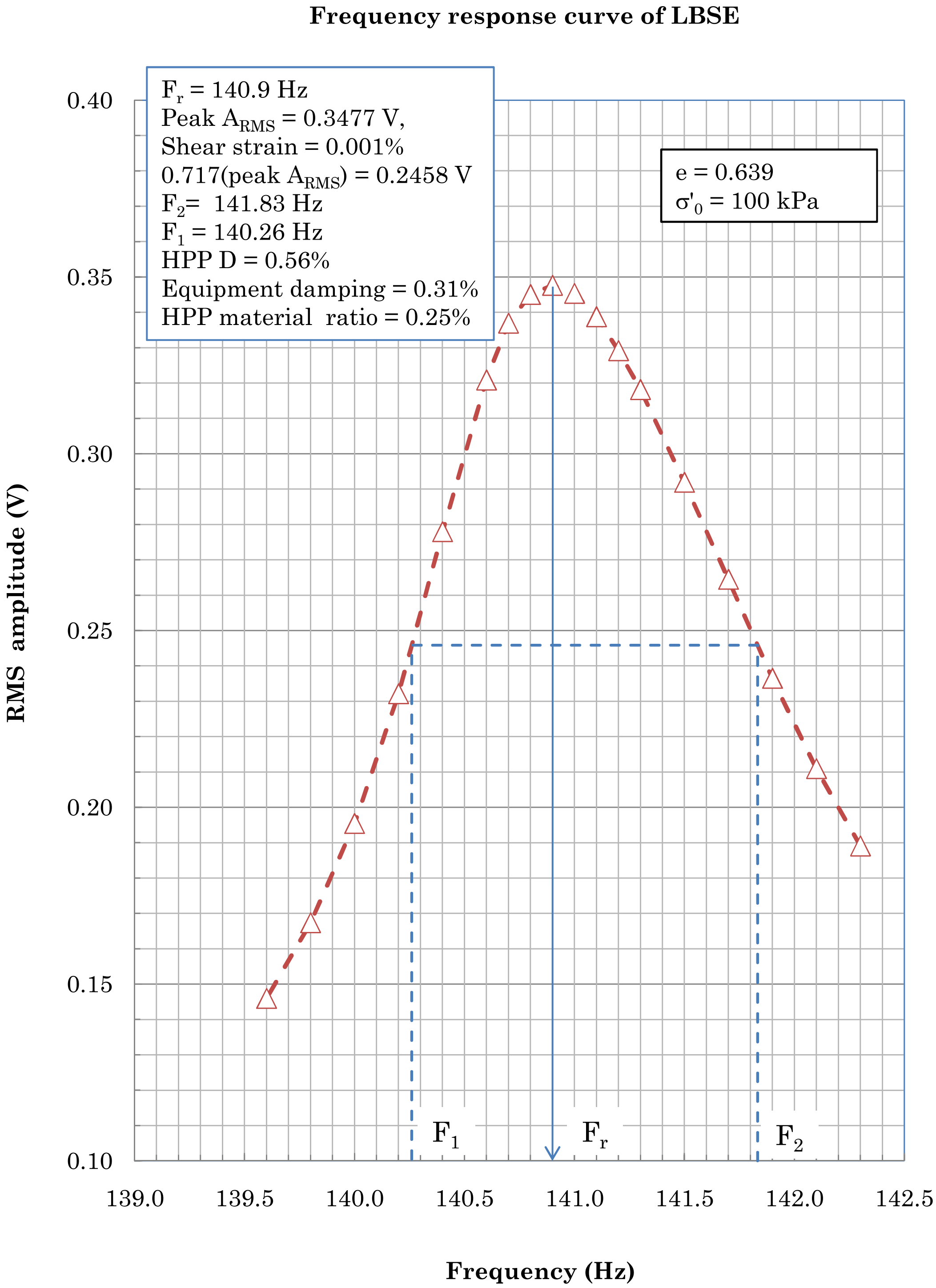

FIGURE 5.11: Typical frequency response curve of LBSE

(a) Shear modulus of LBSE

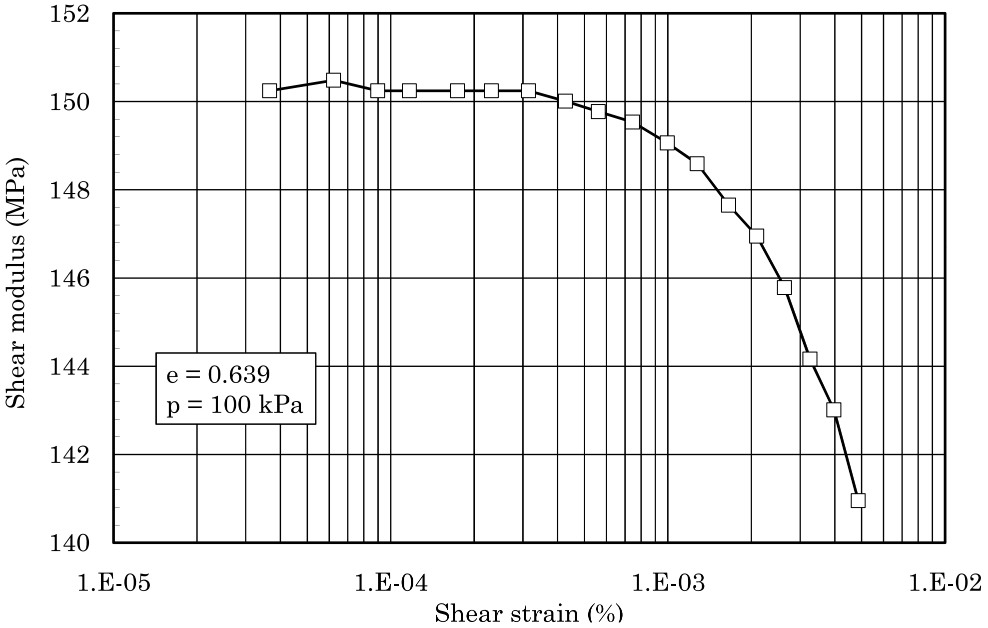

(b) Normalised shear modulus of LBSE

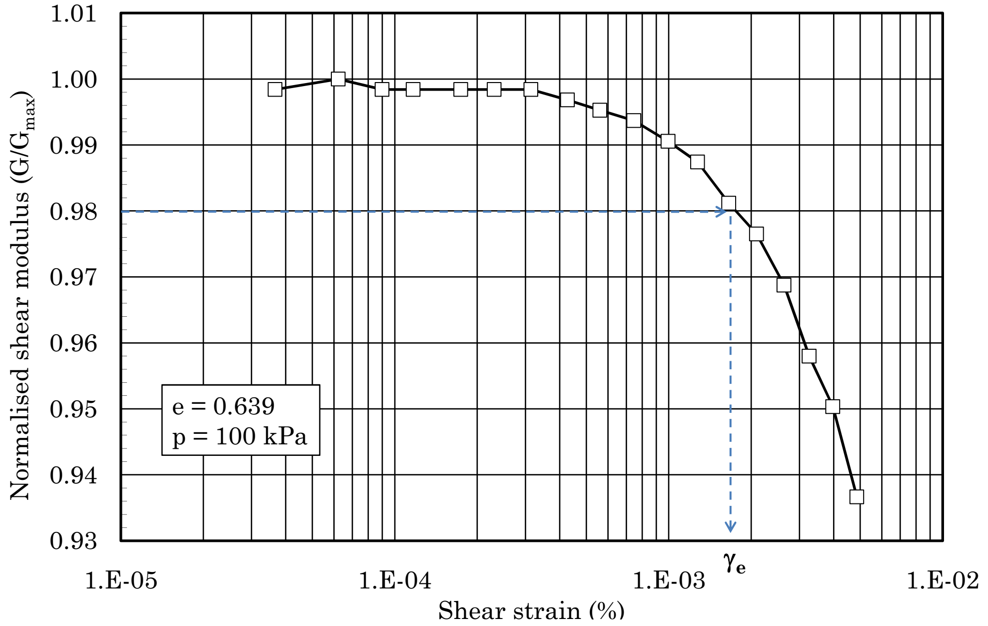

FIGURE 5.12: Typical shear modulus versus shear strain of LBSE

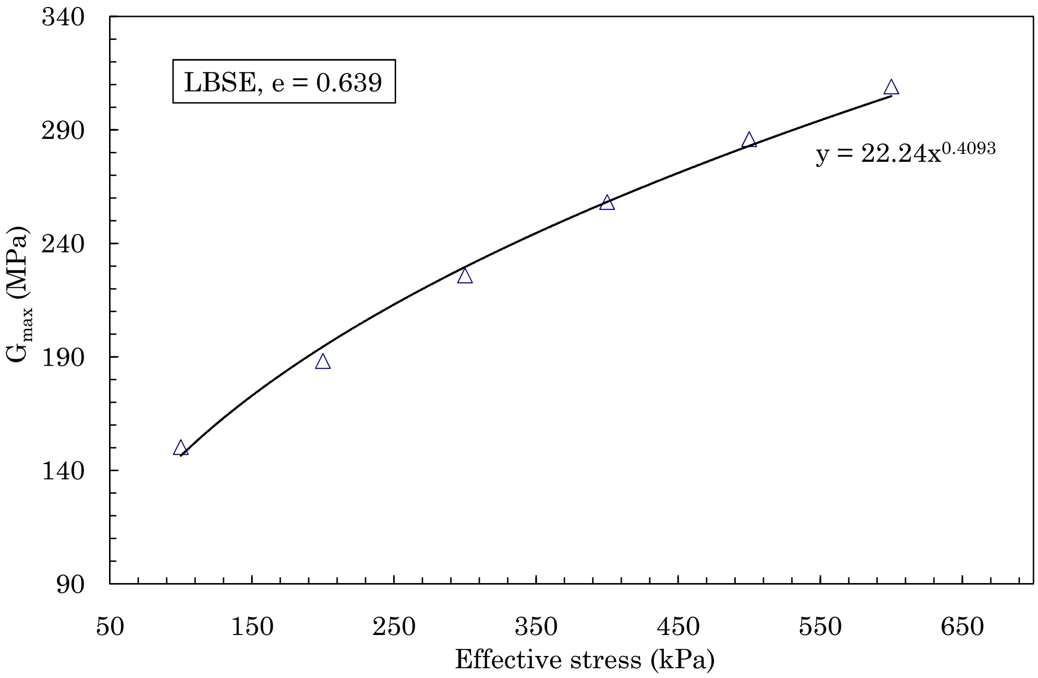

Figure 5.13: G_{max} of LBSE as a function of effective stress

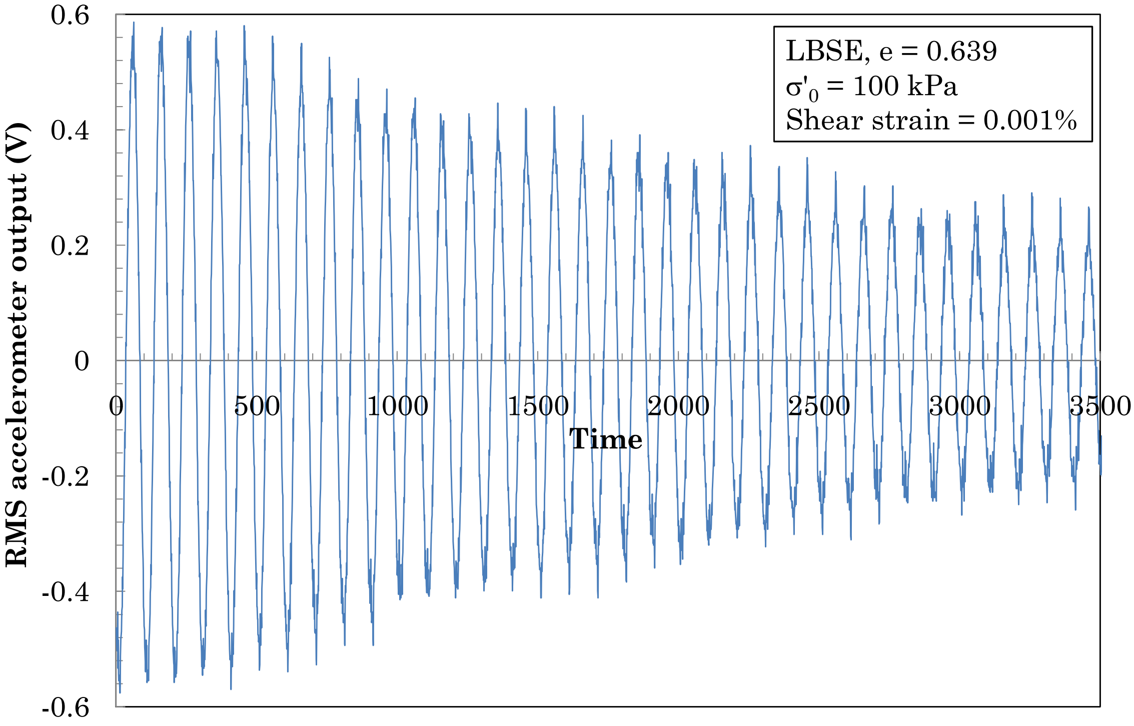

FIGURE 5.14: Typical FVD curve for LBSE

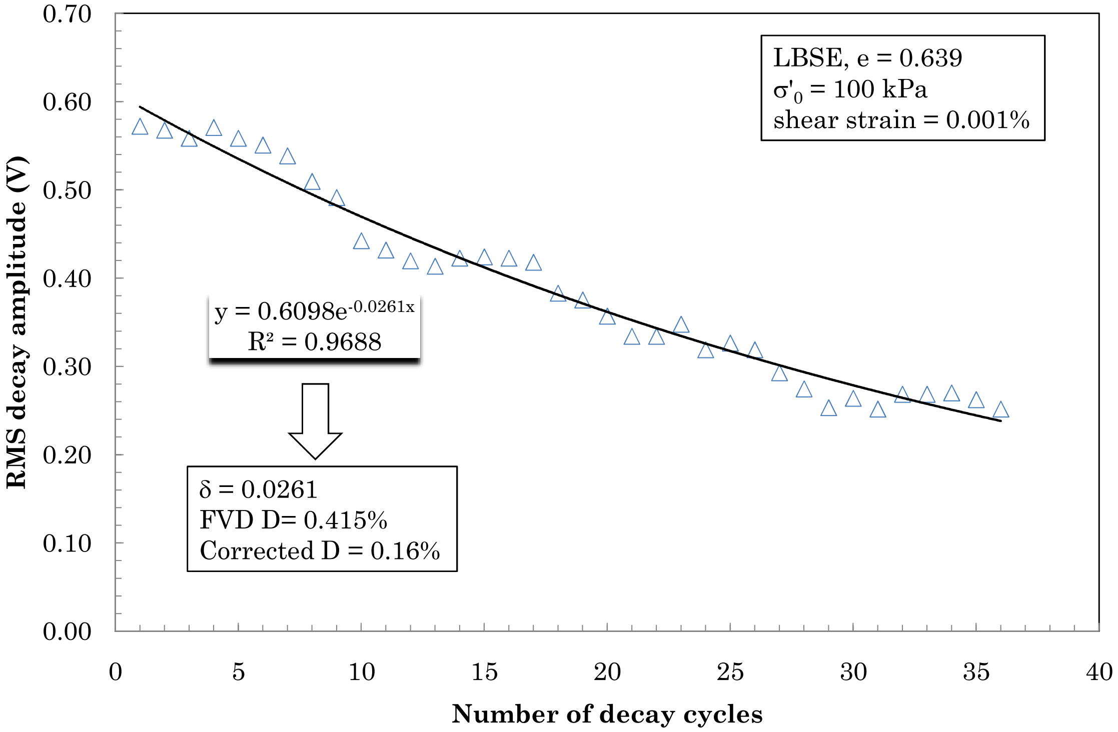

FIGURE 5.15: Plot *RMS* amplitude versus number of cycles obtained from Fig. 5.14

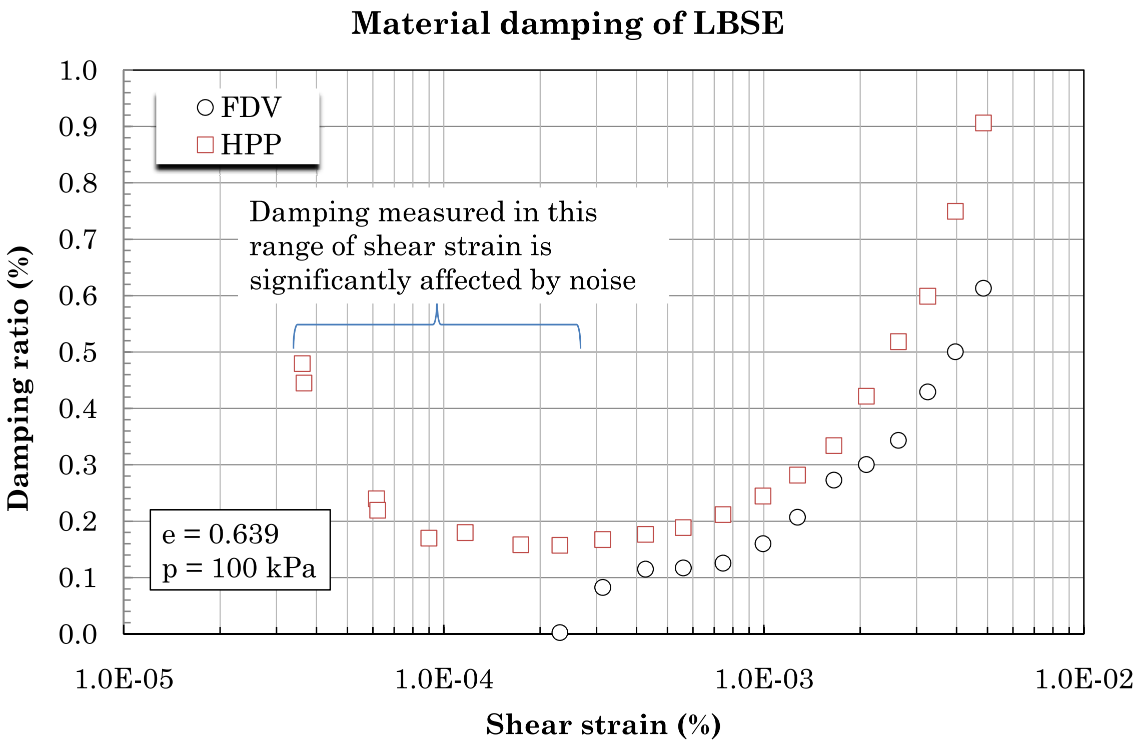

FIGURE 5.16: Damping ratio of LBSE determined using the HPP and the FVD method

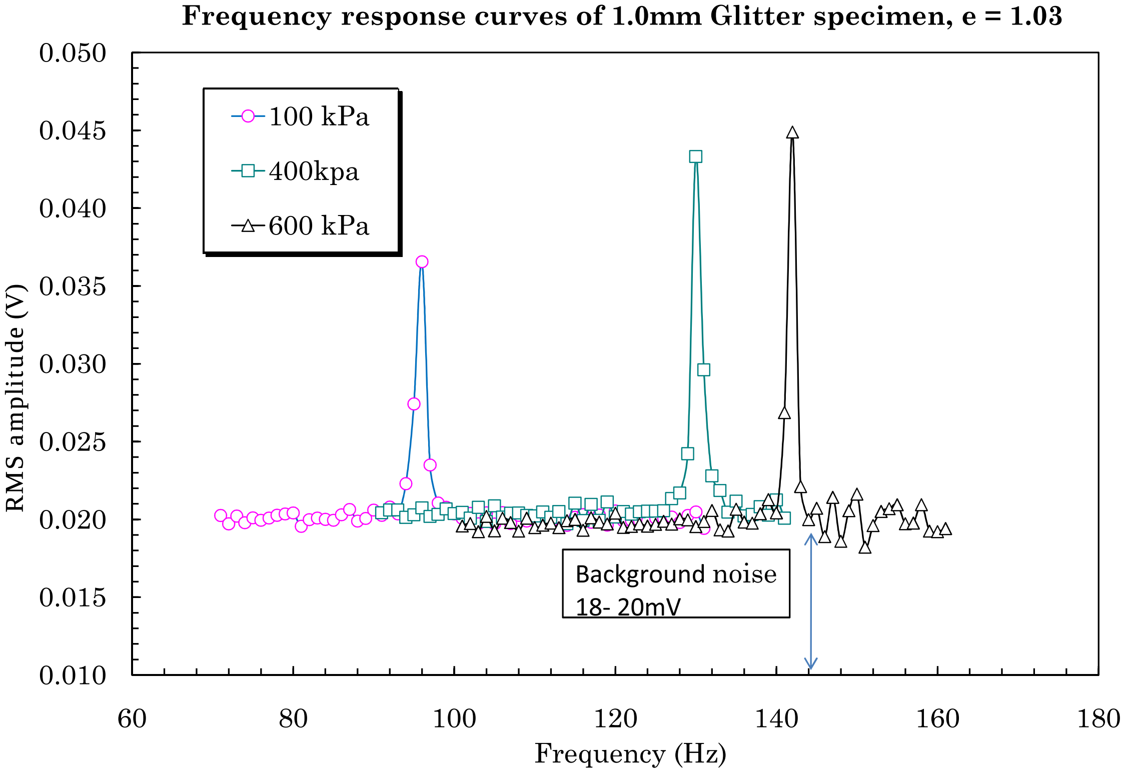

FIGURE 5.17: Noise amplitude produced by the RCA

(a) Frequency response curve at low amplitude

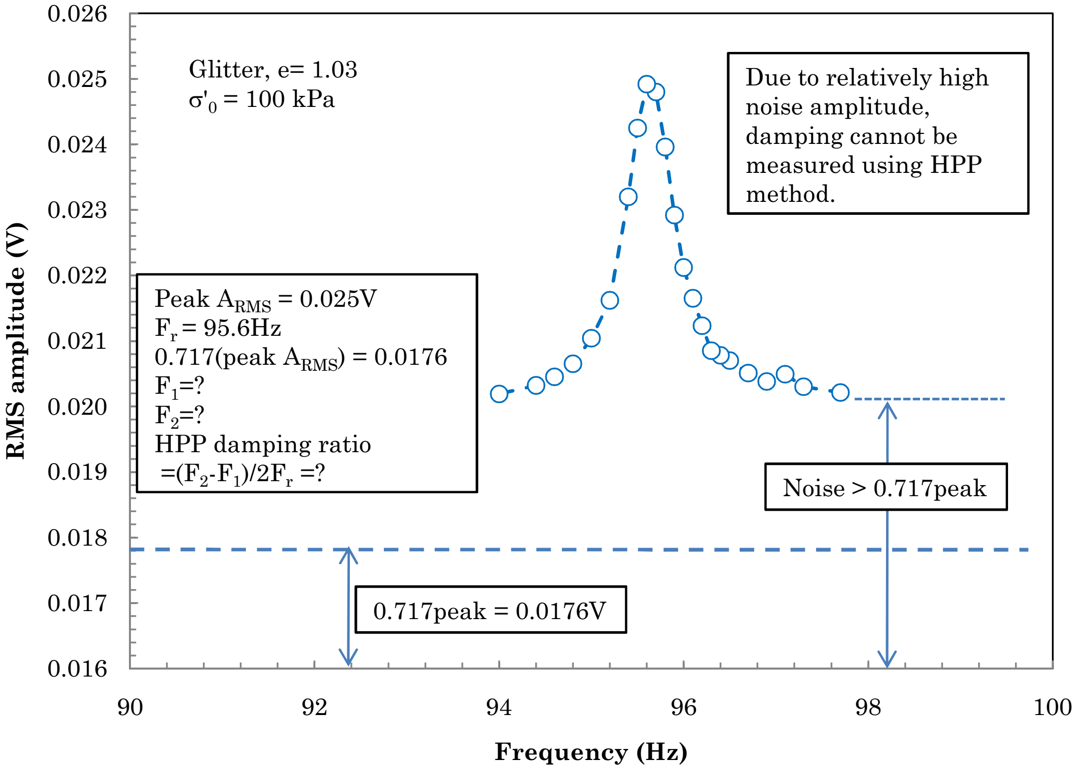

(b) '*Decay*' filtered signal at low amplitude

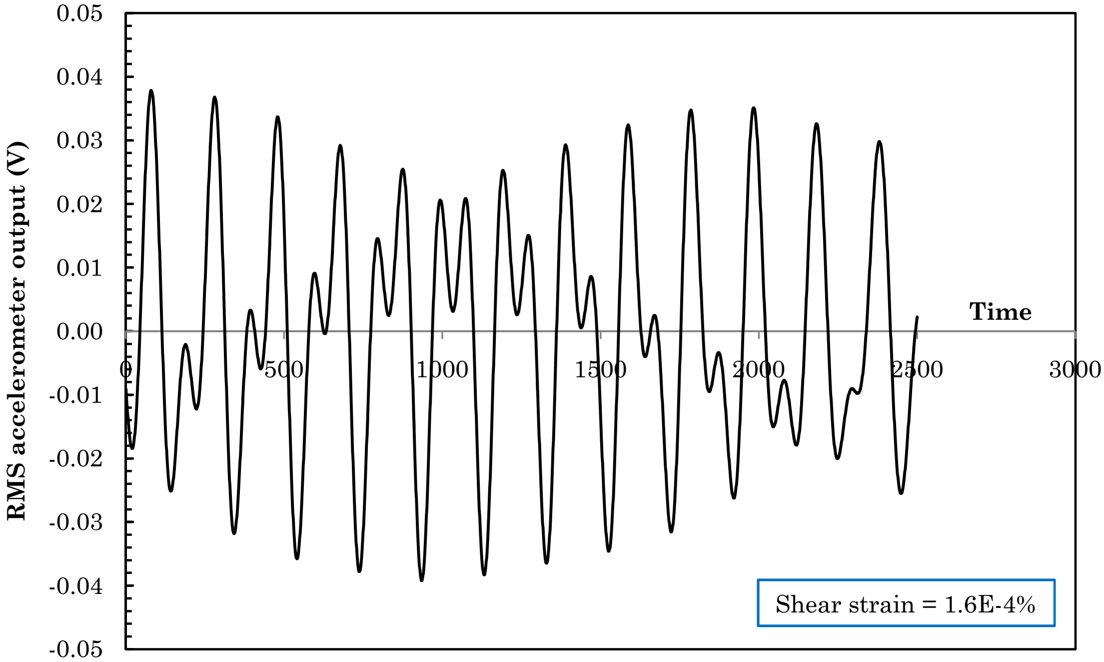

FIGURE 5.18: Effect of noise on damping measurement at low strain

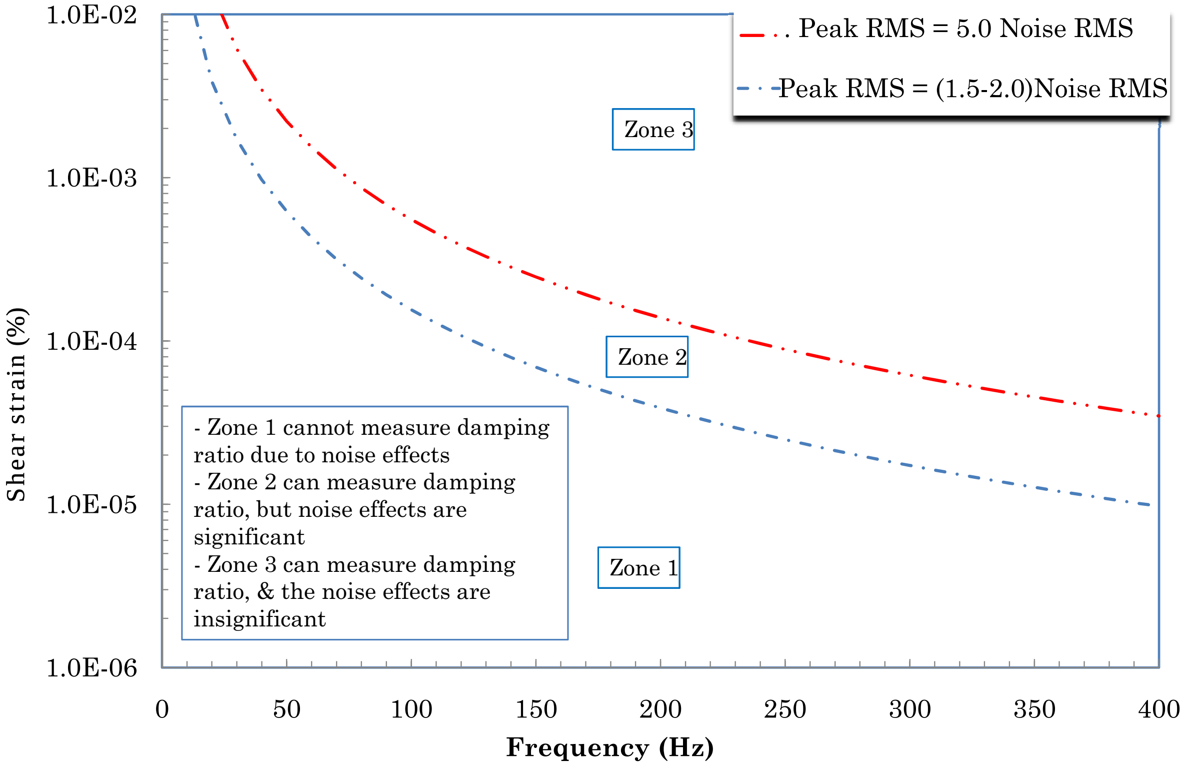

FIGURE 5.19: Zones of noise effect

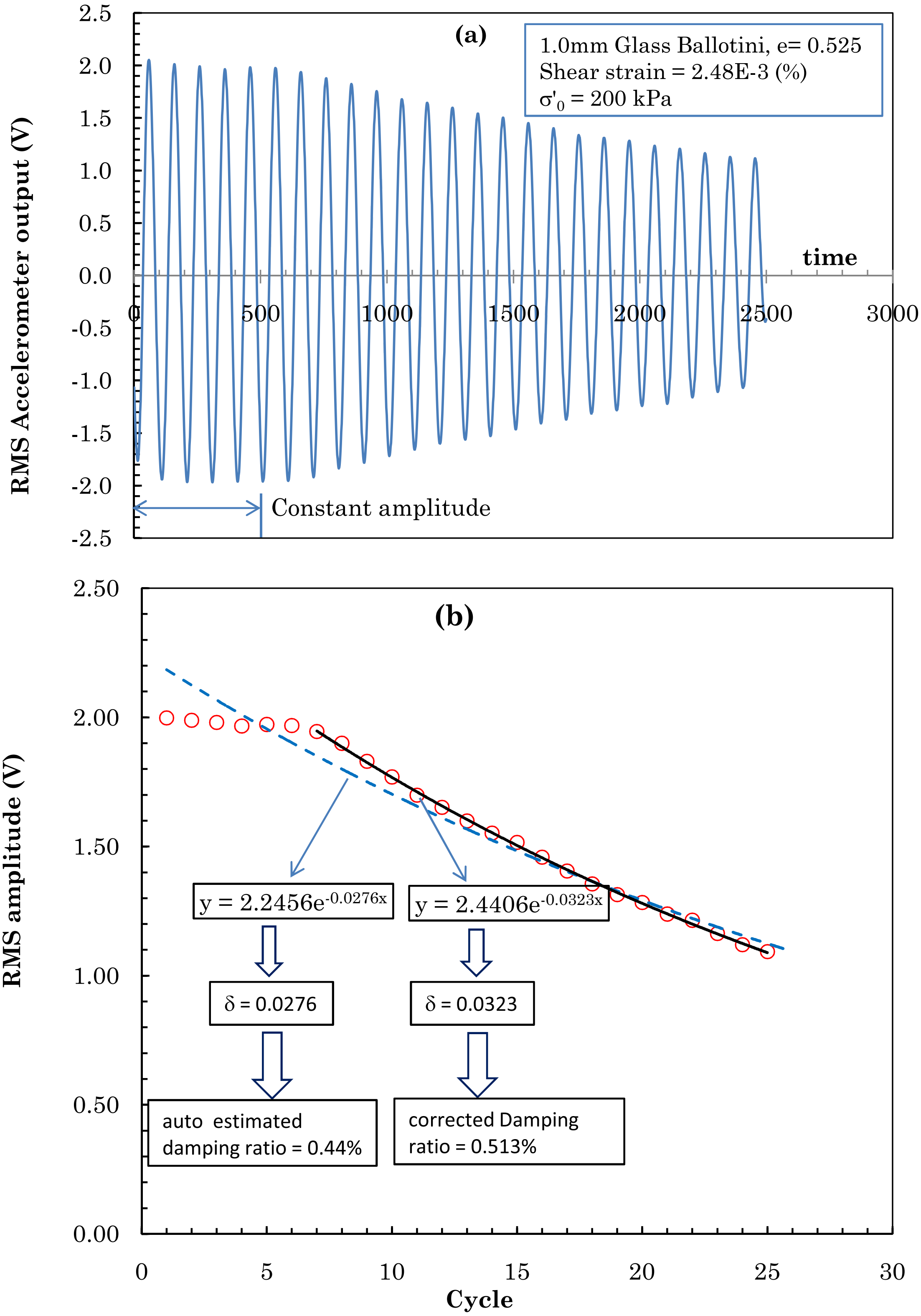

FIGURE 5.20: Checking and correcting damping ratio estimated automatically by the software. (a) FVD curve obtained automatically using the computer software; (b) Automatic and manual calculation of damping ratio based on plot of peak decay amplitude per cycle

Chapter 6

Results and discussions

This chapter discusses the results obtained from tests on the granular materials (highlighted in Chapter 5) under different testing conditions such as void ratio, effect stress, and shear strain. The first section of this chapter presents the general small strain behaviour of the test materials, such as shear modulus and damping ratio as a function of shear strain, effective stress and void ratio. The first section sets the context for the second and the third section to highlight and discuss effects of particle characteristics on G_{max}, shear modulus degradation, stress exponent, elastic threshold strain, and damping of the materials, etc. The discussion of the effects of particle size and particle shape are presented in separate sections, and the effects of particle characteristics on the small strain behaviour of geomaterials are viewed taking into account the effects of void ratio. Finally, a soil model termed the porous discontinuous-solid model, in which the shear wave velocity at contacts between particles is emphasised, is proposed[1] to explain the effects of particle size and shape on the small strain response of the geomaterials. Based on the porous discontinuous-solid model, the theoretical (universal) void ratio functions for V_s and G_{max} are derived.

6.1 Small strain behaviour of the materials

6.1.1 Shear modulus - shear strain relationship

The values of normalised shear modulus (G/G_{max}) as a function of shear strain for each material at $\sigma' = 100kPa$ were presented in Fig. 6.1. It can be seen that for all specimens there are regions where the normalised shear modulus are somewhat independent of shear strain, as shown by the stiffness plateaux ($G/G_{max} \approx 1.0$). In general, the elastic threshold strain, γ_e, for each material is dependent on void ratio (or relative density) and effective stress. This agrees with the observations of other researchers such as Hardin & Drnevich (1972*b*); Kokusho *et al.* (1982); Shibuya & Tanaka (1996); Lo Presti *et al.* (1997) and Stokoe *et al.* (1999).

It is observed that γ_e increases with an increase in effective stress. It is also observed that,

---

[1] Due to the limitation of the study time and volume of the thesis, only the main concepts and fundamental equations of the model are presented. The model will be reported in detail in another publication.

in general, γ_e decreases with an increase in void ratio. The values of γ_e for all materials at different level of effective stress and void ratio were summarised in Table 6.2. It can be seen from Table 6.2 that, in general, the elastic threshold strain, γ_e, for platy particles (i.e. Glitter and Nugget) are significantly larger than that for the bulky particles. Further discussions on the influence of particle shape on γ_e are presented in Section 6.3

For all the materials tested, when shear strain induced in a specimen exceeds γ_e, the shear modulus of the specimen starts to decrease. It can be seen in Fig. 6.1 that stiffness degradation, the ratio of G at a certain shear strain level to G_{max}, for Nugget and Glitter are the lowest among the materials (significantly less than that for LBSB, LBSE, and GB), although the void ratios of Nugget and Glitter are relatively high. At a shear strain of 0.004%, G/G_{max} for Nugget and Glitter are about 96-97% (Table 6.3). In contrast, G/G_{max} for a dense 1.0 mm GB specimen at the same shear strain is only 92%.

6.1.2 G_{max} as a function of effective stress

Fig. 6.5 presents G_{max} of test materials as a function of effective stress. It is noted that the figure presents the results for specimens with similar void ratio (from 0.6 to 0.8). The results presented in Fig. 6.5 show that G_{max} increases in an exponential manner with effective stress:

$$G_{max} = \alpha_0 {\sigma'_0}^n \tag{6.1}$$

where α_0 can be termed *material coefficient*, which is a function of particle characteristics and void ratio. Both α_0 and n were obtained from the best fit curves (Fig. 6.5) applied to the data for each specimen. The results, summarised in Table 6.1, show that stress exponents during loading varies from 0.403 to 0.488, with an average value of 0.439. During unloading stress exponents are somewhat higher than those during loading. The stress exponents obtained in this research fall within the range of stress exponents obtained by other researchers (from 0.4 to 0.62, see Table 2.1).

In addition, the data in Table 6.1 indicate that stress exponents for the platy particles (i.e. Nugget and Glitter) are higher than those for bulky particles (i.e. GB, LBSB, and LBSE). This may be attributed to either particle characteristics or differences in void ratio between the platy and the rotund specimens. It could be hypothesised that the platy particles may be crushed during loading at relatively high pressure, hence significantly reducing void ratio and consequently causing an increase in stress exponent. Considering values of α_0 for a single material, it can be seen in Table 6.1 that α_0 decreases with an increase in void ratio. Effects of particle characteristics on stress exponent and α_0 will be explored and presented in Section 6.3.

6.1.3 G_{max} as a function of void ratio

Fig. 6.6 presents G_{max} of all materials at an effective stress of 100 kPa versus specimen void ratio. The figure shows that G_{max} decreases with increasing void ratio. In addition, the figure indicates that G_{max} of the materials can be fitted with Eq. 2.2 (Hardin &

Blandford, 1989; Jamiolkowski *et al.*, 1995; Stokoe *et al.*, 1999):

$$G_{max} = \alpha_0 {\sigma'_0}^n = C_p \times F(e) \times {\sigma_r}^{1-n} \times {\sigma'_0}^n \ (MPa) \tag{6.2}$$

where C_p can be termed *particle characteristic coefficient*, which is dependent on particle characteristics (e.g. specific gravity, size, and shape), cementation/ bonding, OCR etc., $\sigma'_0 = 100kPa$, $\sigma_r = 1.0kPa$, $n = 0.5$ is a stress exponent, and $F(e)$ is a void ratio function of the form:

$$F(e) = (1+e)^{-3} \tag{6.3}$$

Eq. 6.3 is derived from a theoretical model termed porous discontinuous-solid model developed by the author (see more details in the Section 6.4). The form of Eq. 6.3 is similar to Shibuya's empirical equation, $F(e) = (1+e)^{-2.4}$, which was derived from a regression analysis, and reported to be applicable to geomaterials with a wide range of void ratio (Shibuya *et al.*, 1997). Both Shibuya's equation and Eq. 6.3 were plotted together with experimental data collected from the literature (presented in Fig. 2.17). Fig. 6.7 shows that Eq. 6.3 is a better fit to the experimental data over a wide range of void ratio (from stiff sand to soft clay), and hence can better represent the effect of void ratio on G_{max}. It can be seen in Fig. 6.7 that the curve with an average C_p of 45 lies in the middle of the experimental data collected in the literature. This suggests that Eq. 6.2 with $n = 0.5$ and $C_p = 45$ may be used to predict G_{max} of geomaterials in a feasibility study.

It is noted that stress exponents for different materials are different (as summarised in Table 6.1). To discuss the effect of void ratio, and to compare the test results of this research with the data collected in the literature, in this section the stress exponent was simply taken as 0.5, which is the average stress exponent widely used by many researchers (Hardin & Richart, 1963; Hardin & Black, 1966, 1968; Hardin & Drnevich, 1972*b*; Marcuson & Wahls, 1972, see Table 2.1). Section 6.3.2 will present effects of particle shape on stress exponent for the test materials.

Results presented in Fig. 6.6 and Fig. 6.7 show that no single curve can be used to predict G_{max} of geomaterials; The particle characteristic coefficient, C_p, is not constant for all materials, but varies from 35 (for Glitter) to 83 (for LBSB). It should be noted that the derived values of C_p ($= \frac{G_{max}}{F(e) \times \sigma_0^{0.5}}$) will change if the stress exponent is not taken as 0.5. Fig. 6.6 also shows the variation of G_{max} of GB due to the difference in diameter of the spheres. In addition, it can be seen in Fig. 6.6 the variation of G_{max} for the mixtures of LBSB and 0.1 mm Mica due to the variation of mica content.

There is a significant difference between the range of C_p obtained from this research and that in the literature. Fig. 6.6 shows that values of C_p for the test materials varies from 35 to 83, which is higher than those obtained in the literature, where C_p varies from 30 to 60 (Fig.6.7). In other words, the range of G_{max} of geomaterials measured in the past was lower than that obtained in this research. The difference in C_p increases with increasing specimen stiffness; For example, the difference at the upper bound (for stiff materials such as LBSB) is $\Delta C_p = 83 - 60 = 23$ or about 28%, and the difference at the lower bound (for soft materials such as Glitter) is $\Delta C_p = 35 - 30 = 5$, or about 15%. This may be due to effects of apparatus compliance. It is supposed that values of G_{max} measured by other researchers were not corrected for the compliance of their apparatus. In contrast, the compliance of the Stokoe RCA were taken into account in this research (see Chapter 4).

6.1.4 Damping ratio

Fig. 6.8 presents damping ratios, which were corrected for equipment damping ratios measured in section 3.4.2, against shear strain for several specimens at $\sigma' = 100kPa$. It can be observed that, when shear strains are small (e.g. lower than 0.0001%), measured damping ratios for all specimens are rather scattered due to noise effects. It is found that the material damping ratios for all specimens are small (e.g. less than 3%). Fig. 6.8 shows that damping ratios increases with increasing shear strain. Generally, damping ratios of the platy materials are lower than those of the rotund materials (Fig. 6.8). Considering a single material, in general, damping ratio of the material increases with increasing void ratio (Fig. 6.9), decreases with increasing effective stress (Fig. 6.10) and particle size (Fig. 6.11).

Even though the equipment damping was determined and material damping ratios have been adjusted to remove as far as possible the effect of system damping, in some cases (e.g. at low shear strain) the equipment damping was not successfully removed, because of the following reasons:

- The noise effects are significant at low shear strain and at low resonant frequency (see Section 3.4.2 and Section 5.7.4)
- The equipment damping varies with resonant frequency of the specimens, and linear interpolation was applied to estimate system damping (see Fig. 3.21). This linear interpolation may overestimate/underestimate the equipment damping.

Therefore, in this thesis only material damping ratios at relatively large shear strain, where the noise effects become insignificant and the equipment damping is relatively small compared to that of material damping, are compared and discussed.

6.2 Effect of particle size on small strain behaviour of granular materials

6.2.1 Maximum shear modulus, G_{max}

Fig. 6.12 presents G_{max} of GB specimens with similar void ratios, $e = 0.52 - 0.53$ (Fig. 6.12a) and $e = 0.58 - 0.60$ (Fig. 6.12b). These graphs show that G_{max} significantly increases with an increase in particle size. For example, at an effective stress of 200 kPa, G_{max} of GB (with e = 0.58-0.6) increases by $38MPa$ (or 22%) when particle diameter increases from 0.1 mm to 3.0 mm. To remove effects of void ratio, G_{max} of the materials were normalised by the theoretical void ratio function (Eq. 6.3). The normalised values were plotted against particle size in Fig. 6.13, clearly showing that G_{max} is significantly affected by particle size.

This result makes an important addition to the conclusions given by previous researchers. Hardin & Drnevich (1972*b*) suggested that particle size influences G_{max} of soils only through influencing void ratio of the soils. They explained that smaller size soils consists more porous; thus G_{max} of fine soils is lower than that of coarse soils. Iwasaki & Tatsuoka (1977) supported the premise of Hardin & Drnevich (1972*b*), and suggested that G_{max} was independent of particle size because the effects of void ratio had been already taken into account using a void ratio function. Schreiber (1968); Hamilton (1970, 1971); Hamilton & Bachman (1982); Buckingham (2005) in the field of geophysics have observed effects of D_{50} on V_p of marine sediments and suggested that the effect was related to change in the porosity of the sediments.

It is stressed that the effects of particle size on G_{max} of GB presented in Fig. 6.13 were observed after normalising with respect to void ratio. For example, at the same void ratio, G_{max} of 3.0 mm GB is significantly higher than that of 1.0 mm GB. This suggests that particle size influences G_{max} of a real soil because particle size changes not only void ratio (macro effect) but also other contact mechanical properties (micro effect). The later point will be explored more in Section 6.4.

6.2.2 Elastic threshold strain and shear modulus degradation

The elastic threshold strains, γ_e, for GB at an effective stress of 100 kPa were summarised in Table 6.2, and plotted against particle size in Fig. 6.14a. The trendline with a very low coefficient of determination ($R^2 < 0.1$) indicates a poor correlation between particle diameter and γ_e at an effective stress of 100 kPa. However, at an effective stress of 200 kPa, the correlation between particle diameter and γ_e (with a higher coefficient of determination) is more consistent. Fig. 6.14b shows that γ_e increases with increasing particle diameter.

In connection with the above effect, it is observed that the shear modulus degradation, G/G_{max}, as a function of shear strain for GB is also influenced by particle size. Values of G/G_{max} for GB at a shear strain of 0.004% were interpolated and plotted in Fig. 6.15, showing that G/G_{max} increases with an increase in particle size. The results suggest that stiffness of smaller particle soils is more susceptible to shear strain than that of larger particle soils.

6.2.3 Stress exponent, n, and particle characteristic coefficient, C_p

As was shown in Section 6.1.2, G_{max} increases in exponential manner with effective stress (Eq. 6.1). Based on regression analysis (Fig. 6.16), the stress exponents for GB with different particle size were obtained, and summarised in Table 6.1. It is observed that stress exponents for GB varies from 0.403 to 0.488, which are significantly higher than the theoretical value (1/3) for a packing of spheres suggested by other researchers (Duffy

& Mindlin, 1957; Duffy, 1959; Walton, 1987; Chang *et al.*, 1991; Liao *et al.*, 2000). The stress exponents for GB were plotted against particle size in Fig. 6.17, showing that stress exponent for GB decreases (from 0.488 to 0.403) with increasing particle size (from 0.5mm to 3.0 mm).

The material coefficients, α_0, obtained from Fig. 6.16, were plotted against particle diameter in Fig. 6.18. The results show that α_0 increases with increasing particle diameter. Considering the same material (the same particle size), it is also observed that α_0 increases with an increasing void ratio, and stress exponents decreases with an increase in void ratio. This agrees with the observation of other researchers, suggesting that α_0 is a function of void ratio (Hardin & Black, 1966, 1968; Hardin & Drnevich, 1972*b*; Marcuson & Wahls, 1972; Kokusho *et al.*, 1982; Shibuya *et al.*, 1997; Lo Presti *et al.*, 1997; Stokoe *et al.*, 1999).

To reduce the variation of α_0 due to the difference in void ratio, values of G_{max} were normalised by $F(e)$ (Eq. 6.3) before regression analysis. The normalised values of G_{max} versus effective stress were plotted in Fig. 6.19. The regression analysis with the normalised data leads to the particle characteristic coefficient, C_p. In other words, C_p is estimated using the following equation:

$$C_p = \frac{\alpha_0}{F(e)} = \frac{G_{max}}{F(e)\sigma_0'^{\,n}} \tag{6.4}$$

Fig. 6.20 shows that C_p for GB increases with an increase in particle diameter, e.g. C_p increases from 61 to 100 when particle diameter increases from 0.5mm to 3.0 mm. It is noted that values of C_p in Fig. 6.20 were obtained using stress exponents corresponding to each material (Table 6.1), which was less than 0.5 (Fig.6.19). This leads to the higher values of C_p in Fig. 6.20 when compared to those presented in Fig. 6.6.

6.2.4 Material damping, D

As discussed, to avoid the noise effects presented in Section 5.7.4, damping ratios at large shear strains were used to explore the effect of particle size on material damping. Fig. 6.21 presents material damping of GB measured by both FVD and HPP methods at shear strains of 0.001% and 0.004%. It is observed that the material damping is considerably influenced by particle size; the damping ratio decreases with an increase in particle size. For instance, at a shear strain of 0.004% and $\sigma_0' = 100kPa$, the material damping ratio of GB decreases by about 50% (from 1.4% to 0.7%) when the diameter increases from 0.5mm to 2.0 mm. The above effect of particle size on material damping is supported by the theoretical damping ratio presented in Fig. 2.12. The results presented in Fig. 6.21 are consistent with the suggestion given in the previous section that the stiffness of smaller particle soil is more susceptible to shear strain than that of larger particle soil.

6.3 Effect of particle shape on small strain behaviour of granular materials

6.3.1 Maximum shear modulus, G_{max}

To remove the effects of effective stress, only values of G_{max} at the same effective stress (e.g. 100 kPa, as illustrated in Fig. 6.6) or values of G_{max} normalised by ${\sigma'_0}^n$ (Fig. 6.22) were compared and discussed. It is noted that, except for LBSE and mixtures of LBSB and 0.1mm Mica, Fig. 6.22 presents normalised values of G_{max} for 1.0 mm materials only. The stress exponent used in Fig. 6.22 is 0.439, which is the average stress exponent for all of the test materials. The figure shows that G_{max} decreases with an increase in void ratio. However, at the same void ratio, G_{max} of different materials vary over a wide range, e.g. at void ratio of 0.66, G_{max} may vary from 75 MPa (for Glitter) to about 180 MPa (for LBSB). It is noted that the specific gravity, G_s, of LBSB and LBSE is 2.65 (Table 5.1), which is higher than that of the glass materials (2.50). It is hypothesised that a difference in G_s may lead to a difference in G_{max}. To remove the variation of G_{max} due to the variation in G_s, the values of normalised G_{max} presented in Fig. 6.22 were further normalised by G_s and plotted in Fig. 6.23. The graph shows that after normalising by G_s, the variation in G_{max} reduces. However, the variation is still significant. It is hypothesised that the variation is attributed to the difference in particle shape.

To verify this hypothesis, values of G_{max} for all specimens under an effective stress of 100kPa were normalised by both $F(e)$ (Eq. 6.3) and G_s. The normalised values were plotted against a particle form descriptor (e.g. Corey's shape factor, CSF, Fig. 6.24), and a particle roundness descriptor (e.g. angularity index, AI, Fig. 6.25). In addition, the normalised values were also plotted against scalene ellipsoid equivalent sphericity (SEES, Fig. 6.26). The figures show that both particle form and particle roundness have good correlations with normalised shear modulus. It is observed that G_{max} increases with increasing sphericity (Fig. 6.24 & 6.26) and roundness (Fig. 6.25). The results suggest that G_{max} is strongly affected by particle shape. It is emphasised that the above findings are independent of the effects of particle size, void ratio, and material specific density.

However, it can be observed in Fig. 6.24 to 6.26 that the normalised G_{max} of GB is lower than that of LBSB despite the higher sphericity and roundness of GB. This observation may be due to the combined effects of the very smooth surface of GB, which may lead to very small inter-particle friction and the resultant very small contact area between two spheres. These effects will be further discussed in Section 6.4.

6.3.2 Stress exponent, n, material coefficient, α_0, and particle characteristic coefficient, C_p

The stress exponents obtained from the 1.0 mm materials (summarised in Table 6.1) were plotted versus particle form descriptor (CSF) and particle roundness descriptor (AI) in Fig. 6.27. The graph in Fig. 6.27a suggests that stress exponents decreases with increasing CSF, e.g. the stress exponents for platy particles are higher than those for rotund particles. In addition, Fig. 6.27b suggests that stress exponents increase with an increase in particle angularity, e.g. the stress exponents for round particles (e.g. LBSB) are lower than those for angular particles (e.g. Nugget and Glitter). The figure also shows the variation of stress exponent due to the variation of void ratio; In general, stress exponents for dense materials are lower than those for loose materials.

Similarly, the material coefficients, α_0, for 1.0 mm materials (Table 6.2) were plotted versus CSF and AI in Fig. 6.28. It is observed that α_0 increases with an increase in CSF (Fig. 6.28a) and decreases with an increase in AI (Fig. 6.28b). The figure also shows the variation of α_0 due to the variation of void ratio; values of α_0 for dense materials are higher than those for loose materials.

Cho *et al.* (2006) reported similar effects of particle sphericity and roundness on stress exponent, n and material coefficient, α_0. However, they did not note the effects of void ratio, and particle size (as shown in Section 6.2.3). The mean particle diameter, D_{50}, of the materials used by Cho *et al.* (2006) varied from 0.15 to 0.6.

To eliminate the effect of void ratio on α_0, the values of α_0 for 1.0 mm materials were normalised by $F(e)$ (Eq. 6.3) to give particle characteristic coefficients, C_p (see Eq. 6.4). The values of C_p were plotted versus particle shape descriptors in Fig. 6.29. The relative high value of determination coefficients ($R^2 \approx 0.9$) in Fig. 6.29 indicates good correlations between C_p and both particle form (Fig. 6.29a) and particle roundness (Fig. 6.29b). The results show that C_p significantly increases with an increase in sphericity and roundness.

The above results combined with the results presented in the previous section (6.2) suggest that:

1. The effects of particle size, particle shape, and particle (specific) density can be taken in to account using a particle characteristic coefficient, C_p, which is almost independent of void ratio and effective stress.

2. Fine, angular, and platy particles have higher stress exponents, n, and lower particle characteristic coefficients, C_p, than bulky, round and rotund (spherical) particles do. In other words, stiffness of fine, angular, and platy particles is lower than that of bulky, round and rotund (spherical) particles. This implies that bonding/cemented and overconsolidated soils, which are relatively stiff in general, will have relatively low stress exponents, and relatively high particle characteristic coefficients.

6.3.3 Elastic threshold strain, γ_e

The elastic threshold strains, γ_e, (under an applied effective stress of 100 kPa) for the 1.0 mm specimens were plotted versus void ratio in Fig. 6.30, In general, γ_e is affected by void ratio. However, it is observed that when grouping the data for materials with similar particle shape together, γ_e is considerably affected by particle shape, e.g. the values of γ_e for the platy particles are significantly larger than those for the rotund particle.

To explore these effects further, values of γ_e were plotted against CSF and AI. To somewhat remove the effect of void ratio, only values of γ_e for specimens at similar void ratio (e = 0.6 - 0.8) were considered. Fig. 6.31 shows that γ_e is significantly influenced by particle shape, e.g. values of γ_e for platy particles are three to four times larger than those for rotund particles (Fig. 6.31a). It can be seen that γ_e decreases with an increase in CSF (Fig. 6.31a), and increases with an increase in AI (Fig. 6.31b).

6.3.4 Shear modulus degradation, G/G_{max}

The values of shear modulus degradation, G/G_{max}, obtained at a shear strain of 0.004% for the specimens with nominal particle diameters of 1.0 mm were plotted in Fig. 6.32, showing that G/G_{max} is influenced by void ratio. G/G_{max} values for the higher relative density specimens are higher than those of the lower relative density specimen. However, it can be observed in Fig. 6.32 that G/G_{max} is also significantly affected by particle shape.

Fig. 6.33 plots G/G_{max} versus the two particle shape parameters. Again, only the materials with similar void ratio were considered. It is observed that G/G_{max} decreases with increasing sphericity (Fig. 6.33a) and increases with increasing angularity (Fig. 6.33b). For example, at a shear strain of 0.004%, values of G/G_{max} of the rotund particles are about 84%-85%, and those of the platy particles are from 95%-97%. The results suggest that stiffness of platy and angular particles at small strain is less susceptible to increasing shear strain than that of rotund particles.

6.3.5 Material damping

Fig. 6.34 and 6.35 present the material damping ratios, calculated using the HPP method, at shear strains of 0.001% and 0.004%, respectively. It is noted that, except for LBSE (particle size 0.1 mm), all the specimen presented in the figures have the same particle size (1.0 mm), and were all subjected to the same applied effective stress of 100 kPa. The graphs in the figure show that material damping is significantly influenced by particle shape. For example, the material damping ratio of the rotund particles may be twice that of the platy particles. It is observed that, at similar void ratio, material damping increases with increasing sphericity (Fig. 6.36a and 6.37a) and roundness (Fig. 6.36b, 6.37b).

6.3.6 Effect of fine mica on G_{max}

Two specimens of LBSB mixed with 0.1 mm Mica were made with different mica contents, i.e. 10% and 20% by mass. It is noted that the specimen with 10% mica was only tested at 100 kPa. Therefore, stress exponent, n, and material coefficient, α, for this specimen were unavailable.

To remove the effect of effective stress, values of G_{max} of LBSB specimens and two LBSB-mica specimens were normalised by ${\sigma'_0}^n$ (where $n = 0.439$ is the average stress exponent), and plotted versus void ratio in Fig 6.38. It can be observed in Fig. 6.38 that at the same void ratio, the normalised shear moduli for the mixtures are significantly lower than those for the LBSB alone. As an alternative interpretation, the values of G_{max} of two LBSB specimens (at different void ratio) and two LBSB-mica specimens were plotted versus effective stress as shown in Fig 6.39. The graph in Fig 6.39 shows that at the same effective stress, G_{max} values of the mixtures are lower than those of the LBSB. In addition, the results show that G_{max} decreases with an increase in mica content.

The finding in this research are similar to that of Lee *et al.* (2007), who used a conventional oedometer cell equipped with bender elements to measure V_s of mixtures of Ottawa sand with different mica contents and with various mica-to-sand size ratios (L_{mica}/D_{sand} = 0.33, 1, 3). However, the observation of Lee *et al.* (2007) was not normalised for the effect of void ratio, which significantly increases with mica content (Fig. 2.22) due to the bridge packing of the relatively large mica size. In contrast, the size of mica used in this research is very small compared to that of LBSB. It is emphasised due to the small size of the mica and the specific specimen preparation method, the void ratios of the sand-mica specimens in this research are lower than those of the LBSB specimen.

To remove the effect of void ratio, the maximum moduli were normalised by the theoretical void ratio function and plotted against effective stress in Fig. 6.40. The results shows that the normalised G_{max} values for the mixtures are significantly lower.

The above effects could be due to the combined effects of particle shape (which is platy) and particle size (which is fine, 0.1 mm) of mica as explained in Section 6.4.4.

6.4 Hypothesis and explanation

This section proposes a new soil model, which can be used to explain the effects of particle size and particle shape on the small strain response of geomaterials.

6.4.1 Introductions

Some researchers (e.g. Duffy & Mindlin, 1957; Duffy, 1959; Petrakis & Dobry, 1987; Wang & Nur, 1992) have used a static stress-strain approach combined with Hertz and Mindlin contact theories to establish relationships between material parameters and G_{max} of some regular packing, i.e. simple cubic, body centred cubic, tetragonal, face-centre cubic, and close packed hexagonal) of spheres under isotropic load. Despite the fact that their results did not agree well with their experimental data, it can be said that they were the pioneers who have showed how material elastic constants and confining pressure could influence G_{max} of the packing. For example, all the analytical solutions have indicated that G_{max} was an exponential function of confining stress with the stress exponent of 1/3.

For a random packing of spheres under isotropic loading, Digby (1981), Walton (1987), and Chang *et al.* (1991) has used a *microstructural continuum* approach (or *kinematic hypothesis*, as termed by Liao *et al.* 2000), which postulates that displacement of every particle in a packing follows a uniform displacement field. For example, Chang *et al.* (1991) applied their microstructural continuum model to the small strain case where tangential forces do not exceed frictional strength at contacts, and proposed the following equation:

$$G_{max} = \frac{5-4\nu}{10-5\nu}\left[\sqrt{\frac{3}{2}}\frac{\bar{N}_c}{\pi(1-\nu)}\right]^{2/3}\left[\frac{1}{(1+e)}\right]^{2/3} {G_{grain}}^{2/3}{\sigma_0}^{1/3} \tag{6.5}$$

where $\bar{N}_c$ is the coordination number, G_{grain} and ν are the shear modulus and Poisson's ratio of particle, respectively. The key results that can be drawn from Eq. 6.5 are:

1. The theoretical void ratio function (for a random packing of smooth sphere) is $(1+e)^{-2/3}$
2. The stress exponent is 1/3
3. G_{max} is a function of coordination number, $\bar{N}_c$
4. G_{max} is proportional to ${G_{grain}}^{2/3}$
5. G_{max} is a function of the Poisson's ratio of the grains

Eq. 6.5 was used to predict G_{max} of the GB used in this research at various confining pressure and plotted in Fig. 6.41. The Young's modulus of the *Silibead type S* GB, given by the supplier, is $E_{grain} = 63GPa$. The Poisson's ratio is unavailable. However, for illustration, it is taken as two values 0.26 and 0.40, leading to G_{grain} of $25GPa$ and $22.5GPa$, respectively. Fig. 6.41 shows that the calculated values of G_{max} are significantly higher than those measured in this research. For example, at 100kPa, the calculated G_{max} is 2.4 times higher than that of 3.0 mm GB. This may be explained by the factors below:

1. Effects of grain stiffness may be overestimated as Eq. 6.5 suggested that G_{max} is proportional to ${G_{grain}}^{2/3}$. Experimental data, however, suggest that the effect G_{grain} on G_{max} is not of that magnitude. For example Cascante (1996) and Santamarina & Cascante (1998) have reported that V_s of a steel ball specimen (with e = 0.6) at an effective stress of 100 kPa is about $270m/s$ which is lower than that ($352m/s$) of a LBSB specimen (obtained in this research) at similar void ratio (e = 0.61) and effective stress. It is noted that the shear modulus of steel is $78GPa$ (Santamarina *et al.*, 2001) or 2.5 times higher than that of quartz. As an adjustment, Chang *et al.* (1991) suggested that in order to obtain a relatively good agreement between experimental data and predicted values, G_{grain} of a sand (used in Eq. 6.5) needs to be reduced ten times.

2. The theoretical void ratio function, $f(e) = (1+e)^{-2/3}$ (Eq. 6.5), is quite different from the empirical void ratio functions summarised in Table 2.1, and hence may not reflect the influence of void ratio on G_{max} in practice.

3. The equation ignores the effects of other particle characteristics, such as particle size, inter-particle friction, particle roughness, and specific density of the granular materials.

Liao *et al.* (2000) argued that the kinematic hypothesis, used to derive Eq. 6.5, imposed a packing constraint that leads to the overestimation of G_{max} presented above. To overcome the problem, they proposed a *best-fit hypothesis*, which hypothesised that the mean displacement field in a packing is the best fit for the actual displacement field. Using the best-fit hypothesis, they derived the following relationship:

$$G_{max} = \frac{5-5\nu}{10-7\nu}\left[\sqrt{\frac{3}{2}}\frac{N_C}{\pi(1-\nu)}\right]^{2/3}\left[\frac{1}{(1+e)}\right]^{2/3} {G_{grain}}^{2/3}{\sigma_0}^{1/3} \qquad (6.6)$$

It can be seen that the only difference between Eq. 6.6 and Eq. 6.5 is the first term related to the effect of Poison's ratio. Eq. 6.6 was plotted in Fig. 6.41, showing that, similarly to Eq. 6.5, Eq. 6.6 gives the calculated G_{max} for GB significantly higher than the experimental data.

These relationships, however, cannot be applied in this research to explain the effects of particle characteristics on the small strain behaviour of the geomaterials presented in the previous sections. There are a few questions remained to be unanswered. For example, why do particle size and particle shape affect G_{max} even when the effect of void ratio is normalised? Why are rates of stiffness degradation of specimens with different particle shape different? Why are damping ratios of platy particles less susceptible to shear strain than bulky particles? In addition, there are some issues that have not been well understood. For example, (i) do the elastic plateaus really exist (Wood, 2007), and why are the elastic threshold strain very narrow (e.g. less than 0.001%)? (ii) Why does shear modulus decrease as shear strains increase? (iii) Why is V_s of a steel specimen (in the example presented above) lower than that of a LBSB specimen with the same void ratio?

In order to clarify the above issues, this section presents a different and simple approach to study the parameters controlling G_{max}. The shear wave velocity, V_s, propagating in a dry granular medium is considered as a combination of a shear wave velocity through solid particles, termed V_{grain}, and a shear wave velocity through the contact network, termed $V_{contact}$. To quantify the effect of void ratio (macro effect) and $V_{contact}$ (micro effect), a soil specimen is simplified as a system of two phases namely porous phase and discontinuous-solid phase, which consists of cubic particles in array (with zero contact thickness) as shown in Fig. 6.42. The soil model is, therefore, termed porous discontinuous-solid model. Walton (1987) postulates that the contact areas between two particles are of fundamental importance, since they are the only means by which energy (shear wave) can be transmitted through the packing. Therefore, the size (and number particles) in the discontinuous solid phase will depend on the contact area.

6.4.2 Basic concepts of the porous discontinuous-solid model

Fundamentally, V_s is the ratio of a travel length to a travel time. Considering the discontinous-solid phase only, it is rational that the total travel time of shear wave through the discontinuous solid phase, $t_{dis.solid}$, is a combination of travel times through particles,

t_{grain}, and travel times through the contact network, $t_{contact}$ (Fig. 6.42). This can be summarised by the following equation:

$$t_{dis.solid} = \sum t_{grain} + \sum t_{contact} \tag{6.7}$$

Dividing the both sides of Eq. 6.7 by the travel length through the discontinuous solid phase, $L_{dis.solid} = 1$, which is also the travel length through solid particles (see Fig. 6.42), we have:

$$\frac{1}{V_{dis.solid}} = \frac{1}{V_{grain}} + \frac{1}{V_{contact}} \tag{6.8}$$

Eq. 6.8 reflects the obvious fact that stiffness of a discontinuous solid material ($V_{dis.solid}$) is lower than that of a continuous material (V_{grain}) due to the *discontinuities* ($V_{contact}$). It is noted that Eq. 6.8 is established for the discontinuous solid phase only. When taking into account void ratio of a specimen, Fig. 6.42 indicates that the travel length through both phases is $(1 + e)$ times higher that through the discontinuous solid phase only. Therefore, V_s of a specimen is $(1 + e)$ times lower than that of the discontinuous solid phase:

$$V_s = \frac{V_{dis.solid}}{1+e} \tag{6.9}$$

Substitution of Eq. 6.9 to 6.8 leads to:

$$\frac{1}{V_s} = (1+e)\left[\frac{1}{V_{grain}} + \frac{1}{v_{contact}}\right] \tag{6.10}$$

It is noted that V_{grain} is a function of shear modulus, G_{grain}, and specific density, ρ_s, of particles:

$$V_{grain} = \sqrt{\frac{G_{grain}}{\rho_s}} \tag{6.11}$$

It is obvious that V_{grain} is independent of (i) the number of particles in the specimen, (ii) effective stress, and (iii) shear strain amplitude. For example, if G_{grain} of quartz is 31GPa, V_{grain} through a quartz grain is about $3400 m/s$, or nearly 10 times higher than V_s $(377 m/s)^2$ of a dense packing of LBSB at 100 kPa. This implies that grain stiffness may not be the most important material parameter controlling V_s of granular materials. As discussed, V_s through a packing of steel balls can be lower than that of a LBSB specimen with similar void ratio and effective stress, although G_{grain} of steel is 2.5 times higher than that of quartz. This suggests that effects of $V_{contact}$ (micro effect) and void ratio (macro effect) on V_s of granular materials at a given shear strain and effective stress may be more important than the effect of grain stiffness (see Eq. 6.10).

Since V_{grain} can be determined (using Eq. 6.11) and V_s can be measured in the laboratory, the only unknown parameter in Eq. 6.10 is $V_{contact}$. Different from V_{grain}, which is a constant, $V_{contact}$ may be a function[3] of tangential contact stiffness (defined as the ratio of

---

[2] Measured in this research.

[3] This section explains the effect of particle characteristics on the small strain response of geomaterials. The determination of $V_{contact}$ is out of the scope of this study, and hence not presented in this study.

tangential force to tangential compliance at contact), inter-particle frictional coefficient, contact area, coordination number, $\bar{N}_v$, number of contact per unit solid volume, $\bar{N}_c$, and bonding/cementation etc. Based on Hertz theory of contact between two elastic spheres, Mindlin & Deresiewicz (1953) suggests that tangential stiffness (or tangential compliance) is a function of particle elastic properties, contact pressure, shear strain (magnitude of tangential force), and inter-particle friction at the contacts. This helps to explain why G_{max} is a function of many parameters such as effective stress, shear strain, void ratio, particle characteristics, etc...

In general, it is rational that when the number of contact per unit solid volume, $\bar{N}_v$, increases, (the total contact compliance increases) the total travel time at contacts increases (see Eq. 6.7). Hence $V_{contact}$ through the contact network decreases, resulting in a decrease in V_s (Eq. 6.10).

Eq. 6.10 indicates that the theoretical void ratio function for shear wave velocity is:

$$F(e)_V = \frac{1}{1+e} \tag{6.12}$$

Fig. 6.43 shows that V_s of two sands (i.e. Ottawa sand and crushed Quartz) measured by Hardin & Richart (1963) (see Fig. 2.16) are very well correlated to the theoretical void ratio functions. This suggests that a distance between two correlative lines for the two soils (Fig. 6.43) represents the magnitude of effects of particle characteristics (such as particle size and particle shape).

Eq. 6.10 suggests that one of the macro effects, which is also the main effect, of void ratio on G_{max} is to change travel length. In addition, void ratio influences coordination number, $\bar{N}_c$, of a packing of granular material (Smith *et al.*, 1929; McGeary, 1961; Field, 1963; Oda, 1977; Chang *et al.*, 1991). Void ratio also influences contact pressure between two particles (micro effect). For example, Cascante & Santamarina (1996) suggests that the average normal contact force, P, in a random assembly of single-size spheres is a function of confined pressure, p_0, diameter, void ratio, and coordination number, $\bar{N}_c$:

$$P = D^2 p_0 \frac{\pi(1+e)}{\bar{N}_c} \tag{6.13}$$

For an elastic soil, G_{max} can be calculated from V_s propagating in the soil with mass density, ρ, from the following relationship:

$$G_{max} = \rho {V_s}^2 = \frac{G_s}{(1+e)} {V_s}^2 \tag{6.14}$$

Substitution of Eq. 6.14 to 6.9 gives:

$$G_{max} = \frac{G_s}{(1+e)} \left[\frac{V_{dis.solid}}{1+e} \right]^2 = \frac{G_s}{(1+e)^3} {V_{dis.solid}}^2 \tag{6.15}$$

where G_s is particle specific density. Denote:

$$G_{max.dis.solid} = G_s {V_{dis.solid}}^2 \tag{6.16}$$

is the maximum shear modulus of a discontinuous material (without pore space). Substitution of Eq. 6.16 to Eq. 6.15 We have:

$$G_{max} = \frac{G_{max.dis.solid}}{(1+e)^3} \tag{6.17}$$

Eq. 6.17 indicates that the maximum shear modulus of a soil including both discontinuous solid phase and porous phase, G_{max}, is lower than the maximum shear modulus of a discontinuous solid material, $G_{max.dis.solid}$, by a factor of $(1+e)^{-3}$. In order words, the (macro) effect of void ratio on G_{max} of geomaterials can be taken into account using the theoretical void ratio function, $F(e) = (1+e)^{-3}$, as introduced previously (Eq.6.3).

It is emphasised that, before this research, there was neither a theoretical nor an empirical void ratio function that can be reasonably applied for all soils over wide range of void ratio. As presented, a few researchers such as Walton (1987); Chang *et al.* (1991); Liao *et al.* (2000) have made attempts to establish a theoretical relationship between G_{max} and other material parameters of a random packing of spheres. However, theoretical void ratio functions obtained from these relationships do not represent the effect of void ratio. Experimentally, the influence of void ratio has been taken into account using an empirical void ratio function, $F(e)$, and various forms of $F(e)$ (as summarised in Table 2.1) has been proposed for various types of soil. They can be classified into two groups; hyperbolic functions (Hardin & Black, 1966, 1968; Hardin & Drnevich, 1972*b*; Kokusho *et al.*, 1982; Lo Presti *et al.*, 1993; Shibuya *et al.*, 1997; Wichtmann & Triantafyllidis, 2004), and exponential functions (Athanasopoulos & Richart, 1983; Jamiolkowski *et al.*, 1995; Shibuya *et al.*, 1997). However, each void ratio function can only be applied for a certain soil with a limited void ratio range.

In addition, Eq. 6.15 indicates that G_{max} of geomaterials is also a function of particle specific gravity, G_s. The above hypotheses will be used in the next section to explain the effects of particle size and particle shape on the small strain behaviour of granular materials.

6.4.3 Explanation of the effects of particle size

The effects of particle size on G_{max} can be attributed to the following:

1 An increase in particle size will decrease number of contact per unit solid volume, $\bar{N}_v$, resulting in an increase in G_{max}.

2 An increase in particle size will increase contact area, and contact force, leading to an increase in friction strength and hence contact stiffness.

The first point is explained in the previous section and illustrated in Fig. 6.44 (and Fig. 6.46). It is logical that due to the difference in $\bar{N}_v$, the $V_{contact}$ of specimen No 1 in Fig.

6.44 is higher than that of specimen No 2, leading to V_s of specimen No 2 being slower than that of specimen No 1.

According to Hertz's theory of contact between two elastic spheres under the normal contact load P (Fig. 6.45), the contact pressure, p, (at any radius r) can be calculated by (Johnson, 1987):

$$p = \frac{3P}{2\pi a^2}\left[1 - \left(\frac{r}{a}\right)^2\right]^{1/2} \tag{6.18}$$

where a is contact radius calculated by:

$$a = \left[\frac{3PD(1-\nu^2)}{16E_{grain}}\right]^{1/3} \tag{6.19}$$

It is noted that these equations are derived for two spheres with the same diameter and elastic constants. The normal contact pressure is smallest at the periphery and attains the maximum value at the centre of the contact area (Fig. 6.45).

Equations 6.13, 6.18 & 6.19 indicate that normal contact force[4], contact radius and contact friction (which is proportional to contact area) increase proportionally to ball diameter.

In addition, when a specimen is subjected to a harmonic torque (or shear force), there is a oscillating tangential force with the magnitude T (Fig. 2.9) at a contact between two spheres (Deresiewicz, 1953). The oscillating tangential force does not affect the size and shape of the contact area[5], however it causes the *stick-slip* (no slide) phenomenon (Deresiewicz, 1953), of which the *reversed radius* (or *slip radius*), c' (Fig. 6.47), is calculated from (Deresiewicz, 1953; Mindlin & Deresiewicz, 1953; Johnson, 1987):

$$\frac{c'^3}{a^3} = 1 - k_T/2 \tag{6.20}$$

where $k_T = T/(\mu \times P)$ is a tangential force ratio (of T to friction strength, $\mu \times P$), and μ is a constant coefficient of friction. It will be recalled that the shear strain under the oscillating tangential force can be estimated using Eq. 2.9. At small strains, where G_{max} is measured, the tangential force is much smaller than the frictional strength between two spheres; hence the reversed radius is close to the contact radius.

It can be rational that under the same tangential force, the larger the contact radius (or reversed radius) the smaller the shear strain is (see Eq. 2.9), and hence the higher the contact stiffness[6]. In other words, contact stiffness is a function of reversed radius, which is a function of particle size.

Furthermore, Eq. 6.20 indicates that the reversed radius decreases when shear strain increases (oscillating tangential force increases) , resulting in a reduction in contact stiffness.

---

[4] It is noted that at the same confining pressure, both contact force and contact area between two balls increase proportionally to the square of the ball diameter. As a result, the contact pressure between two balls is unchanged by changes in the ball diameter.

[5] Since the two balls have the same elastic constants, the normal displacements, caused by the tangential traction transmitted between the balls, at any point in the interface, are equal and opposite. Hence the shape and size of the contact area are independent of the tangential force (Johnson, 1987).

[6] Defined as the ratio of the tangential force to the tangential displacement.

This may explain why shear modulus decreases as shear strain increases. In addition, at the same shear strain, when particle size increases, the reversed radius increases. Thus, shear modulus of a larger particle specimen is less susceptible to shear strain increment than that of a smaller particle specimen.

In summary, particle size affects the specimen stiffness through (i) the number of contacts per unit solid volume and (ii) the stiffness of contact between two particles. The contact stiffness is strongly dependent on a few parameters such as contact force, contact radius (or reversed radius), and friction at contact etc; and all of these parameters in turn are functions of particle size.

6.4.4 Explanation of the effects of particle shape

The influence of particle shape on the small strain behaviour of granular materials can be explained by combined effects of many factors, such as number of contact per unit solid volume, $\bar{N}_v$, contact area, contact pressure, coordination number, $\bar{N}_c$, etc. Fig. 6.46 illustrates that with the same volume and density, the number of particles in a rotund specimen is less than that of the platy particle specimen. An increase in number of contact resulted by a decrease in particle sphericity (increase in flatness) will cause a decrease in $V_{contact}$, leading to a reduction in specimen stiffness.

The difference between the packing structure of platy particles and rotund particle could also contribute to the difference in stiffness between them. The soil structure of platy particles, e.g. the particle orientation and the contact patterns (face-to-face or edge-to-face) may be weaker than that of rotund particles at the same density due to the flexibility of the structure, and crushing and bending of the platy particles.

The susceptibility of shear modulus to shear strain of GB can be related to a relatively high reduction in reversed radius due to an increase in shear strain. Two smooth spheres contact to each others in a very small area (spherical contact). When shear strain increases, the reversed radius significantly decreases (Fig. 6.48a), resulting in relatively fast reduction in shear modulus.

Contrary to GB, platy particles such as Nugget or Glitter contact to each other over a relatively larger contact area. It can be seen in Fig. 6.48b that the relative reduction in contact radius (reduction in stick-slip radius) of Nugget or Glitter due to an increase in shear strain is relatively small compared to that of GB[7]. As a result, Nugget and Glitter are less susceptible to shear strain.

The reduction of the stiffness of the mixtures of LBSB and 0.1 mm mica can be explained by the effects of both particle size and particle shape of mica. Fine mica particles may not only fill pore spaces around sand particles but also exist in between them. The mica particles filling the pore space help to reduce the void ratio of the mixture. However, the mica in between the sand particles prevent the direct interaction of the sand particles and significantly increase the number of contact per unit solid volume, $\bar{N}_v$, as illustrated in

---

[7] There are also edge to face contacts in very loose platy specimen.

Fig. 6.49. This causes a reduction in contact stiffness, and hence a reduction in G_{max} compared to that of LBSB alone.

The fact that G_{max} of GB is lower than that of LBSB despite the higher sphericity of GB may be due to the differences in both inherent properties and contact mechanical properties (caused by difference in particle shape) between GB and LBSB, such as:

1. The difference in contact area. The SEM image of LBSB (Fig. 5.1a) shows that LBSB contact to each other in a relatively larger area. In contrast, the contact area between GBs (spherical contact) is smaller.
2. The very smooth surface of GB, resulting in relatively low inter-particle friction for GB.
3. The difference in mineral between GB and LBSB, leading to the difference in specific gravity between GB (2.5) and LBSB (2.65); and leading to the difference in particle shear modulus, G_{grain}, between GB (25GPa) and LBSB (31GPa).

It can also be hypothesised that the smooth and small contact area between GB particles causes significant energy loss when shear wave travels through their contacts. It is noted that at small strain, neither rotation nor slide between particles can occur. However, only the stick-slip phenomenon occurs (Deresiewicz, 1953; Mindlin & Deresiewicz, 1953; Johnson, 1987). Equations 2.5 to 2.10 (in Section 2.2.4) explicitly show that damping ratio at small strain is a function of particle diameter and static inter-particle coefficient of friction. the smooth and small contact area between GBs contribute to the relatively high damping ratio especially at relatively large shear strains of GB specimens. In contrast, contact areas between platy particles are relatively larger (Fig. 6.48b), helping the wave transfer from particle to particle with relatively small losses. This may explain why damping ratios of platy particles are lower and less susceptible to shear strain increment than rotund particles.

Table 6.1: Material coefficient, α_0, and stress exponent, n, of the test materials

Material	Diameter (mm)	void ratio, e	α_0	n
GB	0.1	0.58	18.65	0.4247
GB	0.5	0.53	17.24	0.4884
GB	1.0	0.522	22.90	0.4425
GB	1.0	0.601	18.64	0.4515
GB	2.0	0.537	24.78	0.4276
GB	3.0	0.525	31.23	0.4025
GB	3.0	0.595	23.57	0.4102
LBSB	1.0	0.682	23.84	0.4279
LBSB	1.0	0.61	28.11	0.4287
LBSB (retest)	1.0	0.61	25.51	0.4394
LBSB	1.0	0.511	35.64	0.4238
LBSB+10%Mica(*)		0.447	NA	NA
LBSB+20%Mica		0.475	22.58	0.4688
Glitter1	1.0	0.66	8.39	0.477
Glitter1 (unloading)	1.0	0.634	8.66	0.4815
Glitter2	1.0	1.034	6.73	0.4758
Glitter2 (unloading)	1.0	0.951	4.96	0.5312
Nugget1	1.0	0.772	14.70	0.4057
Nugget2	1.0	1.017	7.89	0.4791
Nugget2 (unloading)	1.0	0.966	8.13	0.4836
LBSE	0.1	0.639	22.24	0.4093
LBSE	0.1	0.694	16.81	0.4207
LBSE(*)	0.1	0.748	NA	NA

(*) The specimen was tested manually using a oscilloscope.

TABLE 6.2: Elastic threshold strain, γ_e, of the test materials

Material	Diameter (mm)	e	γ_e (10^{-4}%) at σ'_0 (kPa)					
			100	200	300	400	500	600
GB	0.1	0.58	12.0	12.2	13.9	17.0	18.2	20.4
GB	0.5	0.53	7.9	13.9	17.6	23.3	27.2	27.9
GB	1.0	0.522	7.8	12.9	16.3	20.8	22.9	27.8
GB	1.0	0.601	1.8	3.0	3.3	3.7	NA	NA
GB	2.0	0.537	10.1	17.4	25.1	25.1	33.6	32.7
GB	3.0	0.525	8.1	14.7	19.3	23.5	25.3	31.8
GB	3.0	0.595	8.7	17.7	21.6	29.0	31.4	30.9
LBSB	1.0	0.682	7.6	9.5	11.0	14.3	12.7	13.5
LBSB	1.0	0.61	3.0	4.3	4.6	5.5	NA	NA
(retest)	1.0	0.61	3.2	5.1	5.3	5.1	NA	NA
LBSB	1.0	0.511	5.1	9.8	11.9	14.2	NA	NA
LBSB+10%Mica		0.447	8.1	NA	NA	NA	NA	NA
LBSB+20%Mica		0.475	8.3	9.1	9.5	11.0	12.4	11.4
Glitter1	1.0	0.66	23.8	37.1	41.8	56.7	51.4	54.8
(unloading)		0.634	20.2	24.2	43.0	44.0	46.1	NA
Glitter2	1.0	1.034	23.9	37.2	42.1	45.5	53.2	53.8
(unloading)		0.951	16.9	22.5	25.4	31.3	37.1	47.6
Nugget1	1.0	0.772	17.4	30.6	36.0	NA	NA	NA
Nugget2	1.0	1.017	15.7	19.3	23.8	24.5	25.5	46.1
(unloading)		0.966	15.5	20.9	NA	32.3	NA	48.0
LBSE	0.1	0.639	18.0	30.9	34.0	33.0	36.1	37.8
LBSE	0.1	0.694	17.7	31.7	30.9	34.5	NA	NA
LBSE	0.1	0.748	17.0	NA	NA	NA	NA	NA

TABLE 6.3: Shear modulus degradation, G/G_{max}, at shear strain of 0.004%

Material	Diameter (mm)	e	G/G_{max} (%) at σ'_0 (kPa)					
			100	200	300	400	500	600
GB	0.1	0.58	90.3	92.7	93.3	94.8	95.0	95.5
GB	0.5	0.53	90.0	93.4	95.2	96.3	97.0	97.5
GB	1.0	0.522	91.9	94.7	95.9	96.5	96.9	97.2
GB	1.0	0.601	77.4	82.4	84.7	86.0	NA	NA
GB	2.0	0.537	94.0	96.0	96.9	97.2	97.7	97.6
GB	3.0	0.525	92.8	95.5	96.3	96.9	97.0	97.5
GB	3.0	0.595	93.3	96.1	96.8	97.4	97.5	97.6
LBSB	1.0	0.682	90.1	92.4	93.5	94.6	94.7	95.1
LBSB	1.0	0.61	80.7	86.2	87.7	88.1	NA	NA
(retest)	1.0	0.61	84.6	89.3	90.5	89.1	NA	NA
LBSB	1.0	0.511	89.0	92.2	92.9	94.4	NA	NA
LBSB+10%Mica		0.447	87.8	NA	NA	NA	NA	NA
LBSB+20%Mica		0.475	86.8	88.2	89.6	90.5	92.1	91.8
Glitter1	1.0	0.66	96.5	97.9	98.1	98.7	98.5	98.7
(unloading)		0.634	95.9	96.9	98.1	98.1	98.3	NA
Glitter2	1.0	1.034	96.6	97.8	98.1	98.3	98.5	98.6
(unloading)		0.951	16.9	96.5	97.0	97.5	97.9	98.3
Nugget1	1.0	0.772	96.0	97.4	97.8	NA	NA	NA
Nugget2	1.0	1.017	94.6	96.2	96.8	96.8	96.9	98.3
(unloading)		0.966	94.4	96.0	NA	97.6	NA	98.4
LBSE	0.1	0.639	94.9	97.1	97.5	97.4	97.8	97.8
LBSE	0.1	0.694	94.7	97.2	97.2	97.6	NA	NA
LBSE	0.1	0.748	93.4	NA	NA	NA	NA	NA

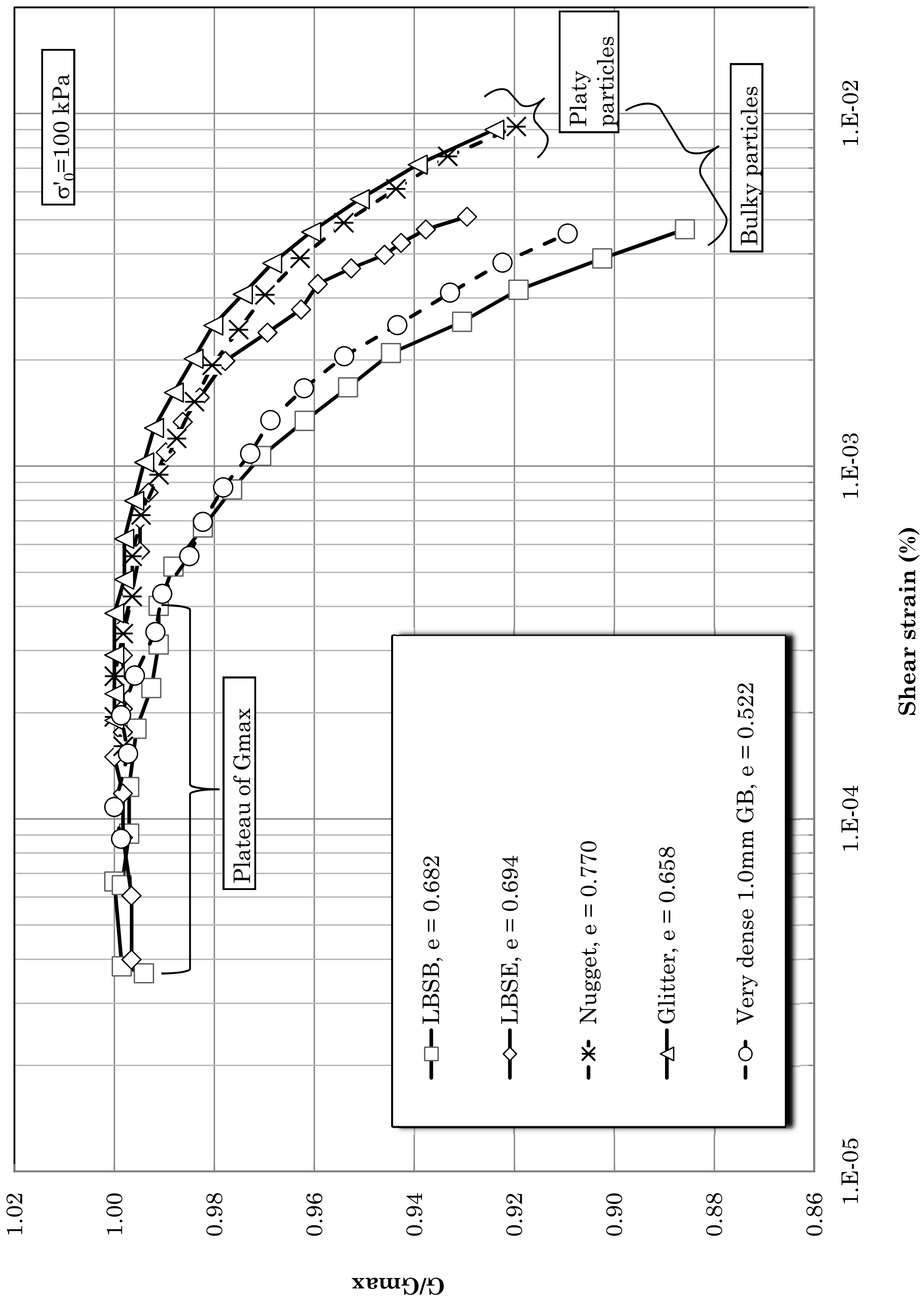

Figure 6.1: Shear modulus as a function of shear strain

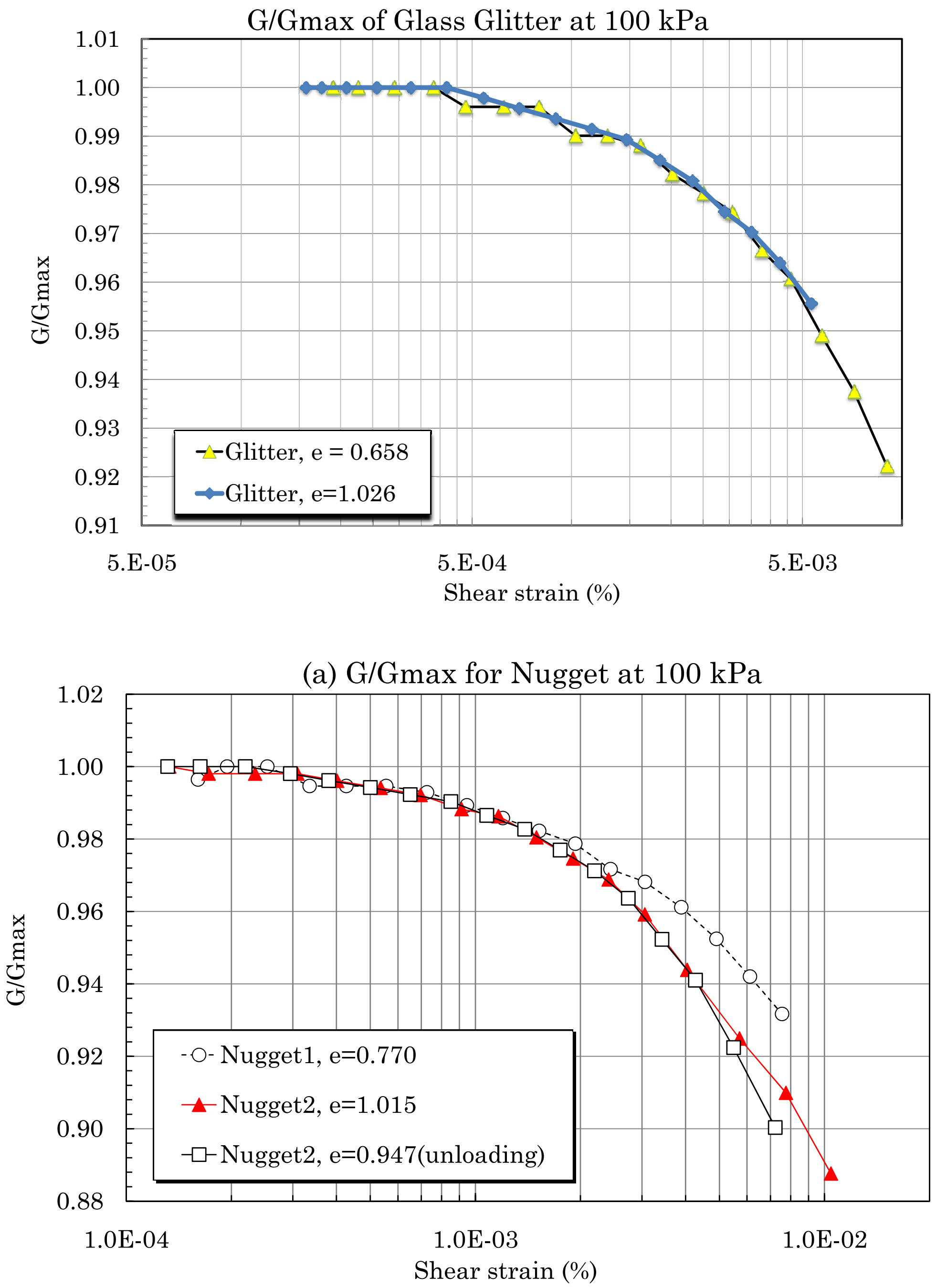
G/Gmax of Glass Glitter at 100 kPa

(a) G/Gmax for Nugget at 100 kPa

FIGURE 6.2: Shear modulus degradation curves of Glitter and Glass Nugget

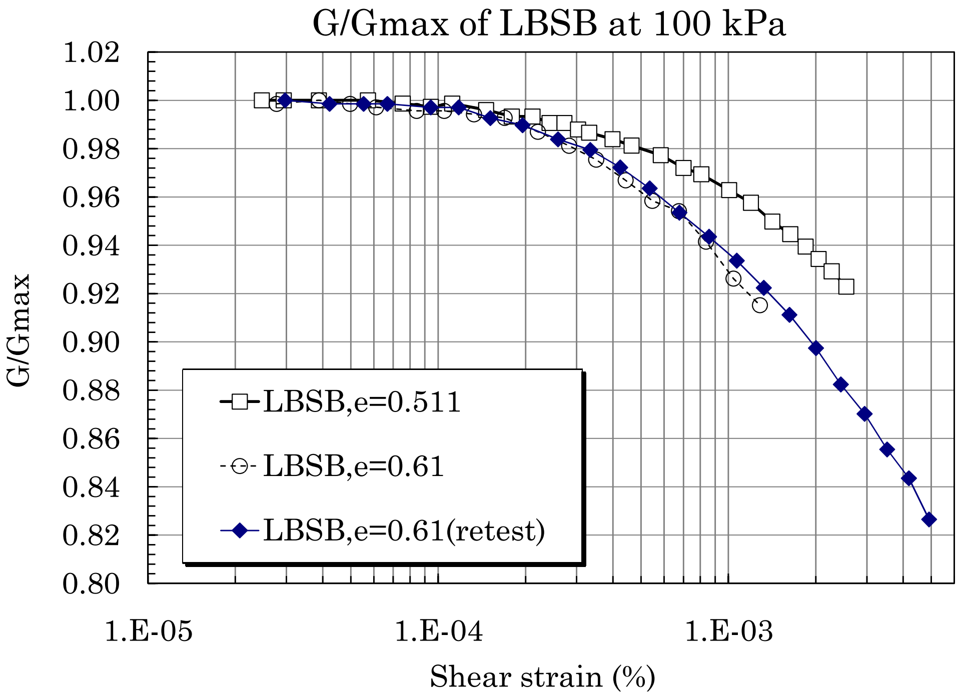

(b) G/Gmax for LBSE at 100 kPa

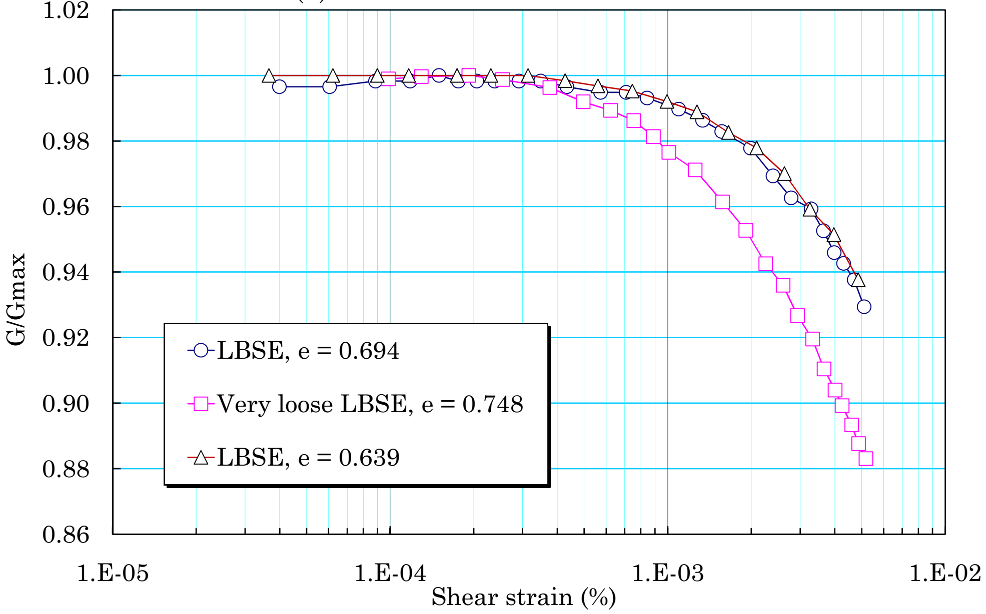

FIGURE 6.3: Shear modulus degradation curves of LBSB and LBSE

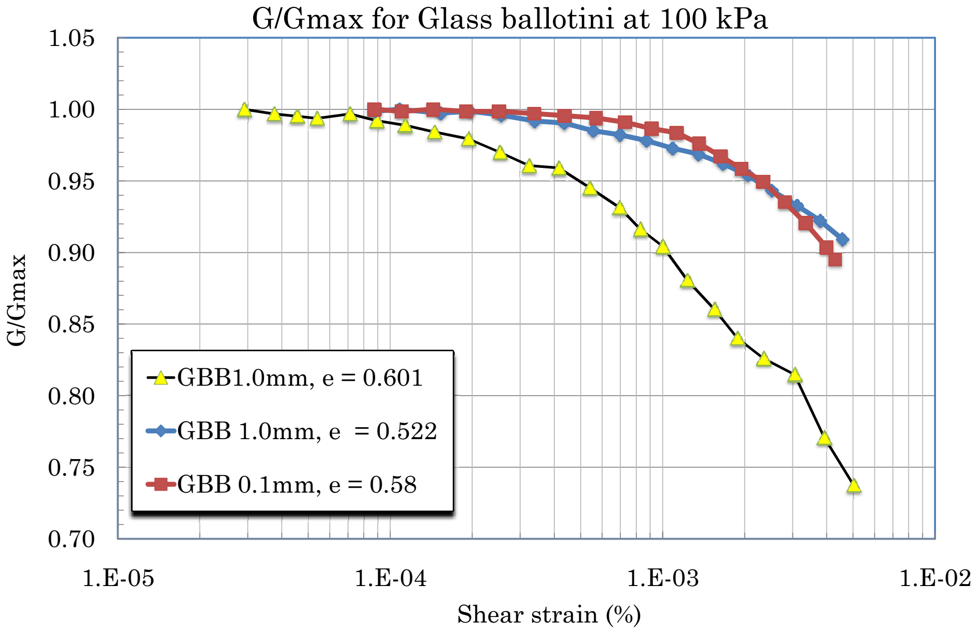

Figure 6.4: Shear modulus degradation curves of Glass Ballotini

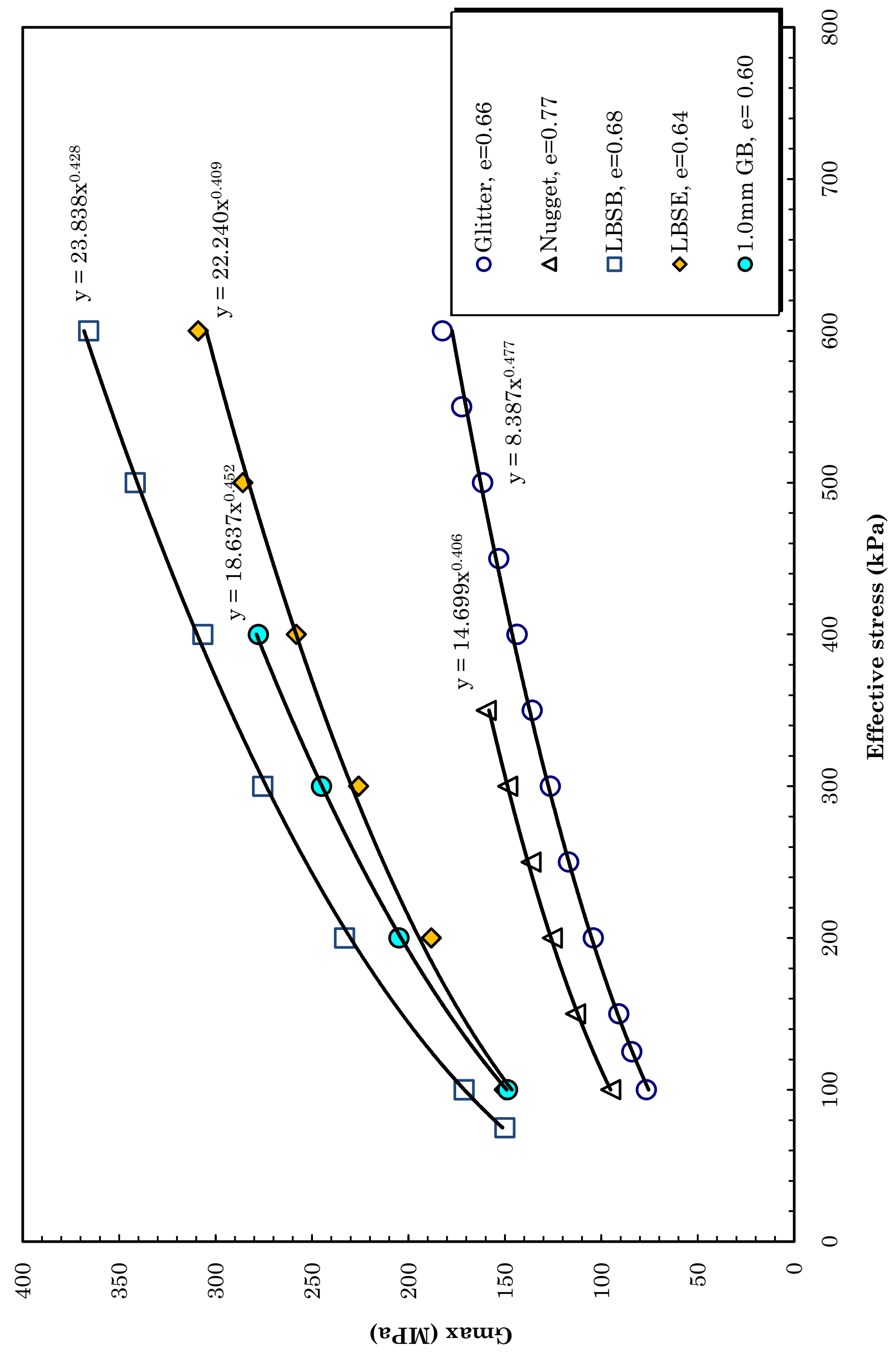

FIGURE 6.5: Shear modulus of the test materials as a function of effective stress

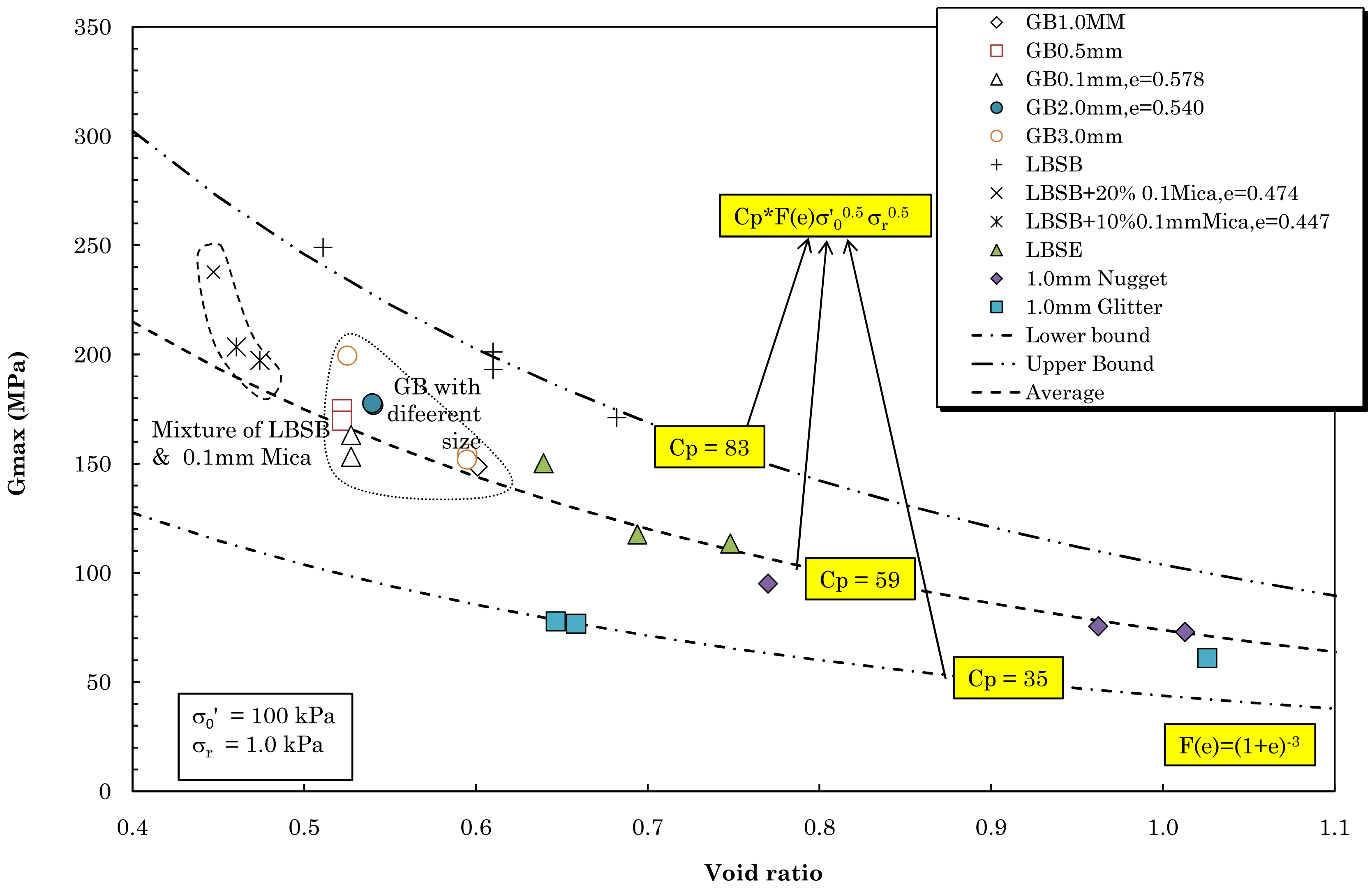

FIGURE 6.6: Effect of void ratio on G_{max} at effective stress of 100 kPa

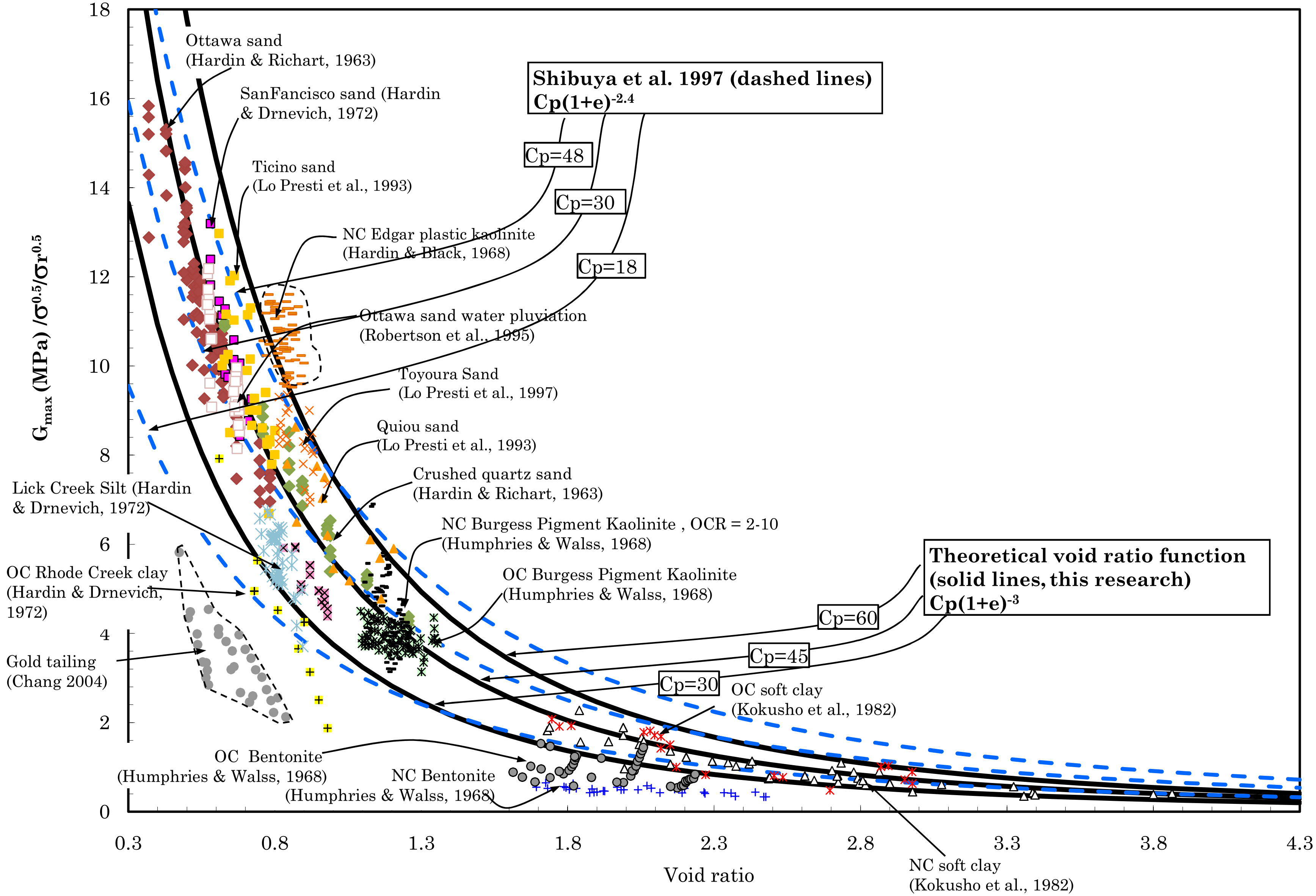

FIGURE 6.7: New proposed theoretical void ratio function

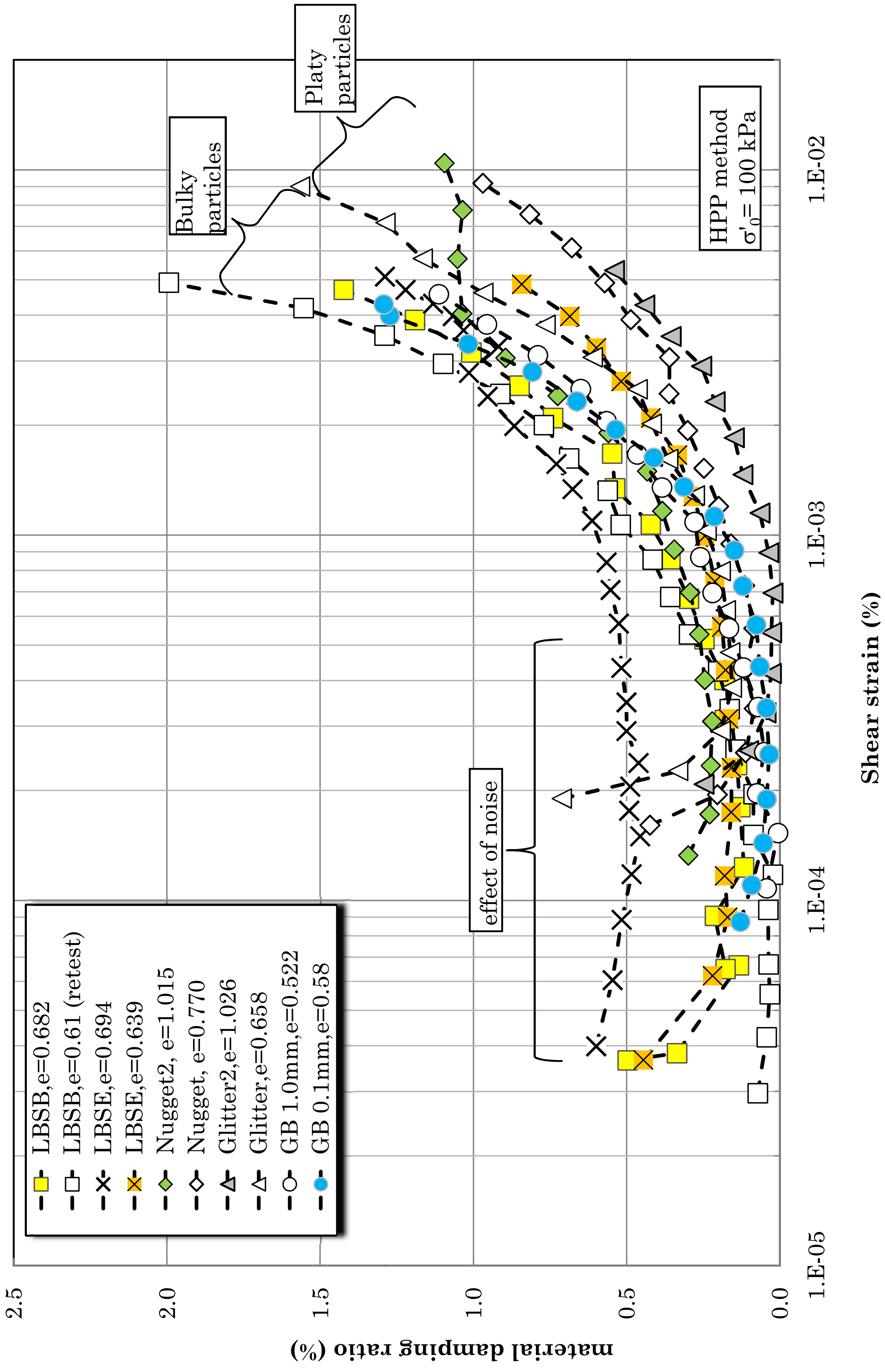

Figure 6.8: HPP material damping for some test materials at $\sigma' = 100\ kPa$

(a) Material damping for Nugget

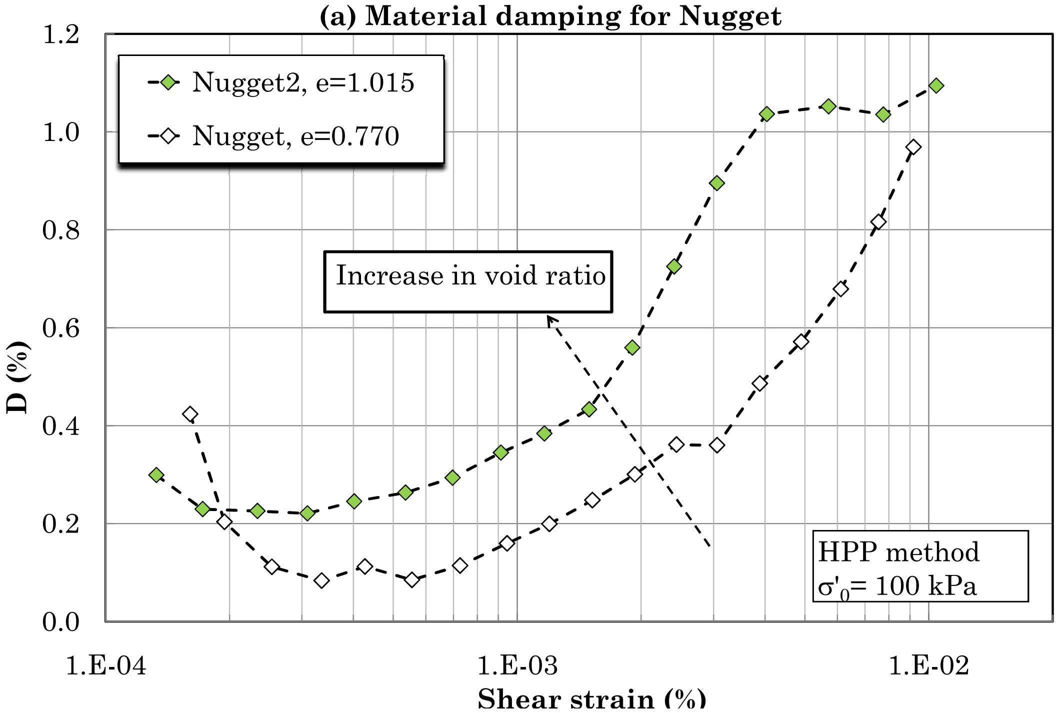

(b) Material damping for LBSE

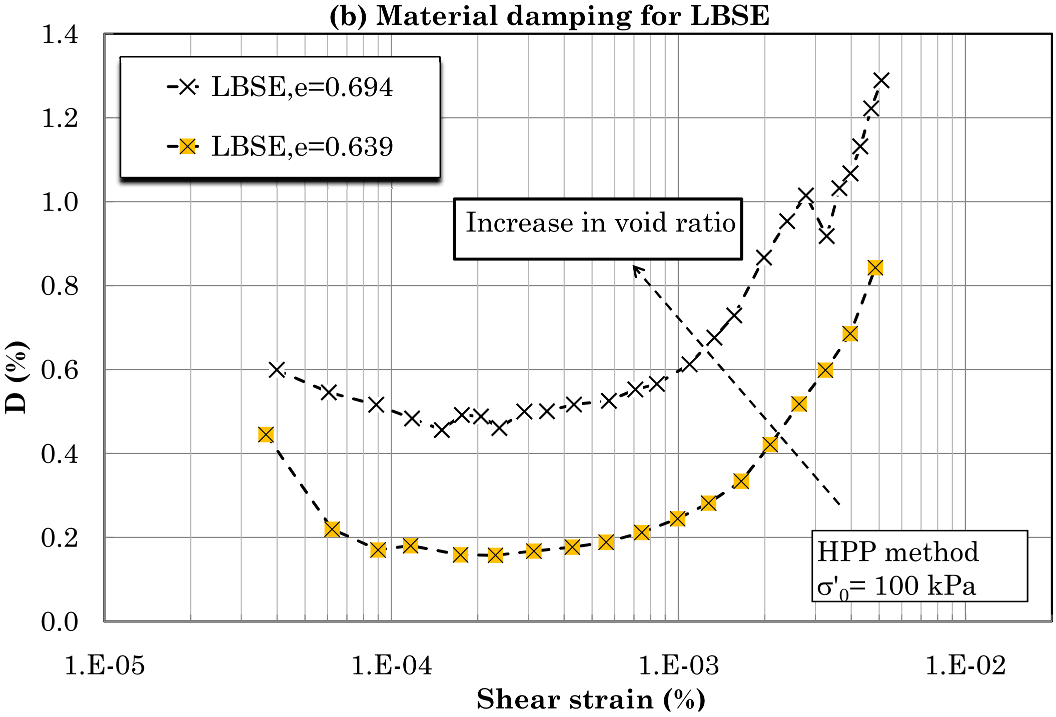

FIGURE 6.9: Effect of void ratio on material damping for Nugget and LBSE at $\sigma' = 100\ kPa$

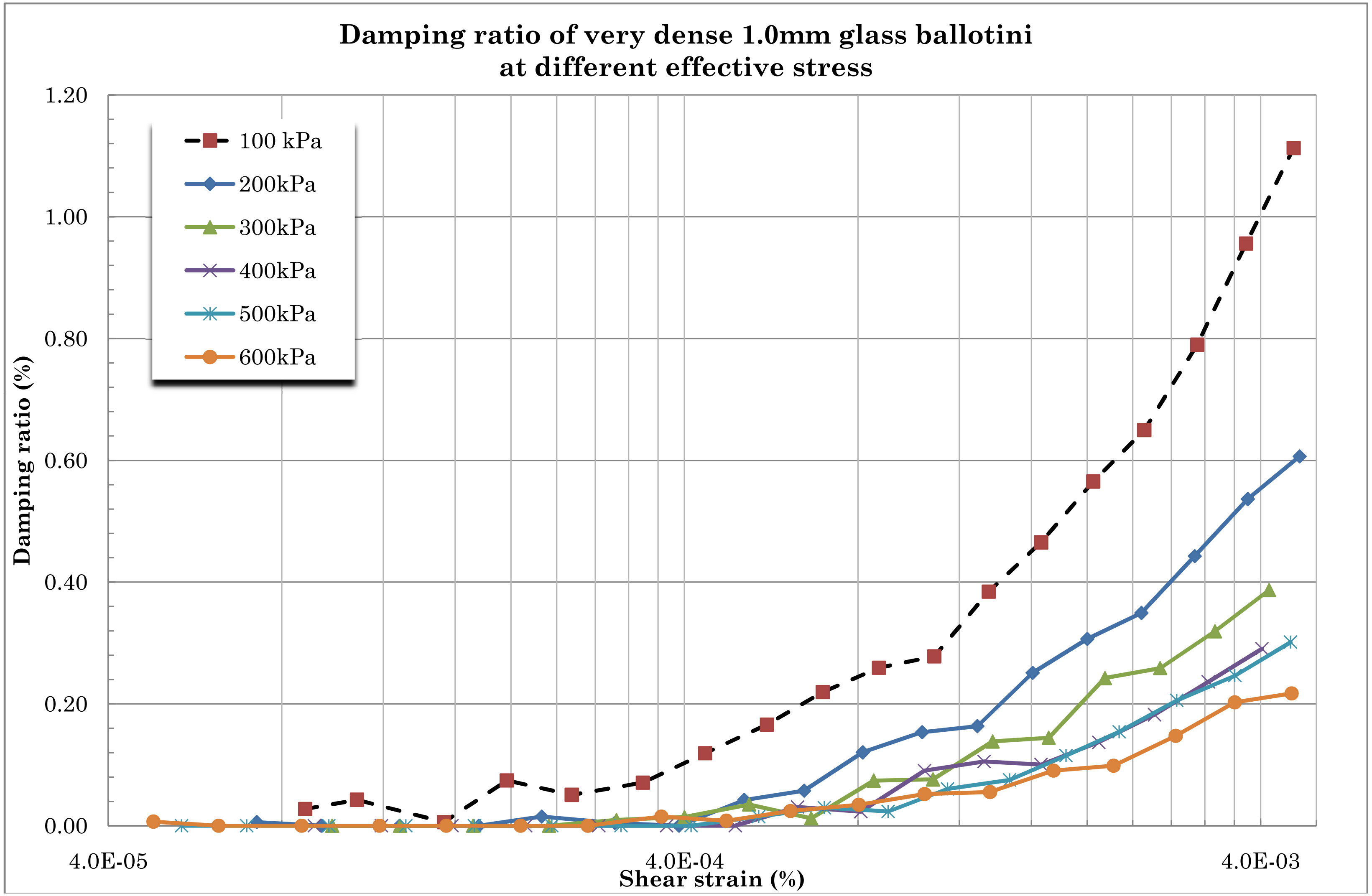

FIGURE 6.10: Material damping for 1.0 mm GB versus shear strain at different effective stress

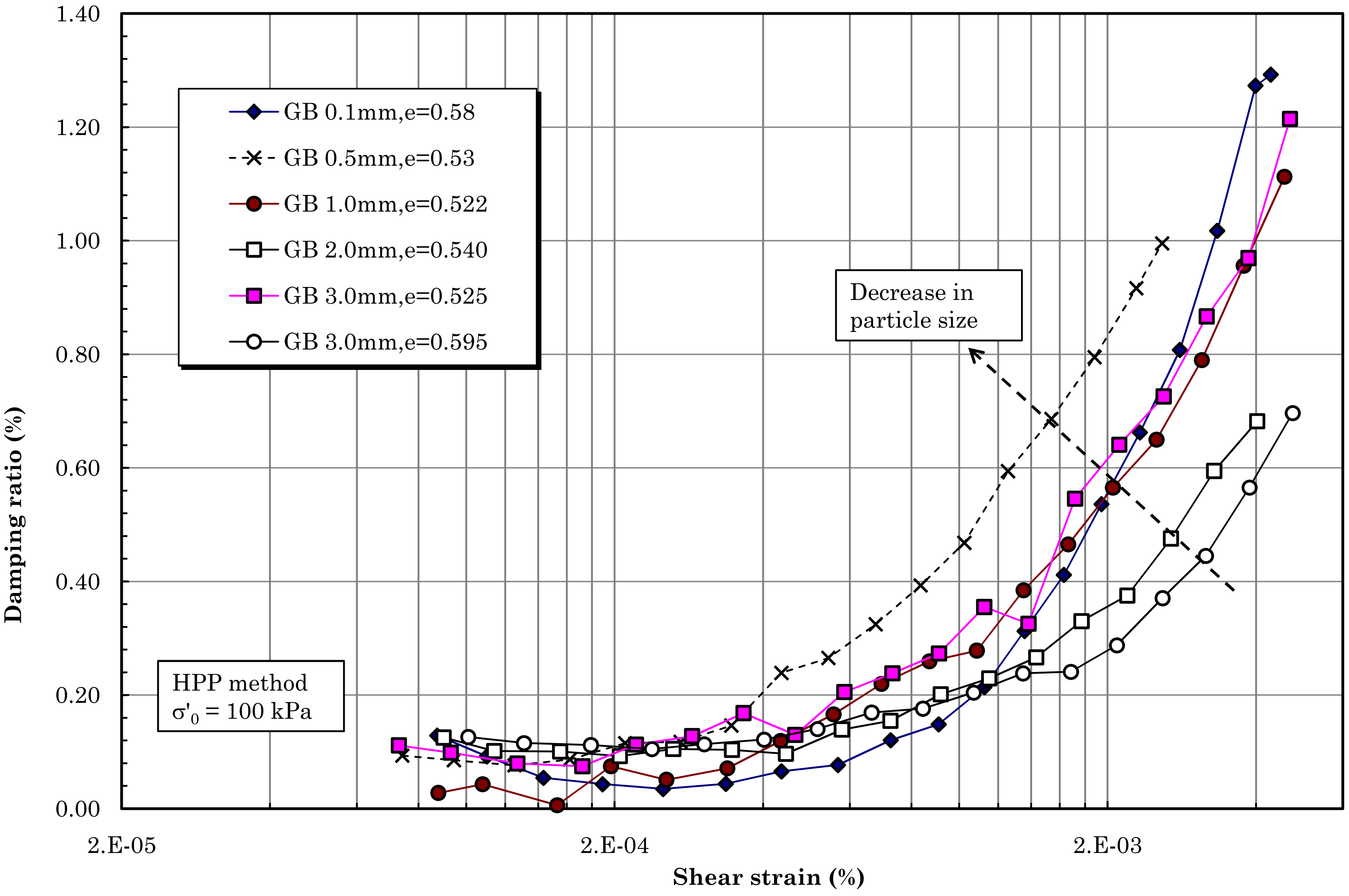

FIGURE 6.11: Material damping for GB at $\sigma' = 100\ kPa$

(a) G_{max} of GB with e = 0.52 - 0.54

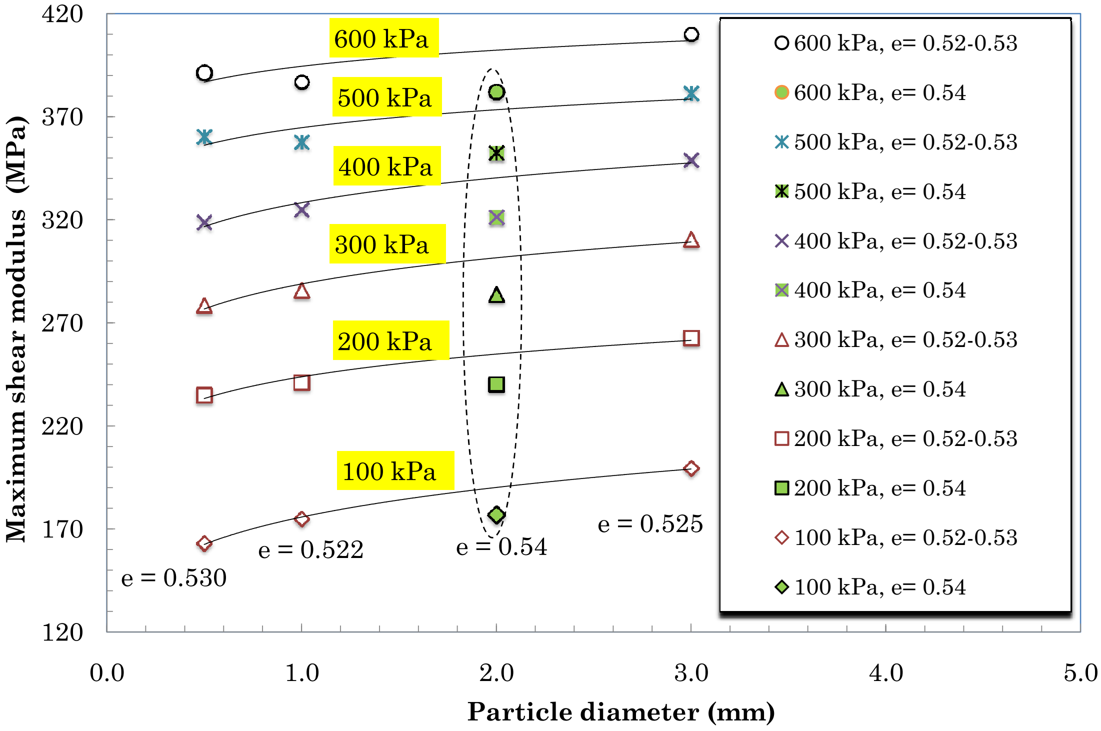

(b) G_{max} of GB with e = 0.58-0.60

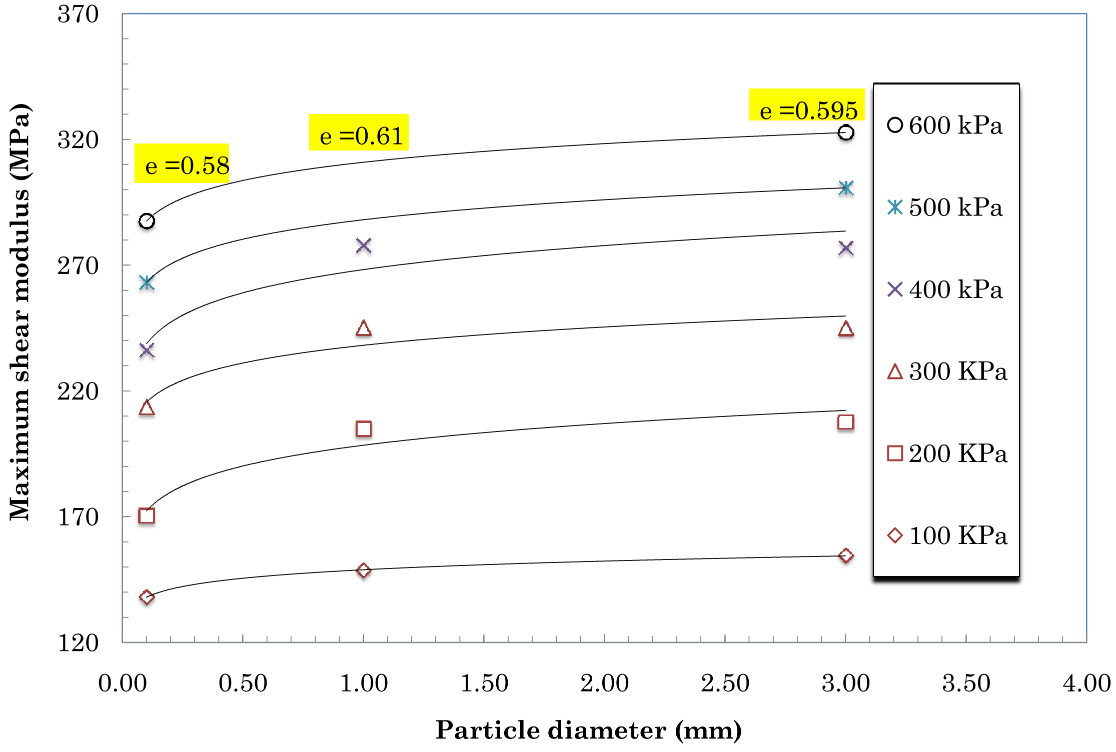

FIGURE 6.12: Influence of particle size on G_{max} of GB

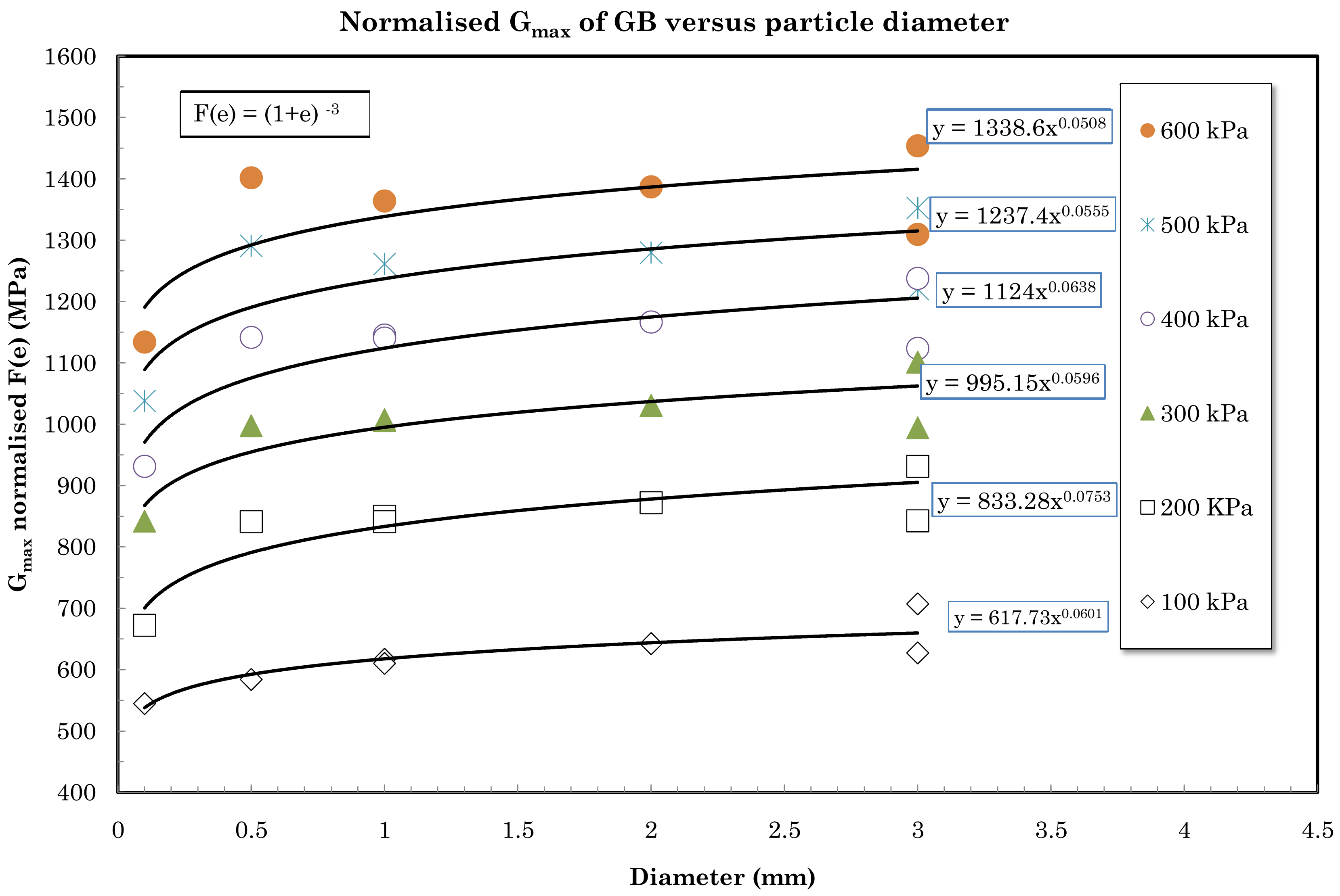

FIGURE 6.13: Influence of particle size on G_{max} normalised by void ratio of GB

(a) γ_e of GB at 100 kPa

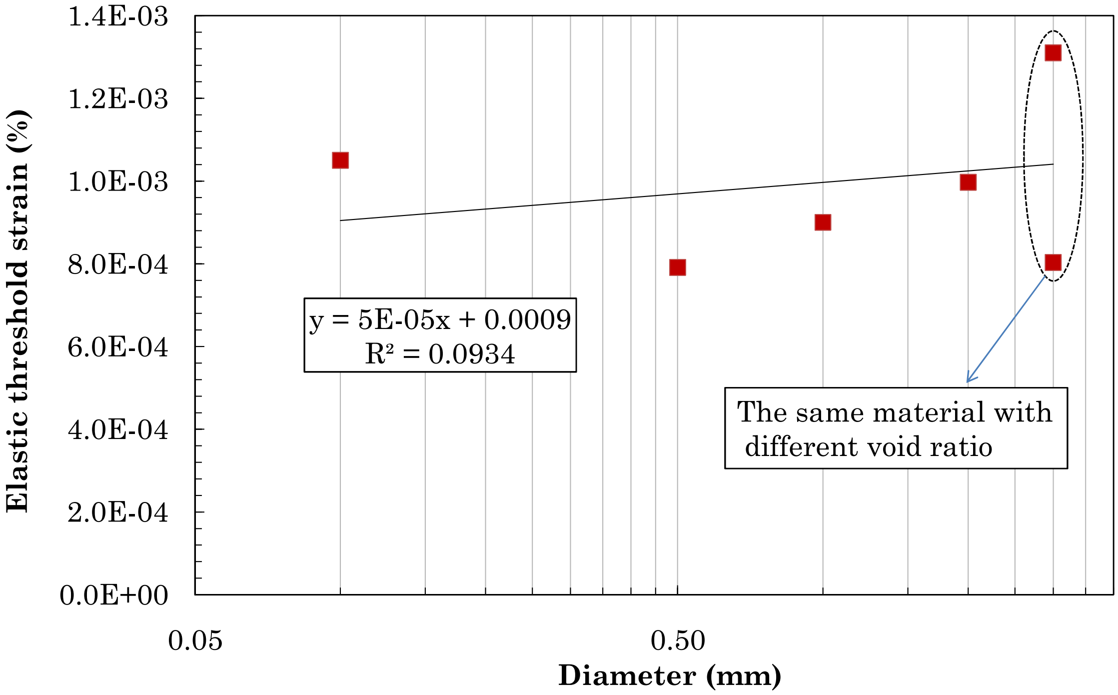

(b) γ_e of GB at 200 kPa

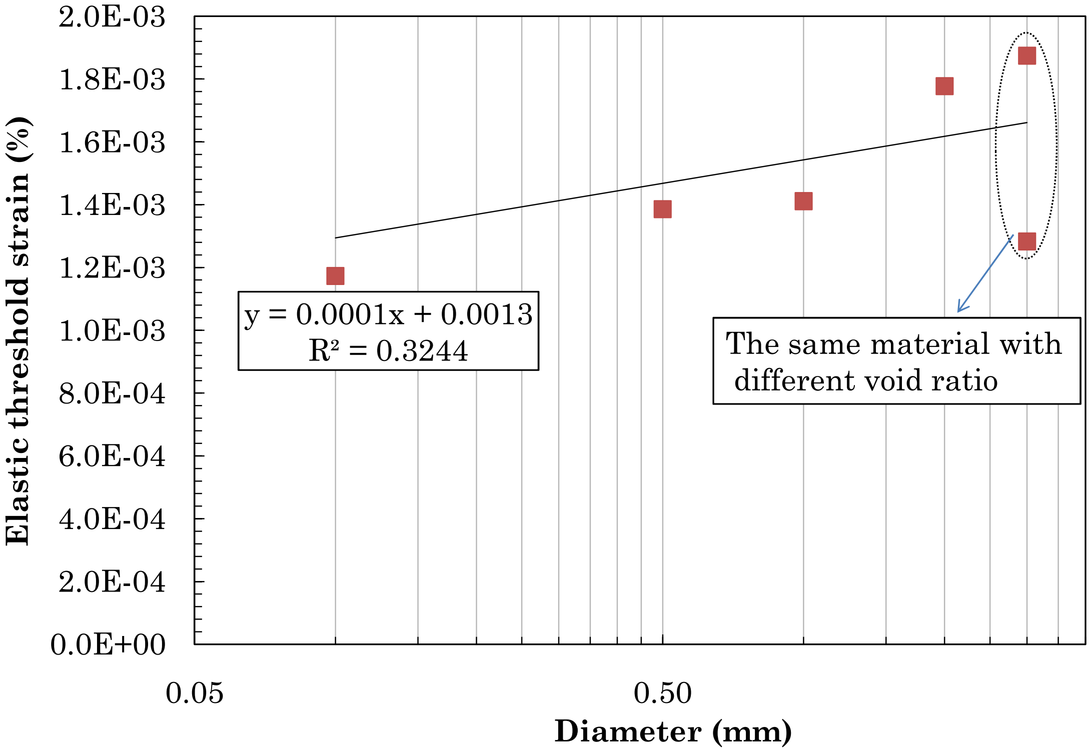

FIGURE 6.14: Elastic threshold strain of GB versus particle size

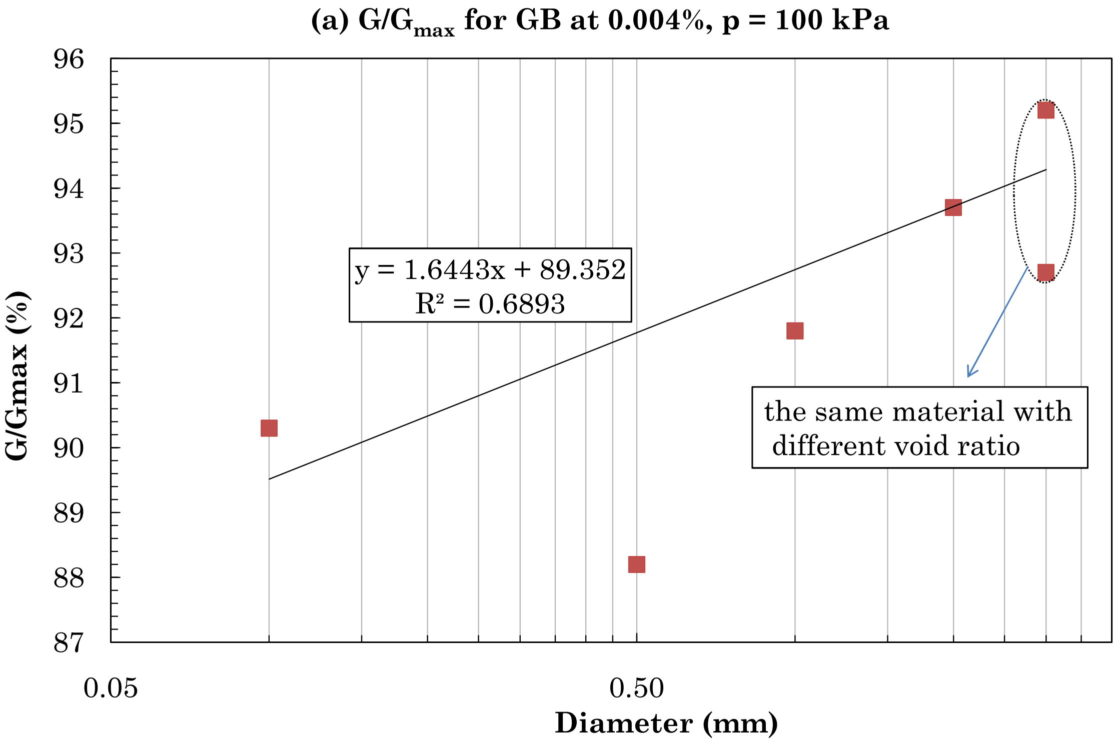

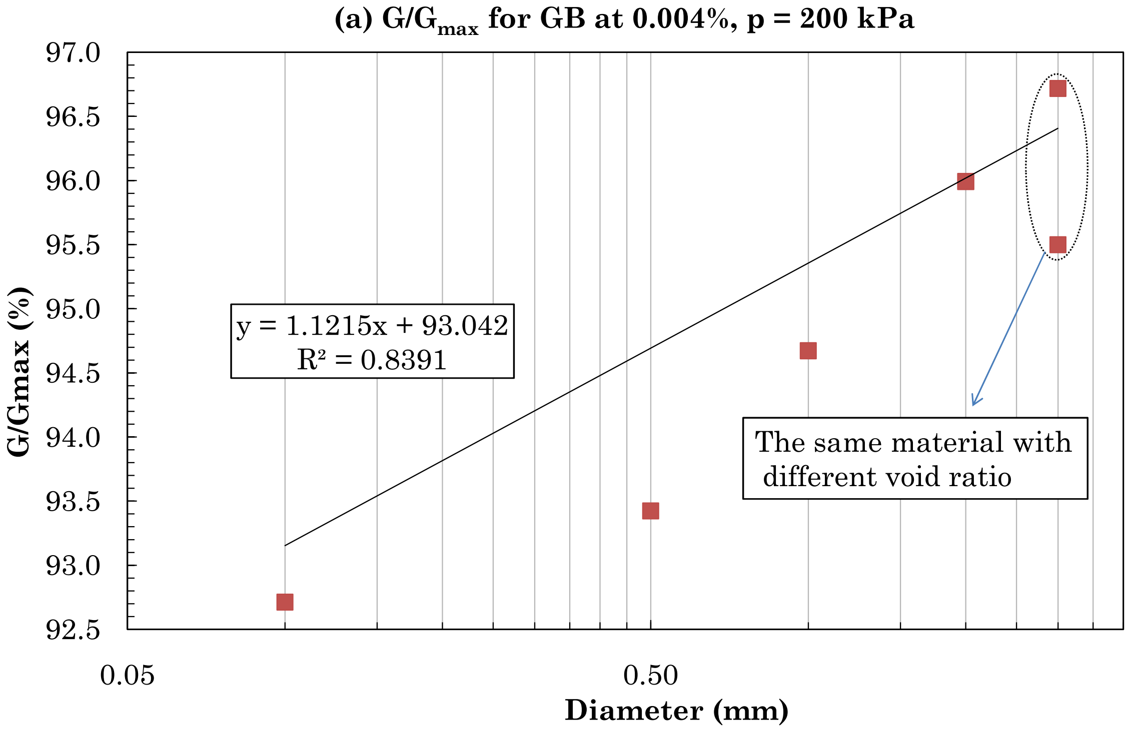

FIGURE 6.15: Shear modulus degradation of GB versus particle size at shear strain of 0.004%

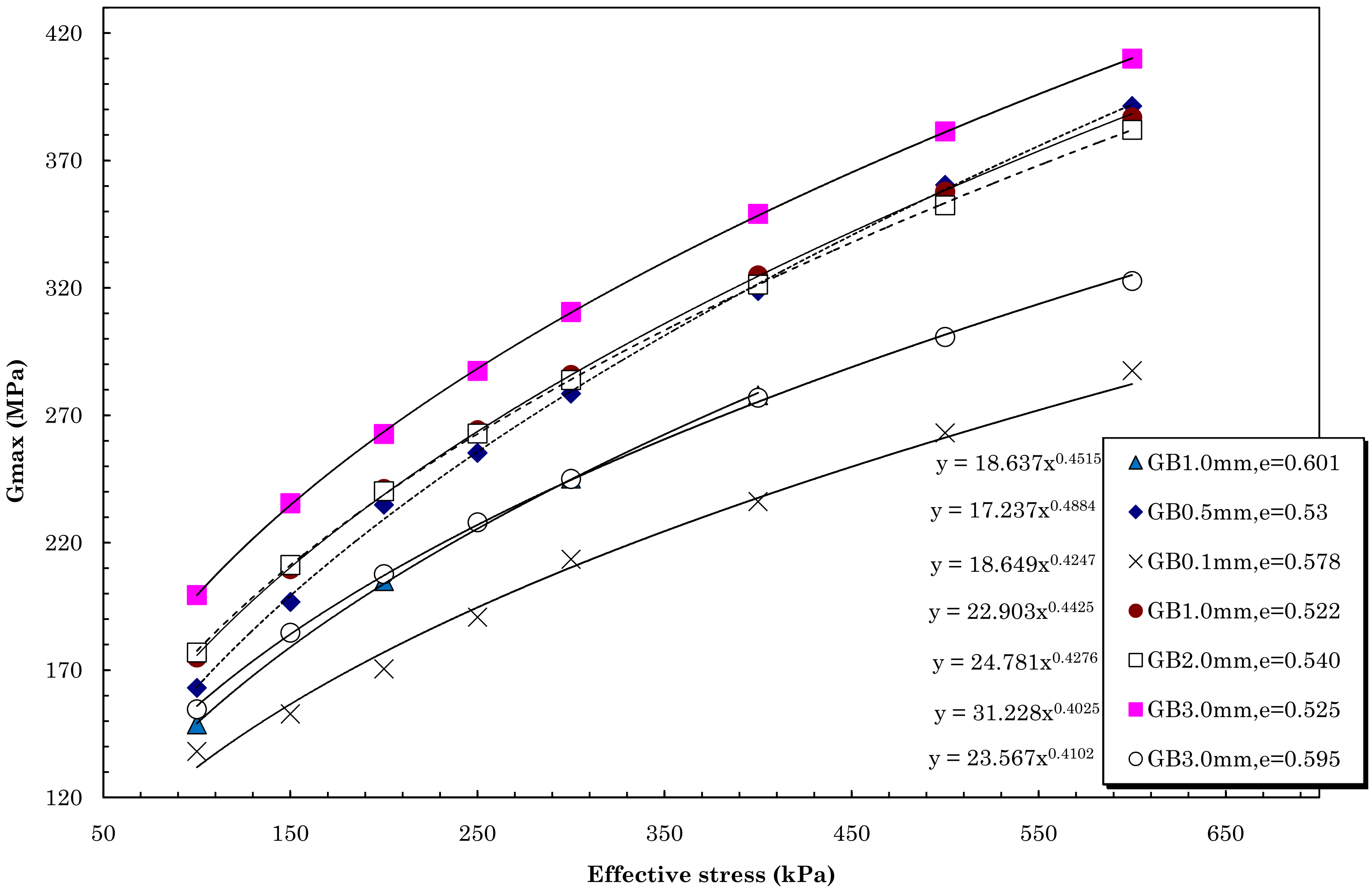

Figure 6.16: G_{max} of GB as a function of effective stress

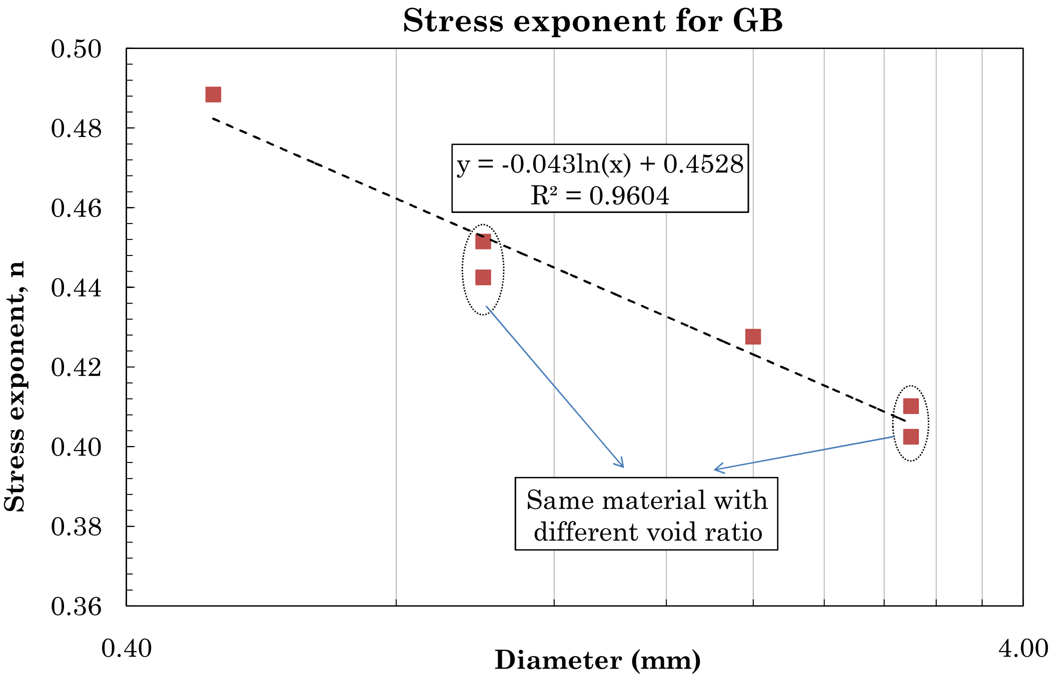

FIGURE 6.17: Stress exponent for GB as a function of particle size

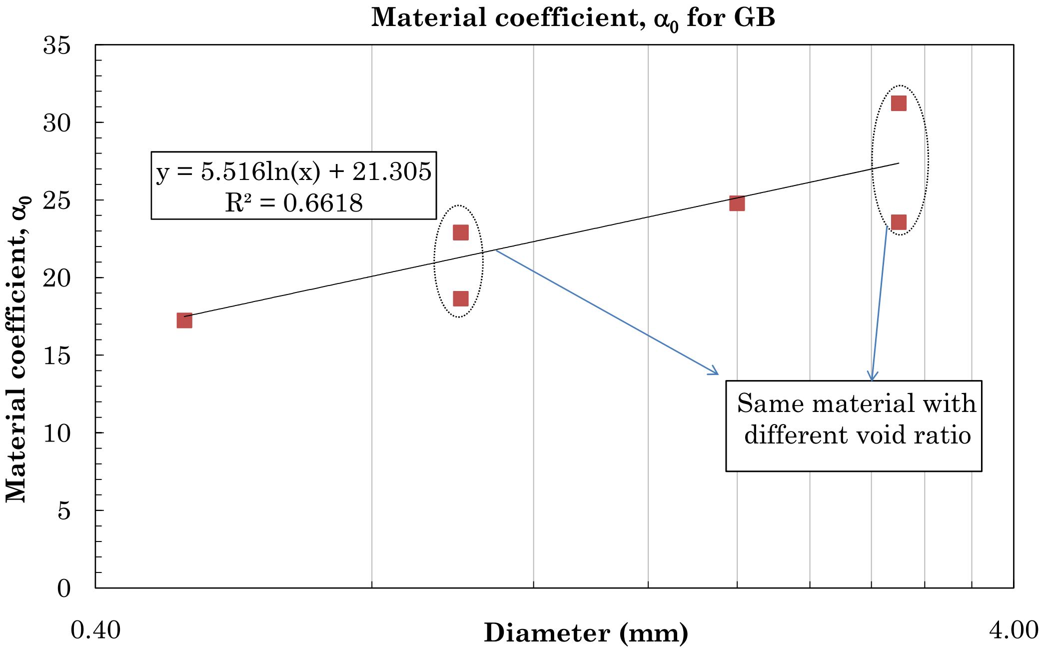

FIGURE 6.18: Material coefficient, α_0, for GB as a function of particle size

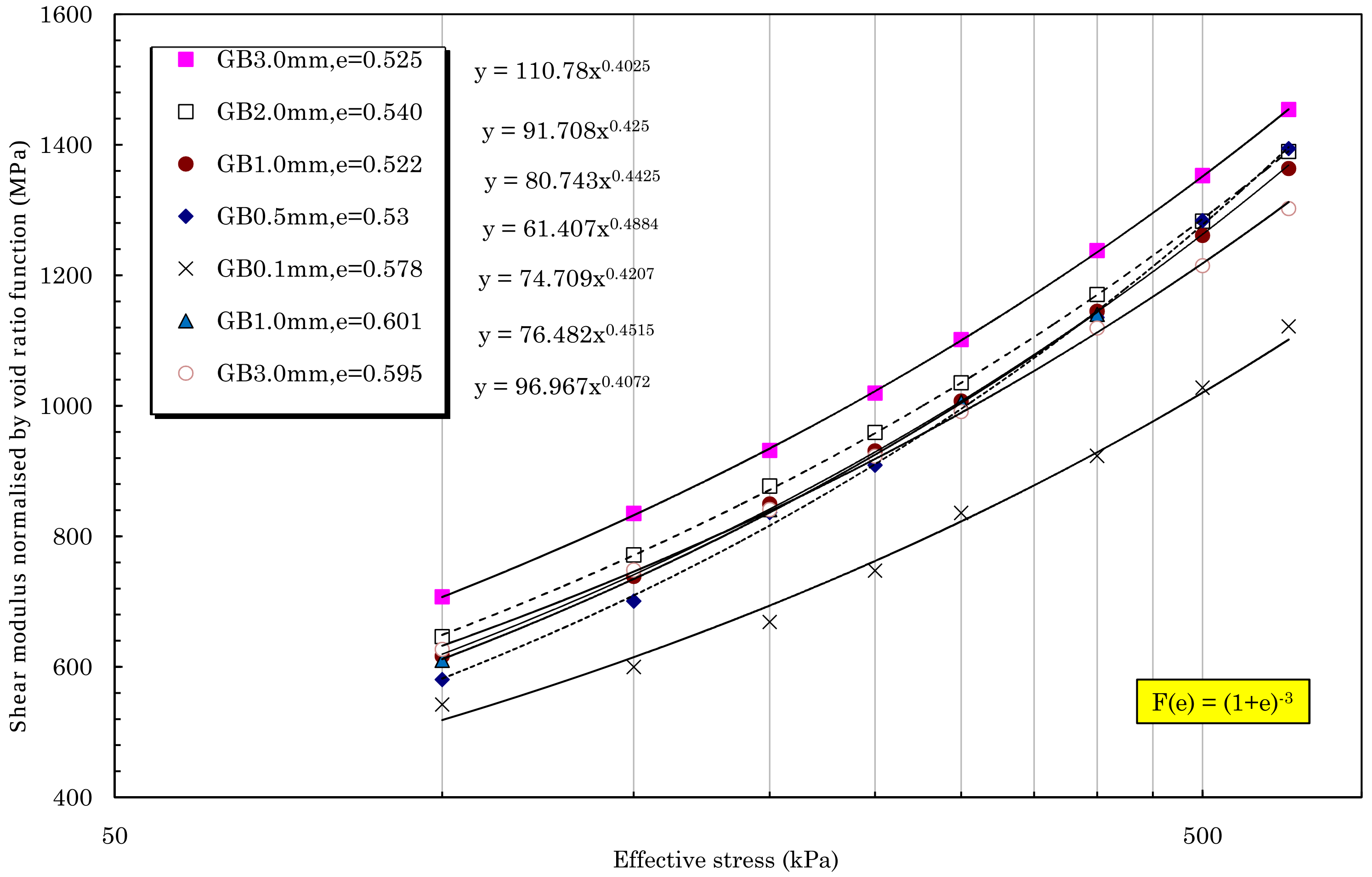

FIGURE 6.19: G_{max} normalised by $F(e)$ versus effective stress for GB

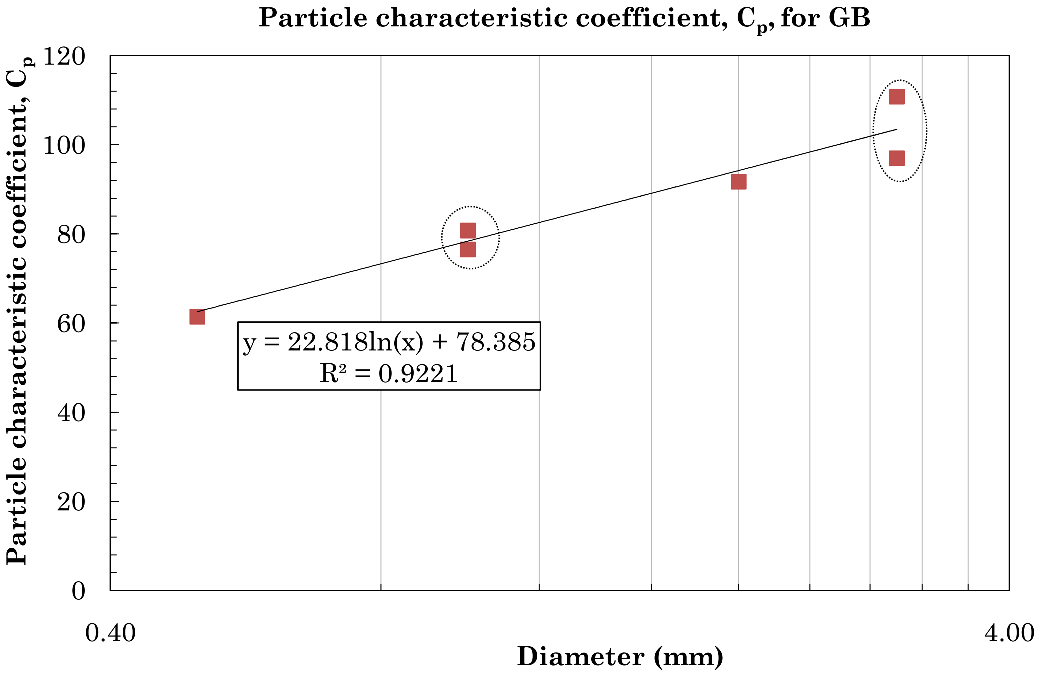

FIGURE 6.20: Particle characteristic coefficient, C_p, for GB as a function of particle size

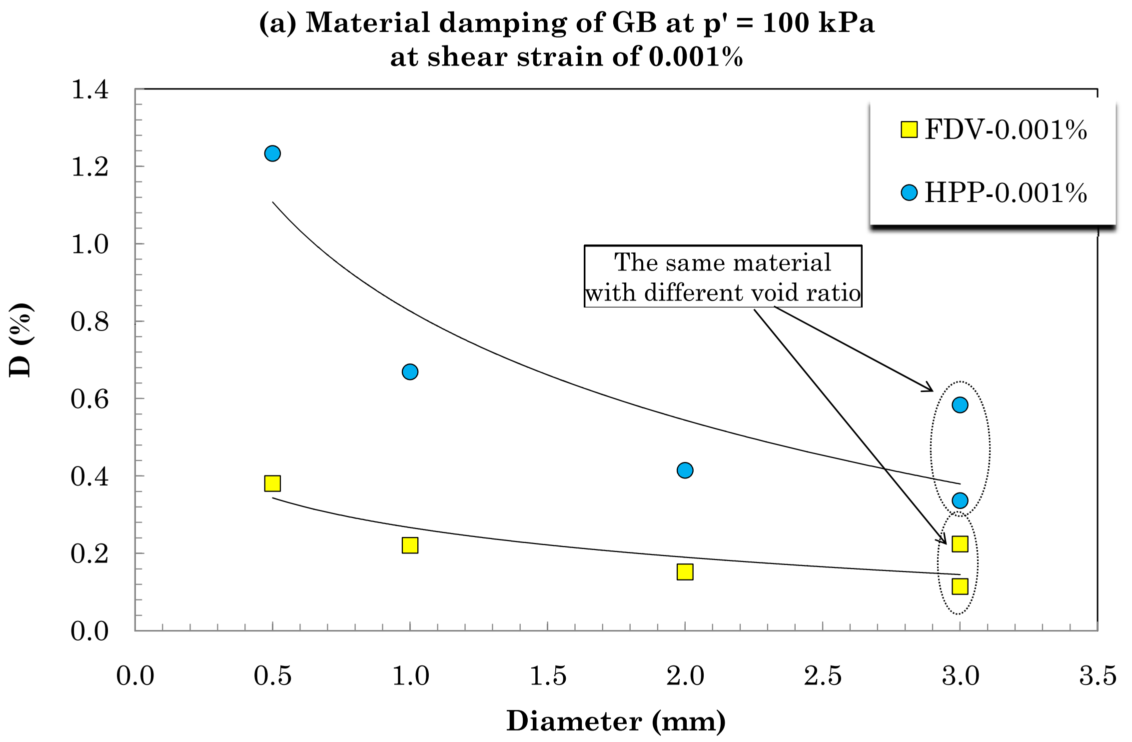

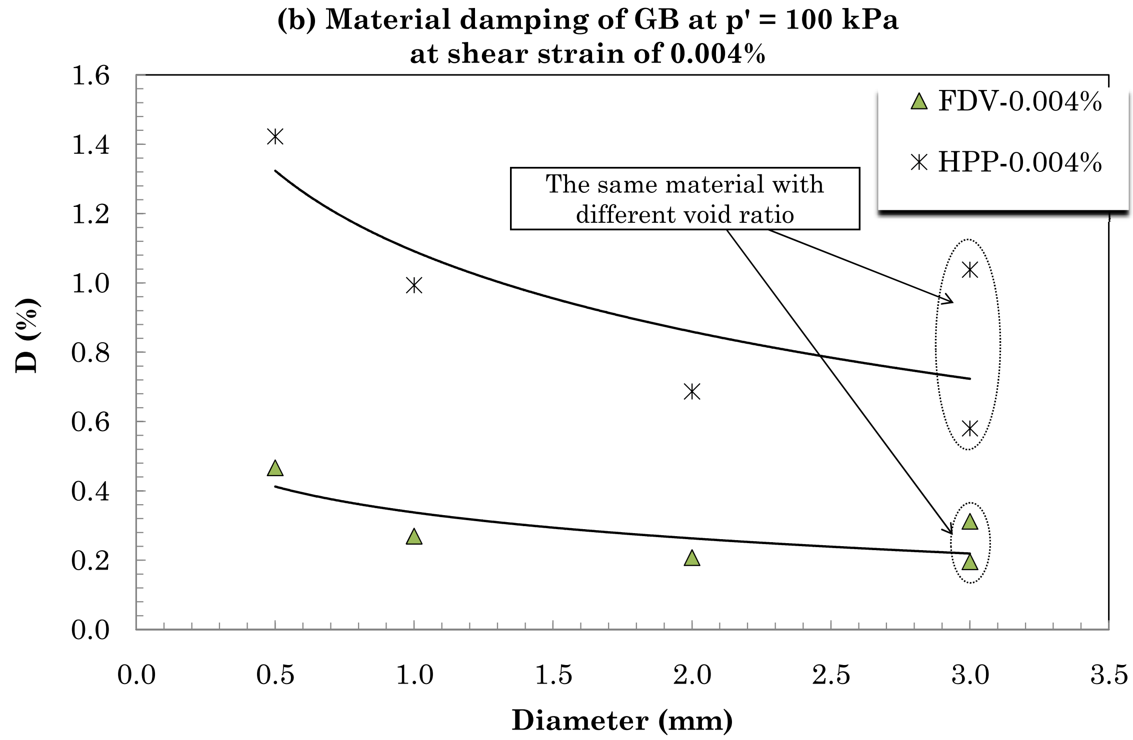

FIGURE 6.21: Effect of particle size on material damping of GB

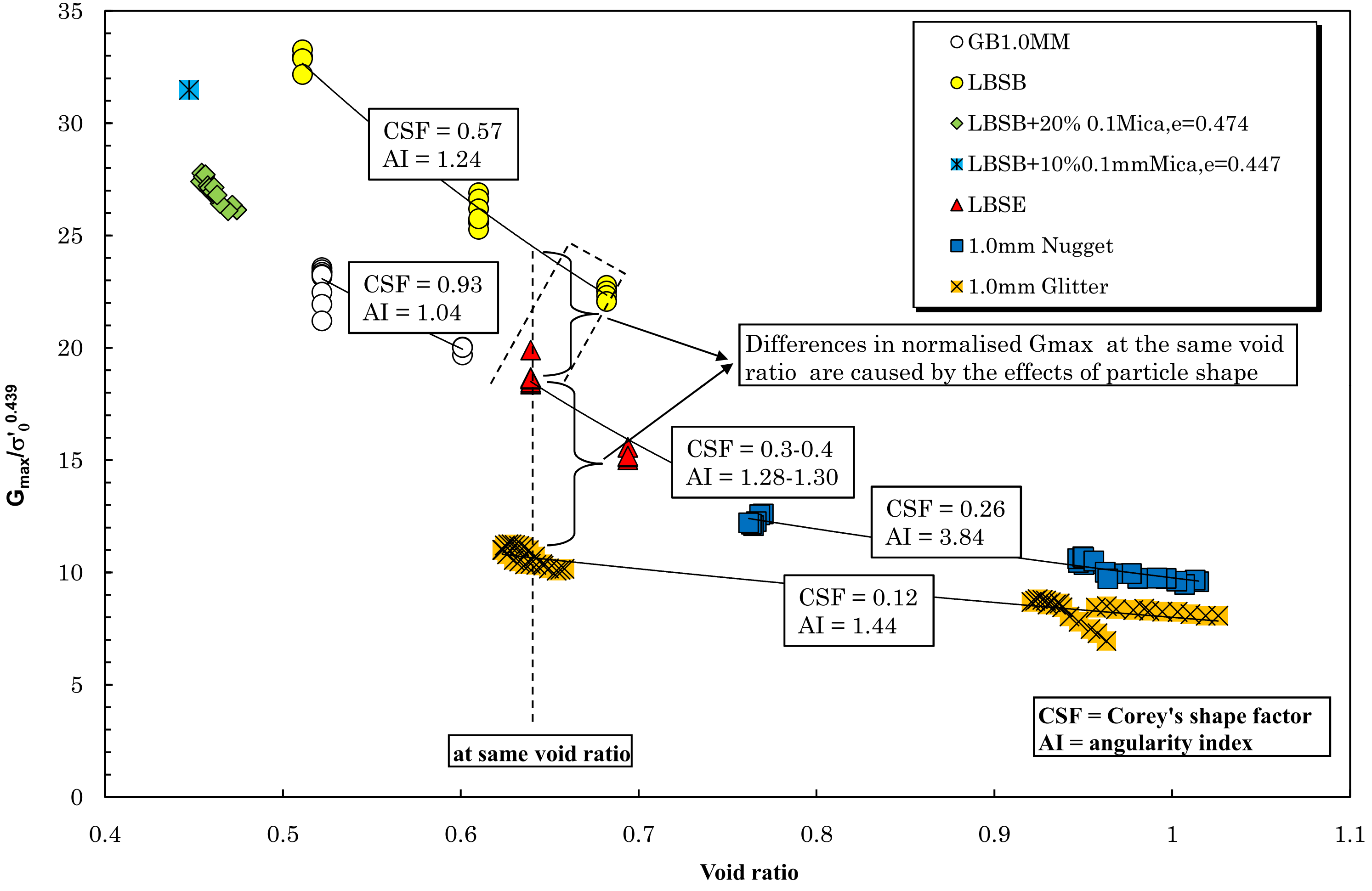

FIGURE 6.22: Maximum shear modulus normalised by effective stress versus void ratio for 1.0 mm materials

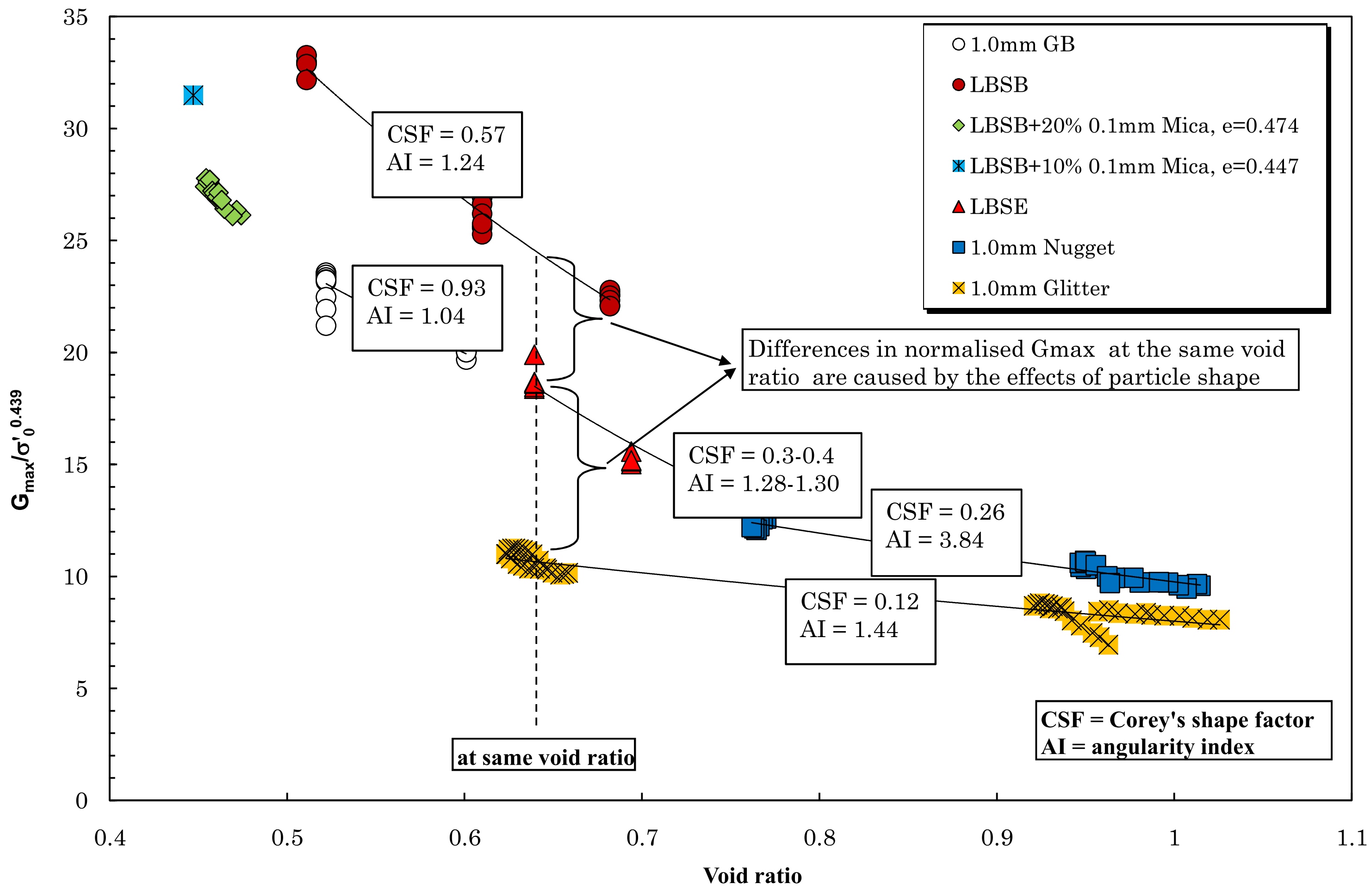

FIGURE 6.23: Maximum shear modulus normalised by effective stress (using the average stress exponent) and specific gravity versus void ratio for 1.0 mm materials

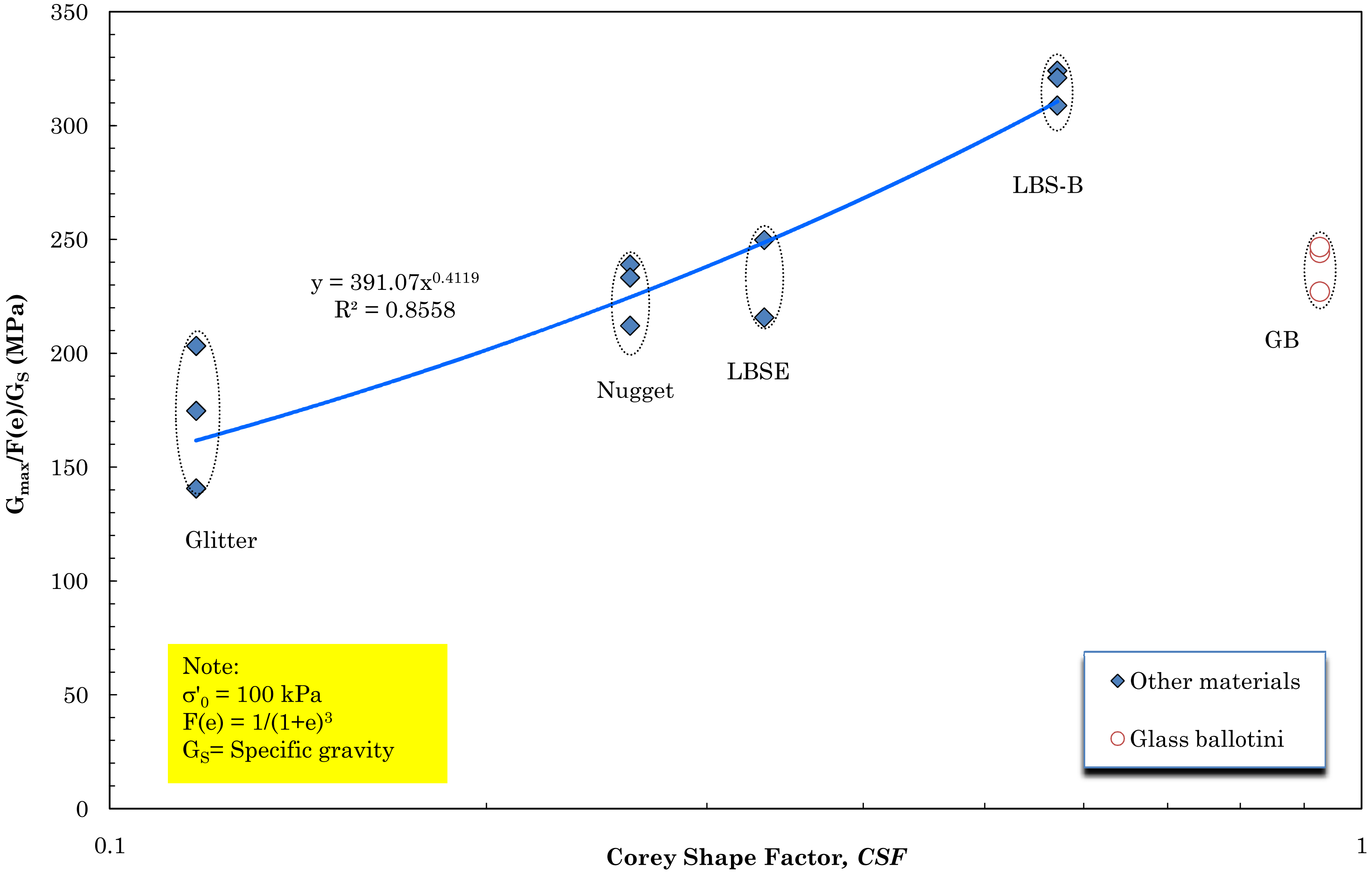

FIGURE 6.24: Effect of sphericity on G_{max} of 1.0 mm materials

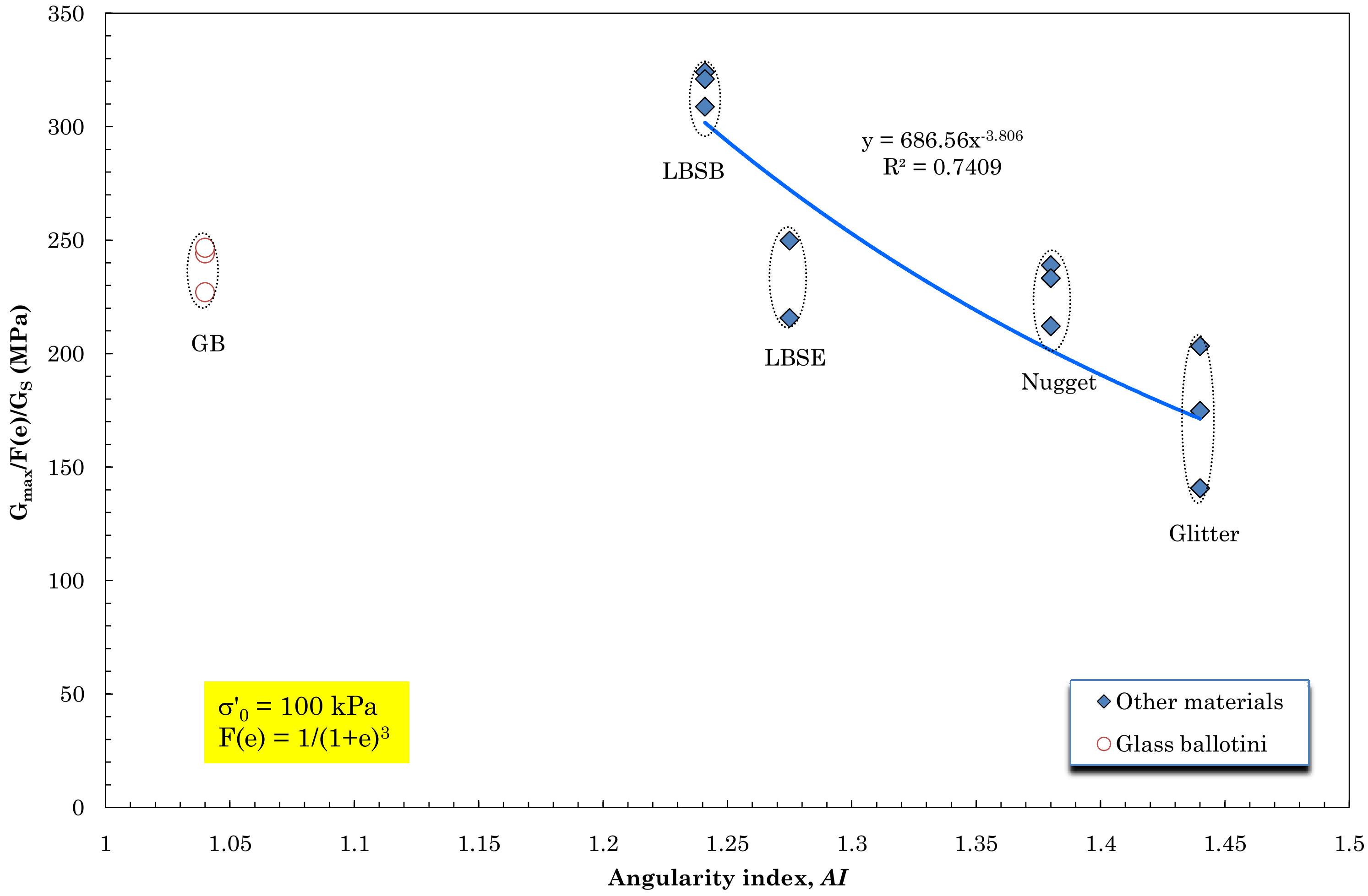

FIGURE 6.25: Effect of roundness on normalised shear modulus of 1.0 mm material

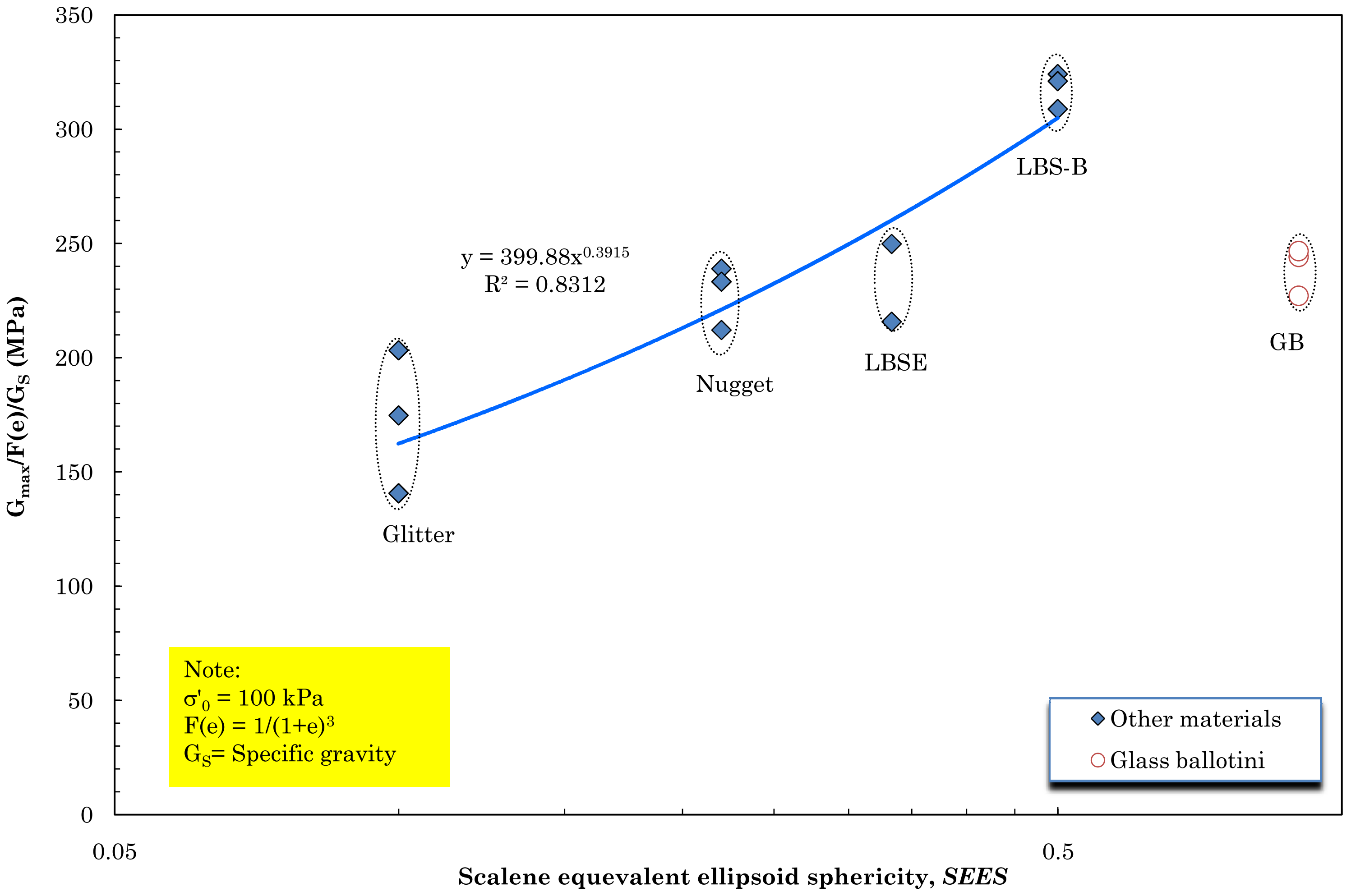

FIGURE 6.26: Effect of SEES on normalised shear modulus of 1.0 mm material

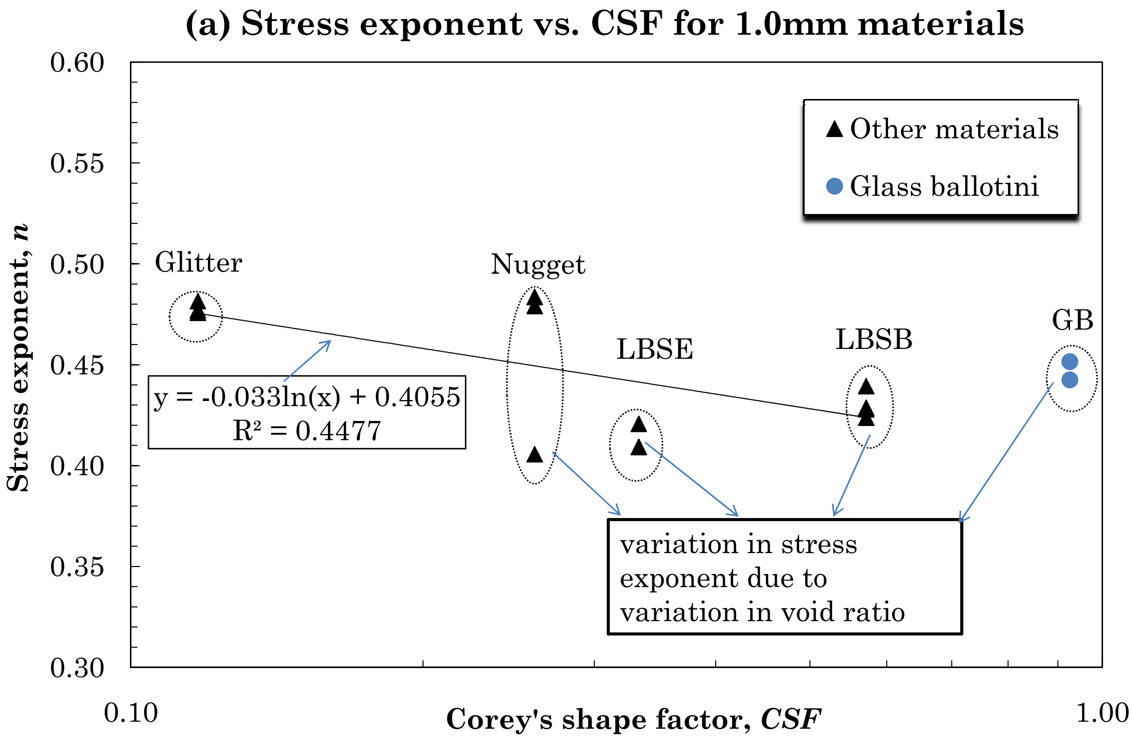
(a) Stress exponent vs. CSF for 1.0mm materials

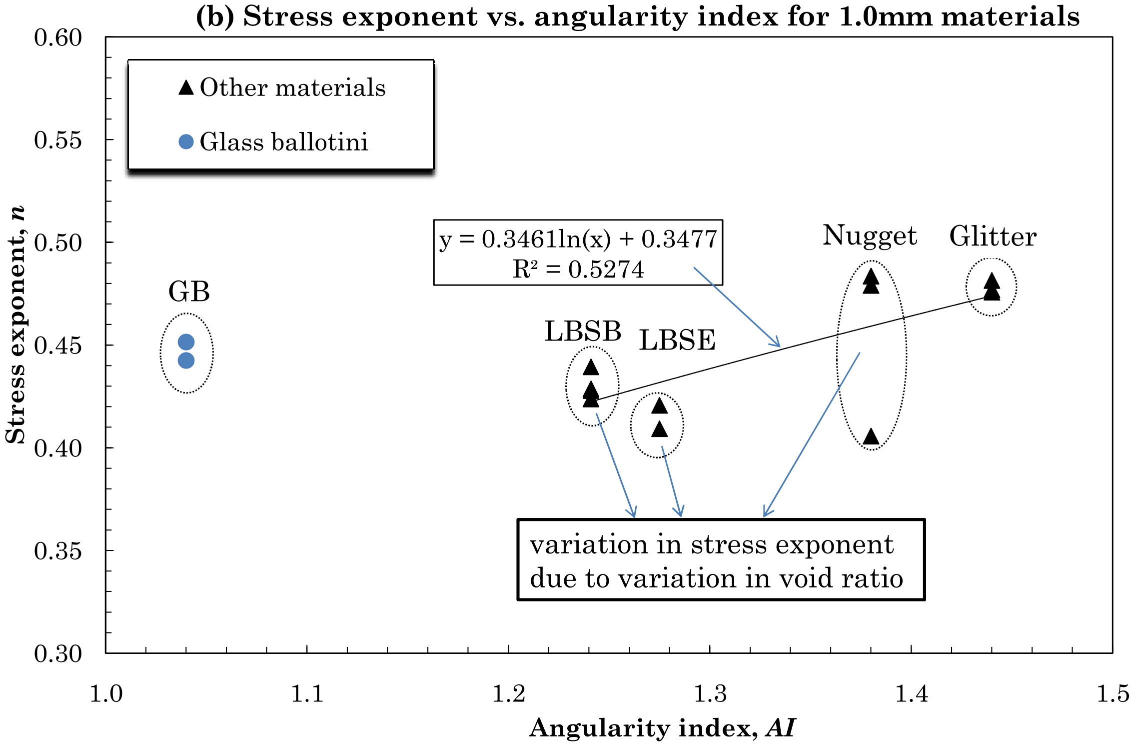
(b) Stress exponent vs. angularity index for 1.0mm materials

FIGURE 6.27: Influence of particle shape on stress exponent for 1.0 mm materials

(a) Material coefficient vs. CSF for 1.0mm materials

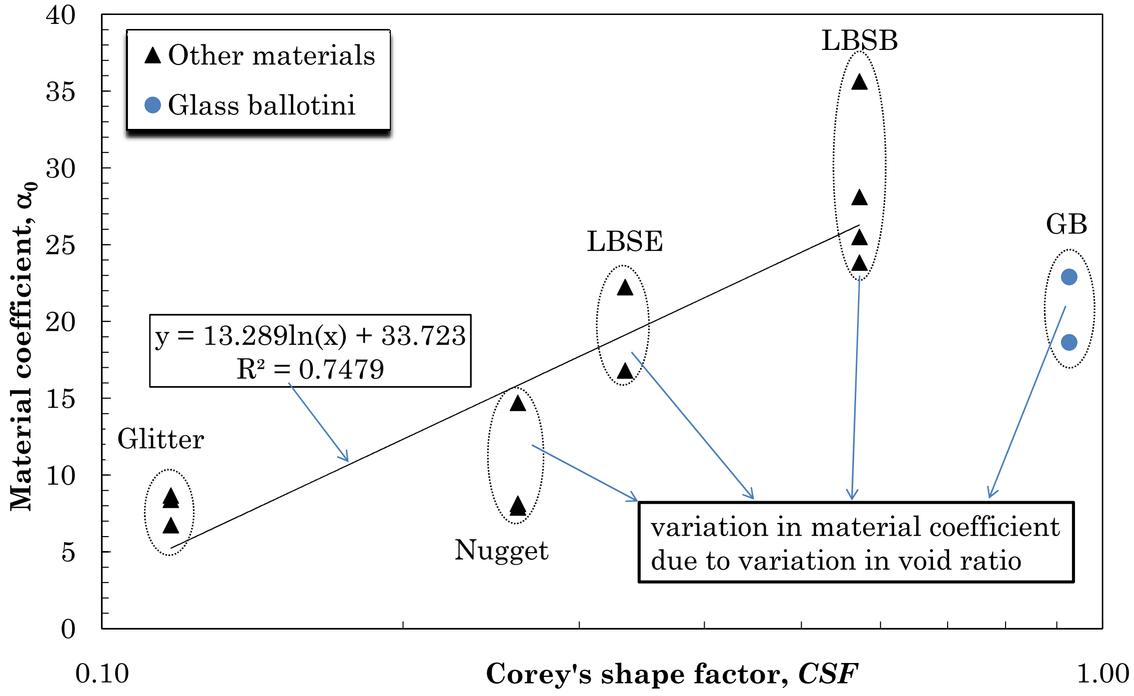

(b) Material coefficient vs. angularity index for 1.0mm materials

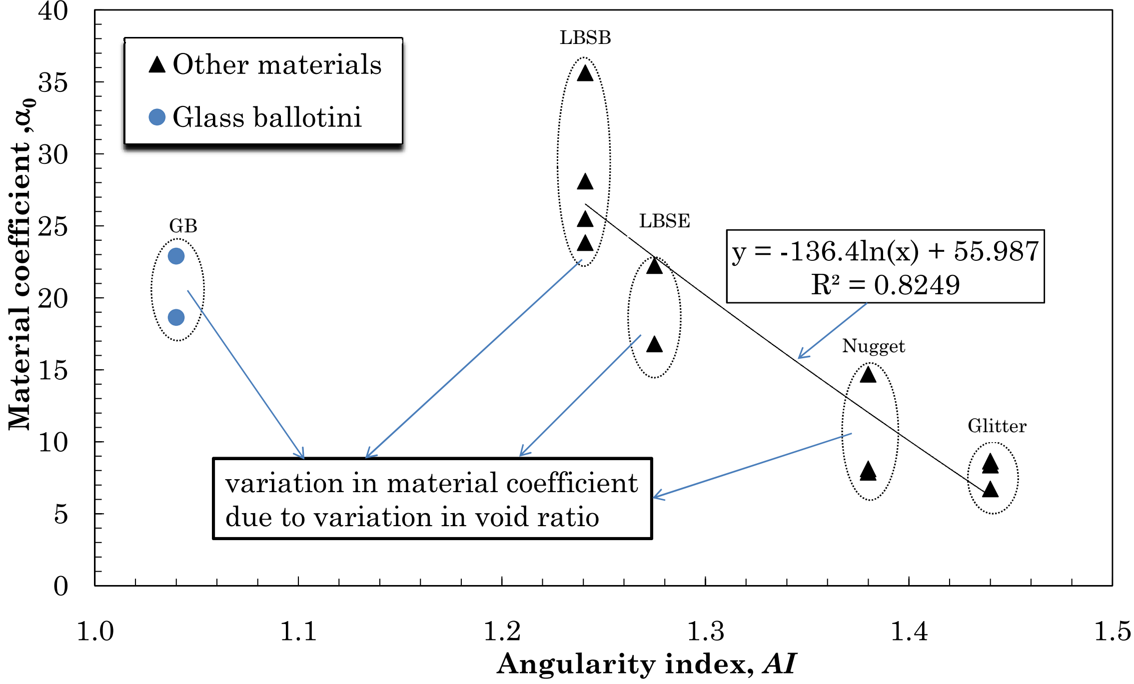

FIGURE 6.28: Influence of particle shape on material coefficient for 1.0 mm materials

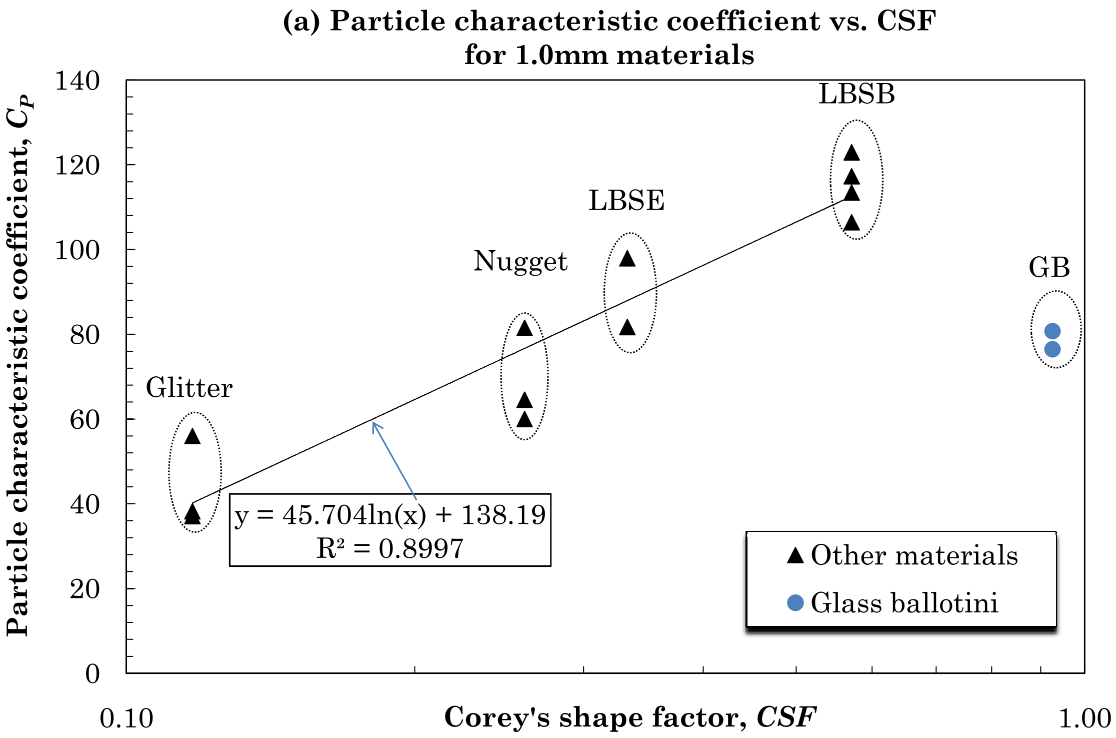
(a) Particle characteristic coefficient vs. CSF for 1.0mm materials

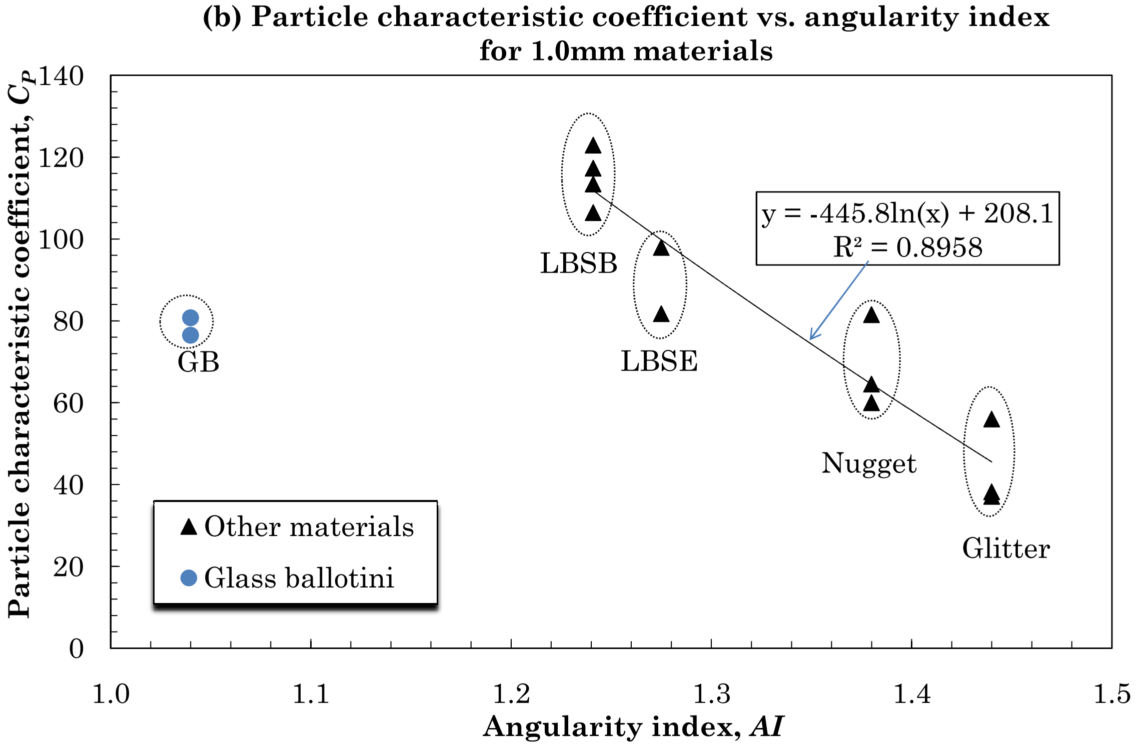
(b) Particle characteristic coefficient vs. angularity index for 1.0mm materials

FIGURE 6.29: Influence of particle shape on particle characteristic coefficient for 1.0 mm materials

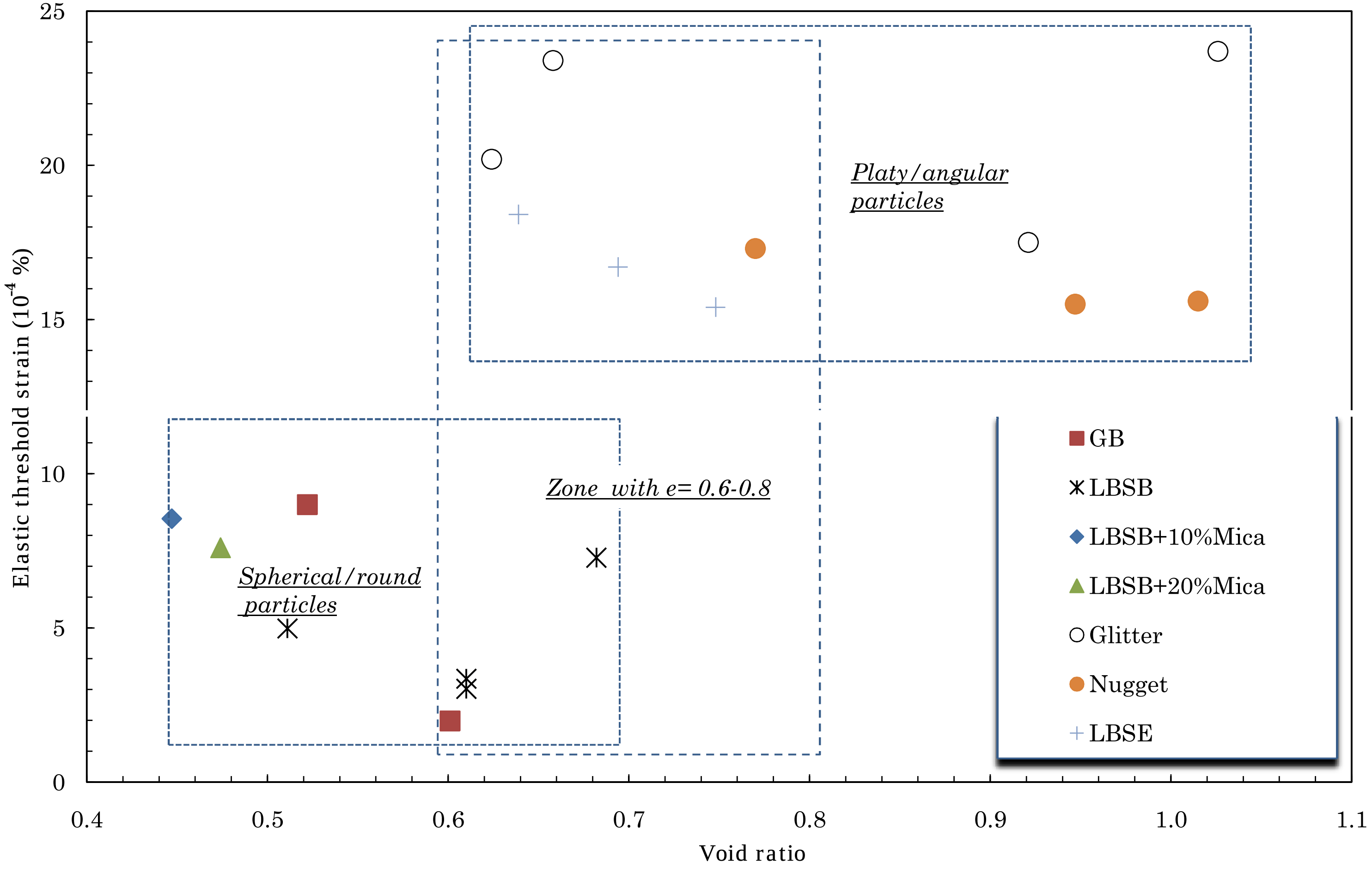

FIGURE 6.30: Elastic threshold strain at an effective stress of 100kPa and shear strain of 0.004% versus void ratio for 1.0 mm materials

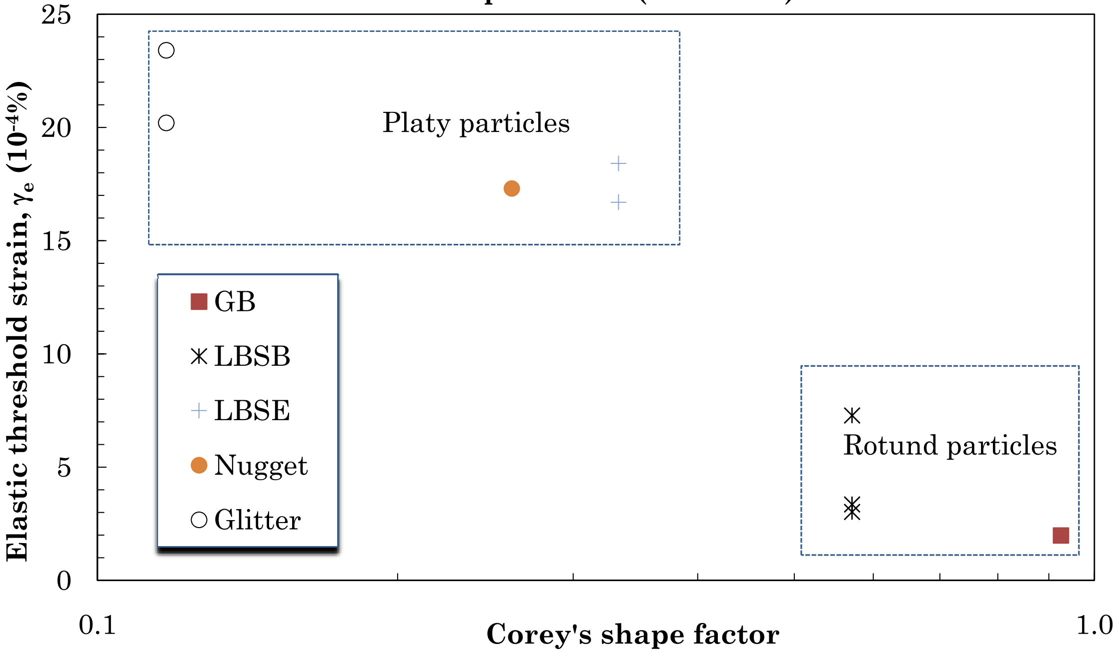

(a) Elastic threshold strain vs. CSF for the specimens (e = 0.6-0.8)

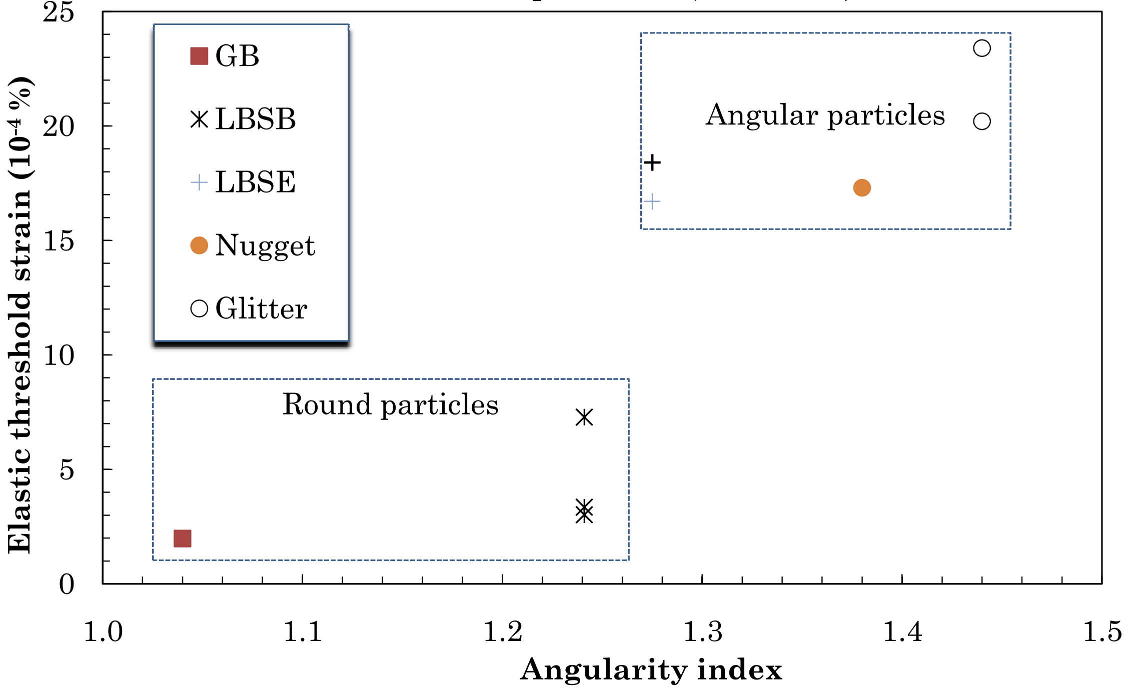

(b) Elastic threshold strain vs. angularity index of the specimens (e = 0.6-0.8)

FIGURE 6.31: Influence of particle shape on elastic threshold strain at an effective stress of 100kPa

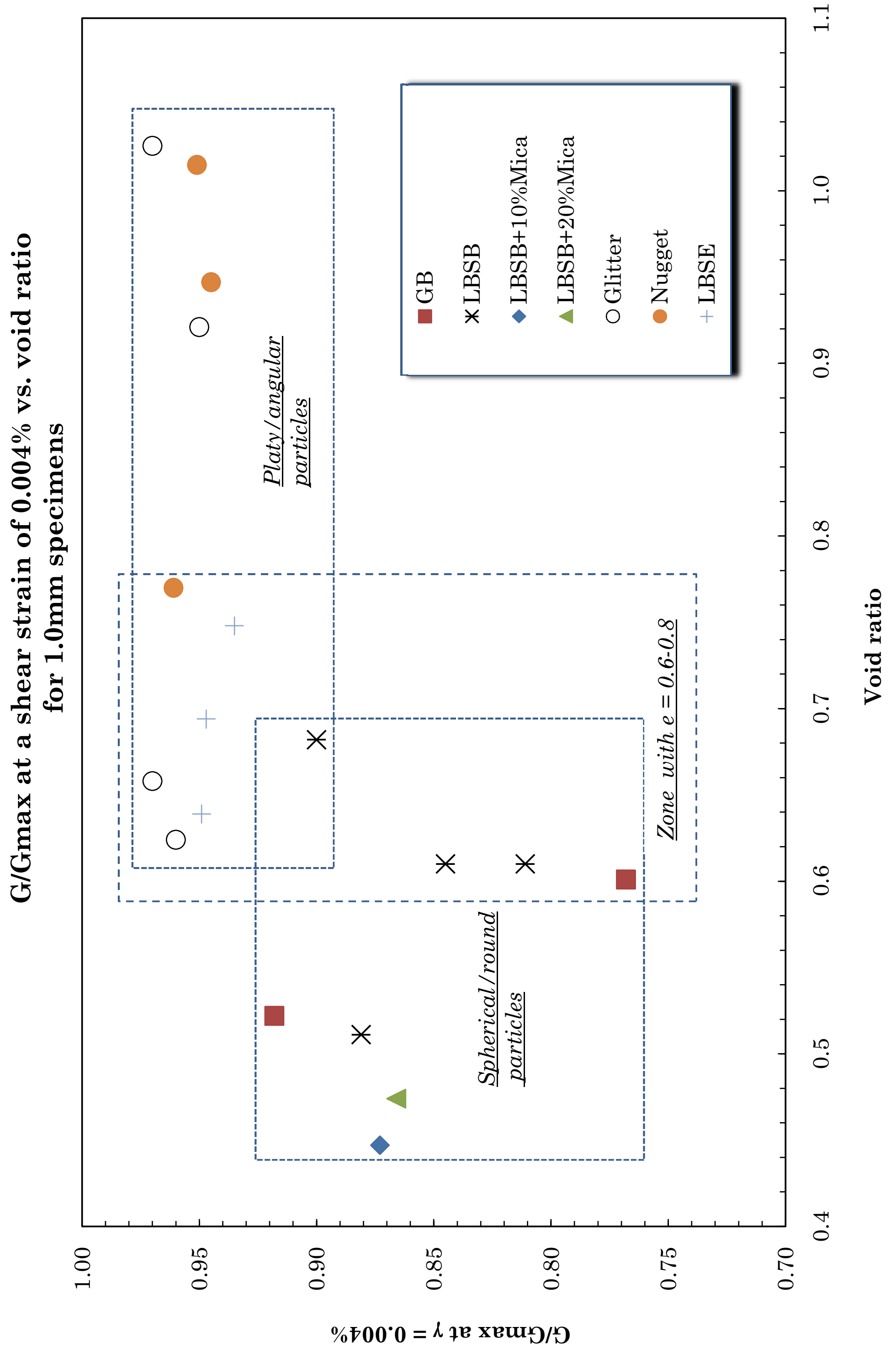

FIGURE 6.32: Shear modulus degradation at an effective stress of 100kPa and shear strain of 0.004% versus void ratio for 1.0 mm materials

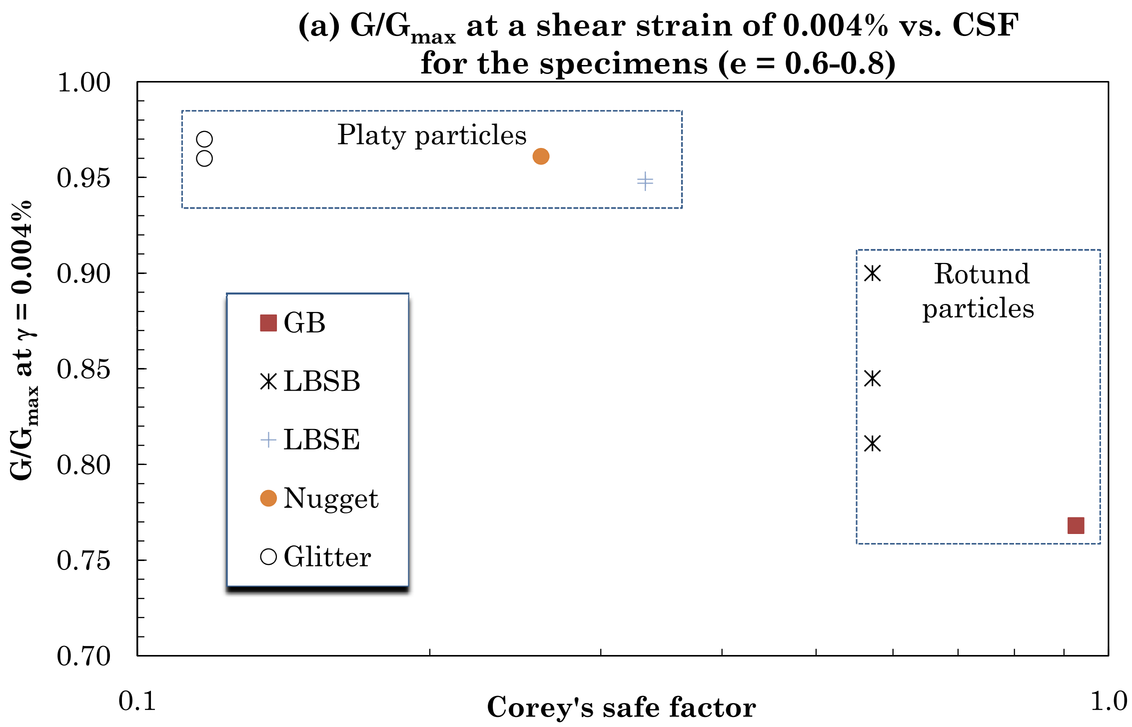

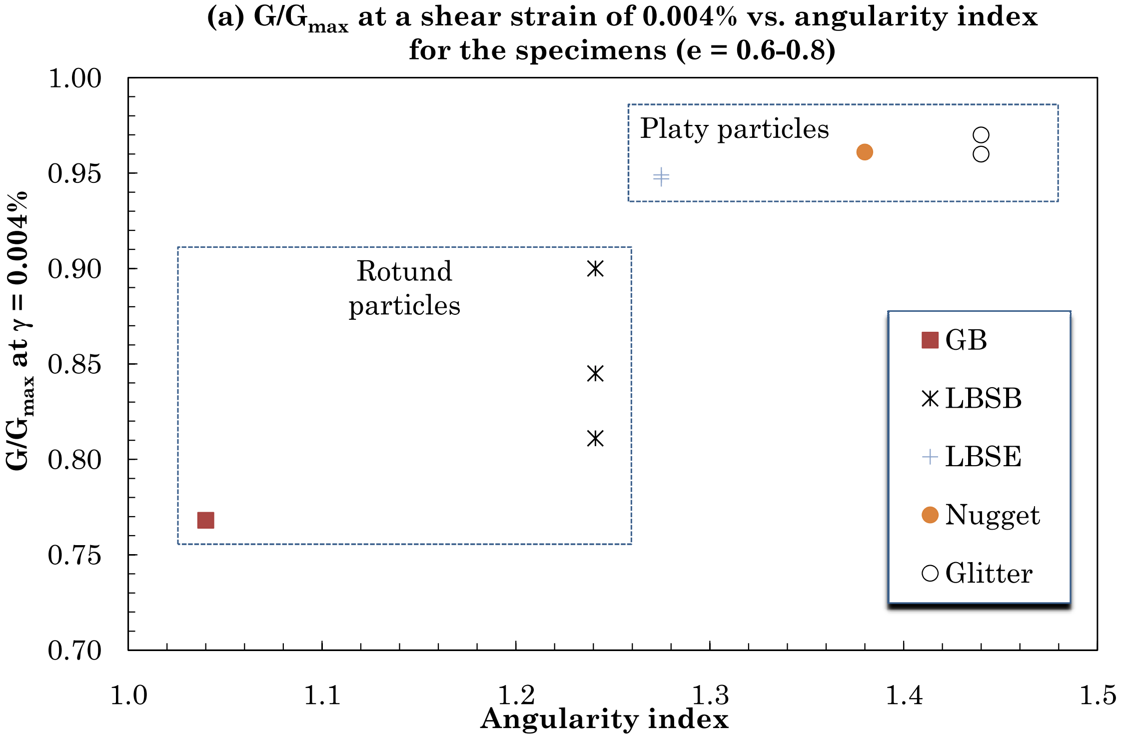

FIGURE 6.33: Influence of particle shape on shear modulus degradation at effective stress of 100kPa

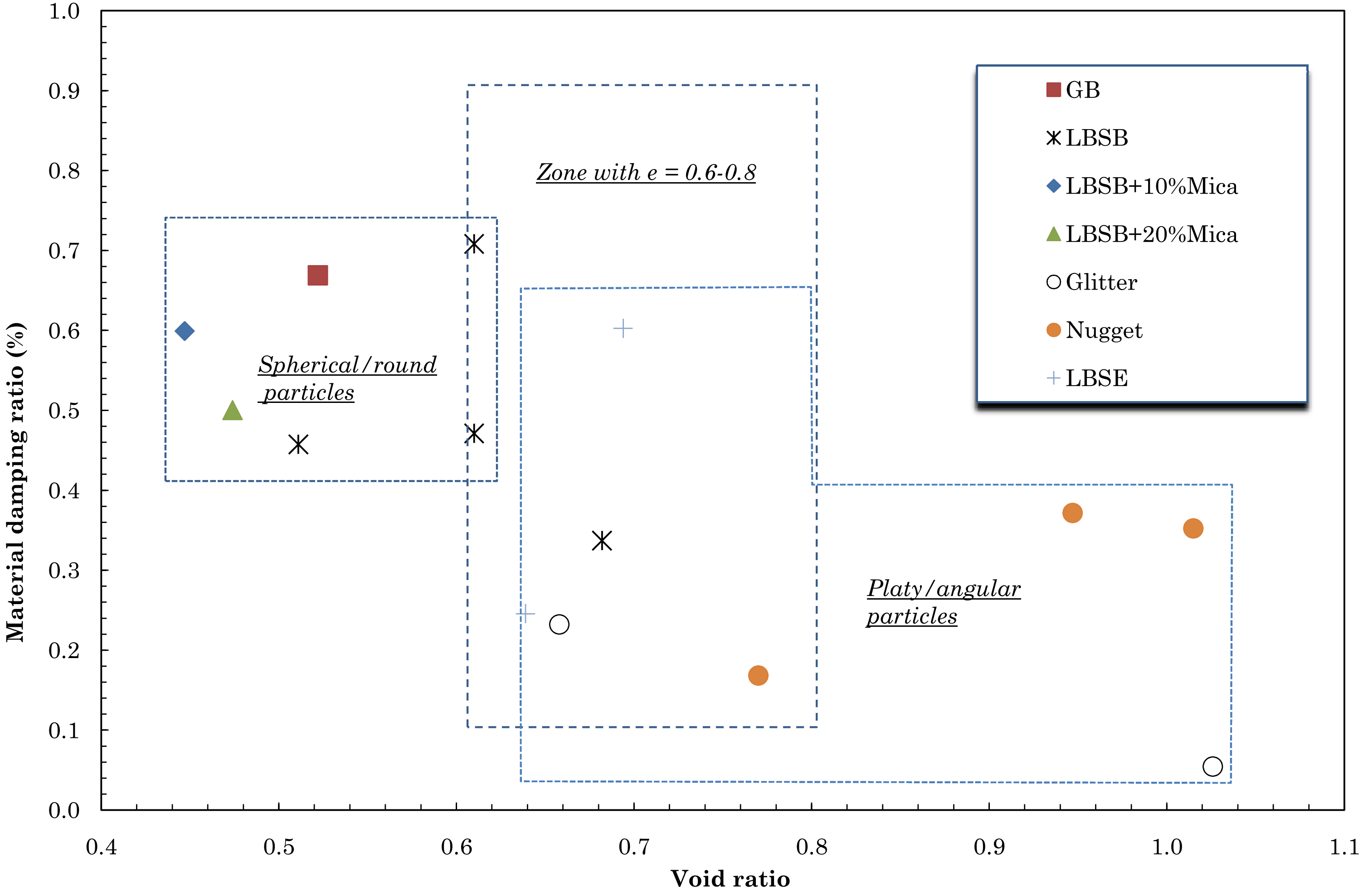

FIGURE 6.34: Material damping at effective stress of 100kPa and shear strain of 0.001% versus void ratio for 1.0 mm materials

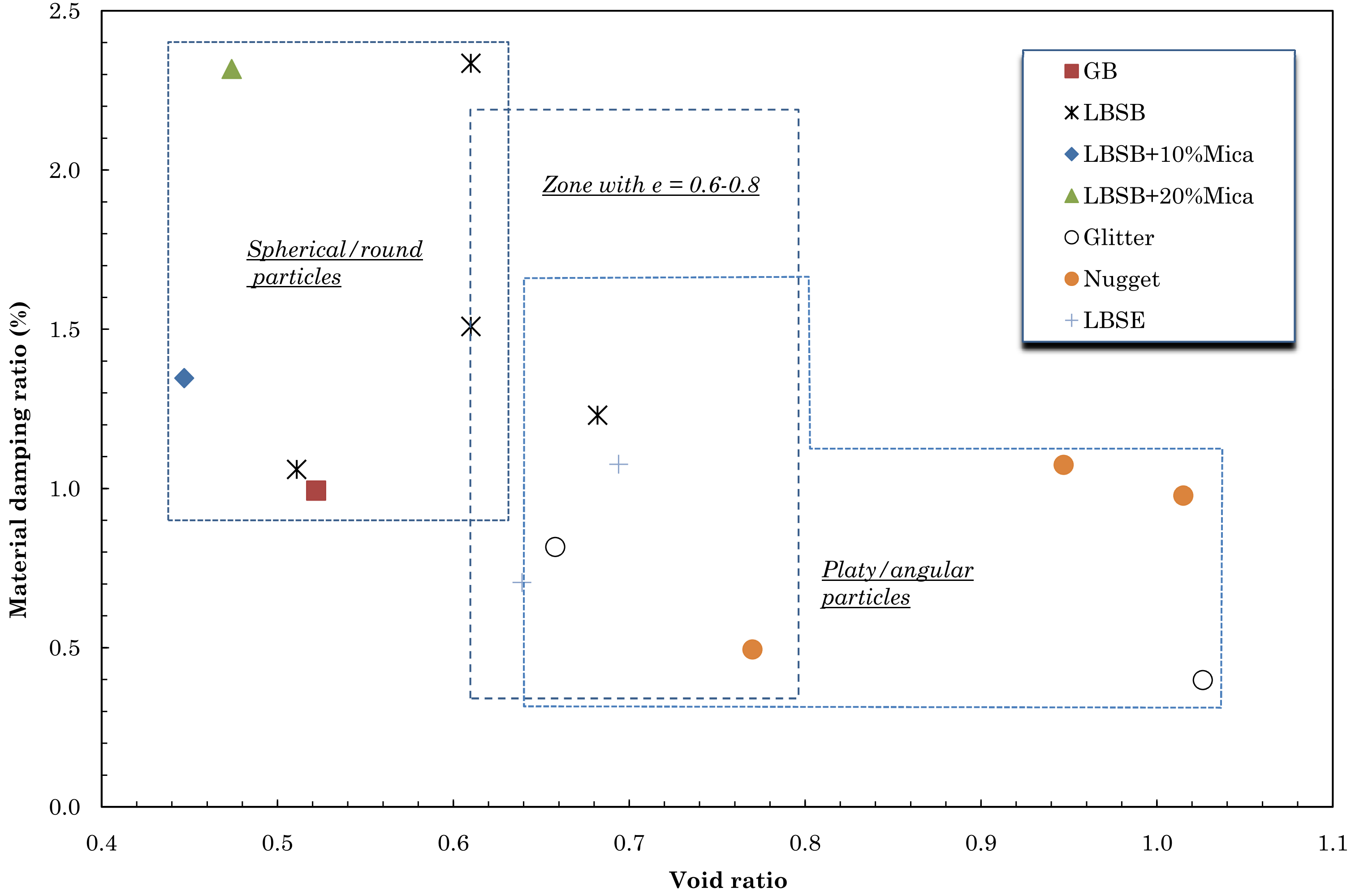

FIGURE 6.35: Material damping at effective stress of 100kPa and shear strain of 0.004% versus void ratio for 1.0 mm materials

(a) Material damping at a shear strain of 0.001% vs. CSF of the specimens (e = 0.6-0.8)

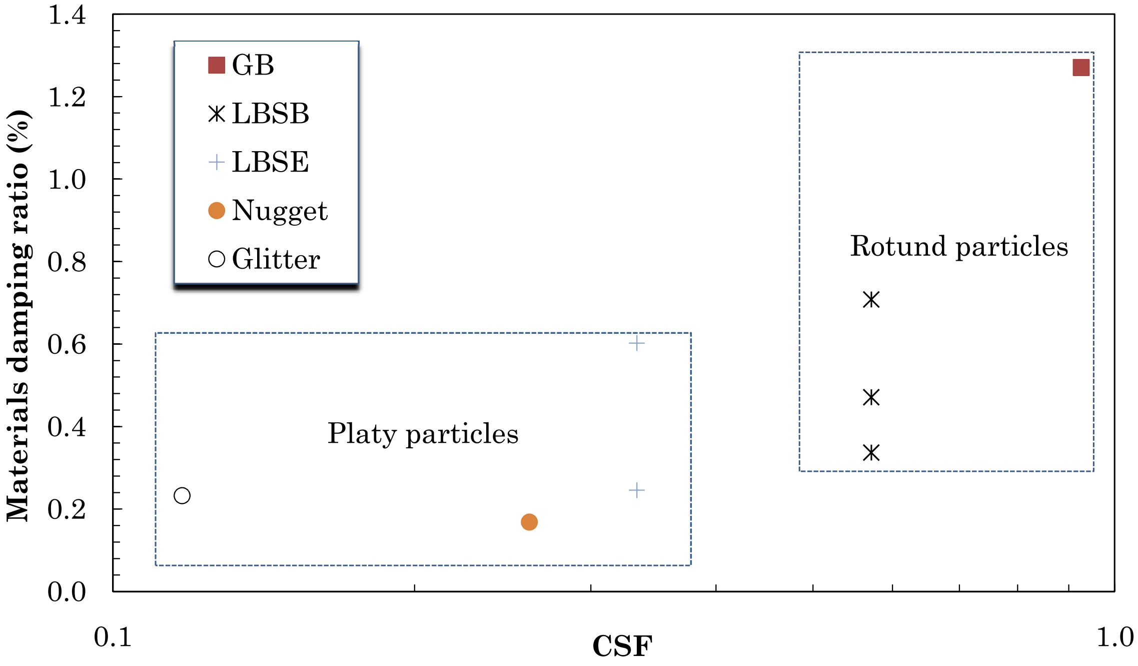

(b) Material damping at a shear strain of 0.001% vs. angularity of the specimens (e = 0.6-0.8)

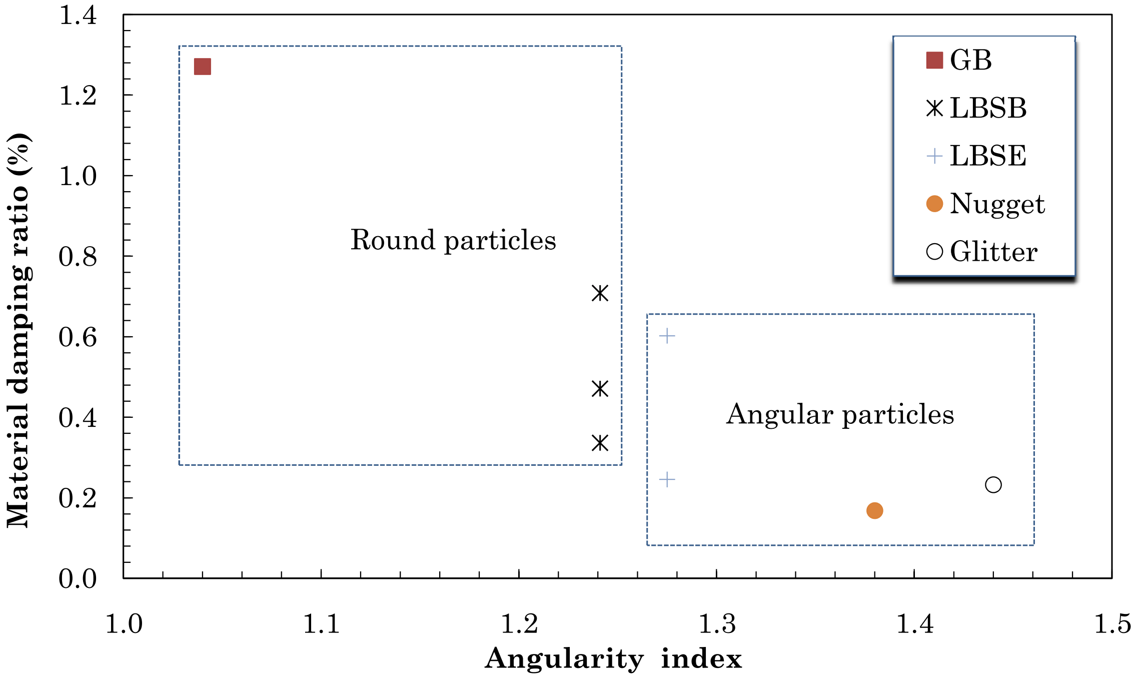

FIGURE 6.36: Influence of particle shape on material damping at a shear strain of 0.001%,$\sigma'_0 = 100kPa$

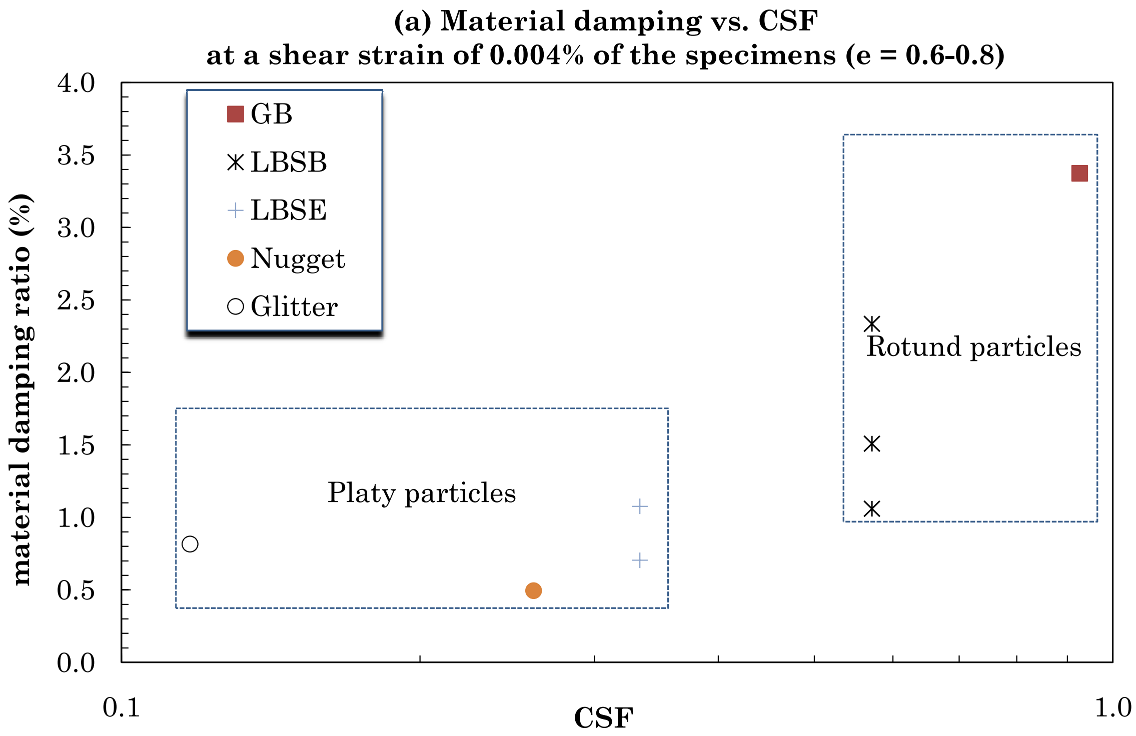
(a) Material damping vs. CSF at a shear strain of 0.004% of the specimens (e = 0.6-0.8)

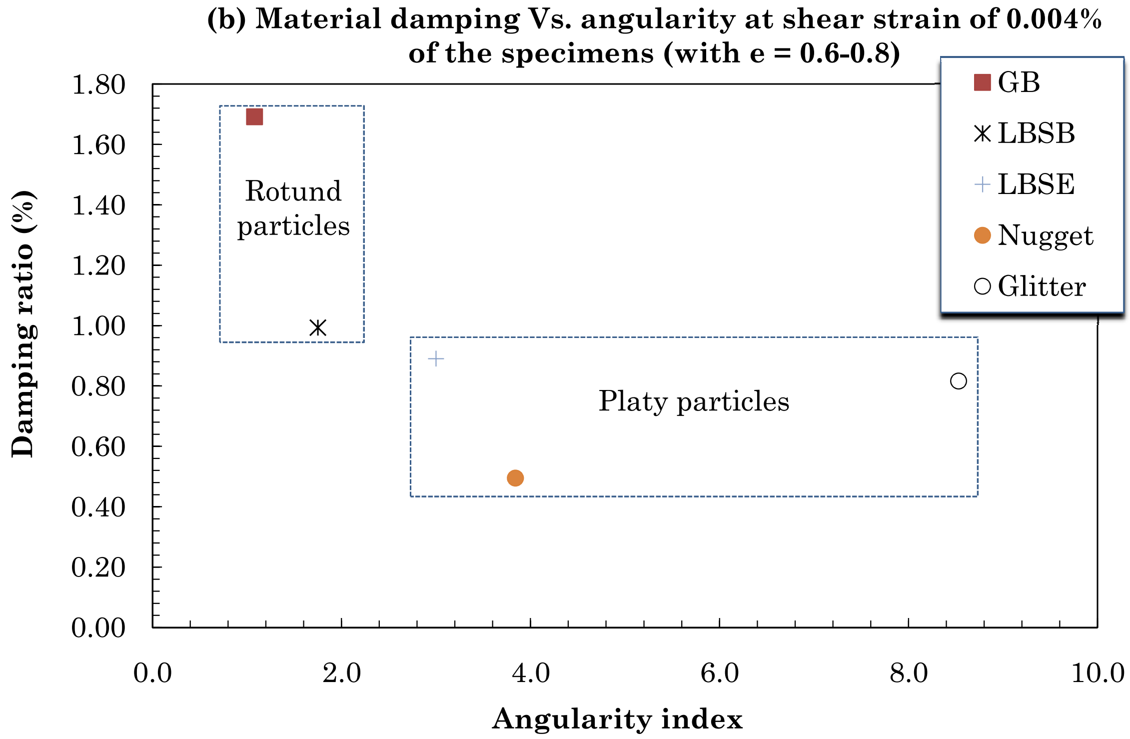
(b) Material damping Vs. angularity at shear strain of 0.004% of the specimens (with e = 0.6-0.8)

FIGURE 6.37: Influence of particle shape on material damping at a shear strain of 0.004%, $\sigma'_0 = 100kPa$

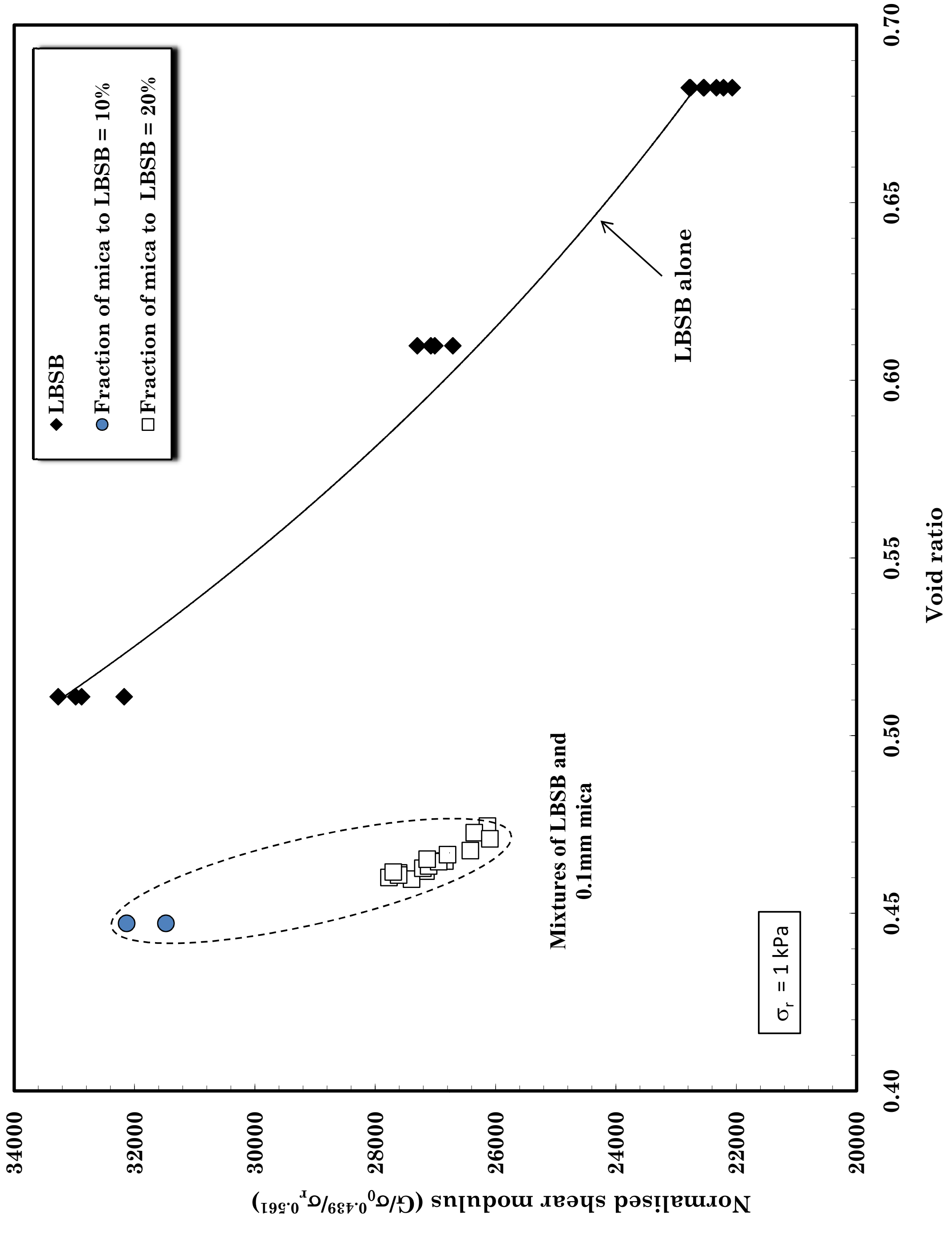

FIGURE 6.38: Normalised shear modulus versus void ratio for mixture of sand and mica

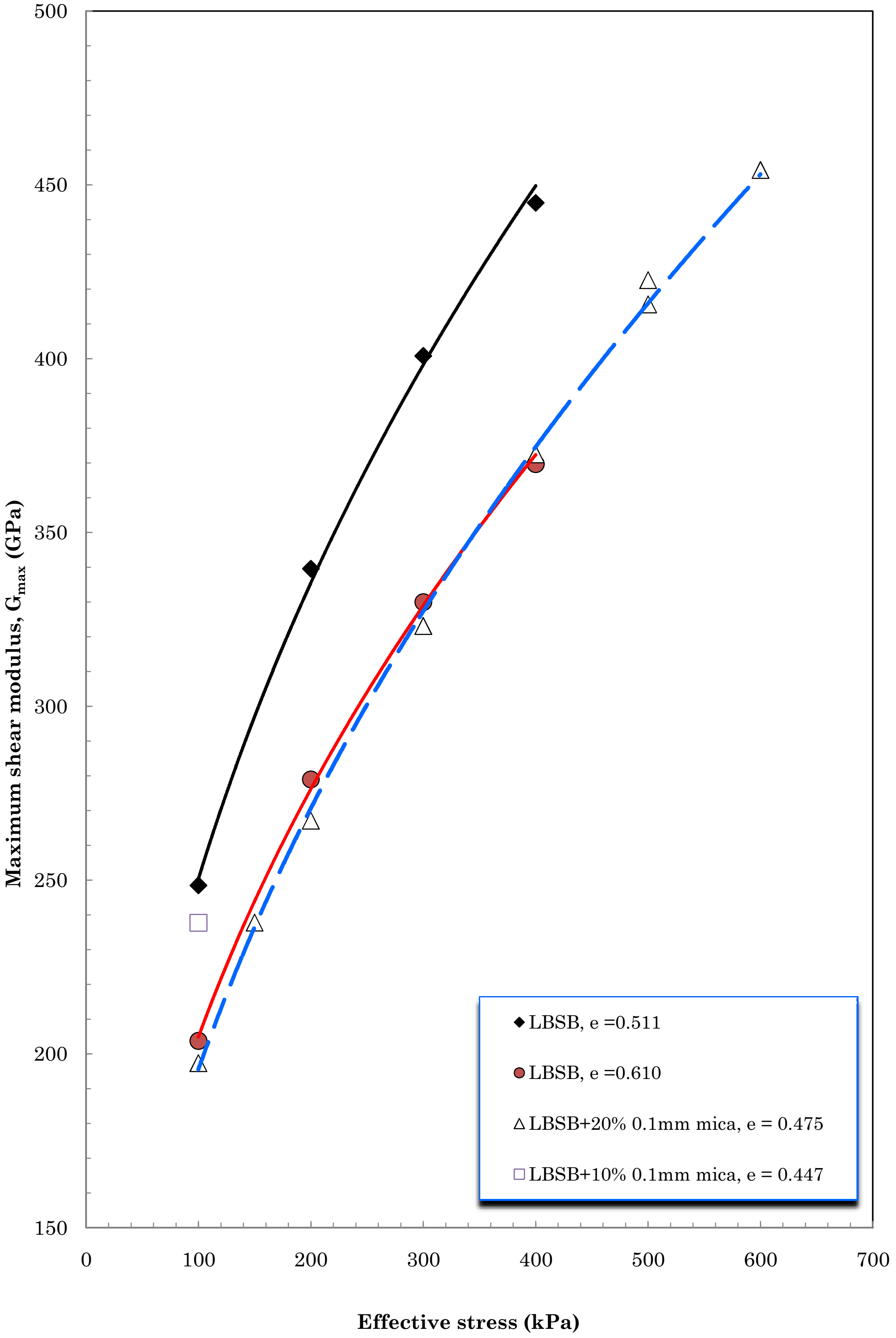

FIGURE 6.39: Shear modulus versus effective stress of the mixtures of sand and mica

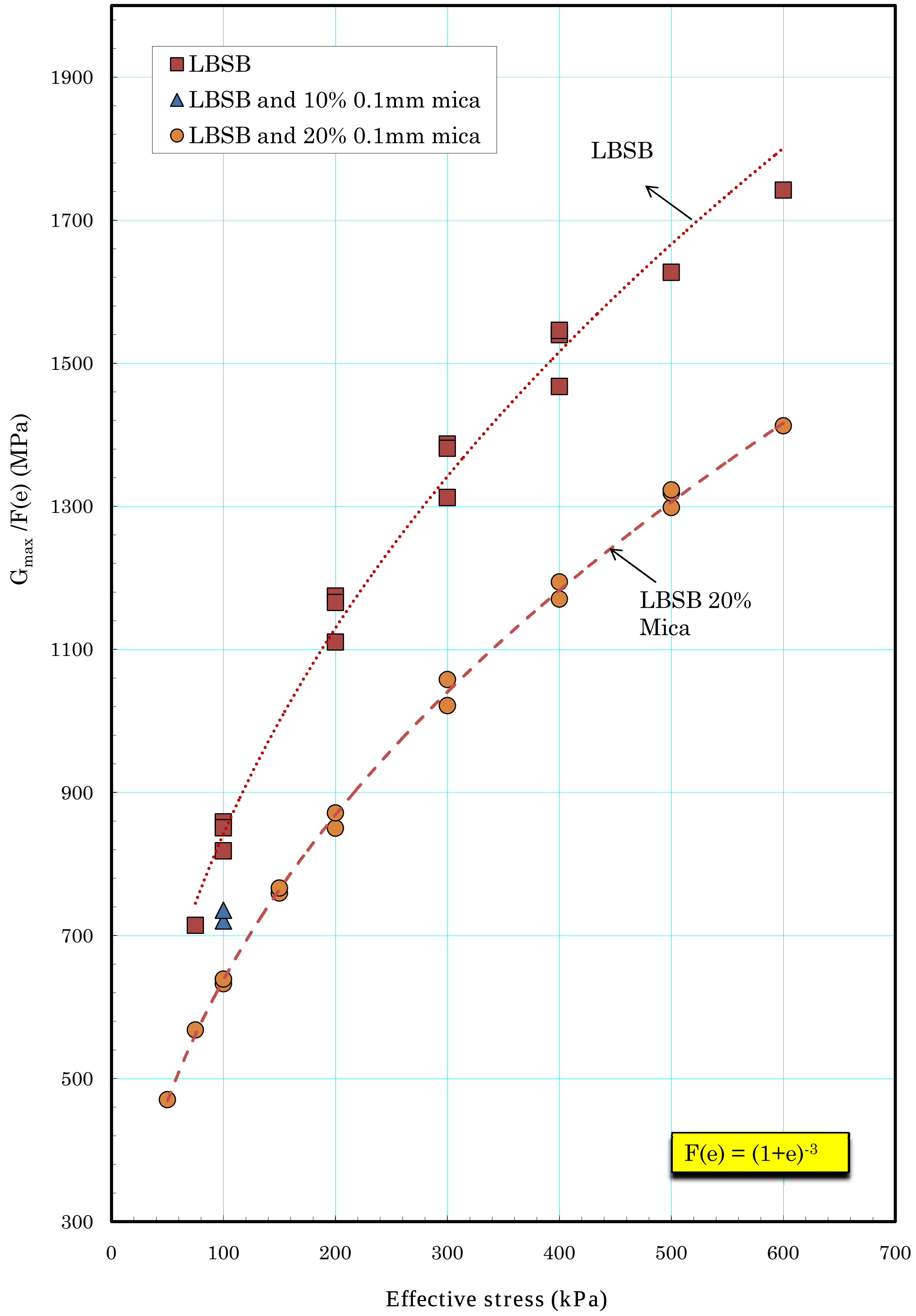

FIGURE 6.40: Shear modulus normalised by F(e) versus effective stress of LBSB specimens and the mixtures of LBSB and 0.1 mm mica

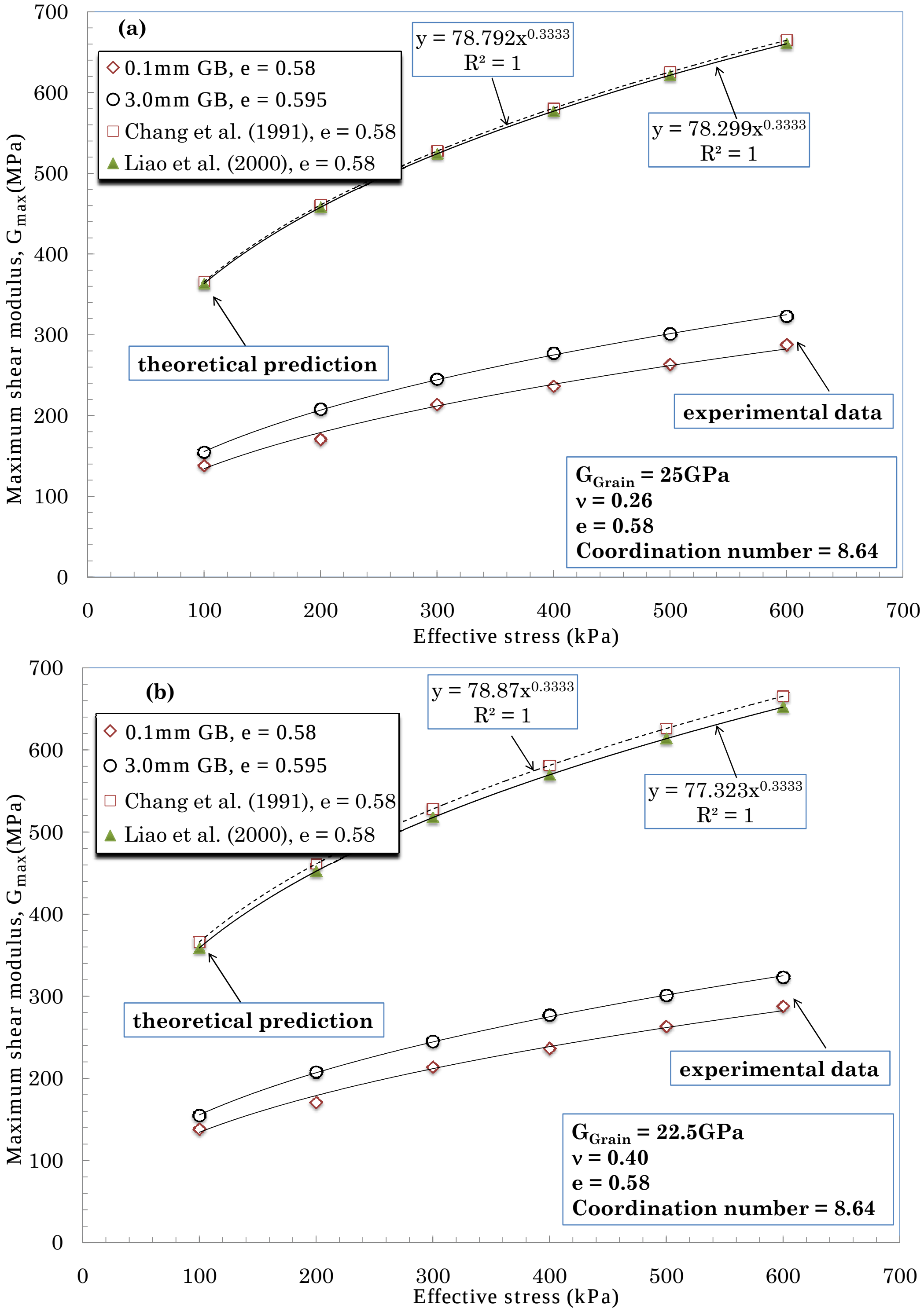

FIGURE 6.41: Comparison of G_{max} of GB obtained by experiment and by the theoretical solutions of Chang *et al.* (1991) and Liao *et al.* (2000). (a) Theoretical solutions with $\nu = 0.26$; (b) Theoretical solutions with $\nu = 0.40$

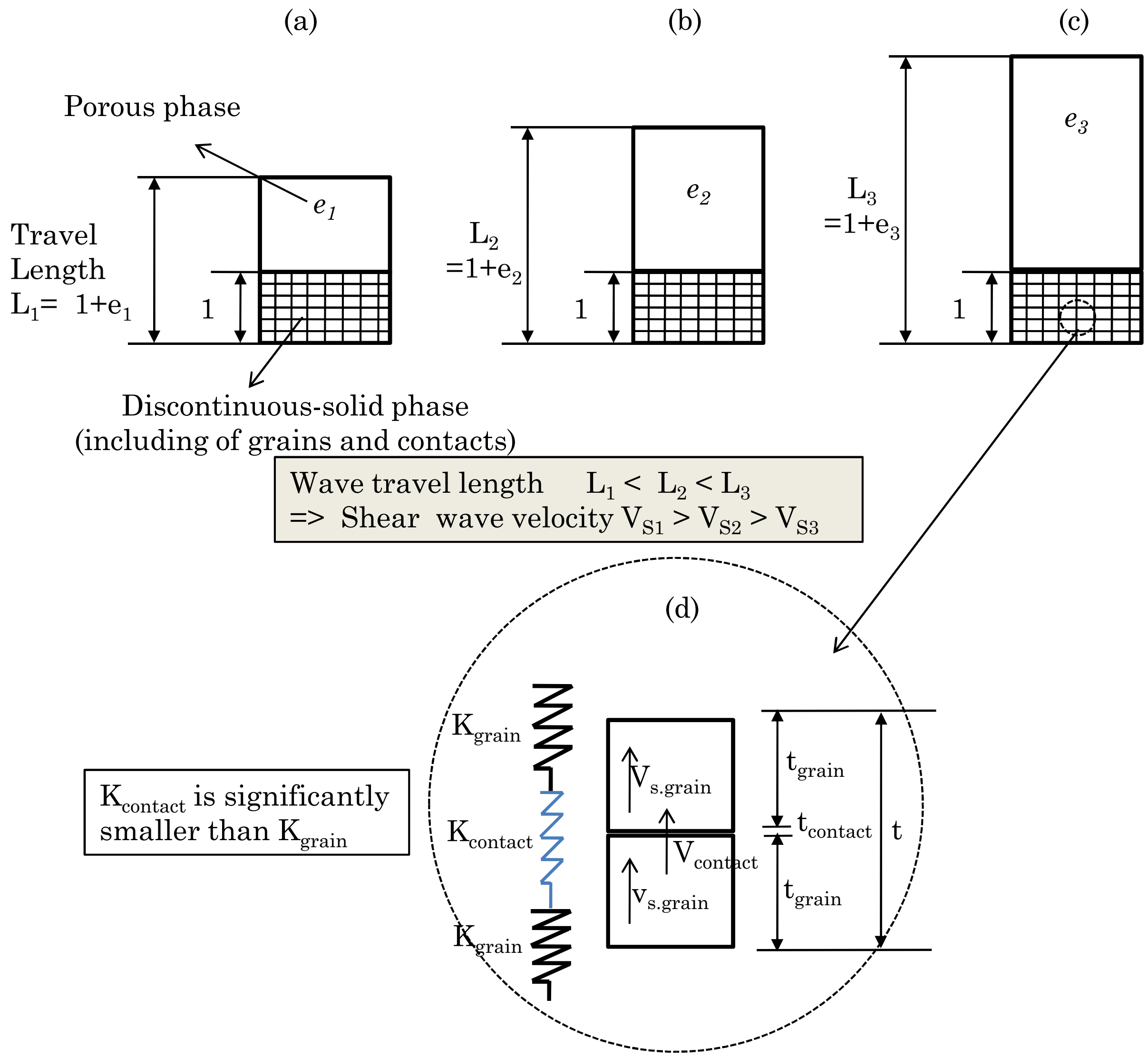

FIGURE 6.42: Porous-discontinuous solid model

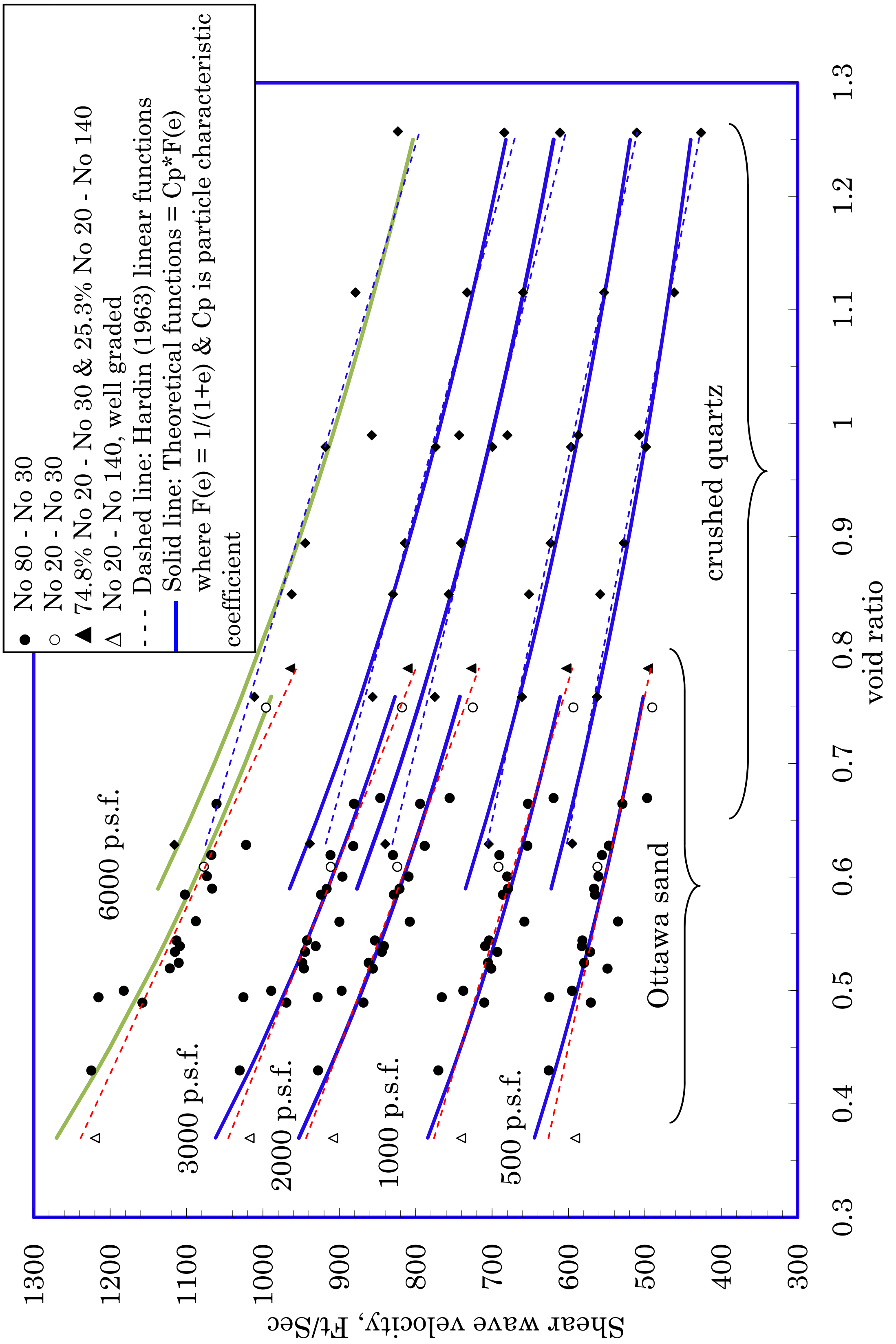

FIGURE 6.43: Application of the theoretical void ratio function to V_s of two sands measured by Hardin & Richart (1963)

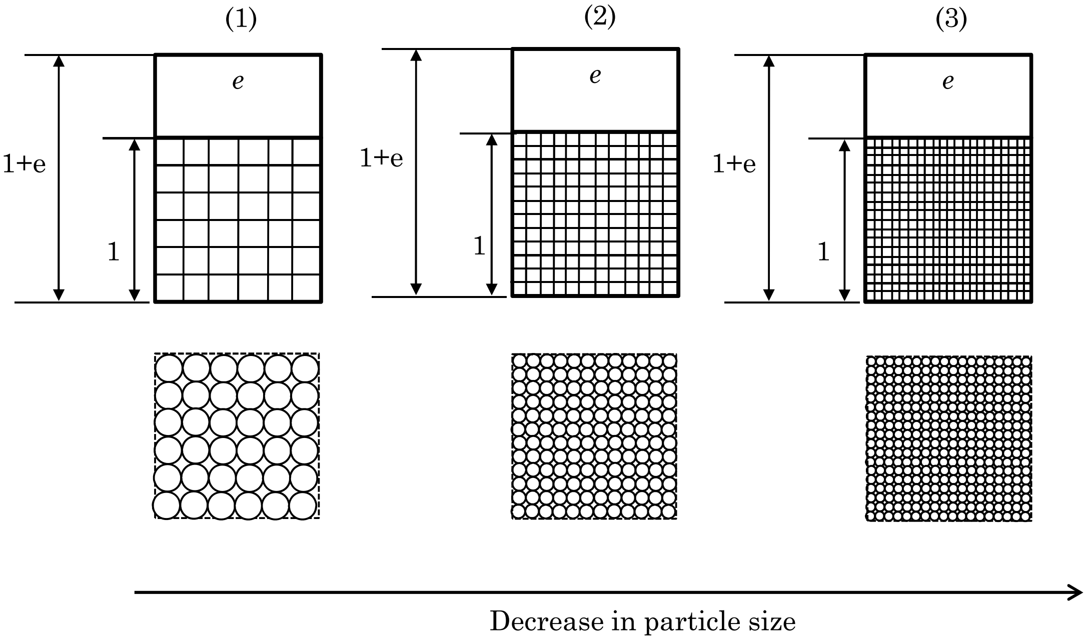

Number of contact per unit volumes: $Nc_1 < Nc_2 < Nc_3$
⇒Travel time at contacts: $t_1 < t_2 < t_3$
⇒ Shear wave velocity at contact: $V_{c1} > V_{c2} > V_{c3}$
⇒ Shear wave velocity: $V_{S1} > V_{S2} > V_{S3}$

A decrease in particle size will increase number of contacts per unit solid volume, hence decrease specimen stiffness

Figure 6.44: Hypothesis for the effect of particle size on G_{max}

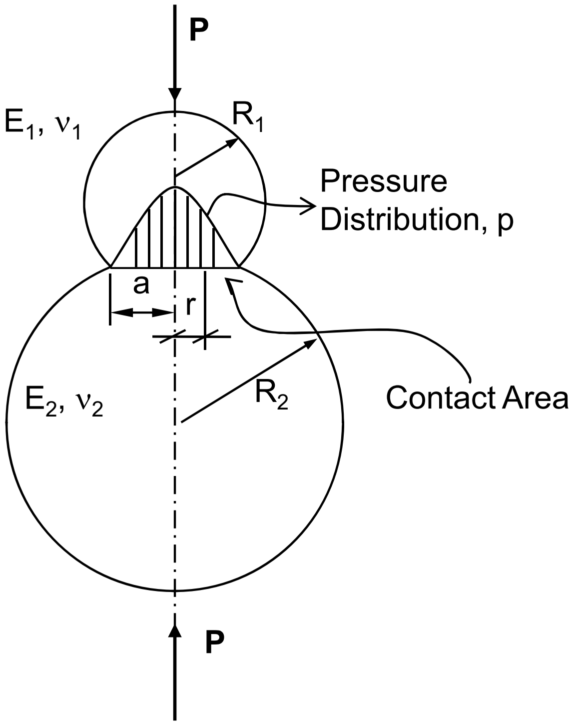

FIGURE 6.45: Hertzian contact between two spheres (drawn from Eq. 6.18 Johnson, 1987)

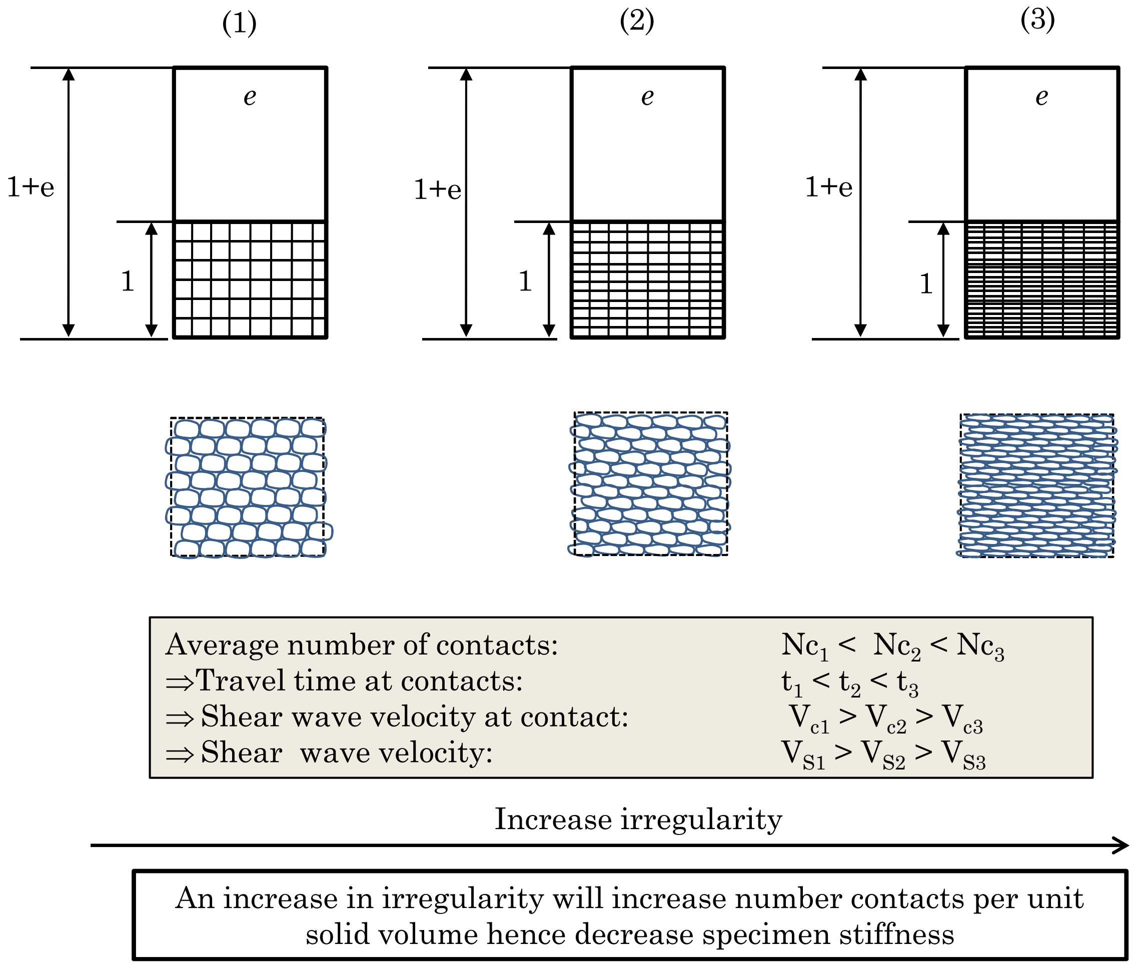

Average number of contacts:	$Nc_1 < Nc_2 < Nc_3$
⇒Travel time at contacts:	$t_1 < t_2 < t_3$
⇒ Shear wave velocity at contact:	$V_{c1} > V_{c2} > V_{c3}$
⇒ Shear wave velocity:	$V_{S1} > V_{S2} > V_{S3}$

An increase in irregularity will increase number contacts per unit solid volume hence decrease specimen stiffness

FIGURE 6.46: Hypothesis for the effect of particle shape on G_{max}

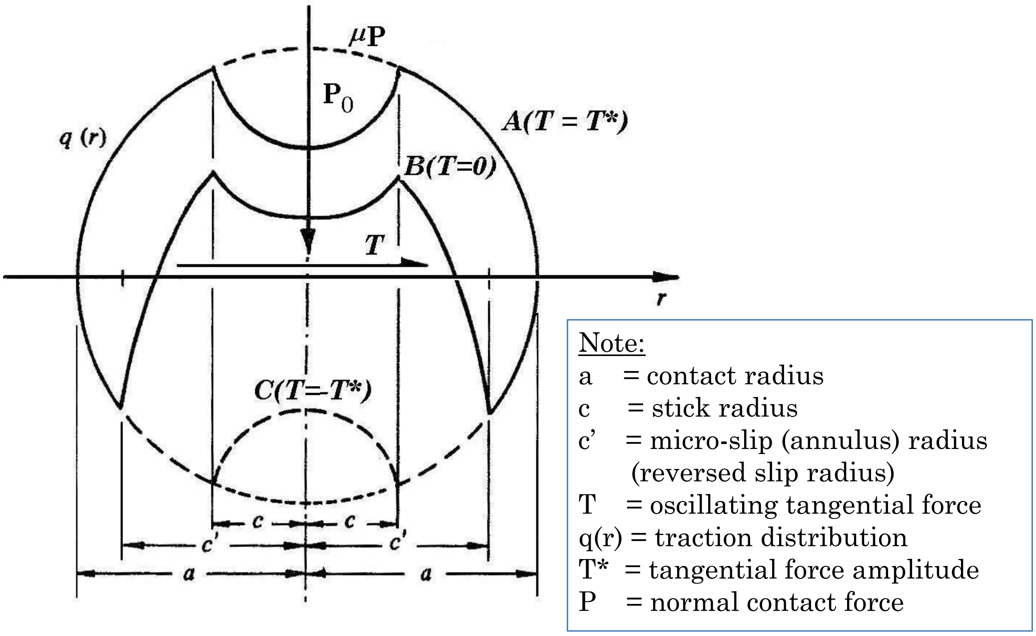

Note:
a = contact radius
c = stick radius
c' = micro-slip (annulus) radius (reversed slip radius)
T = oscillating tangential force
q(r) = traction distribution
T* = tangential force amplitude
P = normal contact force

(a) Traction distribution at A(T=T*), B(T=0), and C(T=-T*)

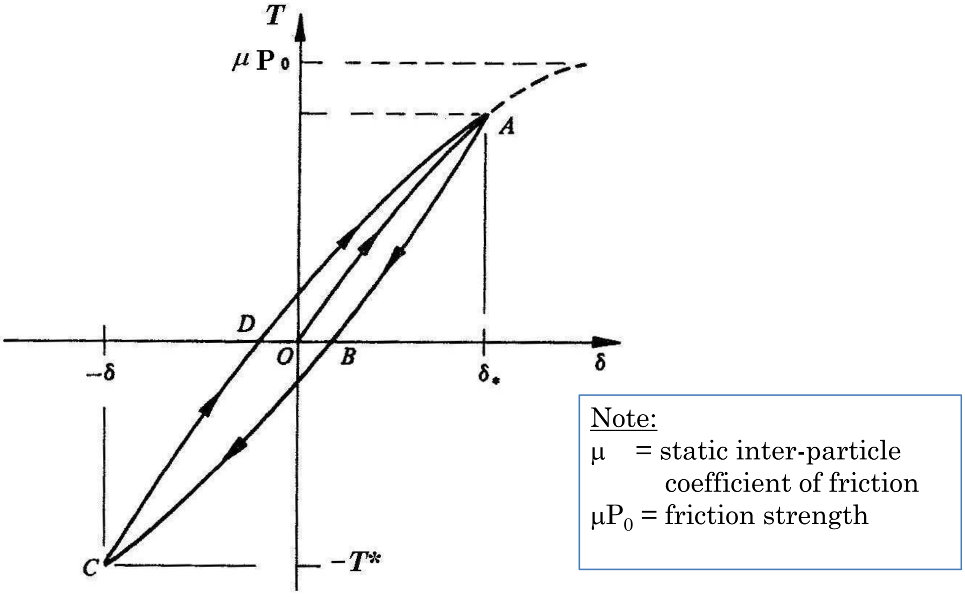

Note:
μ = static inter-particle coefficient of friction
μP_0 = friction strength

(b) Load-displacement cycle

FIGURE 6.47: Circular contact subjected to a steady normal load and an oscillating tangential load (Johnson, 1987)

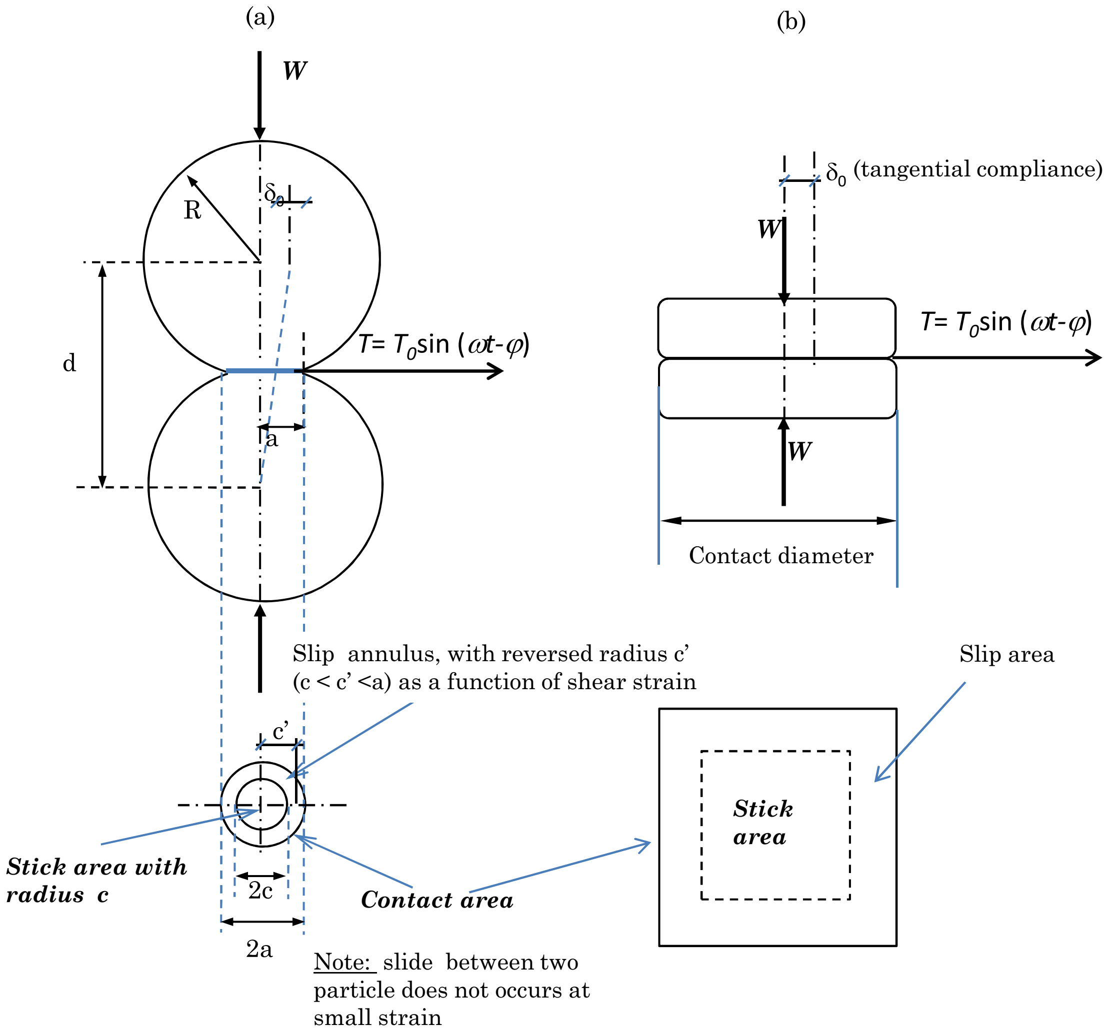

FIGURE 6.48: Particle shape and *stick-slip annulus*. (a) *Stick-slip annulus* between two spheres (Deresiewicz, 1953); (b) application of the stick-slip phenomenon to two flat particles in contact

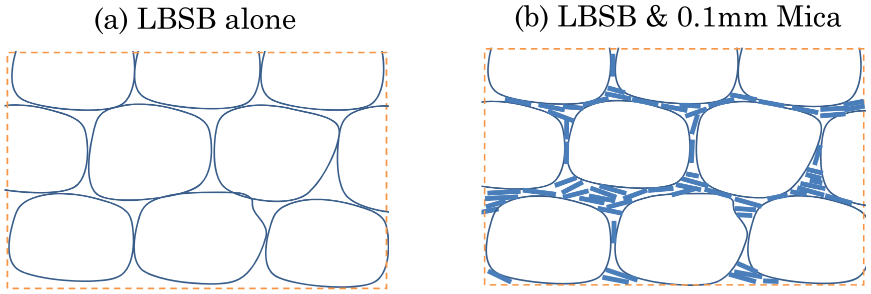

FIGURE 6.49: Structure of the dense mixture of LBSB and fine mica

Chapter 7

Conclusions and recommendations

Chapter 2 highlighted that the small strain response (or stress-strain relationship at small strain) of granular materials can be described by stress-strain hysteretic loops, of which maximum shear modulus, G_{max}, shear modulus degradation (G/G_{max}) as a function of strain, and damping ratio, D, are the key representative parameters. They are also the very important parameters in design of geotechnical structures where the deformations are small. Chapter 3 identified that Stokoe RCA is a well established laboratory apparatus that can be used to investigate the small strain response of geomaterials. To investigate the RCA compliance issues observed in Chapter 3, Chapter 4 analysed several ABAQUS models, and identifies the sources of compliance. The chapter found that the effects of the system compliance on the small strain response of geomaterials were significant, and therefore, the chapter developed a mathematical model termed two spring model to correct for the effects of system compliance.

Based on the results of the RC tests conducted in Chapter 5 on granular materials with varying particle sizes and shape, Chapter 6 has identified whether or not, how, and why particle size and particle shape influence the small strain response of geomaterials. Effects of particle size and particle shape were examined from the viewpoint of micro-mechanics, taking into account the effects of void ratio using a theoretical (universal) void ratio functions. Particle shape has been characterised using both 3D (Corey's shape factor) and 2D (roundness) shape descriptors. This chapter highlights the main findings drawn from the research.

7.1 Conclusions

7.1.1 From the literature

- The literature review in Chapter 2 showed that void ratio and mean effective stress significantly influence the small strain response of soils. To take into account the effects of void ratio, many empirical void ratio functions have been proposed. However, these void ratio functions can only be applied for certain soils with a narrow void ratio range. Other parameters identified that affect the small strain behaviour of soils are inherent anisotropy, confinement time, number of cyclic loadings, cementation/bonding etc. Overconsolidation ratio significantly affects the small strain properties of clays, but not sands.

- Particle characteristics (e.g. particle shape, particle size and mineral composition), are fundamental parameters of geomaterials. It has been shown that they control many other soil parameters such as void ratio range ($e_{max}-e_{min}$), soil fabric, particle strength, contact force, contact area, and co-ordination number etc.
- The influence of particle size and particle shape on the small strain response of soils has not been well understood. In the past, it was suggested that particle shape is an unimportant parameter for small strain shear modulus. Particle shape influences G_{max} through changing void ratio range, and when a void function $F(e)$ was taken into account, particle shape could be ignored. Recently, it was suggested that particle shape is an important parameter influencing G_{max}, despite variations in void ratio and particle size.
- The combination of Hertz and Mindlin contact theories and stress-strain hysteretic loops yields explicit equation (Eq. 2.8) for calculation of damping ratio. The equation indicates that damping ratios of soils at small strains are proportional to the square of tangential force. At small strains, the theoretical material damping ratios are very small, suggesting that in linear elastic region, damping ratios measured in practice are mainly caused by apparatus damping.

7.1.2 Effects of system compliance

- When testing relatively stiff specimens using the Stokoe RCA, the apparatus compliance leads to a significant underestimation of natural frequency.
- The analyses of finite element (ABAQUS) model showed that the torsional mode was well separated from other modes of vibration (e.g. flexural mode). This suggests that mode coupling is unlikely. However, poor base fixity or low base mass will reduce measured resonant frequencies as well as cause mode coupling between *torsional* modes of specimen and apparatus (coupling between pseudo and actual torsional vibration) modes.
- The analyses also indicates that significant errors in measurement of resonant frequency are due to compliance of many parts of the apparatus such as:
  - The drive mechanism deformability, especially the weak drive magnet connections, which can cause more than three fourth of the difference between the measured and the calculated natural frequency of aluminium calibration bar No4.
  - Poor base fixity, low base mass, and poor specimen fixity
  - Structure/design of the calibration bars.

- The influence of system compliance can be overcome by using the two spring model. The key parameters i.e. stiffness of the equipment, $K_{equipment}$, and I_0 of the model can be calibrated through testing of a series of aluminium calibration bars.

7.1.3 Laboratory tests

- Corey's shape factor and angularity index (Wilson *et al.*, 1997) have been used to characterise the particle form and angularity of the test materials, respectively.
- A computer program, written using *TestPoint*, has allowed for complete automation of resonant tests. The program could control and reduce significantly number of loading cycles and detect resonant frequency with a small error ($\pm 0.1Hz$). At a given shear strain amplitude, about 5,000 loading cycles were enough for determination of frequency response and FVD respose, from which the peak amplitude, the resonant frequency, and the damping ratio of a specimen could be automatically computed. At an applied effective stress, the program could undertake a full strain excursion, from which a shear modulus degradation curve could be obtained.

7.1.4 Effect of particle characteristics on small strain response

- Particle size significantly influences the small strain response of GB. It is found that, at the same void ratio and effective stress, G_{max} increases with an increase in particle diameter. Elastic threshold strain, γ_e, and G/G_{max} also increase with an increase in particle diameter. In addition, it is suggested that stress exponent and material damping ratio decrease with increasing particle diameter. It can be concluded that fine soils are more susceptible to an increment in shear strain and effective stress than coarse soils. It is emphasised that this conclusion has been reached after normalising for the effect of void ratio
- Particle shape also significantly influences the small strain response of granular materials. It is found that both particle form and particle roundness have significant correlations with values of G_{max} normalised by $F(e)$. Normalised G_{max} increases with increasing sphericity and roundness. Stress exponent, elastic threshold strain, and shear modulus degradation at a given shear strain for granular materials decrease with an increase in sphericity and roundness. Material damping has also been found to increase with sphericity and decrease with angularity. These conclusions imply that platy/angularity materials, which are relatively soft, are less susceptible to increasing shear strain, however more susceptible to an increment in effective stress than round/rotund particle. It is emphasised that these conclusions have been reached after removing the effects of other parameters, such as void ratio, particle size and specific gravity.
- The effects of particle size, particle shape, and particle density (specific gravity) can be taken into account using a particle characteristic coefficient, C_p, which increases with an increase in particle diameter, sphericity, and roundness, but is independent

of void ratio and effective stress. The experimental data suggest that G_{max} of geomaterials can be expressed using the following equation:

$$G_{max} = C_p(1+e)^{-3} \times {\sigma_r}^{1-n} \times {\sigma'_0}^{n} \ (MPa) \tag{7.1}$$

where σ_r and σ'_0 are in kPa.

- An addition of fine, platy mica into rotund sand cause a considerable reduction in stiffness of the rotund sand even though the void ratio of the mixture is lower than that of the rotund sand alone. The reduction in stiffness increases with an increase in mica content

7.1.5 Explanation why particle shape and size influence the small strain response of geomaterials

The thesis has successfully explained why particle size and particle shape influences the small strain response of geomaterials.

- The effects of particle characteristics on the small strain response of granular materials have been explained using the porous discontinuous-solid model. A dry soil element is assumed to consist of two phases, namely the pore and the discontinuous-solid, where the stiffness of discontinuities is represented by a shear wave velocity through the contact network, $V_{contact}$. The research postulates that $V_{contact}$ is a function of particle characteristics, which influence soil structure and contact properties such as number of contact per unit solid volume, contact area, contact pressure, friction strength and hence contact stiffness. The relationship between $V_{contact}$ and shear wave velocity, V_s, through a specimen with void ratio e has been shown to be:

$$\frac{1}{V_s} = (1+e)\left[\sqrt{\frac{\rho_s}{G_{grain}}} + \frac{1}{v_{contact}}\right] \tag{7.2}$$

  where G_{grain} and ρ_s are shear modulus and specific density of particles.

- Particle size and particle shape create both macro effects (e.g. effect of void ratio) and micro effects (at the contact level) on the small strain response of granular materials. As suggested by other researchers particle size and particle shape influence V_s of granular materials by changing void ratio (macro effect). The porous discontinuous-solid model suggests that void ratio influence travel length. At the same solid volume, an increase in void ratio will increase travel length, and hence decrease V_s. The model suggests that the macro effect of void ratio on V_s and G_{max} can be taken into account using the theoretical (universal) void ratio functions, which have a good fit to experimental data collected in the literature:

$$F(e)_V = \frac{1}{1+e} \tag{7.3}$$

Or

$$F(e)_G = \frac{1}{(1+e)^3} \tag{7.4}$$

- The macro effect of void ratio can be normalised, and by doing so the micro effects of particle shape and particle size can be observed. The micro effects of particle size on the small strain response of granular materials are due to two main factors: (i) particle size controls number of contact per unit solid volume, $\bar{N}_v$, which influences $V_{contact}$, and (ii) particle size controls contact area, contact force, contact friction (as a product of contact pressure, contact area, and coefficient of friction), and hence contact stiffness. Similarly, the influence of particle shape on the small strain behaviour of granular materials can be explained by the combined effects of some factors such as: (i) particle shape controls $\bar{N}_v$, and (ii) particle shape controls other contact properties & soil structure such as coordination number, $\bar{N}_c$, particle orientations, contact patterns, contact area, contact pressure, contact friction and hence contact stiffness.

- The stiffness reduction of the mixtures of LBSB and 0.1 mm mica can be explained by the combination effects of the platy particle shape and fine particle size of 0.1 mm mica.

- The fact that G_{max} of GB is lower than that of LBSB despite its higher sphericity (and higher roundness) of GB could be due to differences in contact area between GB and LBSB, the very smooth surface of GB, and the difference in mineral composition between GB and LBSB.

- The relatively high damping ratio, especially at high shear strains, and the stiffness susceptibility to shear strain of GB could also be explained by the very smooth surface and small contact area between GB.

7.2 Recommendations

- Numerical analyses suggest that calibration tests should be used to evaluate compliance of a RCA.

- Calibration checks should be conducted regularly to detect any changes in the compliance of apparatus components.

- The effects of system compliance are very significant especially when testing relatively stiff materials. Therefore the effects of system compliance should be corrected using a suitable mathematical model, such as the two spring model.

- To avoid effects of coupling between pseudo and actual torsional vibration modes, a Stokoe RCA should be stiffened e.g. increase the base mass or fix the test base to a very rigid frame/ concrete floor. An alternative way to avoid the effects of the mode coupling is to reduce dimensions of a specimen.

- To achieve accurate calibration results and avoid problems encountered due to a poor distribution of data points in a plot of $\frac{1}{k}$ vs $\frac{1}{{\omega_0}^2}$ (as discussed), a set of calibration bars should be made. The diameters of the central stem of the calibration bars should be designed such that all distances between two successive data points in the plot are equal. This requirement can be satisfied if

  $$\triangle x = \frac{1}{k_1} - \frac{1}{k_2} = \frac{1}{k_2} - \frac{1}{k_3} = \cdots = \frac{1}{k_i} - \frac{1}{k_{i+1}} = constant \qquad (7.5)$$

  where K_i is the stiffness of bar i^{th}, including the stiffness of the central stem and top platen. Table 7.1 and Fig. 7.1 present an example of a set of ten calibration bars with the diameters of the central stem calculated using Eq. 7.5.

- The macro effect of void ratio should be taken into account using a void ratio function such as Eq.7.3 and Eq. 7.4. By doing so, the effects of particle characteristics on G_{max} can be taken into account using a particle characteristic coefficient, C_p. Combination of the effects of void ratio, effective stress, and particle characteristics, it is suggested that G_{max} can be predicted using Eq. 7.1. In a feasibility study, an average stress exponent, n, from 0.4 to 0.5, and a C_p from 30 to 83 can be used for a normal consolidated, unbonding/uncemented granular soil. High values of C_p (and low values of n) for rotund/round relatively or large particle soils, and low values of C_p (and high values of n) for platy/angular or fine particle soils can be used correspondingly.

7.3 Further research

This section suggests further research that the author has identified will broaden our collective understanding of the effects of particle characteristics on the small strain response of geomaterials.

- Several particle characteristics have not been investigated in this study. One of them is the **mineral composition** of a particle. The study postulates that G_{max} is linearly proportional to specific gravity (Eq. 6.15). In addition, the porous discontinuous-solid model suggests that elastic constants of a particle may not be the most important parameters controlling V_s of granular materials. This hypothesis may be verified by conducting RC tests on specimens of very smooth spherical particle with the same diameter but different mineral composition, such as steel, aluminium, plastic, glass etc. The inter-particle frictional coefficient of different mineral composition may be different (Skinner, 1969; Procter & Barton, 1974). Therefore, to reduce effects of inter-particle frictional coefficient, silicon oil might be used as a saturated fluid.

- The shape of a particle can be considered to consist of three independent parameters, namely particle form, particle roundness, and **particle roughness** (Barrett, 1980). The effects of the first two parameters on the small strain response of geomaterials have been investigated in this study. However, effects of the third parameter have not been explored. In light of the porous discontinuous-solid model, it can be predicted that rough particles contact each other over a small area (conical contact between asperities) (Santamarina & Cascante, 1998), leading to high stress concentration (yielding) at asperities. In other words, the contact stiffness of two rough particles is relatively low, resulting in a relatively low shear wave velocity at contact, $V_{contact}$, and hence relatively low V_s. This hypothesis may be verified by testing specimens of spherical particles with difference degrees of particle roughness.

- In addition, V_s may be a function of **inter-particle coefficient of friction**, which is also a particle characteristic, since friction has been suggested to be the only mechanism by which shear wave transmits from particle to particle (Mindlin & Deresiewicz, 1953). This hypothesis may be verified by testing specimens of spherical particles with the same particle size, mineral composition and roughness, but different inter-particle frictional coefficient. For example, comparing V_s of a specimen of dry stainless steel balls and that of oil saturated (lubricated) specimen of stainless steel balls (at the same void ratio) might reveal the effects of inter-particle frictional coefficient. Oil has no shear strength[1] hence any difference between V_s of two specimens may be due to the effects of inter-particle frictional coefficient.

- Finally, the porous discontinuous-solid model hypothesises that shear wave velocity through contact network, $V_{contact}$, strongly influences V_s of a granular material. However, an explicit form of $V_{contact}$ has not been given. It is hypothesised that $V_{contact}$ is a complex function of many parameters such as confining pressure, particle characteristics (including particle size, particle shape, inter-particle friction, elastic constants of particle), coordination number, and void ratio etc. Quantification of $V_{contact}$ using (purely) mathematical approach will be a real challenge due to difficulties in mathematical derivation. To avoid this, a semi empirical-theoretical approach, of which regression analyses are applied to test results of GB[2] with different particle sizes and different effective stresses to establish an approximate form of $V_{contact}$, might be used.

---

[1] Oil has viscosity, therefore it may transmit shear in a dynamic test.

[2] Particle characteristics of GB are known.

TABLE 7.1: Diameters of new designed calibration bar

Bar No	Diameter of central stem (mm)	k_{stem} (Nm/rad)	expected resonant frequency (*) (Hz)
1	19.5	2190	136.9
2	20.1	2472	145.0
3	20.8	2835	154.8
4	21.6	3297	166.2
5	22.5	3882	179.4
6	23.8	4860	199.0
7	25.5	6405	225.4
8	28.1	9444	266.7
9	33.0	17963	344.5
10	50.0	94669	544.9

(*) Calculated with $I_0 = 0.00284 kg.m^2$ and $k_{equipment} = 51965 Nm/rad$

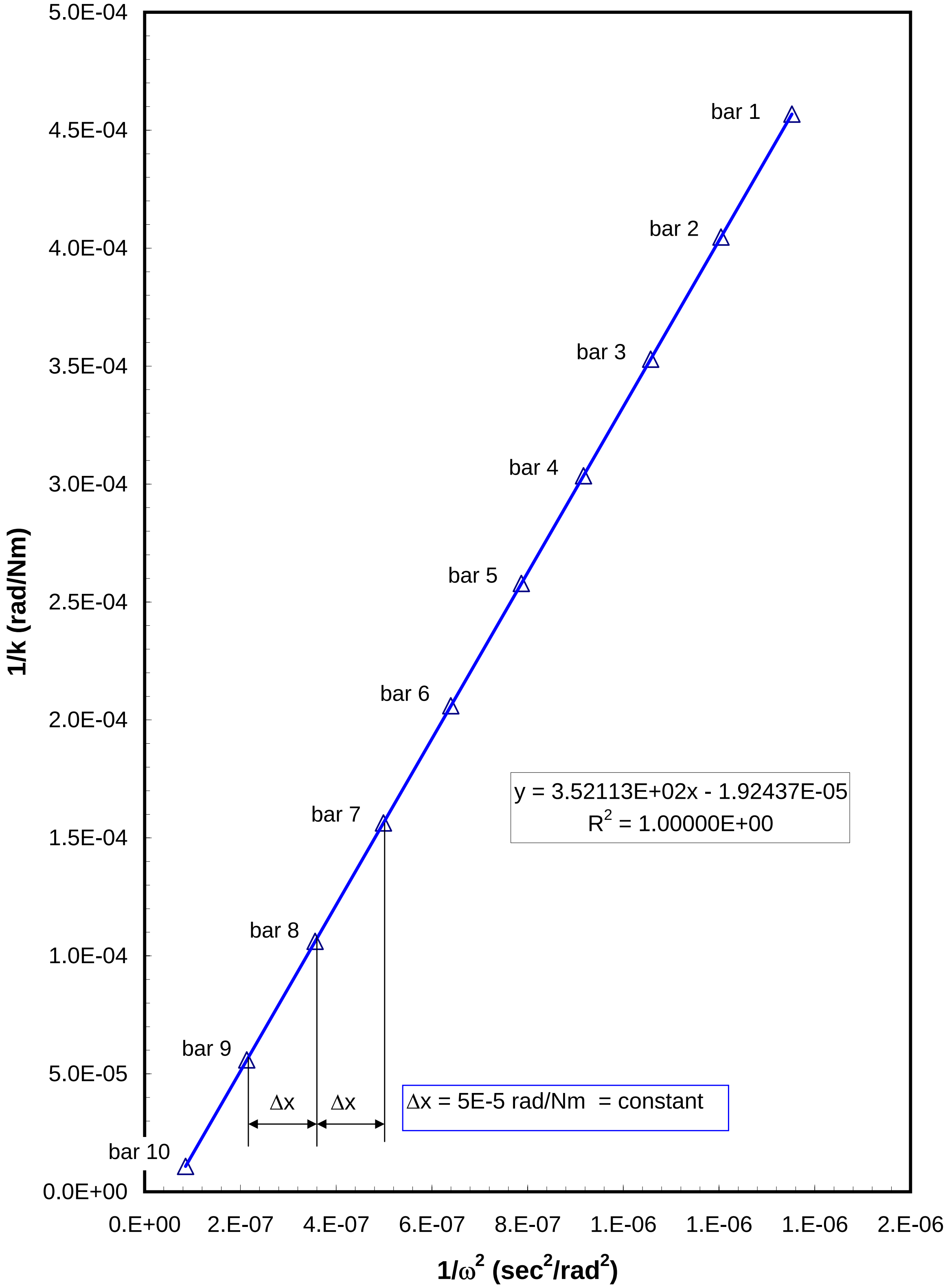

FIGURE 7.1: Plot of $\frac{1}{k}$ vs $\frac{1}{{\omega_0}^2}$ of the new theoretically designed calibration bars

Bibliography

Alshibli, K.A. & Alsaleh, M.I. (2004). Characterizing surface roughness and shape of sands using digital microscopy. *Journal of Computing in Civil Engineering, ASCE*, vol. 18, no. 1, pp. 36–45.

Anderson, D.G. & Stokoe, K.H.II. (1978). Shear modulus: A time dependent soil property. In: Silver, M. & Tiedemann, D. (eds.), *Dynamic geotechnical testing: proceeding of a symposium on Dynamic Soil and Rock Testing in the Field and the Laboratory for Seismic Studies*, 654, pp. 66–90. ASTM Committee D-18 on Soil and Rock for Engineering Purposes, American Society for Testing and Materials, Denver, Colorado.

Aschenbrenner, B.C. (1956). A new method of expressing particle sphericity. *Journal of Sedimentary Petrology*, vol. 26, pp. 15–31.

Ashmawy, A.K. & Drnevich, V.P. (1994). A general dynamic model for the resonant column/ quasi-static torsional shear apparatus. *Geotechnical Testing Journal*, vol. 17, no. 3, pp. 337–348.

ASTM (1995). *D 4015 - 92 (Re-approved 1995): Standard Test Methods for Modulus and Damping of Soils by the Resonant-Column Method.*

Athanasopoulos, G.A. & Richart, F.E.Jr. (1983). Correlation between G_0 and θ_{max} for kaolinite clay. *Journal of Geotechnical Engineering, ASCE*, vol. 109, no. 5, pp. 719–723.

Avramidis, A.S. & Saxena, S.K. (1990). Modified ‘stiffened’ Drnevich resonant column apparatus. *Soils and Foundations*, vol. 30, no. 3, pp. 53–58.

Barrett, P.J. (1980). The shape of rock particles, a critical review. *Sedimentology*, vol. 27, pp. 291–303.

Biot, M.A. (1956). Theory of propagation of elastic waves in a fluid-saturated porous solid. *I*. low-frequency range. *The Journal of the Acoustical Society of America*, vol. 28, no. Issue 2, pp. 168–178.

Blatt, H., Middleton, G. & Murray, R. (1980). *Origin of Sedimentary Rocks.* Englewood Cliffs, N.J : Prentice-Hall.

Bolton, M.D. & Wilson, J.M.R. (1989). An experimental and theoretical comparison between static and dynamic torsional soil tests. *Géotechnique*, vol. 39, no. 4, pp. 585–599.

Bowden, F.P. & Tabor, D. (1950). *The friction and lubrication of solids.* Clarendon Press, Oxford.

Bowman, E.T., Soga, K. & Drummond, W. (2001). Particle shape characterisation using fourier descriptor analysis. *Géotechnique*, vol. 51, no. 6, pp. 545–554.

Buckingham, M.J. (2005). Compressional and shear wave properties of marine sediments: Comparisons between theory and data. *The Journal of the Acoustical Society of America*, vol. 117, no. 1, pp. 137–152.

Burland, J.B. (1989). Ninth Laurits Bjerrum memorial lecture: 'small is beautiful' - the stiffness of soils at small strains. *Canadian Geotechnical Journal*, vol. 26, no. 4, pp. 499–516.

Campanella, R.G. (1994). Field methods for dynamic geotechnical testing: An overview of capabilities and needs. In: Ebelhar, R., Drenevich, V. & L., K.B. (eds.), *Dynamic Geotechnical Testing II, ASTM Special Technical Publication No. 1213*, pp. 3–12. American Society of Testing and Materials.

Cascante, G. (1996). *Propagation of mechanical waves in particulate materials.* Ph.D. thesis, University of Waterloo, Ontario, Canada.

Cascante, G. & Santamarina, J.C. (1996). Interparticle contact behavior and wave propagation. *Journal of Geotechnical Engineering, ASCE*, vol. 122, no. 10, pp. 831–839.

Cascante, G. & Santamarina, J.C. (1997). Low strain measurement using random noise excitation. *Geotechnical Testing Journal*, vol. 20, no. 1, pp. 29–39.

Cascante, G., Vanderkooy, J. & Chung, W. (2003). Difference between current and voltage measurements in resonant column testing. *Canadian Geotechnical Journal*, vol. 40, no. 3, pp. 806–820.

Chang, C.S., Misra, A. & Sundaram, S.S. (1991). Properties of granular packing under low amplitude cyclic loading. *Soil Dynamics and Earthquake Engineering*, vol. 10, no. 4, pp. 201–211.

Chang, N.P.N. & Heymann, G. (2005). Shear wave velocity of gold tailings. *Journal of the South African Institution of Civil Engineering*, vol. 47, no. 2, pp. 15–20.

Cho, G.C., Dodds, J. & Santamarina, J.C. (2006). Particle shape effects on packing density, stiffness, and strength: Natural and crushed sands. *Journal of Geotechnical and Geoenvironmental Engineering, ASCE*, vol. 132, no. 5, pp. 591–602.

Clark, M.W. (1981). Quantitative shape analysis: a review. *Mathematical Geology*, vol. 13, no. 4, pp. 303–320.

Clayton, C.R.I. & Heymann, G. (2001). Stiffness of geomaterials at very small strains. *Géotechnique*, vol. 51, no. 3, pp. 245–255.

Clayton, C.R.I., Priest, J.A. & Best, A.I. (2005). The effects of disseminated methane hydrate on the dynamic stiffness and damping of a sand. *Géotechnique*, vol. 55, no. 6, pp. 423–434.

Clayton, C.R.I., Priest, J.A., Bui, M.T., Zervos, A. & Kim, S.G. (2009). The stokoe resonant column apparatus: effects of stiffness, mass and specimen fixity. *Géotechnique*, vol. 58, no. GEO-D-0700096, pp. 1–9 (accepted for publication).

Clayton, C.R.I., Theron, M. & Vermuelen, N.J. (2004). The effect of particle shape on the behaviours of gold tailing. In: Jardine, R., Potts, D.M. & Higgins, K.G. (eds.), *The Advance in Geotechnical Engineering - the Skempton Conference*, vol. 1, pp. 393 – 404. ICE, Thomas Telford Ltd., the Royal Geographical Society, London, U.K.

Corey, A.T. (1949). *Influence of the shape on the fall velocity of sand grains*. Master's thesis, Colorado A & M College, Fort Collins, Colorado, USA.

Cresswell, A., Barton, M.E. & Brown, R. (1999). Determining the maximum density of sands by pluviation. *Geotechnical Testing Journal*, vol. 22, no. 4, pp. 324–328.

Cubrinovski, M. & Ishihara, K. (2002). Maximum and minimum void ratio characteristics of sands. *Soils and Foundations*, vol. 42, no. 6, pp. 65–78.

Deresiewicz, H. (1953). Effects of an oscillating torsional couple on the contact surfaces of elastic spheres. Tech. Rep., Department of Civil Engineering and Engineering, Columbia University, New York.

Dietrich, W.E. (1982). Settling velocity of natural particles. *Water Resources Research*, vol. 18, no. 6, pp. 1615–1626.

Digby, P.J. (1981). The effective elastic moduli of porous granular rocks. *Journal of Applied Mechanics*, vol. 48, pp. 803–808.

Drnevich, V.P. (1978 June). Resonant column testing-problems and solutions. In: Silver, M. & Tiedemann, D. (eds.), *Dynamic Geotechnical Testing: Proceeding of a symposium on Dynamic Soil and Rock Testing in the Field and the Laboratory for Seismic Studies*, 654, pp. 384–398. ASTM Committee D-18 on Soil and Rock for Engineering Purposes, Denver, Colorado.

Drnevich, V.P. (1985). Recent developments in resonant column testing. In: Woods, R.D. (ed.), *Richart Commemorative Lectures, Geotechnical Engineering Division, ASCE*, pp. 79–106.

Duffy, J. (1959). A differential stress-strain relation for the hexagonal close-packed array of elastic spheres. *Journal of Applied Mechanics, Transactions of ASME*, vol. 26, pp. 88–94.

Duffy, J. & Mindlin, R.D. (1957). Stress-strain relations and vibrations of a granular medium. *Journal of Applied Mechanics, Transactions of ASME*, vol. 24, pp. 585–593.

Ehrlich, R. & Weinberg, B. (1970). An exact method for characterisation of grain shape. *Journal of Sedimentary Petrology*, vol. 40, pp. 205–212.

Field, W.G. (1963). Towards the statistical difination of a granular mass. In: *Proceeding of the 4th Australia-New Zeland Conference on Soil Mechanics*, pp. 143–148.

Frossard, E. (1979). Effect of sand grain shape on interparticle friction; indirect measurements by Rowe's stress dilatancy theory. *Géotechnique*, vol. 29, no. 3, pp. 341–350.

Hamilton, E.L. (1970). Sound velocity and related properties of marine sediments, North Pacific. *Journal of Geophysical Research*, vol. 75, pp. 4423–4446.

Hamilton, E.L. (1971). Elastic properties of marine sediments. *Journal of Geophysical Research*, vol. 76, no. 2, pp. 579–604.

Hamilton, E.L. & Bachman, R.T. (1982). Sound velocity and related properties of marine sediments. *The Journal of the Acoustical Society of America*, vol. 72, no. 6, pp. 1891–1904.

Hardin, B.O. (1961). *Study of Elastic Wave Propagation and Damping Granular Materials*. Ph.D. thesis, University of Florida at Gainesville, Florida.

Hardin, B.O. (1965). The nature of damping of sand. *Journal of the Soil Mechanics and Foundation Division, ASCE*, vol. 11, no. 10, pp. 63–97.

Hardin, B.O. & Black, W.L. (1966). Sand stiffness under various triaxial stress. *Journal of the Soil Mechanics and Foundation Division, ASCE*, vol. 92, no. SM2, pp. 27–42.

Hardin, B.O. & Black, W.L. (1968). Vibration modulus of normally consolidated clay. *Journal of the Soil Mechanics and Foundation Division, ASCE*, vol. 94, no. SM2, pp. 353–369.

Hardin, B.O. & Black, W.L. (1969). Closure to: Vibration modulus of normally consolidated clay. *Journal of the Soil Mechanics and Foundation Division, ASCE*, vol. 95, no. SM 6, pp. 1531–1537.

Hardin, B.O. & Blandford, G.E. (1989). Elasticity of particulate materials. *Journal of Geotechnical Engineering, ASCE*, vol. 115, no. 6, pp. 788–805.

Hardin, B.O. & Drnevich, V. (1972*a*). Shear modulus and damping in soil: Design equation and curves. *Journal of the Soil Mechanics and Foundation Division, ASCE*, vol. 98, no. 7, pp. 667–692.

Hardin, B.O. & Drnevich, V.P. (1972*b*). Shear modulus and damping in soil: Measurement and parameter effects. *Journal of the Soil Mechanics and Foundation Division, ASCE*, vol. 98, no. 7, pp. 603–624.

Hardin, B.O. & Kalinski, M.E. (2005). Estimating the shear modulus of gravelly soils. *Journal of Geotechnical and Geoenvironmental Engineering, ASCE*, vol. 131, no. 7, pp. 867–875.

Hardin, B.O. & Richart, E.F.J. (1963). Elastic wave velocities in granular soils. *Journal of the Soil Mechanics and Foundation Division, ASCE*, vol. 89, no. SM 1, pp. 33–65.

Hight, D.W., Bennel, J.D., Chana, B., Davis, P.D., Jardine, R.J. & Porovic, E. (1997). Wave velocity and stiffness measurements of the Crag and Lower London Tertiaries at Sizewell. *Géotechnique*, vol. 47, no. 3, pp. 451–474.

Holubec, I. & D′Appolonia, E. (1973). Effect of particle shape on the engineering properties of granular soils. In: *Evaluation of relative density and its role in geotechnical projects involving cohesionless soils. ASTM STP 523*, pp. 304–318. America Society for Testing and Materials.

Horn, H.M. & Deere, D.U. (1962). Frictional characteristics of minerals. *Géotechnique*, vol. 12, no. 4, pp. 319–335.

Humphries, W.K. & Wahls, E.H. (1968). Stress history effects on dynamic modulus of clay. *Journal of the Soil Mechanics and Foundation Division, ASCE*, vol. 94, no. SM2, pp. 371–389.

Isenhower, W.M., Stokoe, K.H.II. & Allen, J.C. (1987). Instrumentation for torsional shear/resonant column measurement under anisotropic stresses. *Geotechnical Testing Journal*, vol. 10, no. 4, pp. 183–191.

Ishihara, K. (1996). *Soil Behaviour in Earthquake Geotechnics*. Oxford University Press, New York. ISBN 0-19-856224-1.

Ishimoto, M. & Iida, K. (1936). Determination of elastic constants by means of vibration methods, part 1, young's modulus. *Bulletin of Earthquake Research Institute*, vol. XIV, pp. 632–657.

Ishimoto, M. & Iida, K. (1937). Determination of elastic constants by means of vibration methods, part 2, modulus of rigidity and poisson's ratio. *Bulletin of Earthquake Research Institute*, vol. XV, pp. 67–88.

Iwasaki, T. & Tatsuoka, F. (1977). Effects of grain size and grading on dynamic shear moduli of sands. *Soils and Foundations*, vol. 17, no. 3, pp. 19–35.

Jamiolkowski, M., Lancellotta, R. & Lo Presti, D.C.F. (1995). Remarks on the stiffness at small strains of six italian clays. In: Shibuya, M. & Miura (eds.), *Pre-failure Deformation of Geomaterials*, vol. 1, pp. 817–836. Balkema: Rotterdam.

Johnson, K.L. (1987). *Contact mechanics*. Cambridge University Press. ISBN-10: 0521347963 ISBN-13: 9780521347969.

Koerner, R.M. (1970). Effect of particle characteristics on soil strength. *Journal of the Soil Mechanics and Foundation Division, ASCE*, vol. 96, no. SM4, pp. 1221–1234.

Kokusho, T., Yoshida, Y. & Esashi, Y. (1982). Dynamic properties of soft clay for wide strain range. *Soils and Foundations*, vol. 22, no. 4, pp. 1–18.

Kolbuszewski, J. (1948). An experimental study of the maximum and minimum porosities of sands. In: *Proceedings 2nd International Conference on Soil Mechanics and Foundation Engineering*, vol. 1, pp. 158–165. Rotterdam.

Kramer, S.L. (2003). *Geotechnical Earthquake Engineering.* Prentice-Hall International series in civil engineering. Singapore: Pearson Education,. ISBN : 8129701936.

Krumbein, W.C. (1941). Measurement and geological significance of shape and roundness of sedimentary particles. *Journal of Sedimentary Petrology*, vol. 11, no. 2, pp. 64–72.

Krumbein, W.C. & Sloss, L.L. (1963). *Stratigraphy and sedimentation.* second edition, edn. W.H. Freeman and Company, San Franscisco.

Kumar, J. & Clayton, C.R.I. (2007). Effect of sample torsional stiffness on resonant column test results. *Canadian Geotechnical Journal*, vol. 44, pp. 221–230.

Kuwano, R. & Jardine, R.J. (2002). On the applicability of cross-anisotropic elasticity to granular materials at very small strains. *Géotechnique*, vol. 52, no. 10, pp. 727–749.

Lade, P.V., Liggio, C.D. & Yamamuro, J.A. (1998). Effects of non-plastic fines on minimum and maximum void ratios of sand. *Geotechnical Testing Journal*, vol. 21, no. 4, pp. 336–347.

Lee, D.M. (1992). *The angles of friction of granular fills.* Ph.D. thesis, Cambridge University.

Lee, J., M., G. & Santamarina, J.C. (2007). Micaceous sands: microscale mechanisms and macroscale response. *Journal of Geotechnical and Geoenvironmental Engineering, ASCE*, vol. 133, no. 9, pp. 1136–1143.

Lees, G. (1964). A new method for determining the angularity of particles. *Sedimentology*, vol. 3, pp. 2–21.

Li, X.S., Yang, W.L., Shen, C.K. & Wang, W.C. (1998). Energy-injecting virtual-mass resonant column system. *Journal of Geotechnical and Geoenvironmental Engineering, ASCE*, vol. 124, no. 5, pp. 428–438.

Liao, C., Chan, C.T., Suiker, S.J.A. & Chang, S.C. (2000). Pressure-dependent elastic moduli of granular assemblies. *International Journal for Numerical and Analytical Methods in Geomechanics*, vol. 24, pp. 265–279.

Lo Presti, D.C.F., Jamiolkowski, M., Pallara, O., Cavallaro, A. & Pedroni, S. (1997). Shear modulus and damping of soils. *Géotechnique*, vol. 47, no. 3, pp. 603–617.

Lo Presti, D.C.F., Pallara, O., Cavallaro, A., Lancellotta, R., Armani, M. & Maniscalco, R. (1993). Monotonic and cyclic loading behaviour of two sands at small trains. *Geotechnical Testing Journal*, vol. 16, no. 43, pp. 409–424.

Lo Presti, D.C.F., Pedroni, S. & Crippa, V. (1992). Maximum dry density of cohesionless soils by pluviation and by $ASTMD4253 - 83$: a comparative study. *Geotechnical Testing Journal*, vol. 15, no. 2, pp. 180–189.

Maeda, K. & Miura, K. (1999 Feb). Relative density dependensy on mechanical properties of sands. *Soils and Foundations*, vol. 39, no. 1, pp. 69–79.

Mandelbrot, B.B. (1977). *Fractals: forms, chance and dimension.* San Francisco: Freeman.

Marcuson, W.G. & Wahls, H.E. (1972). Time effects on dynamic shear modulus of clays. *Journal of the Soil Mechanics and Foundation Division, ASCE*, vol. 97, no. SM12, pp. 1359–1373.

McGeary, R.K. (1961). Mechanical packing of spherical particles. *Journal of the American Ceramic Society*, vol. 44, no. 10, pp. 513–522.

Meng, J. & Rix, G.J. (2003). Reduction of equipment-generated damping in resonant column measurement. *Géotechnique*, vol. 53, no. 5, pp. 503–512.

Menq, F.Y. & Stokoe, K.H.II. (2003). Linear dynamic properties of sandy and gravelly soils from large-scale resonant tests. In: Di, B.H., Doanh, T., Geoffroy, H. & Sauzeat, C. (eds.), *The 3rd International Symposium on Deformation Characteristics of Geomaterial*, pp. 63–71. Rotterdam A. A. Balkema Publishers, Lyon, France.

Mindlin, R.D. & Deresiewicz, H. (1953). Elastic sphere in contact under varying oblique forces. *Journal of Applied Mechanics, Transactions of ASME*, vol. 20, pp. 327–344.

Ming, X. (2005). *The Behaviour of Soil Behind Full-Height Integral Abutments.* Ph.D. thesis, School of Civil Engineering and the Environment, University of Southampton.

Mitchell, J. & Soga, K. (2005). *Fundementals of soil behavior.* 3rd edn. John Wiley and Sons, Ltd.

Miura, K., Maeda, K., Furukawa, M. & Toki, S. (1997). Physical characteristics of sand with different primary properties. *Soils and Foundations*, vol. 37, no. 3, pp. 53–64.

Moore, D.F. (1975). *Principles and applications of tribology*, vol. 14 of *International series on materials science and technology.* Oxford : Pergamon.

Oda, M. (1977). Co-ordination number and its relation to shear strength of granualr material. *Soils and Foundations*, vol. 17, no. 2, pp. 29–42.

Pennington, D.S., Nash, D.F.T. & Lings, M.L. (1999). The dependence of anisotropic shear moduli on void ratio and stress state for reconstituted gault clay. In: Jamiolkowski, Lancellotta & Presti, L. (eds.), *Proceedings of the 2nd International Symposium on Pre-failure Deformation Characteristics of Geomaterials*, vol. 1, pp. 229–238. Rotterdam.

Petrakis, E. & Dobry, R. (1987 SEP). Micromechanical modeling of granular soil at small strain by arrays of elastic spheres. Tech. Rep. Accession No ADA191927, Department of Civil Engineering, Rensselaer Polytechnic Inst Troy N.Y.

Powers, M.C. (1953). A new roundness scale for sedimentary particles. *Journal of Sedimentary Petrology*, vol. 23, no. 2, pp. 117–119.

Priest, J.A. (2004). *The Effect of Methane Gas Hydrate on the Dynamics Properties of Sand*. Ph.D. thesis, School of Civil Engineering and the Environment, University of Southampton, UK.

Procter, D.C. & Barton, R.R. (1974). Measurements of the angle of interparticle friction. *Géotechnique*, vol. 24, no. 4, pp. 581–604.

Reddy, A.C.O. (2007). Mphil/PhD transfer report: 3D particle form characterisaton and its influence on packing and shear behaviour. Tech. Rep., School of Civil Engineering & the Environment, University of Southampton, UK.

Reddy, A.C.O. (2008). *Particle Form and its Impact on Packing and Shear Behaviour of Particulate Materials*. Ph.D. thesis, School of Civil Engineering and the Environment, University of Southampton.

Richart, E.F.J., Hall, J.R. & Woods, R.D. (1970). *Vibrations of soils and foundations*. Theoretical and Applied Mechanics series. Prentice-Hall International Englewood Cliffs, New Jersey.

Robertson, P.K., Sasitharan, S., Cunning, J.C. & Sego, D.C. (1995). Shear-wave velocity to evaluate in-situ state of ottawa sand. *Journal of Geotechnical Engineering, ASCE*, vol. 121, no. 3, pp. 262–273.

Roesler, S.K. (1979). Anisotropic shear modulus due to stress anisotropy. *Journal of Geotechnical Engineering, ASCE*, vol. 150, no. GT7, pp. 871–880.

Rollins, K.M., Evan, M.D., Diehl, N.B. & Daily, W.D. (1998). Shear modulus and damping relationships for gravels. *Journal of Geotechnical and Geoenvironmental Engineering, ASCE*, vol. 124, no. 5, pp. 396–405.

Santamarina, J.C. & Cascante, G. (1996). Stress anisotropy and wave propagation: a micromecanical view. *Canadian Geotechnical Journal*, vol. 33, pp. 770–782.

Santamarina, J.C. & Cascante, G. (1998). Effect of surface roughness on wave propagation parameters. *Géotechnique*, vol. 48, no. 1, pp. 129–137.

Santamarina, J.C., Klein, A.K. & Fam, A.M. (2001). *Soils and Waves: Particulate Materials Behaviour, Characterization and Process Monitoring*. WileyBlackwell.

Schreiber, B.C. (1968). Sound velocity in deep sea sediments. *Geophysical Research*, vol. 73, pp. 1259–1268.

Seed, H.B. & Idriss, I.M. (1970). Soil moduli and damping factor for dynamic response analyses, [report No EERC 70-10]. Tech. Rep., Earthquake Engineering Research Centre, University of California, Berkeley.

Seed, H.B., Wong, R.T., Idriss, I.M. & Tokimatsu, K. (1986). Moduli and damping factors for dynamic analyses of cohesionless soil. *Journal of Geotechnical Engineering, ASCE*, vol. 112, no. 11, pp. 1016–1032.

Shibuya, S., Hwang, S.C. & Mitachi, T. (1997). Elastic shear modulus of soft clays from shear wave velocity measurement. *Géotechnique*, vol. 47, no. 3, pp. 593–601.

Shibuya, S. & Tanaka, H. (1996). Estimate of elastic shear modulus in holocene soil deposits. *Soils and Foundations*, vol. 36, no. 4, pp. 45–55.

Shibuya, S., Tatsuoka, F., Teachavorasinskun, S., Kong, X.J., Abe, F., Kim, Y.S. & Park, C.S. (1992). Elastic deformation properties of geomaterials. *Soils and Foundations*, vol. 32, no. 3, pp. 26–46.

Skinner, A.E. (1969). A note on the influence of interparticle friction on the shearing strength of a random assembly of spherical particles. *Géotechnique*, vol. 19, no. 1, pp. 150–157.

Smith, W.O., Foote, P.D. & Busang, P.F. (1929). Packing of homogeneous spheres. *Physical Review*, vol. 34, pp. 1271–1274.

Sneed, E.D. & Folk, R.L. (1958). Pebbles in the lower Colorado River, Texas, a study in particle morphogenesis. *Journal of Geology*, vol. 66, pp. 114–150.

Stokoe, K.H.II., Darendeli, M.B., Andrus, R.D. & Brown, L.T. (1999 June 21-25). Dynamic soil properties: Laboratory, field and correlation studies, theme lecture. In: *Proceeding of the 2nd International Conference on Earthquake Geotechnical Engineering*, vol. 3, pp. 811–845. Portuguese Geotechnical Society, Lisbon, Portugal.

Stokoe, K.H.II., Hwang, S.K. & Lee, J.N. (1995). Effects of various parameters on the stiffness and damping of soils at small to medium strains. In: Shibuya, M. & Miura (eds.), *Pre-failure Deformation of Geomaterials*, vol. 1, pp. 785–816. Balkema: Rotterdam.

Sukumaran, B. & Ashmawy, A.K. (2001). Quantitative characterisation of the geometry of discrete particles. *Géotechnique*, vol. 51, no. 7, pp. 619–627.

Tatsuoka, F., Iwasaki, T., & Takagi, Y. (1978). Hysteretic damping of sands and its relation to shear modulus. *Soils and Foundations*, vol. 18, no. 2, pp. 25–40.

Tatsuoka, F., Iwasaki, T., Fukushima, S. & Sudo, H. (1979). Stress conditions and stress histories affecting shear modulus and damping of sand under cyclic loading. *Soils and Foundations*, vol. 19, no. 2, pp. 29–43.

Terzaghi, K., Peck, B.R. & Mersi, G. (1996). *Soil mechanics in engineering practice.* 3rd edn. John Wiley & Sons Ltd.

Timoshenko, S.P. & Young, D.H. (1962). *Elements of Strength of Materials.* 4th edn. Van Nostrand Company Inc. Princeton, New Jersey, N.Y.

Timoshenko, S.P., Young, D.H. & Weaver, W. (1974). *Vibration Problems in Engineering.* 4th edn. John Willey and Sons, Inc.

Vallejo, L.E. (1995). Fractal analysis of granular materials. *Géotechnique*, vol. 45, no. 1, pp. 159–163.

Wadell, H. (1932). Volume, shape and roundness of rock particles. *Journal of Geology*, vol. 40, pp. 443–451.

Wadell, H. (1933). Sphericity and roundness of rock particles. *Journal of Geology*, vol. 41, pp. 310–331.

Walton, K. (1987). The effective elastic moduli of a random packing of spheres. *Journal of the Mechanics and Physics of Solids*, vol. 35, no. 2, pp. 213–226.

Wang, Y.-H., Cascante, G. & Santamarina, C. (2003). Resonant column testing: The inherent counter emf effect. *Geotechnical Testing Journal*, vol. 26, no. 3, pp. 1–11.

Wang, Z. & Nur, A. (1992). Elastic wave velocities in porous media: a theoretical recipe. *Seismic and Acoustic Velocities in Reservoir Rocks*, vol. 2, pp. 1–35.

Wichtmann, T. & Triantafyllidis, T. (2004). Influence of a cyclic and dynamic loading history on dynamic properties of dry sand, part I: cyclic and dynamic torsional prestraining. *Soil Dynamics and Earthquake Engineering*, vol. 24, no. 2, pp. 127–147.

Wilson, J.D., Klotz, L.D. & Nagaraj, C. (1997). Automated measurement of aggregate indices of shape. *Particulate Science and Technology*, vol. 15, no. 1, pp. 13–35.

Wood, A.B. (1941). *A textbook of sound.* G. Bell & Sons,.

Wood, D.M. (2007). The magic of sands-the 20th Bjerrum lecture presented in Oslo, 25 November 2005. *Canadian Geotechnical Journal*, vol. 44, no. 11, pp. 1329–1350.

Yudhbir & Abendizadeh, R. (1991). Quantification of particle shape and angularity using image analyser. *Geotechnical Testing Journal*, vol. 14, no. 3, pp. 296–308.

Zingg, T. (1935). Beitrag zur schotteranalyse. *Schweiz. Mineral. Petrog. Mitt.*, vol. 15, pp. 39–140.